IUSS
Scuola Universitaria Superiore Pavia

Istituto Universitario di Studi Superiori di Pavia

Development and Verification of Innovative Modelling Approaches for the Analysis of Framed Structures Subjected to Earthquake Action

A Thesis Submitted in Partial Fulfilment of the Requirements
for the Degree of Doctor of Philosophy in

EARTHQUAKE ENGINEERING AND ENGINEERING SEISMOLOGY

Obtained in the framework of the Doctoral Programme in
Understanding and Managing Extremes

by

Romain Sousa

November, 2015

IUSS
Scuola Universitaria Superiore Pavia

Istituto Universitario di Studi Superiori di Pavia

Development and Verification of Innovative Modelling Approaches for the Analysis of Framed Structures Subjected to Earthquake Action

A Thesis Submitted in Partial Fulfilment of the Requirements
for the Degree of Doctor of Philosophy in

EARTHQUAKE ENGINEERING AND ENGINEERING SEISMOLOGY

Obtained in the framework of the Doctoral Programme in
Understanding and Managing Extremes

by

Romain Sousa

Supervisors: António A. Correia, National Laboratory for Civil Engineering
João Almeida, École Polytechnique Fédérale de Lausanne
Rui Pinho, University of Pavia

November, 2015

ABSTRACT

The last decades have witnessed significant progresses in the development of improved numerical models for structural analysis, as proven by hundreds of dissertations, theses, reports and journal papers dedicated to advanced constitutive models of materials and algorithms to model sectional, element and structural response. Nevertheless, the seismic behaviour of structures involves a number of nonlinear material and geometrical phenomena that, ultimately, are impossible to capture exhaustively in a single model. Furthermore, past studies showed that the most correct modelling options from the scientific viewpoint are sometimes challenged by experimental evidence.

This thesis intends to contribute to the ongoing effort of progressively bridging the existing gap between solid theoretical principles adopted in nonlinear modelling and experimental results from shake table or other experimental techniques. Such goal is firstly pursued through the application of a sensitivity analysis to the simulation of the dynamic behaviour of three distinct structures with distributed plasticity beam-column fibre-based elements based on Euler-Bernoulli beam theory. The latter were tested in international blind prediction challenges wherein the author and/or supervisors participated with encouraging results.

The goodness-of-fit for each approach is assessed through comparisons between numerical and experimental results in terms of lateral displacements as well as accelerations (when available), following two post-processing strategies: a more conventional one based on the error associated to the peak values measured during each record, and another using the frequency content characteristics of the entire response history. Sensitivity parameters included equivalent viscous damping, element discretization scheme, strain penetration effects, material constitutive models, numerical integration algorithms and analysis time-step size. The conclusions, which are interpreted in the light of state-of-the-practice recommendations and established theoretical frameworks, address fundamental modelling decisions for engineers and researchers.

The referred sensitivity analysis identified the simulation of strain penetration effects as particularly relevant. They can significantly impact the seismic response of structures, contributing up to 40% of the overall lateral deformation of RC framed structures.

Within this context, the last chapters of the thesis present a novel bond-slip model for RC structures that simulates the member-end deformations associated with strain penetration effects. The model, which in its final form is implemented as a zero-length element, was developed so that it is compatible with any general fibre-based frame analysis software. In a nutshell, the element response is determined from cross-sectional fibre integration, where at each rebar the anchorage mechanism is explicitly modelled through a series of virtual integration points distributed along the anchorage length. The analysis is carried out by an algorithm that enforces both equilibrium and compatibility at every integration point, making use of a state-of-the-art bond stress-slip cyclic constitutive relation applicable to a wide variety of anchorage conditions. Therefore, features such as the expected failure mode (pullout or splitting), or parameters such as the concrete strength, embedment length, cyclic degradation, amplitude of steel strains, rebar type (plain or ribbed), transverse pressure, level of confinement and bond conditions can be explicitly modelled.

The element was implemented in a structural analysis software and its performance was assessed against several experimental tests, showing an encouraging accuracy while retaining appreciable computational efficiency.

ACKNOWLEDGEMENTS

Despite being an individual work, this thesis reflects somehow the contribution of a number of people to whom I would like to express my gratitude.

My first words are necessarily addressed to Professor Rui Pinho. He has been my mentor since I arrived to Pavia, and I will always be grateful to him for offering me the privilege to share both work and personal experiences with such a prominent and enthusiastic person. For this confidence from day one, it is my hope that I have been able to live up to his expectations.

I would like to also express my most sincere thanks to Doctors João Almeida and António Correia. They were my guiding light along these years and I am deeply acknowledged for their teachings and continuous encouragements in the pursuit of improved solutions. At the hardest hours they were always the firsts to push me forward. Above all, I am grateful for being able to preserve and reinforce the friendship with all of my supervisors, which started way before this long journey.

I take this opportunity to informally thank the National Laboratory for Civil Engineering, particularly the Earthquake Engineering and Structural Dynamic Unit for hosting me during a relevant period of the thesis. For the kindness and the exchanged experiences, I would like to thank to all the personnel of the unit, in particular to Doctors Alfredo Campos Costa, Paulo Candeias, Alexandra Carvalho and António Correia (again).

To all the friends I made in Pavia, especially to Ricardo Monteiro, Vítor Silva, Luís Sousa and Claudia Zelaschi, I am thankful for the interesting discussions and great moments spent on the streets of Pavia or in someone's apartment. They were my second family during an important period of my life.

A special word to my family who has always accompanied me in my decisions, being the main support at the good and bad moments. I would like to address some additional words to my brother Hélder, for the interest revealed and promptitude to help at every occasion, and to my little sister Vanessa, for having received me and shared the evenings in her house during my stay in Lisbon. A final word to my little nephews for their contagious joy.

Fátima, more than anyone, you experienced the vicissitudes of this doctoral program. I am not sure if I can find a way to reward you for the countless days and nights we spent apart. Despite everything, you were always a support and an endless source of motivation. More than ever, I know that our love can only grow in the future.

Dear mother and father, my words are too little to thank you for everything you made for me. Thank you for making me feel the proudest a son can be. This humble work is dedicated to you.

"Everything should be made as simple as possible,
but not one bit simpler"

Albert Einstein, (attributed)
US (German-born) physicist (1879 - 1955)

TABLE OF CONTENTS

LIST OF FIGURES

LIST OF TABLES

LIST OF SYMBOLS

a_1, a_2 = Rayleigh Proportionality Parameters

c = Damping Coefficient

d_b = Diameter of Longitudinal Rebar

f = Frequency of Vibration

f_c = Concrete Compressive Stress

f_{cm} = Mean Concrete Compressive Stress

f_{ctm} = Mean Concrete Tensile Stress

f_y = Yield Stress of Steel

f_{ym} = Mean Yield Stress of Steel

f_u = Ultimate Stress of Steel

f_{um} = Mean Ultimate Stress of Steel

f_r = Bond Index

k = Stiffness

m = Mass

r = Strain Hardening Parameter

s = Spacing Between Transvers Reinforcement

t = Time

u = Relative Displacement

$\dot{u}$ = Relative Velocity

$\ddot{u}$ = Relative Acceleration

$\ddot{u}_g$ = Ground Acceleration

w_{cr} = Crack width

A_0 = Area of Monotonic Bond-Slip Curve

A_1, A_2 = Shape Parameters in Reinforcement Models

A_b = Area of Rebar

A_c = Area of Concrete Fibre

A_{cyc} = Cumulative Area of Cyclic Hysteresis

A_s = Shear Area

C_{clear} = Clear Spacing Between Rebar Ribs

D_{hook} = Diameter of Hook

E_c = Modulus of Elasticity of Concrete

E_s = Modulus of Elasticity of Steel

$E_{s,sp}$ = Modulus of Elasticity at Strain Hardening

F_{bar} = Rebar Force

F_{bond} = Bond Force

F_c = Concrete Fibre Force

F_{fibre} = Fibre Force

F_0 = Force at Loaded-End of Rebar

$F_{0,trial}$ = Trial Force at Loaded-End of Rebar

G = Shear Modulus

I = Moment of Inertia

IP = Integration Point

IP_{eq} = Integration Point of Equilibrium

K_{fibre} = Fibre Stiffness

K_{IP} = Integration Point Stiffness

K_s = Shear Stiffness

K_{tan} = Tangent Stiffness

K_Θ = Rotational Stiffness

$K_{unl/rel}$ = Unload and Reload Bond-Slip Stiffness

L_C = Shear Span

L_d = Development Length

L_e = Embedment Length

L_{eq} = Equivalent Embedment Length

L_i = Influence Length

L_{IP} = Distance Between Integration Points

L_p = Plastic Hinge Length

L_s = Straight Embedment Length

L_{SP} = Strain Penetration Length

M = Bending Moment

N = Axial Force

P_b = Perimeter of Rebar

P_{tr} = Transverse Pressure

R_r = Relative Rib Area

S = Rebar Slip

S_0 = Slip at Loaded-End of Rebar

S_{Lz} = Slip at Free-End of Rebar

S_R = Rib Spacing

T = Period of Vibration

α = Bond Stress Parameter

ε_s = Steel Strain

ε_{s0} = Steel Strain at Loaded-End of Rebar

$\varepsilon_{s,y}$ = Yield Steel Strain

$\varepsilon_{s,u}$ = Ultimate Steel Strain

ε_c = Strain at Peak Concrete Stress

μ = Ductility

ξ = Critical Damping Ratio

π = Pi

ρ_l = Longitudinal Reinforcement Ratio

ρ_v = Transverse Reinforcement Ratio

σ = Stress

σ_c = Concrete Stress

τ = Bond Stress

τ_i = Generic Bond Stress

τ_m = Modified Bond Stress

τ_{max} = Maximum Bond Stress

τ_f = Friction Bond Stress

ω = Angular Frequency of Vibration

Δ = Displacement

Δt = Time-Step

Θ = Rotation

$\emptyset$ = Rebar Diameter / Curvature

$\emptyset_y$ = Yield Curvature

Ω_{cr} = Longitudinal Cracking Bond Factor

Ω_{cyc} = CyclicDegradation Bond Factor

$\Omega_{p.tr}$ = Transverse Pressure Bond Factor

Ω_y = Rebar Yielding Bond Factor

1. INTRODUCTION

1.1 RESEARCH MOTIVATION AND OBJECTIVES

Since the appearance of simplified methodologies in the mid-20th century (e.g. [Muto, 1956]), the seismic analysis of structures witnessed a great evolution up to the present days. Modern seismic design and assessment of structures tends to rely heavily on numerical simulation tools. Their development has accompanied the exponential growth of computational power, the advancement of solution algorithms, and the increasing availability of experimental data for model calibration.

Among the available methodologies, nonlinear dynamic analysis appears as the most advanced simulation tool since it allows for an explicit simulation of the structural response to an actual ground motion. Past blind prediction tests showed that, by making use of specific combinations of modelling options, the nonlinear dynamic response of reinforced concrete (RC) structures can be predicted with satisfactory accuracy. Figure 1.1 presents a summarised comparison between the experimentally measured maximum displacements and the numerical estimates submitted by the author and supervisors to two different international blind prediction challenges [Terzic *et al.*, 2015; Costa *et al.*, 2012]. Although the authors won the competition for Structures 2 and 3 (among 38 international teams), and obtained an 'Award of Excellence' for Structure 1 (among 41 international teams), it can be observed that there is ample space for simulation improvements.

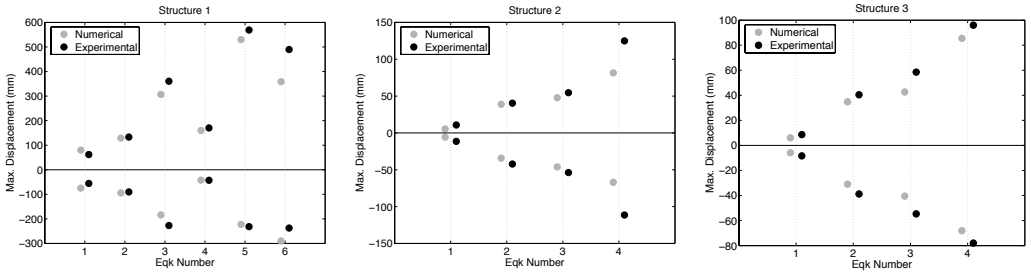

Figure 1.1. Comparison between experimental results and numerical simulations submitted by the authors to different blind prediction challenges: maximum displacements for seismic motions of increasing intensity

The comparison of other physically measurable quantities at a more local level would further emphasize this preliminary observation. The abovementioned structures, which will be used throughout the present work, are described along with their corresponding experimental program in Section 3.1.

Furthermore, the preceding blind challenges have also evidenced a significant dispersion of predictions between the participating teams, which is more meaningful upon observation that such scatter takes place also between teams using the same structural simulation software as the winning team. This clear symptom of lack of consensual modelling principles causes concern and makes it fundamental to identify the main sources of inaccuracy in nonlinear structural analysis so as to progressively reach an agreement on the modelling options that minimize the gap between experimental and numerical response.

Figure 1.2, which shows the results achieved by all the participants on the blind prediction pier test corresponding to Structure 1 [Terzic *et al.*, 2015; Schoettler *et al.*, 2015], further supports the comments above. It is noted that, even for such a rather simple structure (a single pier with a mass at the top), the predictions for the response parameters submitted by the different teams vary by more than one order of magnitude.

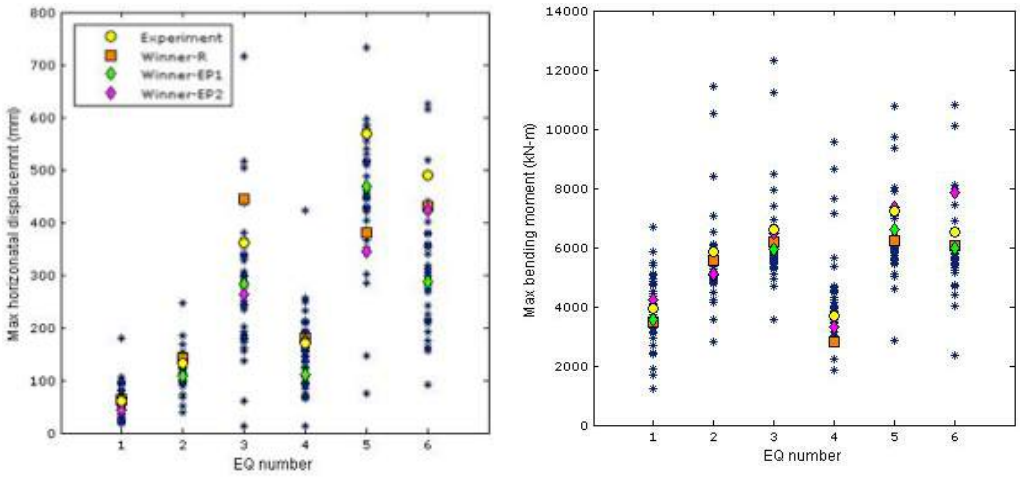

Figure 1.2. Comparison between experimental results and numerical simulations on the 'Concrete Column Blind Prediction Contest 2010': maximum horizontal displacement (left) and maximum bending moment (right) (adapted from Terzic *et al.* [2015])

A first and crucial decision that every engineer faces when modelling a frame structure for seismic analysis – which is further conditioned by the available structural analysis software – is related to the choice of the element type. Amongst the available approaches, frame models developed in the framework of the Euler-Bernoulli beam theory with distributed plasticity are often considered to offer the best compromise between the degree of output detail and computational demand, at least for research or specialized earthquake engineering applications. Lumped plasticity models are simpler and computationally lighter, but they do not allow modelling the spread of inelasticity throughout the member. In addition, the use of such approach requires the *a priori* knowledge of the location and extension of inelasticity, which is only possible under certain limiting assumptions [Hines *et al.*, 2004]. Moreover, modelling elements through lumped plasticity models requires a high level of expertise in order to define appropriate constitutive hysteretic relations taking into account the variations of axial force. Hereinafter, the present work focuses solely on distributed plasticity models.

Recent attempts have been made to identify and measure the importance of different modelling options (e.g., [Sousa *et al.*, 2012; Blandon, 2012; Yazgan and Dazio, 2011a, 2011b]). The current study intends to consolidate some of these findings and to further extend them in order to progressively bridge the gap between solidly established theoretical principles and experimental results from shake table tests. Based on the conclusions of previous studies and preliminary tests by the authors, it was found particularly pertinent to analyse the following modelling options given their potential to more critically affect the finite element simulation results and therefore the prediction of engineering demand parameters (EDPs) on which performance-based assessment is ultimately based:

1. Equivalent viscous damping models
2. Element formulation and discretization scheme
3. Strain penetration effects
4. Material constitutive models
5. Numerical integration and time-step size

These variables were used in the numerical applications presented in Chapter 3, wherein the shake table responses of the three foregoing RC structures served as a benchmark. The goodness-of-fit of each approach, assessed in terms of lateral displacements, as well as accelerations when available, is determined based on the error associated with the peak values measured during each time-history record, together with a new frequency-domain error capable of evaluating the records under comparison in terms of both amplitude and frequency content.

The sensitivity study carried out shows that some of the modelling options seem to present a matured level of development and implementation, namely regarding the material constitutive models as well as the time-domain integration algorithms and time-step size. However, important limitations were identified in other modelling options, namely with respect to the use of equivalent viscous damping models, alternative discretization schemes and the simulation of strain penetration effects. In particular, the simplified modelling approaches that are typically used to model the latter in common nonlinear software packages appear to be highly unsatisfactory.

When subjected to seismic loading, RC members often depict localized member-end deformations due to rebar slippage between adjacent members, such as beam-column and column-footing joints. Past experimental programs (e.g., [Sezen and Moehle, 2004] and [Goodnight *et al*., 2015a]) indicate that the resultant member-end rotations can contribute up to 40% of the lateral deformation of the RC members (Figure 1.3).

Despite the recognized importance of strain penetration effects on the response of RC structures, the consideration of such effects in numerical models is still not widespread. The employment of advanced bond-slip models within detailed 3D finite element (FE) formulations, capable of simulating continuous domains with highly discretized meshes, has witnessed great advances over the recent years with encouraging results. Nonetheless, these modelling approaches are computationally heavy and, hence, inapplicable for most practical seismic analysis of RC framed structures.

Alternatively, the consideration of beam-column elements featuring lumped or distributed plasticity represents an alternative solution that is computationally more efficient and, therefore, preferable for most common engineering applications. Unfortunately, for such modelling approaches, the explicit simulation of the interface between the reinforcing bars and the surrounding concrete is not a straightforward task. Therefore, the inclusion of bond-slip effects in beam-column element models has been essentially achieved through the employment of simplified formulations based on empirical relations.

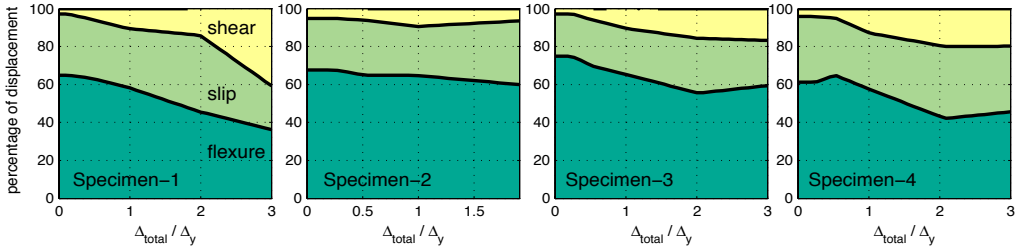

Figure 1.3. Contribution of different deformation mechanisms to the total lateral displacement according to Sezen and Moehle [2004]

The present study aims at overcoming the foregoing limitation through the development of an explicit bond-slip model applicable to general fibre-based beam-column elements. Adopting a state-of-the-art bond stress-slip cyclic constitutive model, it introduces a zero-length element to simulate the localized member-end deformations resulting from the contribution of the bond-slip response associated to each rebar of a given RC cross-section. Along with the material properties and anchorage conditions, the proposed nonlinear model also accounts for cyclic degradation and rebar yielding effects. Validation studies conducted with the proposed numerical formulation reveal a good agreement with past experimental tests, evidencing an encouraging numerical stability and accuracy at the expense of an acceptable additional computational effort.

1.2 THESIS OUTLINE

The present dissertation is organized in 7 chapters. Following the current introductory text (Chapter 1), Chapter 2 presents a brief discussion on the theoretical framework and current recommendations enveloping modelling options that, in the author's opinion, represent some of the main sources of epistemic uncertainty in current nonlinear analysis of RC framed structures. In addition, this chapter also discusses the consideration of simplified wide-column models to simulate the response of RC wall buildings.

Based on the above findings, Chapter 3 presents a sensitivity study using three different RC structures featuring alternative modelling options. The analysis of the results allows extracting important indications on the appropriateness of the different solutions considered. Furthermore, this chapter puts into evidence the need to develop improved numerical models to simulate the strain penetration effects in RC members.

The subsequent three chapters, which constitute the core of the thesis, are dedicated to conceptualize, implement and validate a novel bond-slip model for fibre-based nonlinear beam-column elements. Namely, Chapter 4 provides a detailed state-of-the-art review on bond behaviour under different anchorage conditions, together with the identification and characterization of the most relevant numerical approaches currently available to model strain penetration effects.

Chapter 5 presents the theoretical background of the proposed bond-slip model alongside with the numerical formulation, solution algorithms and implementation strategies adopted. The adopted bond stress-slip constitutive relation is also described and validated.

Chapter 6 is divided in two parts. The first introduces a quantitative study on the relative importance of the different anchorage parameters incorporated in the proposed bond-slip model. The second validates the numerical response computed with the proposed model

against a wide selection of experimental tests, evaluating the response at different structural levels while considering progressively more complex structures and loading demands.

Finally, the main conclusions of the present research work are summarized in Chapter 7, while some suggestions for future developments are proposed.

2. NONLINEAR MODELLING OF RC STRUCTURES

Over the last years, attempts have been made to identify and measure the importance of different modelling options (e.g., [Sousa *et al.,* 2012; Blandon, 2012; Yazgan and Dazio, 2011a, 2011b]). This work intends to consolidate some of these findings and further extend them in order to progressively bridge the gap between solidly established theoretical principles and shaking table tests' results.

The present chapter presents a comprehensive theoretical discussion on the following sensitivity parameters:

- Equivalent viscous damping models
- Element formulation and discretization scheme
- Strain penetration effects
- Material constitutive models
- Numerical integration algorithms and time-step size

In Chapter 3, the response of three different structures used in international blind prediction challenges will serve as benchmarks for a sensitivity study considering the above listed modelling options.

At the end of the present chapter, a discussion on the use of simplified wide-column models to simulate the response of RC wall buildings is carried out. The appropriateness of this simplified solution is appraised against a shake table test of a scaled U-shaped RC mockup representative of a component extracted from a nuclear power plant building.

2.1 DAMPING

"In spite of a large amount of research, understanding of damping mechanisms is quite primitive". This excerpt extracted from Adhikari [2000] summarises the state-of-the-art regarding the comprehension of damping mechanisms and the corresponding simulation with current numerical tools, which are explored in more detail in the subsequent sections.

2.1.1 Damping in Structures

Damping in structures is generally associated with the decay of free-vibration motion due to energy dissipation mechanisms in structural, non-structural, and substructural components. In real structures, several irreversible thermodynamic processes concur to such decay, e.g., global damage in the components, internal friction between materials or at connections, opening and closing of micro-cracks in the materials, and friction between the structure itself and non-structural elements [Chopra, 1995].

Measuring and comparing damping of different structures subjected to distinct loadings is a favoured way to understand the energy dissipation mechanisms in structures. The relation between damping values and structural period of vibration has been recognized for a long time [Wakabayashi, 1986]. In Section 2.4.3.4. of the report PEER/ATC 72-1 [PEER/ATC, 2010], a summary of damping ratios inferred from decrements in peak-to-peak response in free vibrations following shake table or pull-release tests shows that the modal damping values measured in undamaged RC frame (or frame-wall) structures and steel braced frame systems ranged from about 0.5% to 3.5% of critical.

Not surprisingly, significantly damaged structures exhibit modal damping ratios that can go up to 11% [PEER/ATC, 2010]. The compilation of such results indicates that the classical assumption of 5% of critical damping, traditionally adopted in the not-so-distant past as a reference modal damping ratio for RC buildings, may result in a non-negligible overestimation of the energy dissipated during elastic dynamic response.

In order to better understand the energy dissipation associated with different structures, the following sections summarise the results of several studies dedicated to quantify and correlate damping values with distinct structural properties. This information is relevant in the sense that it can provide indications on the amount and type of damping that one can define in nonlinear dynamic analysis.

It should be noted that damping measurements can be influenced by the use of different system identification procedures and quality of the data series considered [Brownjohn and Carden, 2007]. Despite the potential dispersion resulting from this issue, the following observations indicate important trends on what respects the quantification and variation of damping in buildings.

It is commonly accepted that damage, and consequently energy dissipation, increases with the amplitude to which the structures are subjected. Based on a significant full-scale measurement database, Jeary [1986] proposed a model that relates the damping in buildings with the amplitude of their deformations (Figure 2.1).

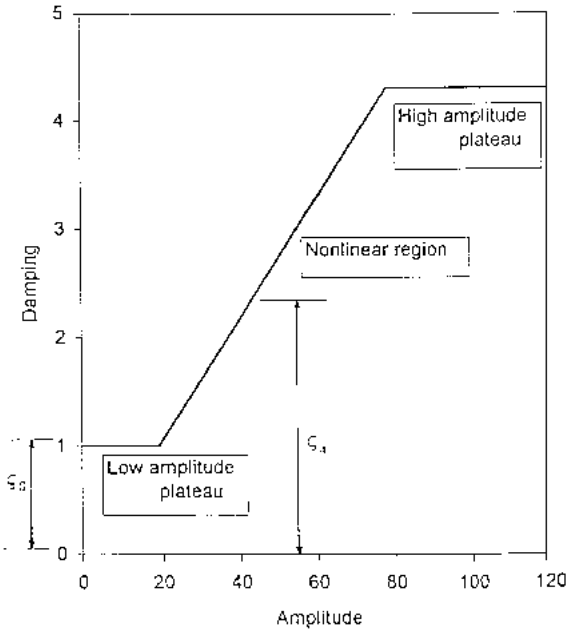

Figure 2.1. Variation of damping with amplitude [Fang *et al.*, 1999]

According to this model, at very low amplitudes only the large-scale imperfections are mobilized (e.g. interface of structural elements), whilst for increasing amplitudes the largest material imperfections start to be mobilized. Eventually, all possible mechanisms are activated and even for increasing amplitude, the energy dissipation remains constant [Jeary, 1997].

Over the last two decades, a number of authors proposed predictive expressions for modal damping ratios based on data measured from hundreds of existing buildings. The results presented in Figure 2.2 provides a comparison between the prediction models proposed by Lagomarsino [1993] and Satake *et al.* [2003] against a large database comprising measurements on 205 buildings in Japan.

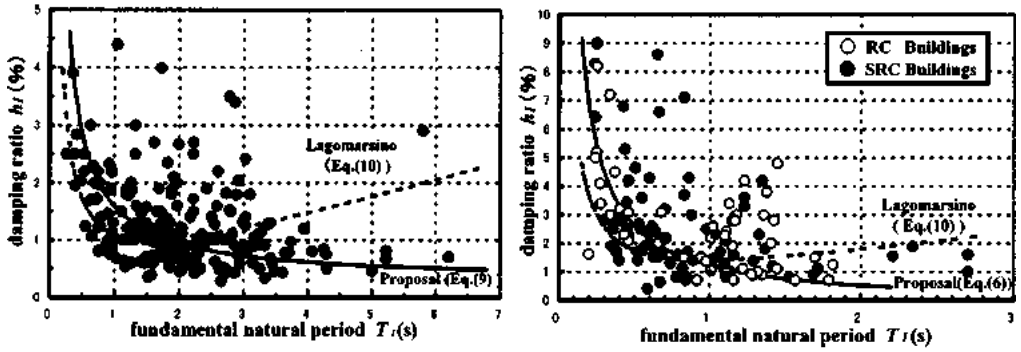

Figure 2.2. Lagomarsino's and Satake's damping predictor with respect to fundamental natural period of buildings [Satake *et al.*, 2003]

It is apparent that the damping ratio decreases with the increase of the fundamental period of vibration. Moreover, the damping in steel buildings tends to be lower than in RC buildings.

Considering the large scatter exhibited in the previous figure, alternative studies were conducted considering databases filtered in order to include buildings whose damping values were obtained only at very low amplitudes (Figure 2.3).

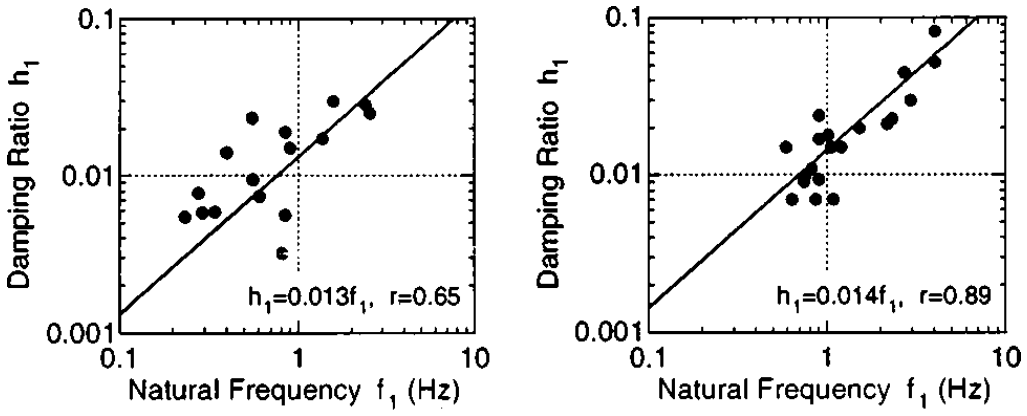

Figure 2.3. Damping ratio versus natural frequency at very low amplitude for steel (left) and RC (right) buildings [Satake *et al.*, 2003]

Among the available studies, Jeary [1986], Lagomarsino [1993] and Satake *et al.* [2003] propose damping estimations at low amplitudes, solely as a function of the fundamental vibration mode:

- Jeary [1986]

$$\xi(\%) = f_1 \tag{2.1}$$

which is applicable for tall buildings.

- Lagomarsino [1993]

$$\xi(\%) = \propto T_1 + \beta/T_1 \tag{2.2}$$

with α=0.72 and β=0.7 for RC buildings, and α=0.32 and β=0.78 for steel-framed buildings.

- Satake *et al.* [2003]

$$\xi(\%) = 1.4f_1 \quad \text{(RC buildings with 10m<h<130m)} \tag{2.3}$$

$$\xi(\%) = 1.3f_1 \quad \text{(steel buildings)} \tag{2.4}$$

In the expressions above, ξ is the damping ratio for the first mode expressed in percentage, while f_1 and T_1 represent the fundamental frequency (in Hz) and period (in s) respectively. As illustrated in Figure 2.4, the previous expressions show that for RC buildings with 0.4 s < T_1 < 2.5 s, the damping estimations vary essentially between 0.5% and 3.5% (using common period-height relations).

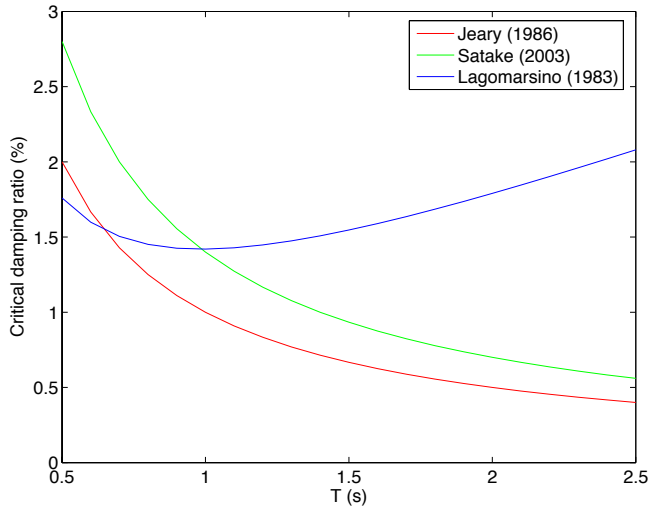

Figure 2.4. Damping predictors for RC buildings

Based on a database of steel buildings higher than 20 storeys subjected to light to moderate wind oscillations, Kareem and Gurley [1996] showed that the damping ratios tend to increase for higher modes of vibration (Figure 2.5).

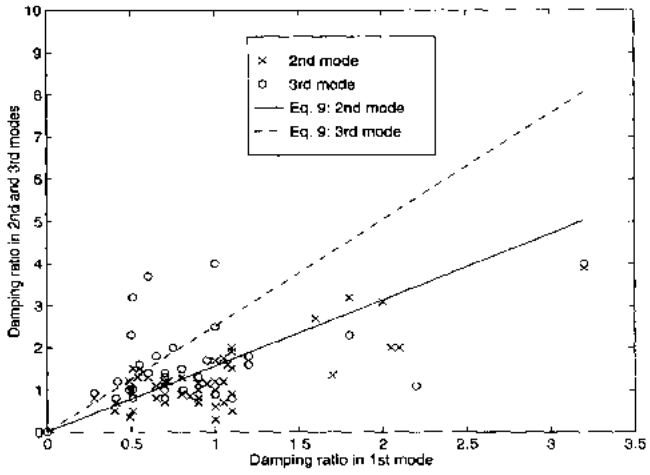

Figure 2.5. Damping ratios at higher modes of vibration [Kareem and Gurley, 1996]

On the other hand, the results obtained by Morita and Kanda [1996] and Arakawa and Yamamoto [2004], indicate that it is difficult to identify a trend for the estimation of damping values associated with the higher models of structures. Figure 2.6 shows the damping values of a bare building determined by Morita and Kanda [1996] considering different measurement methods.

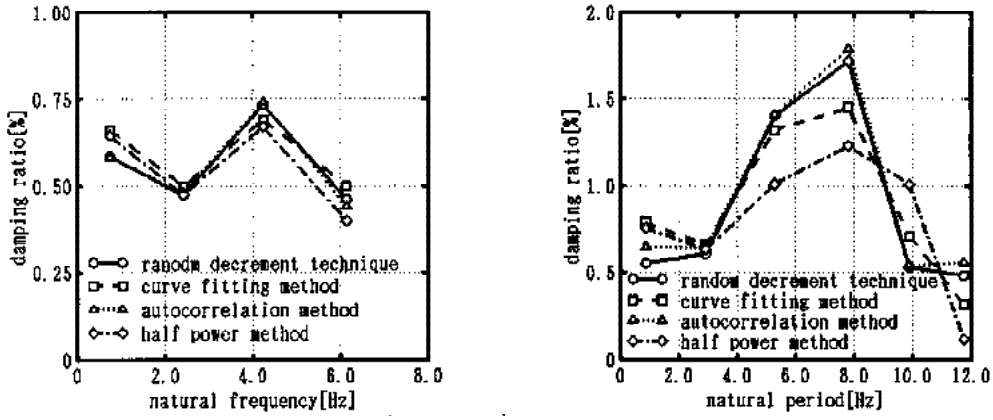

Figure 2.6 Damping ratios at higher modes considering different measurement methods [Morita and Kanda, 1996]

Contrarily to what was observed in Figure 2.5, the figure above indicates that the damping values can change significantly for different higher modes of vibration without a defined trend. In addition, the results reveal that the determined values may be significantly influenced by the measurement technique, as previously referred.

More recently, a study presented by Erwin *et al.* [2007] indicates that the damping ratios measured in structures may diverge significantly in the two horizontal directions, and that the amount of energy dissipated tends to increase with the building aspect ratio (Figure 2.7).

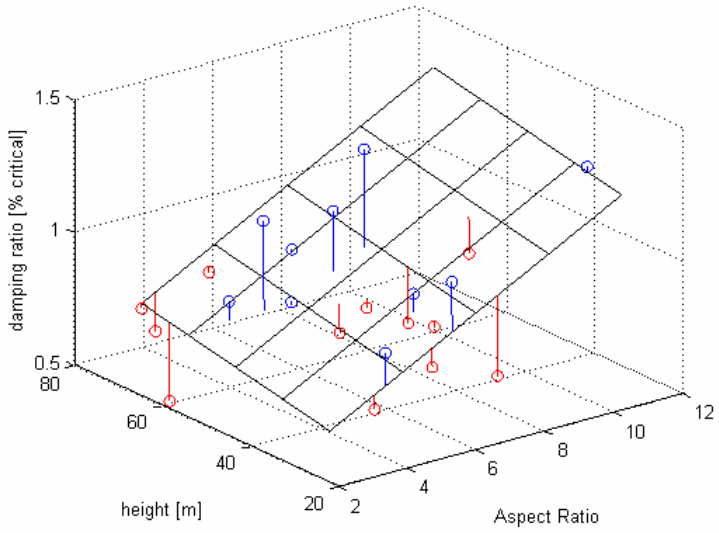

Figure 2.7. Variation of damping ratios with height and aspect ratio [Erwin *et al.*, 2007]

Following this observation, Bentz and Kijewski-Correa [2008] concluded that damping depends on the relative participation of the structural system dominant deformation mechanisms: shear or flexural behaviour. The study defends the hypothesis that damping increases with increasing relative contributions of the shear mechanisms.

Finally, according to Satake *et al.* [2003] the damping ratios vary also with the building occupancy; e.g., office buildings with fewer partitions tend to exhibit lower damping ratios than, for instance, apartment buildings.

In summary, it seems apparent that the energy dissipated in structures tends to decrease with the increase of the fundamental period of vibration, whilst establishing a similar relation regarding higher modes is less straightforward. Despite the relatively low

damping ratios measured under low amplitude vibrations, buildings with structural systems that favour a larger contribution of structural and non-structural components to the global deformed shape under dynamic motions tend to exhibit larger damping values ([Bentz and Kijewski-Correa, 2008] and [Satake *et al.*, 2003]).

2.1.2 Numerical Issues Associated with Equivalent Viscous Damping Models

The previous section presented a summary of several studies dedicated to quantify damping on existing structures and to identify possible correlations with respect do different structural parameters. Moreover, attention was given to the distinction between damping at essentially elastic response of the structures, i.e., without visible damage, and that resulting from higher amplitude deformations.

In view of the difficulties to identify and mathematically describe the dissipating mechanisms in actual structures, damping is usually represented in a highly idealized manner by a set of generalized linear viscous dampers. The damping coefficients are defined so that the dissipated energy is equivalent to the energy associated to all non-modelled dissipation mechanisms. This idealisation is therefore called *equivalent* viscous damping (EVD), which was first introduced by Jacobsen [1930].

In nonlinear analysis, EVD intends to model the energy dissipation at deformation levels within the linear elastic limit. In other words, the energy dissipated by a nonlinear system in a steady-state vibration equals the energy dissipated by an equivalent viscous system. Accordingly, in nonlinear analyses, damping is the result of an elastic component (ξ_{el}), usually modelled through EVD, and a component reflecting the energy dissipation mechanisms explicitly modelled through hysteresis (ξ_{hyst}):

$$\xi = \xi_{el} + \xi_{hyst} \tag{2.5}$$

Considering the well-known equation of motion of a single degree of freedom system:

$$m\ddot{u} + c\dot{u} + ku = -m\ddot{u}_g \tag{2.6}$$

the damping term of the equation depends on the relative velocity ($\dot{u}$) and the damping coefficient (c), which can be expressed as a function of the critical damping ratio (ξ), mass (m) and natural frequency (ω) by:

$$c = 2\xi m\omega \tag{2.7}$$

For multi degree of freedom systems, the determination of the nonlinear response requires the direct integration of the equation of motion and consequently modal superposition is no longer valid. This issue is usually overcome making use of a classical

Caughey damping matrix [Caughey, 1960]. If only the two first terms of the Caughey series are considered, one obtains the well-known Rayleigh damping approach [Rayleigh, 1877]:

$$C = a_0 m + a_1 k \tag{2.8}$$

where a_0 and a_1 are the Rayleigh proportionality parameters that assume the following form:

$$a_0 = 2\xi\omega \qquad a_1 = \frac{2\xi}{\omega} \tag{2.9}$$

If the first or the second equation is set to zero, the Rayleigh damping model becomes simply proportional to the system stiffness (SPD) or the system mass (MPD), respectively. Moreover, when using stiffness-proportional damping, one can define the damping to be proportional to the initial (i.e., elastic) stiffness (ISPD) or to the tangent (i.e., current) stiffness of the system at every instant of the analysis (TSPD).

Figure 2.8 shows the evolution of the damping ratios with the natural frequency for the different Rayleigh damping options described before.

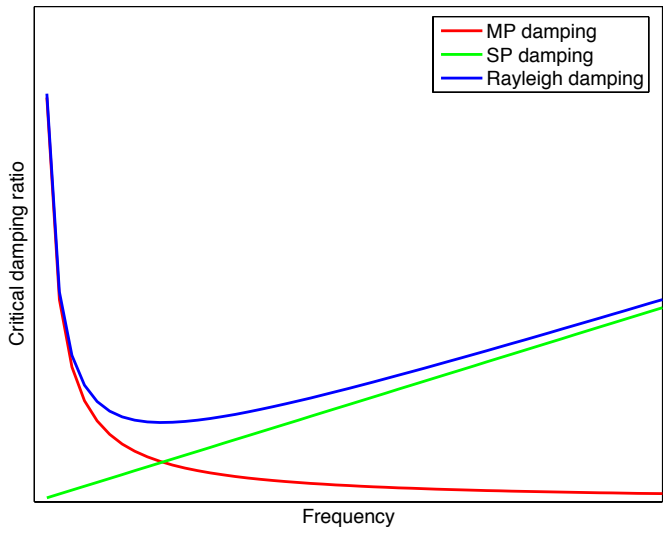

Figure 2.8. Variation of damping ratios with natural frequency for different EVD models

Within the scope of nonlinear frame analysis, the majority of the dissipated energy is explicitly accounted for through hysteretic material models. The use of generalized damping is however needed to reproduce sources of energy dissipation that, given their phenomenological complexity, are difficult to be explicitly simulated.

Hence, the required damping for a given nonlinear dynamic analysis will necessarily depend on the level of detail of the model and the capabilities of the numerical tool used. Sakai and Unjoh [2007] showed that relatively small values of damping (2% Rayleigh) are appropriate to estimate the linear response of columns, whilst residual or no damping (0.1%) leads to better estimations for the nonlinear range.

In this respect, distributed plasticity models tend to require the specification of lower damping ratios since most of the nonlinearity is modelled throughout the extension of the elements. On the other hand, for lumped plasticity models where the dissipation of energy is modelled only at the extremities of the members, larger damping values should be considered. Based on the comparison of an experimental test of a bridge column with nonlinear models considering lumped and distributed plasticity, Petrini *et al.* [2008] realise that when using a distributed plasticity models the best approximation was achieved with no damping, whilst with a lumped model the best agreement was obtained with 5% tangent stiffness proportional damping.

Despite the prevalence of EVD models in seismic analysis, such mechanism is not observed in real structures. Instead, a friction model can more closely reproduce the observed response [Wyatt, 1977]. Realising that energy dissipation in structures results essentially from friction phenomena, several authors proposed alternative damping models with particular focus on friction models. To be noted, among others, the work by Yang and Menq [1998], Menq and Yang [1998], Adhikari and Woodhouse [2000], Adhikari and Woodhouse [2001] and Ruderman and Torsen [2010]. Nonetheless, given the relative complexity with respect to EVD models, such models are potentially less attractive from a numerical simulation viewpoint. Alternatively, Smyrou *et al.* [2011] and Jehel *et al.* [2013] propose useful analytical tools to build damping models with control on the damping ratios throughout inelastic analysis. They focused mainly in the definition of strategies to control the damping forces at higher modes and for increased levels of ductility, i.e., with period elongation.

Some of the inconsistencies found in equivalent viscous damping models can be summarised in the following points:

- Initial Stiffness-Proportional Damping (ISPD)

According to this option, damping forces developed in structures remain proportional to their elastic stiffness, regardless of the ductility demand. Hence, this solution may result in an overestimation of the energy dissipated through viscous damping. Analyses performed by Priestley and Grant [2005] indicate that the energy absorbed by elastic damping in ISPD may approximate the energy dissipated through hysteresis, even for large ductility levels. Consequently, it is very likely that such damping model produces a significant underestimation of peak response displacements during nonlinear dynamic analyses. Moreover, as in general the structural stiffness decreases during earthquake loading, the damping forces may assume unrealistically large values when compared to the member (restoring) forces [Hall, 2006]. Furthermore, Bernal [1994] showed that spurious damping forces are likely to arise in massless degrees of freedom (or with relatively small inertia); the latter tend to undergo abrupt variations in velocity when stiffness changes, leading to unrealistically large viscous damping forces [Jehel *et al.*, 2013].

- Tangent Stiffness-Proportional Damping (TSPD)

Currently, the use of tangent stiffness-proportional damping appears to be the most consensual option within the scientific community. It models a decrease in the energy dissipated through EVD for increasing ductility demands, which reflects an intuitively meaningful physical concept. Nevertheless, this model also presents important setbacks; namely, when the stiffness matrix becomes negative-definite, this model leads to an unrealistic energy input in the structure.

- Stiffness-Proportional Damping (SPD)

The use of SPD models, regardless of the model adopted (ISPD or TSPD), may introduce artificial and significantly large axial forces in the members, leading to convergence issues and potential instability during the analyses. Moreover, as demonstrated by Correia *et al.* [2013], when employing stiffness-proportional damping the member forces are not in equilibrium with the support reactions.

- Mass-Proportional Damping (MPD)

Mass-proportional damping, despite not having an easily identifiable physical meaning, does not exhibit the numerical deficiencies of the previous models. Nonetheless, Hall [2006] reported several weaknesses when large rigid-body modes occur, leading to excessively high velocities; such situation is not common in typical structures but may be important, e.g., when dealing with base isolated buildings. In addition, the damping ratio in MPD models decreases exponentially with a decrease of the vibration period, thus possibly leading to an underdamped higher-mode response.

2.2 ELEMENT FORMULATION AND DISCRETIZATION SCHEME

A first and crucial decision – often conditioned by the available structural software package – that every engineer faces when modelling a frame structure for seismic analysis, is related to the choice of the element model. Lumped plasticity approaches are simpler and computationally lighter, but they do not allow modelling the spread of inelasticity throughout the member. In addition, the use of such approach requires the a priori knowledge of the location and members' extend where the inelasticity would concentrate – something that, according to recent studies, e.g. [Hines *et al.*, 2004], may vary significantly depending on the level of ductility demand. Moreover, modelling elements through lumped plasticity models, requires an high level of expertise in order to define the appropriate moment moment-curvature diagram at the critical section taking into account the materials degradation and variations in the axial force. Alternatively, in order to simulate the spread of inelasticity along the member, distributed plasticity approaches require sufficiently discretized models, either in terms of mesh refinement or number of integration points (IPs). Such issue is discussed in the following section, wherein both cases of displacement-based (DB) and force-based (FB) formulations are analysed.

Independently of the discretization options, under certain conditions a phenomenon known as strain localization (or simply localization) occurs. In frame elements, it can affect both lumped plasticity models [Jirásek, 1997] and distributed plasticity models (DB and FB). The triggering conditions and the description of how it manifests in this latter category of models deserve further separate insight, provided in Section 2.2.2.

2.2.1 Numerical accuracy

If or while localization does not take place during an inelastic analysis, an adequate simulation of the spread of inelasticity along the structural member requires a 'sufficient' mesh refinement of the finite element model. The underlying idea is that it is not necessary to have an extremely refined mesh or countless integration points per member to obtain a close-to-exact response. From the scientific viewpoint, the problem is one of numerical integration accuracy. In fact, the evaluation of the basic element forces (and corresponding stiffness matrix) for DB formulations, or of the basic element displacement (and corresponding flexibility matrix) for FB formulations, requires the evaluation of an integral along the element length [Neuenhofer and Filippou, 1997]. Hence, if the problem is well-posed, the larger the number of integration points (for FB formulations) or the number of elements per member (for DB formulations), the more accurate will be the numerical integration output. Determining the level of refinement for which the results are acceptably close to the exact response is of fundamental importance to keep the model as computationally light as possible. To do so it is extremely relevant to bear in mind that the response can be assessed at the global or/and at the local level as well; i.e., respectively in relation to nodal displacements or curvatures at the IPs. Each

level exhibits distinct convergence properties, as discussed hereinafter. Further, since the concept of a 'sufficiently' discretized scheme holds different meanings depending on whether a DB or a FB approach is adopted, it will be addressed in separate sub-sections. Finally, it is also underlined that the aforementioned 'exact' response holds for the context of an Euler-Bernoulli beam theory, which can bring about important deviations with respect to the 'exact' results that would be obtained from experimental measurements. This point will be addressed in Section 3.4.2.

2.2.1.1 *Displacement-based approach*

Employing the usual cubic displacement interpolation functions for the transverse displacement field creates an artificial restraint amongst the IPs of the same DB element concerning the development of inelastic curvatures. The insensitivity of DB meshes to the increase of the number of IPs per element is intimately related to such feature; therefore, it is not justified to use more than two IPs per element, alongside with a Gauss-Legendre quadrature rule. It is recalled that the latter leads to the exact integration of a polynomial up to degree $2n$-1, where n is the number of IPs.

Capturing the spread of inelasticity can thus only be achieved at the expense of refining the element mesh. A balance—which is dependent on the loading and boundary conditions - should be struck between the desired numerical accuracy and computational cost. In general, a member model with three elements provides an unrealistically stiff response at both the global and local levels. That effect is even more pronounced with two elements - see also Neuenhofer and Filippou [1997], whilst a one-element mesh is wholly unable to simulate the member inelastic behaviour. It can be roughly said that a 'sufficiently' discretized DB scheme implies a minimum of four to six elements per structural member. However, whist the previous rule of thumb usually provides close-to-exact results at the global level, it can simultaneously fall short of yielding acceptable local-level responses: computed inelastic curvatures may underestimate significantly the exact value. Such apparently contradictory feature can be attributed to the fact that DB elements only satisfy equilibrium in an average (integral) sense. If a reliable local-level response is also sought, a very refined DB mesh - around one order of magnitude larger than the previously mentioned rule of thumb - may have to be considered [Calabrese *et al.*, 2010].

2.2.1.2 *Force-based approach*

Unlike the DB approach, force interpolation functions - which strictly verify equilibrium - used in FB elements do not restrain the expected development of inelastic curvatures along the IPs of the same element. Consequently, only one element per structural member is required. Furthermore, the use of a Gauss-Lobatto integration scheme is

advised as it controls the end sections of the element, which are privileged locations for the occurrence of seismic inelastic response.

Consider now the linear elastic response of a planar beam-column element with six degrees of freedom (three at each end node), under geometric linear behaviour. It is straightforward to demonstrate that the element stiffness matrix including the rigid-body modes, obtained according to the FB approach, depends on the number of Gauss-Lobatto IPs used in its derivation:

a) Two integration points:

$$\mathbf{K}_{elem}^{2\text{ IPs}} = \begin{bmatrix} \frac{EA}{L} & 0 & 0 & -\frac{EA}{L} & 0 & 0 \\ & \frac{4EI}{L^3} & \frac{2EI}{L^2} & 0 & -\frac{4EI}{L^3} & \frac{2EI}{L^2} \\ & & \frac{2EI}{L} & 0 & -\frac{2EI}{L^2} & 0 \\ & & & \frac{EA}{L} & 0 & 0 \\ & SYM. & & & \frac{4EI}{L^3} & -\frac{2EI}{L^2} \\ & & & & & \frac{2EI}{L} \end{bmatrix}$$

b) Three or more integration points:

$$\mathbf{K}_{elem}^{\geq 3\text{ IPs}} = \begin{bmatrix} \frac{EA}{L} & 0 & 0 & -\frac{EA}{L} & 0 & 0 \\ & \frac{12EI}{L^3} & \frac{6EI}{L^2} & 0 & -\frac{12EI}{L^3} & \frac{6EI}{L^2} \\ & & \frac{4EI}{L} & 0 & -\frac{6EI}{L^2} & \frac{2EI}{L} \\ & & & \frac{EA}{L} & 0 & 0 \\ & SYM. & & & \frac{12EI}{L^3} & -\frac{6EI}{L^2} \\ & & & & & \frac{4EI}{L} \end{bmatrix}$$

The stiffness matrix depicted on the right-hand side is a classical result of introductory structural theory, and can be exactly retrieved with three or more IPs. On the other hand, the stiffness matrix on the left-hand side shows the consequences of under-integration with two Gauss-Lobatto points: the basic linear elastic response cannot be simulated, as opportunely mentioned elsewhere [Scott and Fenves, 2006]. The use of two Gauss-Lobatto points per FB element is thus strongly discouraged and should be avoided.

Whilst at least three FB Gauss-Lobatto IPs are required to reproduce the linear elastic response, capturing the spread of inelasticity claims for a larger number of IPs. Naturally, the further apart they lie, the less able is the element to realistically simulate the aforementioned physical phenomenon. Once again, a compromise between numerical accuracy and computational time must be found. A 'sufficiently' discretized FB scheme calls for around five IPs to obtain accurate global-level results, while a close-to-exact local-level output typically requires a marginally larger number of IPs (around six to seven). It is recalled that the equivalent local-level accuracy requirements for the DB-mesh counterpart are incomparably more stringent.

2.2.2 Numerical Localization

Formally, localization corresponds to the loss of ellipticity of the governing differential equations, resulting in the loss of uniqueness of its mathematical solution. The initial boundary-value problem thus becomes mathematically ill-posed and a numerical solution becomes mesh-dependent. From the computational mechanics viewpoint, localization is intrinsically related to softening or post-peak constitutive behaviour. In the context of distributed plasticity frame models, localization occurs following the attainment of a post-peak descending branch of the moment-curvature relation at a given IP.

The problem of localization can perhaps be better understood through the lens of the auxiliary notion of objectivity [Coleman and Spacone, 2001]. Consider several DB and FB discretization schemes with an increasing degree of refinement according to the suggestions of Section 2.2.1: if the corresponding global and local-level responses converge to the same (exact) value, the response is said to be objective. If instead divergent results show up, the response is deemed as non-objective and localization takes place, with inelastic curvatures concentrating at one (or possibly more) IP(s).

As stated above, the distinctive fundamental trait of this concentration of inelastic curvatures is that it only occurs upon reaching a softening branch of the moment-curvature relation. This concentration corresponds to the solution of an ill-posed problem, hence it cannot be directly related to a corresponding physical meaning. Additionally, it is accompanied by simultaneous unloading in the neighbouring IPs (or elements, see discussion in Section 2.2.3). In order to maintain post-peak objectivity, regularization techniques must be employed, which are briefly addressed in the following section.

On the other hand, if the sectional response at every IP depicts a fully hardening post-yield behaviour or, equivalently, if the member is not loaded beyond the attainment of a possible peak of the sectional moment-curvature curves, the model response is objective. Hence, arising inelastic curvatures correspond to a well-posed problem (the solution exists and is unique) and carry a clear physical meaning. Their accuracy remains nonetheless dependent on the adoption of a 'sufficiently' discretized scheme, as discussed above in Section 2.2.1.

It should hence be clear that the concentration of curvatures in one element or IP does not necessarily imply localization, in the sense of non-objectivity. From an alternative standpoint, it is also fair to note that if the incursion in the post-peak branch is limited, the effects of localization may not be relevant. The objective of the above discussion was to help clarifying the distinguishing features between a numerical accuracy problem and a numerical pathologic sensitivity to finite element discretization.

2.2.3 Regularization Techniques

The abovementioned distinct features of localization affecting FB and DB approaches naturally call for different ways of maintaining the post-peak objectivity of the results. These constitute the so-called regularization techniques, which require a user-defined parameter specifying the physical dimension of the region into which curvatures localize. In earthquake engineering, the latter corresponds to the expected length of the plastic hinge. Some authors, e.g., Almeida *et al.* [2014], have explicitly adopted the term *real* plastic hinge length to emphasize that confusion often arises with existing well-known formulas for the *equivalent* plastic hinge length. The latter fictitious quantity is in principle only applicable to plastic hinge analysis.

Historically, regularization techniques were first applied to DB elements, since the latter correspond to the original formulation of the Finite Element Method. In nonlinear fibre frame elements, the average verification of equilibrium in DB formulations poses various difficulties in the interpretation of the element behaviour. In particular, it becomes impossible to predict a priori if localization will take place in the most strained IP [Calabrese *et al.*, 2010] or simultaneously in both IPs of the element [Almeida *et al.*, 2014], which probably corresponds to the most common case. In fact, the distinct axial forces determined in each of the two member IPs - their value being symmetric with respect to the applied element axial load - induce different moment-curvature relations and eventually distinct sectional flexural capacities (again, if a fibre approach is employed at the sectional level). The largest moment demand may thus occur at an IP whose flexural capacity is artificially larger than the one of the neighbouring integration point and consequently the softening branch of the moment-curvature curve may be attained first in this latter IP (and only at larger inelasticity demands in the former IP). In short, it is not possible to know in advance, i.e., before running the analysis, if the appropriate regularization method should imply setting the length of the element as the length of the expected plastic hinge length, or rather twice this value.

The first regularization method for FB elements was suggested by Coleman and Spacone [2001]. Due to its time-consuming two-stage application, more recent techniques were proposed [Scott and Fenves, 2006; Addessi and Ciampi, 2007]. They are based on *ad hoc* integration schemes and the observation that, unlike DB approaches, the post-peak accumulation of curvatures in FB elements is bound to happen in the most strained IP; therefore, such approaches scale the integration weights at the element ends to match the value of the expected plastic hinge length. The main problem with such approaches is that they can simulate an unrealistically flexible response when an (objective) strain-hardening constitutive behaviour occurs. To circumvent this problem, a new quadrature rule was advanced by Scott and Hamutçuoğlu [2008], which includes two additional IPs at the extremities. More recently, a versatile adaptive integration scheme that warrants

high numerical accuracy in the pre-peak phase and a regularized response in the post-peak branch was proposed by Almeida *et al.* [2012].

2.3 STRAIN PENETRATION AND ANCHORAGE SLIP

RC members subjected to flexural loading often depict localized deformations occurring between the reinforcement and the concrete of the adjacent members (beam-column and/or column-footing joints). Although relatively large anchorage lengths are provided in modern seismic design and failure is thus not usually expected, the corresponding deformations should be accounted for in analysis. This mechanism can become critical in older RC structures with deficient anchorage detailing and/or smooth rebars with much-reduced bond strength, leading possibly to anchorage failure as observed in a recent blind-test challenge 'Prémio Ricardo Teixeira Duarte' (more information available at the website: http://jpee2014.lnec.pt/concurs_2.html).

The fixed-end rotations result from the spread of reinforcing strains through the anchorage region, which causes strain incompatibility between the reinforcement and the surrounding concrete and potential bond-slip deformations along the anchorage length. These phenomena are often referred in the literature with different terminology, such as strain penetration effects (SP, which will be herein adopted), bond behaviour, anchorage slip or bond-slip mechanisms. If adequate anchorage length is provided, the deformation results solely from penetration of tensile strains along a fraction of the anchorage length. However, if inadequate anchorage is provided, the strain penetration may extend through the entire anchorage length, leading to additional deformations due to bond slip of the complete rebar.

According to Sritharan *et al.* [2000] and Sezen and Moehle [2004], the total lateral displacement of RC members can be increased by up to 40 % due to SP effects. It is observed that, despite the importance of considering strain penetration effects in a general case, these deformations are often neglected in most numerical models of RC structures for seismic analysis. A summary of reference numerical models that do take SP effects into account are herein briefly reviewed. A more detailed investigation is addressed in Chapter 4.

2.3.1 Explicit Strain Penetration Models

Over the last years numerous authors proposed alternative ways to determine and numerically accommodate strain penetration effects. The development of 3D solid finite element models to explicitly simulate the interaction between the longitudinal rebars and the surrounding concrete (e.g., Salem and Maekawa [2004] and Jendele and Cervenka [2006]) appears to be the most realistic way to describe such behaviour. These models are essentially based on fracture mechanics employing advanced material and bond

constitutive relations. Nevertheless, notwithstanding their obvious simulation capabilities, such approaches are computationally demanding and hence the analysis of large complete structures featuring such models is still generally unfeasible.

Monti and Spacone [2000] presented a RC beam element that explicitly accounts for the slip between the reinforcing bars and the surrounding concrete at the cross-sectional level. In this approach, the fibre-section state determination is computed considering that the steel fibre strain is given by the sum of the effects of the rebar deformation outside the anchorage zone and the bond-slip occurring along the strain penetration length. The big advantage of this model is that the SP deformations are directly accounted for at the member formulation, avoiding the need to define additional elements or assume supplementary modelling considerations. Despite being simpler than detailed 3D finite elements analysis, such model is still computationally expensive given the extensive discretization required to accurately capture the rebar response along the embedded length [Zhao and Sritharan, 2007]. In addition, such model is not available in most current software packages, preventing its generalized use by structural engineers.

2.3.2 Implicit Strain Penetration Models

In view of the above mentioned limitations, the development of link elements appears as a natural alternative solution, in particular for frame analysis. They are based on the assumption that the strain penetration deformations can be lumped into a single element located at the member end(s), usually in the form of a zero-length element. The properties of such link elements are generally developed based on empirical data and can be defined at the material (reinforcement and concrete) level [Zhao and Sritharan, 2007] or at the cross-sectional level with suitable moment-rotation relations [Sezen and Moehle, 2004]. Although both solutions appear to compare reasonably well with the provided verification examples, their use is still somewhat restricted to the research community. On the other hand, practicing engineers typically look for alternative simplified approaches readily applicable to the generality of the available structural frame-analysis software.

Along the previous lines, one of the simplest approaches often used in practice - which unfortunately misses clear application guidance - involves the reduction of the Young's Modulus of the reinforcing steel to simulate the increase in member flexibility due to SP effects. Alternatively, the member can be extended by an estimated strain penetration length, which represents another common and simple method that has attracted more attention during past research. The underlying idea of this approach relies on the assumption that these deformations spread along the strain penetration length, contributing to the overall member deformation. In the framework of an equivalent plastic hinge methodology [Fardis, 2009; Priestley *et al.,* 2007], different expressions have

been empirically calibrated to provide an estimation of the equivalent SP length (L_{SP}) at the onset of flexural failure. The following Equations (2.10) and (2.12) by Priestley *et al.* [2007] and Eurocode 8 – Part 3 [CEN, 2005] are widely used:

- Priestley *et al.* [2007]

$$L_{SP} = 0.022 f_y d_b \quad (f_y \; in \; MPa) \tag{2.10}$$

- CEN [2005]

$$L_{SP} = k \frac{f_y d_{bl}}{\sqrt{f_c}} \quad (f_{ye} \; in \; MPa) \tag{2.11}$$

where f_{ye} is the expected yield stress of the longitudinal rebars, d_b is the diameter of the longitudinal rebars, f_c is the concrete compressive strength, and k can assume values of 0.11 or 0.24 depending on the concrete confinement model considered to estimate the overall member deformation. If an improved concrete model is employed (k = 0.11), both expressions produce similar values for a typical concrete strength ($f_c \approx$ 30 MPa). Moreover, despite being calibrated to be applied at ultimate condition, L_{SP} seems to be also valid at flexural yielding [Fardis, 2009]. It is relevant to note that a recent extensive experimental program on bridge columns, wherein detailed strain and slip instrumentation of rebars was carried out, has shown that a constant equivalent strain penetration length was suitable to describe the measured fixed-end rotations throughout the (large) range of curvature ductility demands [Goodnight *et al.*, 2014].

The previous procedure seems to be particularly suitable to predict the response of structures that are expected to respond in the nonlinear range. Nonetheless, a setback of this approach relates to the fact that the modified member becomes artificially more flexible up to yield, when the strain penetration mechanism is expected to be fully developed over L_{sp}. Accordingly, the additional deformability is spread along the length of the artificially elongated member instead of corresponding to a localized flexibility at the element end(s). Moreover, given that the shear span of the element increases for the same sectional flexural capacity, the shear forces computed with a longer element will necessarily be underestimated. The magnitude of this error is nevertheless limited, given that the strain penetration length is of the order of 5 % of the member length. It is also noted that this SP modelling option becomes increasingly difficult to apply as the number of bays and storeys increases, due to evident geometrical compatibility issues.

The last option herein reviewed to model strain penetration, which overcomes some of the previous limitations, considers an elastic rotational spring at the base of the columns, thus keeping the element dimensions unchanged. The elastic stiffness of the spring can be determined such that the stiffness of the system with the spring is the same than the

stiffness-at-yield of a similar element, fixed at the base, but elongated by the strain penetration length [Correia, 2011]. The option to equate the system stiffness at yielding reflects the hypothesis that the strain penetration length is essentially fully mobilized when the longitudinal rebars yield. A graphical interpretation is shown in Figure 2.9, from which the rotational stiffness can be derived:

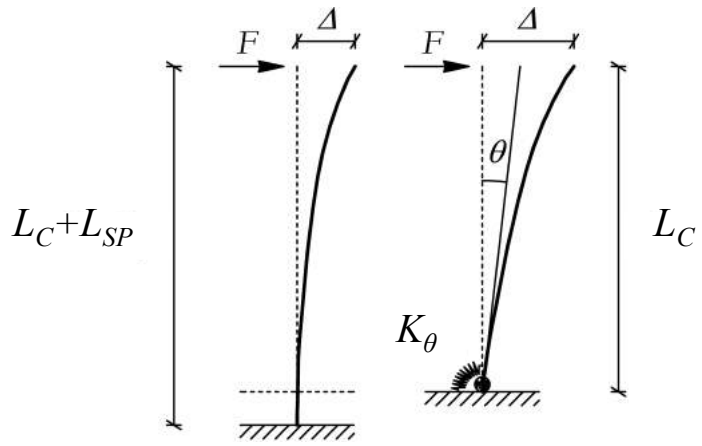

Figure 2.9. Graphical representation of two common SP modelling approaches: elongated element (left) and base spring (right)

Following the reasoning behind the previous figure, one can estimate the rotational stiffness required to achieve the same yielding displacement of an element elongated by the strain penetration length [Correia, 2011]:

$$K_\theta = 3EI_y \frac{L_c^2}{\left[\left(L_c + L_{sp}\right)^3 - L_c^3\right]} = \frac{M_N}{\phi_y} \frac{3L_c^2}{\left[\left(L_c + L_{sp}\right)^3 - L_c^3\right]} \tag{2.12}$$

where L_{SP} can be readily computed with Equation (5) or (6), M_N is the nominal yield moment, and ϕ_y is the yield curvature. The latter can be determined from a bilinear idealization of a cross-sectional moment-curvature analysis.

Figure 2.10 represents the capacity curves of a column (extracted from Structure 2 and structure 3, in Section 3.1), modelled with alternative strain penetration options: (i) no strain penetration, (ii) elongated element and (iii) base spring.

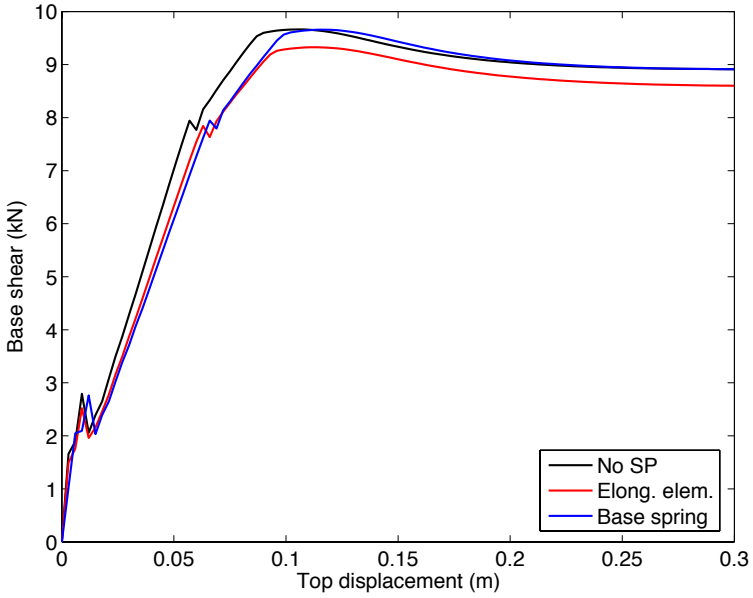

Figure 2.10. Capacity curves of a column of Structure 2 considering alternative strain penetration options

The results show that the use of a base spring approaches as well as the option of an elongated element manage to capture the additional flexibly of the elements when compared with the case in which the strain penetration effects are neglected. Moreover, and contrarily to the longer element solution, the shear forces developed at the element with the base spring are, as desired, in agreement with those computed without strain penetration effects.

2.4 MATERIAL STRESS-STRAIN MODELS

The selection of appropriate material models and corresponding parameters is a key decision in nonlinear modelling of RC structures, in particular for cyclic or dynamic analyses. The uniaxial stress-strain relations adopted for both concrete and steel affect the cross-sectional response at each integration point of the element and correspond to the primary source of structural material nonlinearity.

Amongst the available uniaxial material laws, and despite the numerous models available in literature, Mander's concrete model [Mander *et al.*, 1988] and Menegotto-Pinto steel model [Menegotto and Pinto, 1973] prevail as two of the most commonly adopted in nonlinear analyses of RC structures. Previous studies addressing the effect of the selected material models on the computed response of RC structures (e.g., the works by Yazgan

and Dazio [2011b] and Blandon [2012]) have shown that the choice of different material models, in particular those for steel, may have a significant impact on the computed maximum and residual displacements.

In the following sections, a brief description of some reference models is introduced, highlighting the main features for each case.

2.4.1 Concrete and Confinement

The parameter that most affects the maximum concrete strength and corresponding strain is the confining reinforcement. In the parametric study carried out in the following sections, three concrete constitutive relations featuring different confinement models were considered: (i) Mander *et al.* [1988]), (ii) Madas and Elnashai [1992], and (iii) Kappos and Konstantinidis [1999]. Moreover, the analyses employing Mander's model will consider two options for the tensile strength: one neglects it, while the other considers a tensile strength of $0.75\sqrt{f_c}$ [MPa], as proposed by Priestley *et al.* [1996] for members subjected to flexure. In the latter case, the tensile stress is assumed to increase linearly with strain up to the tensile strength, followed by a subsequent abrupt loss of tensile resistance.

The first model considered - defined as the reference case - is the uniaxial nonlinear model proposed by Mander *et al.* [1988] with the cyclic rules suggested by Martinez-Rueda and Elnashai [1997]. The confinement effects provided by the transverse reinforcement are incorporated through the rules advanced by Mander *et al.* [1988], whereby constant confining pressure is assumed throughout the entire stress-strain range.

Following the same constitutive relation assumed by Mander *et al.* [1988], the model proposed by Madas and Elnashai [1992] considers a confinement factor that varies during the analysis. This coefficient depends on the cross-sectional properties of the elements (dimensions of the cross-section, mechanical characteristics and detailing of the transversal reinforcement) and on the sectional axial load at each step of the analysis.

Kappos and Konstantinidis [1999] observed that, despite the maximum strength of confined concrete being well predicted by most of the confinement models, higher dispersion between the different stress-strain relations was observed beyond the peak stress. Accordingly, they proposed an alternative constitutive model, calibrated for high-strength concrete, following the relation proposed by Nagashima *et al.* [1992] and incorporating the confinement effects through the modified Sheikh and Uzumeri [1982] factor (i.e., the so-called confinement effectiveness coefficient). Contrarily to the Madas and Elnashai [1992] model, the one proposed by Kappos and Konstantinidis [1999]

assumes a constant confinement throughout the entire stress-strain range, which is identical to the one defined in the Mander's model.

Figure 2.11 illustrates the response under compression of the same fibre using the above mentioned alternative concrete constitutive models, at the base section of Structure 1 (presented later in Section 3.1) when subjected to a cyclic history of lateral displacements.

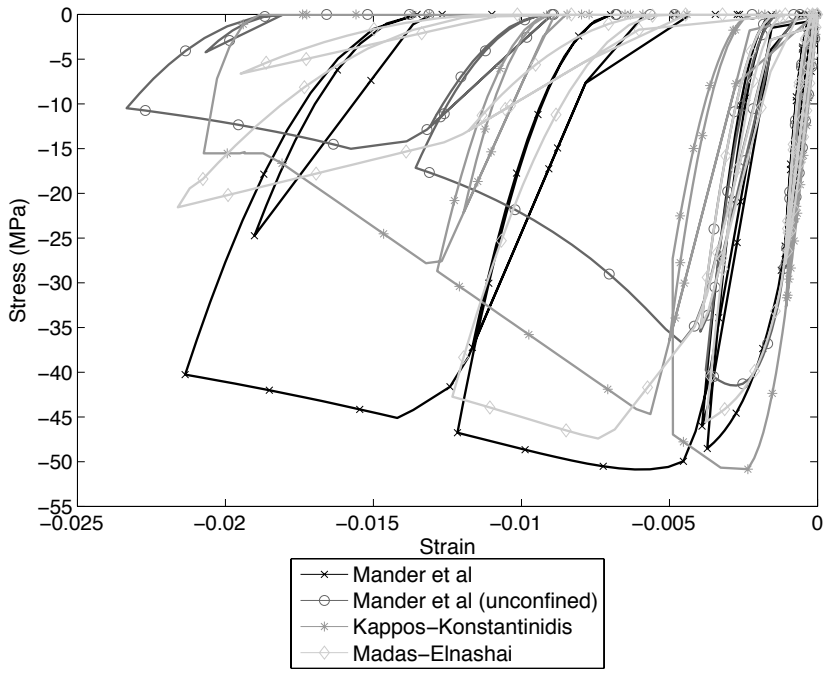

Figure 2.11. Cyclic response of the same concrete fibre in the base section of Structure 1 using distinct uniaxial models, for the same cyclic history of imposed lateral displacements

It can be observed that distinct confinement models modify significantly the stress-strain response. It is clear that Mander's model follows the less steep softening branch when compared to the other confined concrete models. Consequently, it is expected that member response wherein Mander's model is employed will in general show less pronounced localization effects (see Section 2.2.2).

2.4.2 Reinforcement

In the current study, the well-known stress-strain relation proposed by Menegotto and Pinto [1973] is adopted as the reference uniaxial steel model. This model has been shown to be numerically stable and is able to capture the main behavioural features of complex

cyclic loading histories. The Bauschinger effect is accounted for through the definition of a pair of parameters (A1 and A2) that adjust the shape of the transition curves. Considering that the fundamental properties of the rebars, such as yield strength, modulus of elasticity, or strain-hardening related properties, are defined according to the actual properties of the materials, the current parametric study comprises only the evaluation of the different unloading/reloading transition curves. Namely, two values for A2 were assumed: 0.15, in the reference model, and A2 = 0.075 that results in smoother transition curves. The latter facilitate the numerical convergence of nonlinear analysis, but excessively low values of A2 can result in underestimation of the hysteretic energy dissipation.

The simple bilinear uniaxial rebar model, which neglects the Bauschinger effect and hence overestimates the energy dissipation, was also considered in this study. Its abrupt pre-to-post yield stiffness change proved to be numerically more challenging for the analyses than when the Menegotto-Pinto model was employed.

Finally, the Monti-Nuti steel model was also considered. This model uses the Menegotto-Pinto stress-strain relation together with the buckling rules proposed by Monti and Nuti [1992]. It accounts for the reinforcing bar slenderness ratio (s/d_b) in the response of longitudinal rebars undergoing large inelastic deformations, where s is the specified tie spacing and d_b is the longitudinal rebar diameter. In order to overcome stability issues associated with small strain reversals, the considered model incorporates the improvements introduced by Fragiadakis *et al.* [2008].

Previous studies (e.g., Bae *et al.* [2005], Cosenza and Prota [2006] and Fragiadakis *et al.* [2008]) indicate that buckling in longitudinal rebars is mainly dependent on the slenderness of the rebar, the stiffness and the rigidity of the hoops and the strain hardening of steel, and is favoured for slenderness ratios greater than around 5. For the structures considered in this work this ratio is 4.2, 15 and 5 for Structure 1, 2 and 3, respectively. Accordingly, it is expected that the use of Monti-Nuti steel model introduces improvements in the numerical results, in particular for the cases in which buckling is prone to occur.

As for the concrete models, Figure 2.12 illustrates the static cyclic response of the alternative reinforcement constitutive models described before.

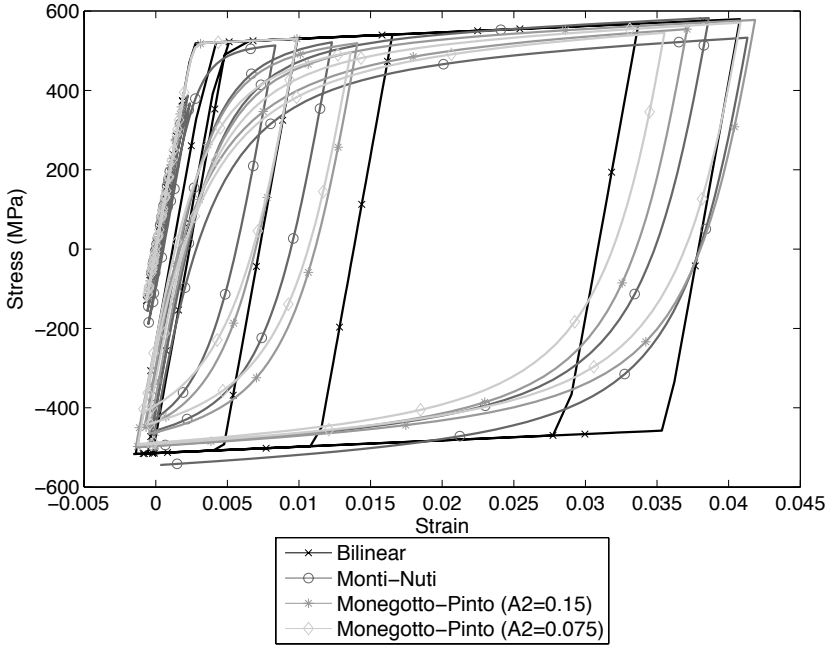

Figure 2.12. Cyclic response of the same reinforcement fibre in the base section of Structure 1 using distinct uniaxial models, for the same cyclic history of imposed lateral displacements

The observation of the hysteretic curves presented in Figure 2.12 shows that, as expected, the bilinear model exhibits a much larger loop area. More interestingly, and contrarily to what can be seen for the concrete fibre responses, the rebar strain levels attained at the end of each imposed displacement cycle may diverge considerably, in particular for larger displacement demands. In fact, as the element response enters the nonlinear range, the neutral axis moves towards the compressed zone of the cross-section and consequently the strains in the tensile zone become more sensitive to small variations in the cross-sectional curvature.

2.5 NUMERICAL INTEGRATION AND TIME-STEP

The integration of the equation of motion in seismic analysis requires the application of advanced numerical algorithms. Among the different options currently available, Newmark's method [Newmark, 1959] appears as one of the most popular because of its superior accuracy. Among the family of Newmark's methods, the constant average acceleration option (resulting from the combination of $\gamma = 0.5$ and $\beta = 0.25$) became widely used since it is an unconditionally stable method, i.e., the stability is verified independently of the time-step of the analysis [Chopra, 1995]. Nonetheless, despite

providing bounded solution regardless of the time-step adopted, there are always computational errors inherent to any numerical solution.

The error attributed to a given numerical method is usually measured in terms of amplitude decay and period elongation/shortening of the response motion, and is associated with the ratio between the time-step of the analysis and the periods of vibration of the structure. Figure 2.13 shows how the period elongation and the amplitude decay of the numerical solution vary with four alternative integration algorithms, reflecting the amount of numerical damping artificially considered in the analysis. It is noted that the "New algorithm" indicated in the figure on the right hand side identifies the well-known Hilber-Hughes-Taylor (HHT) algorithm [Hilber *et al.*, 1977].

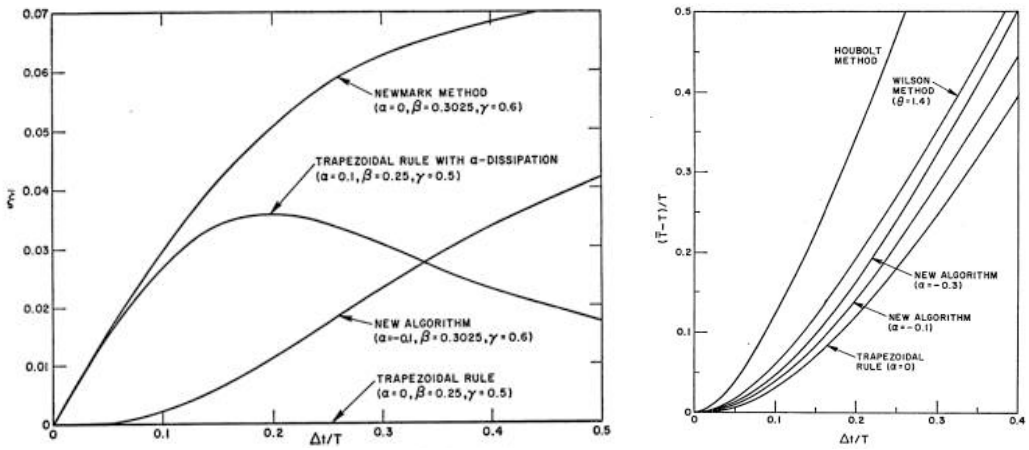

Figure 2.13. Variation of amplitude decay and period elongation with respect to $\Delta t/T$, for different numerical integration methods (adapted from Hilber *et al.* [1977])

Both methods described before are available in most common structural analysis software packages and have been extensively used to perform dynamic analysis. The main difference between them is thus associated with the manner in which the HHT method intentionally filters out the contribution of higher modes (illustrated in the previous figure), reducing, in this way, potential structural spurious responses.

In addition to the selection of the numerical algorithm, the ratio between the analysis time-step and the relevant period of vibration of the structure is a key option regarding the numerical accuracy. A traditional rule of thumb suggests that a time-step equal or lower than 0.1 T, and smaller than 0.02 seconds, is generally sufficient to produce reasonably accurate results, at the same time it ensures a smooth transition between the

steps of the analysis [Chopra, 1995]. Nevertheless, for large structures, the consideration of a reduced time-step can make the analysis time unreasonable, without visible improvements in terms of accuracy.

2.6 SIMPLIFIED WIDE-COLUMN MODELS FOR U-SHAPED WALL BUILDINGS

Reinforced concrete (RC) structures with tri-dimensional asymmetries tend to exhibit torsional effects that are of great concern in the field of earthquake engineering, in particular at large ductility levels where they become more relevant [Mansuri, 2009]. Within the previous idea, the research project SMART 2013 ('Seismic design and best-estimate Methods Assessment for Reinforced concrete buildings subjected to Torsion and non-linear effects') was conducted in order to improve the knowledge on the seismic response of irregular RC structures (experimental test) and to provide reference data for modelling developments and validation (benchmark contest). In addition, the structure analysed in the present project brings an additional challenge in what respects the simulation of RC wall structures with beam-column (line) elements.

After a short description of the SMART 2013 mock-up and corresponding loading protocol, the following sections describes the properties of the numerical model used considered in the blind challenge and compares the numerical results with those obtained from the experiments. The analysis of the results provides indications on the validity of simplified wide-columns to simulate the behaviour RC wall structures, in line with previous studies conducted by Luu *et al.* [2013] and Almeida *et al.* [2014].

2.6.1 Description of the Test Unit and Loading Protocol

In order to assess the capacity of buildings to withstand earthquake loading and evaluate the level of accelerations that can be transferred to the non-structural components at a given floor, a reduced scale model (¼ scale) representing, in a simplified way, half part of an electrical nuclear building (Figure 2.14) was subjected to a large set of dynamic experimental tests. The model was tested at the AZALEE shaking table (Saclay, France) as part of the SMART 2013 project. This project was supported by the Commissariat à l'Énergie Atomique et aux Énergies Alternatives (CEA) and by Electricité de France (EDF).

Figure 2.14. SMART 2013 mock-up

The SMART 2013 mock-up was designed according to the French nuclear regulations and current guidelines for a design spectrum anchored to a peak ground acceleration (PGA) of 0.2 g and a damping ratio of 5 % [Richard and Chaudat, 2014].

The experimental mock-up exhibits a trapezoidal shape in plan (Figure 2.15) and features structural RC walls with openings of variable dimensions, which favour the development of important torsional components. Table 2.1 summarises the main dimensions of the different walls of the mock-up.

For what concerns the material properties, the concrete compressive strength ranges from 35.5 MPa to 46.6 MPa, whilst the yielding strength of the reinforcing bars varies from 500 MPa to 665 MPa, for the different structural elements.

Assuming that most of the mass is concentrated at the floors, additional mass blocks were fixed to the slabs, totalling about 11 tons per floor in addition to the self-weight of the mock-up (approximately 12 tons). The design drawings can be downloaded from the SMART 2013 website: http://www.smart2013.eu.

Table 2.1. Dimensions of mock-up structural elements

Structural component	Length (m)	Thickness (m)	Height (m)
Wall #V01 and #V02	3.1	0.1	3.65
Wall #V03	2.55	0.1	3.65
Wall #V04	1.05	0.1	3.65
Beams	1.45	0.15	0.325
Column	0.2	0.2	3.9

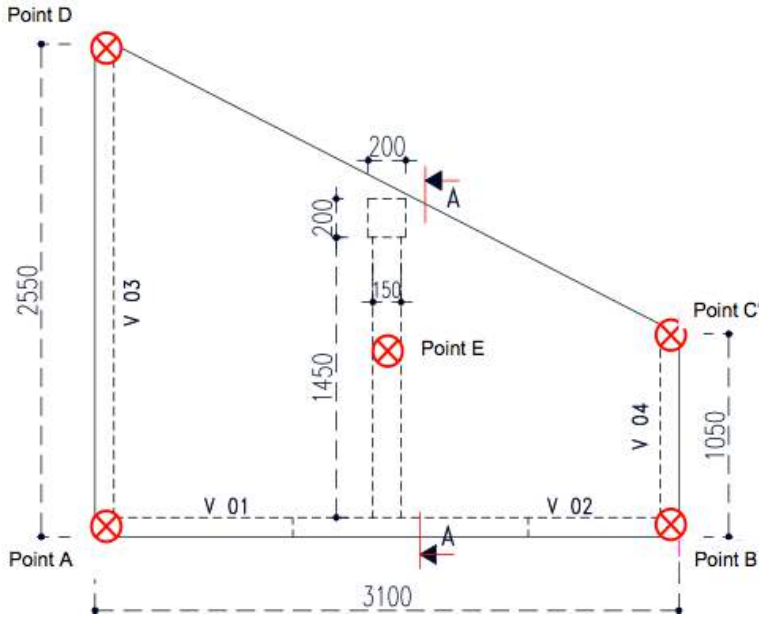

Figure 2.15. Plan view and dimensions of the mock-up (in mm)

The structure was subjected to a series of seismic excitations that can be subdivided into three groups: synthetic (white noise), natural earthquakes and natural aftershocks. While the first group, featuring very low acceleration amplitudes, aims at identifying the dynamic properties of the system, the second one was defined to impose a progressively larger seismic demand up to the desired design level. Finally the third group considers two ground motions representative of actual aftershock motions. Table 2.2 shows the input sequence considered for the models discussed below, together with the peak ground acceleration associated to each run.

Table 2.2: Ground motions' sequence considered in the blind prediction contest

Run Label	Targeted PGA - X (g)	Targeted PGA - Y (g)	Percentage nominal signal (%)	Realized PGA - X (g)	Realized PGA - Y (g)	Type
6	0.1	0.1	100	0.1	0.1	Synthetic white noise
7	0.1	0.1	50	0.13	0.14	Design signal
9	0.2	0.2	100	0.22	0.23	Design signal
11	0.2	0.11	11	0.21	0.16	Northridge earthquake
13	0.4	0.21	22	0.4	0.21	Northridge earthquake
17	0.8	0.42	44	0.6	0.4	Northridge earthquake
19	1.78	0.99	100	1.1	1	Northridge earthquake
21	0.12	0.07	33	0.14	0.14	Northridge (aftershock)
23	0.37	0.31	100	0.7	0.4	Northridge (aftershock)

In addition, the SMART 2013 international benchmark was composed of four main stages. While the firsts two stages (RUN 6 and RUN 7) were essentially dedicated to perform a dynamic characterization of the mock-up and to calibrate the numerical model based on the linear elastic properties of the mock-up, for the third stage of the benchmark the participants were asked to predict the nonlinear response of the structure when subjected to high intensity seismic motions (RUN 9 to RUN 23, as indicated in Table 2.2). The accuracy of the predictions is assessed in terms of displacements and accelerations measured at five different locations at each floor (points A to E in Figure 2.15) along the three coordinate axes.

Additional details regarding the experimental protocol and benchmark stages can be found in Richard and Chaudat [2014].

2.6.2 Properties of the Numerical Model

Beam-column elements (with concentrated or distributed plasticity) are widely used by structural engineers to simulate the nonlinear response of structures. The application of such formulation has proved to be very suitable for framed structures, combining the accuracy of global response parameters with appreciable computational efficiency, e.g., Bianchi *et al.* [2011], Yazgan and Dazio [2011a] and Blandon [2012].

Whilst slender frame elements tend to exhibit a response dominated by their flexural component, the response of wall structures combines other deformation mechanisms that are difficult, if not impossible, to be explicitly modelled with beam-column elements implemented in current state-of-the-practice structural analysis programs. In particular, it is difficult to capture the important shear contribution through the development of inclined cracks in the wall panels, the localized response at the wall-foundation interface, or the interaction with adjacent walls, among other effects.

Despite the above mentioned limitations, the model considered in this study follows a wide-column analogy because it combines the merits of representing a three-dimensional wall structure with inelastic properties while being computationally more efficient, simple and easy to set up when compared to shell or solid finite element models. Furthermore, it is of particular interest to verify the applicability limits of frame models for simulating the behaviour of walls wherein shear deformations should be non-negligible. The numerical model considered was built in the *SeismoStruct* platform [Seismosoft, 2013], using a number of modelling assumptions that are briefly described hereafter.

The cross-sectional properties of the walls were defined considering the (confined) concrete uniaxial nonlinear model proposed by Mander *et al.* [1988] and the well-known steel stress-strain relation proposed by Menegotto and Pinto [1973]. These models are numerically stable and able to capture the behaviour of complex cyclic loading histories.

Given that in a wide-column analogy the vertical elements (walls) are reproduced with line elements, it is not possible to connect directly adjacent elements or define a continuous slab to simulate the floors. Hence, special care should be taken with the definition of the connection between the elements. The connection between adjacent walls was guaranteed through the definition of rigid elastic elements that link the centre of the wall (where the frame element is placed) to the corner where the adjacent wall is connected. It is important to note that the torsional stiffness of these elements should be very low in order to avoid the (unrealistic) transfer of the corresponding sectional forces to the adjoining wall. Moreover, considering the restraining effect of the slab, it was assumed that the relative deformation between the walls, in particular in the out-of-plan direction, was negligible. For that purpose, regarding the modelling of the slabs, a grid of elastic elements approximately reproducing the estimated elastic stiffness of the RC slab was defined, connecting the main structural nodes. Despite requiring a larger number of elements, this solution proved to be numerically more stable, for this particular structure, than the simpler alternative of defining a rigid diaphragm.

In view of the absence of a continuous slab in the numerical model, the additional mass blocks distributed along the slab of the mock-up were lumped at the main structural nodes according to the associated tributary areas. The self-weight of the mock up was implicitly modelled through the specific weight of the materials.

An important decision when modelling a frame structure for seismic analysis is related to the choice of the element model. Lumped plasticity approaches are simpler and computationally lighter, but they do not capture the spread of inelasticity throughout the member as the alternative distributed plasticity models do. Within the later group, force-based (FB) and displacement-based (DB) formulations are usually available, which verify equilibrium along the element length in an exact and average way, respectively. Despite this clear advantage of the FB approach, the analyses performed with FB elements exhibited important convergence difficulties when subjected to large ductility demands. For this reason, the model adopted considers four DB elements for each RC wall.

As previously mentioned, the majority of beam-column formulations available in current software packages do not account for shear deformations. Hence, in order to consider such additional flexibility of the wall elements, zero-length shear springs were introduced at mid-height of each wall. The stiffness of these springs were determined according to the recommendations proposed by Beyer *et al.* [2008]:

$$k_s = \frac{GA_s}{h_{sp}} \tag{2.13}$$

where G is the shear modulus, h_{sp} is the vertical spacing between shear springs and A_s is the shear area, which was taken as 80 % of the gross area of the cross-section. The stiffness computed for each wall was then assigned to the corresponding spring in the in-plane direction, while all other degrees of freedom were rigidly connected (the contribution of shear flexibility in the out-of-plan direction being neglected).

Although the modelling choices of this wide-column model had the purpose of providing an improved response at larger ductility levels, it is also important to evaluate its dynamic properties at initial elastic conditions. Hence, a complementary model with elastic shell elements was built in *SAP2000* [CSI, 2009], additionally incorporating the contribution of the mass and flexibility properties of the shake table subsystem (Figure 2.16, left).

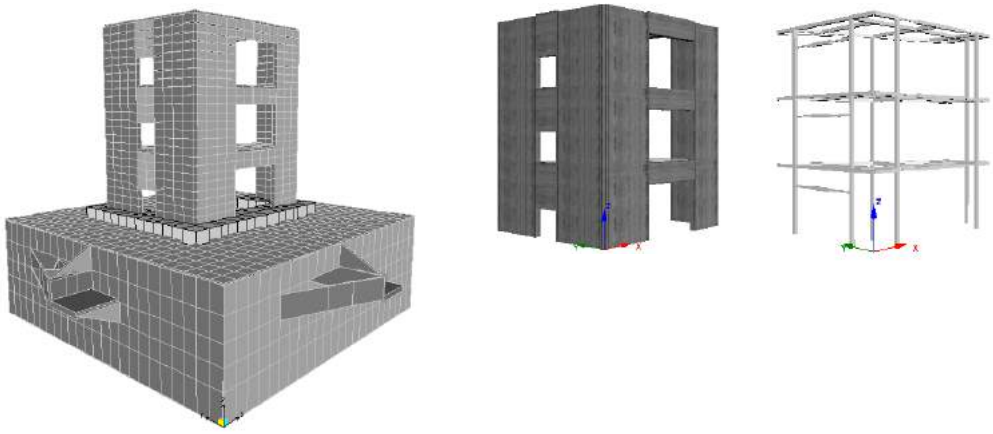

Figure 2.16. Numerical model with shell elements (left) and wide-column analogy (centre and right)

Given that the experimental measurements provided are associated with the complete system, i.e., RC structure and shake table, a first comparison was made with respect to the complete numerical model constructed with shell elements. Once this model has been calibrated, in terms of matching its modal frequencies to the experimental ones, a new shell model was considered without the contribution of the shake table subsystem, i.e., assuming that all nodes at the base of the structure were fixed. This third model was defined in order to allow the direct comparisons of the model with shell elements with the one assuming the wide-column analogy with a fixed base (Figure 2.16, centre and right). Since the seismic input used in the numerical model was the one measured on top of the shake table, and ignoring the local deformations of the shake table, the dynamic interaction effects between the mock-up and the shake table subsystem are directly accounted for in the input motion. The authors are aware that this claim is correct only while the mock-up responds in the elastic range and if the numerical model exactly reproduces its elastic dynamic characteristics. Otherwise, a complete simulation should be performed that includes such dynamic interaction. Time constraints and lack of information prevented the pursuit of such ambitious task.

The dynamic properties obtained with the shell model including the shake table reveal a slight difference with respect to the experimental values for the three first periods of vibration (Table 2.3, 2nd and 3rd columns). Similar differences were again observed between the shell elements model without the shake table and the one using the wide-column approach (Table 2.3, 4th and 5th columns). Considering the potential variability associated with the measurements, material properties, geometry, mock-up transportation, etc., it was considered that the differences in the computed values were within a reasonable tolerance.

Table 2.3. Comparison between the periods of vibration measured in the experimental test and computed with different numerical models

	Period (s)			
	Mock-up + Table		Mock-up	
	Measured	*SAP2000*	*SAP2000*	*SeismoStruct*
Mode 1 (x-dir.)	0.159	0.184	0.111	0.109
Mode 2 (y-dir.)	0.127	0.120	0.061	0.068
Mode 3 (torsion)	0.060	0.053	0.034	0.040

For what respects the nonlinear dynamic analyses (which, as noted above, were run using the equivalent wide-column frame elements), it is relevant to mention that the Hilber-Hughes-Taylor integration scheme [Hilber *et al.*, 1977] was deliberately adopted, as its numerical damping filters out the contribution of higher modes, thus avoiding potential spurious response. The time-step of the analysis was kept constant with respect to the input ground motions provided by the organizing commission, i.e., about 0.001 s.

In addition to the energy dissipated through material hysteresis, an additional source of energy dissipation was defined through equivalent viscous damping (EVD) defined with a Rayleigh damping model with 2.5 % of critical damping assigned to the first and second fundamental modes of vibration. This relatively large damping value, in comparison to what was observed in other validation analyses (presented in Chapter 3), intends to account for hysteretic shear response, not accounted for in the wide-column modelling adopted herein.

During the experimental campaign, the specimen was subjected to several consecutive ground motion of varying intensity as indicated in Table 2.2. Figure 2.17 illustrates the set of records considered for the numerical model. The analyses comprise RUN 9 to RUN 23 in order to account for the cumulative damage induced to the structure by each individual earthquake. The first two records (RUN 6 and RUN 7) where not considered given their low amplitude. A 10 s gap between each record was defined in order to allow the structure to return to rest after each seismic excitation.

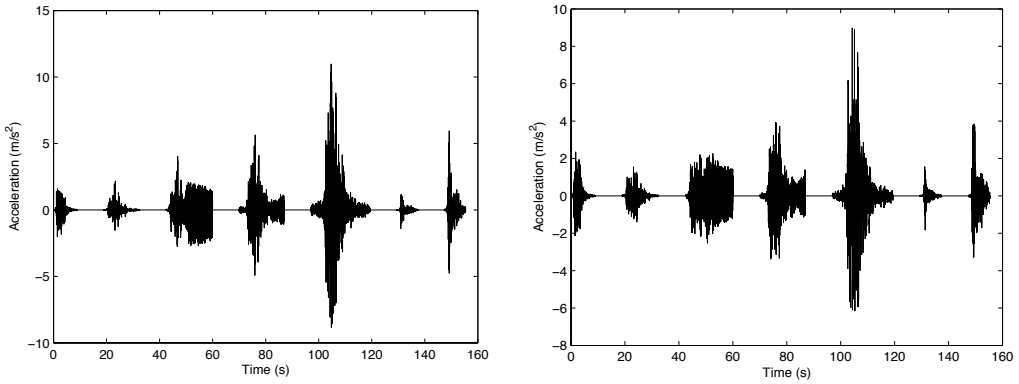

Figure 2.17. Ground motion considered in the numerical analyses: X (left) and Y (right) direction

2.6.3 Results

The present section shows a summary of the results obtained in terms of relative displacements measured with respect to the shake table and absolute accelerations of point B and D (see Figure 2.15) at the third storey of the mock-up.

While the identification of maximum values measured during strong ground motions is of primary importance, the response during lower intensity and aftershocks allows for an assessment regarding the response under essentially elastic behaviour as well as the damage accumulation along the large set of ground motions. The time-histories of accelerations and displacements illustrated in Figure 2.18 and Figure 2.19 show the comparison between the experimental and numerical response of the structure during the strongest motion of the set, RUN 19. The title of each plot indicates (separated by a dash) the Run, point, storey and directions, respectively. It is important to note that the initial value of each plot was set to zero in order to avoid possible incongruences in the residual deformation resulting from intermediate experimental tests.

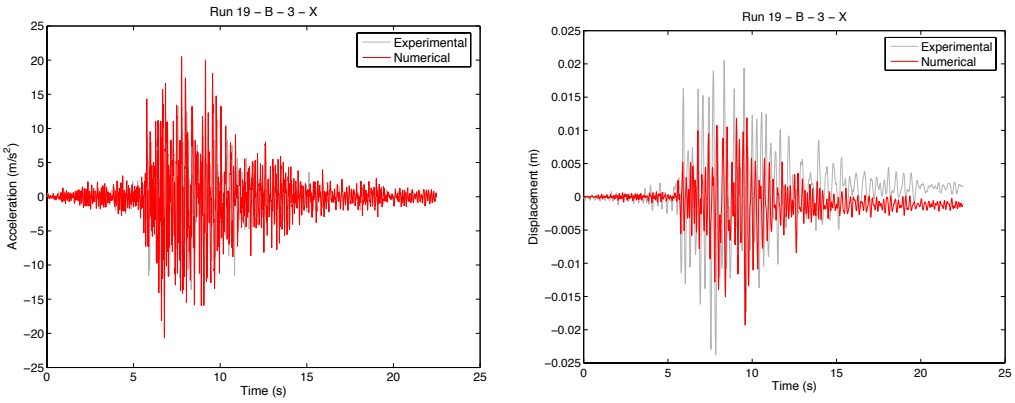

Figure 2.18. History of accelerations and displacements – RUN 19, X-direction, point B

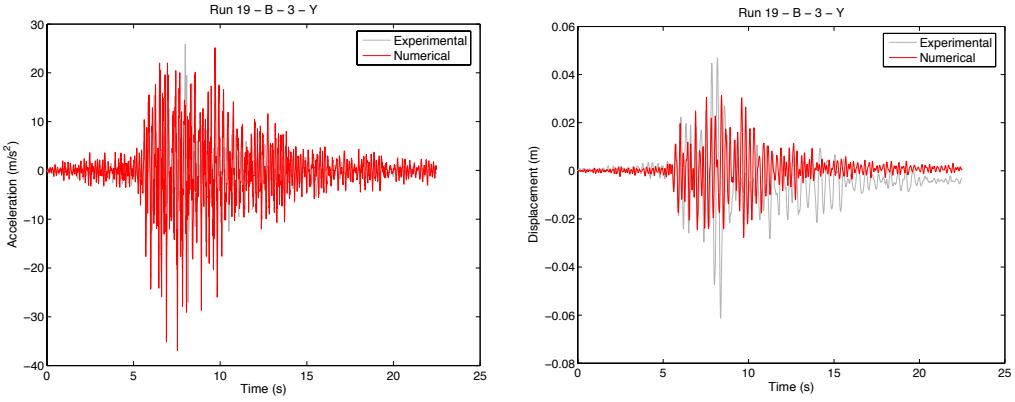

Figure 2.19. History of accelerations and displacements – RUN 19, Y-direction, point B

The results presented above show that the numerical accelerations seem to be relatively well predicted, while displacements measured during RUN 19 tend to be underestimated by the numerical model. An important contribution to the differences observed could be attributed to the rupture of the connection between the RC walls and the foundation observed during the experimental test, which seems to be associated with the slippage of the longitudinal reinforcement linking these two elements. Moreover, it is important to note that the numerical model does not take into account the additional flexibility resulting from strain penetration effects.

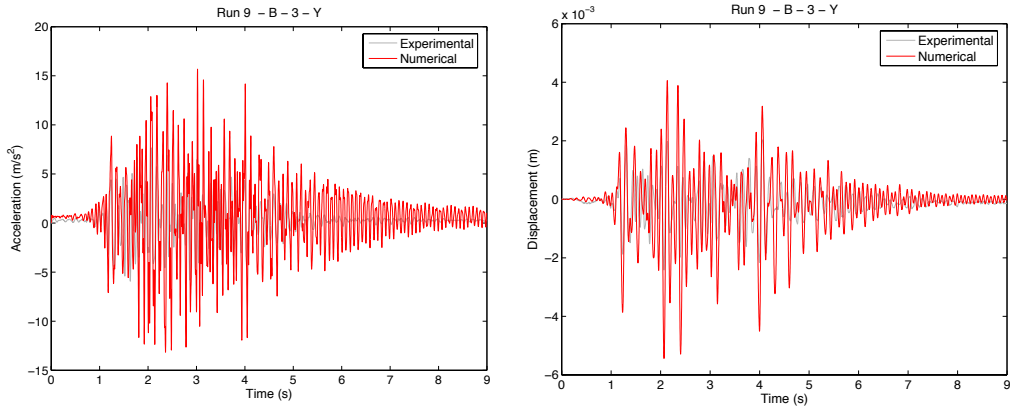

Figure 2.20. History of accelerations and displacements – RUN 9, Y-direction, point B

The results presented in Figure 2.20 show that under lower seismic input (RUN 9), the differences are also relevant, but now the accelerations and displacements are overestimated. At this stage, the structure is undamaged and the response is essentially governed by its modal properties. This difficulty in reproducing the (essentially) elastic behaviour can be attributed to possible incongruences associated with the material properties, namely tension stiffening effects, variability in the tensile strength and modulus of elasticity of the concrete. Moreover, it is important to recognize potential limitations associated with the wide-column model regarding the definition of the slab, connections between adjacent walls and the contribution of shear deformations.

The results presented in Figure 2.21 illustrate the comparison of accelerations and displacements during the last ground motion (RUN 23). Similarly to what was observed during RUN 19, the numerical displacements are underestimated with respect to the experimental ones. Moreover, as it is possible to observe in the same figure, the modelled structure oscillates with a higher frequency than the model tested in the shake table. Hence, and considering the lower displacement demand induced in the previous runs (and consequently lower structural damage), the structure presents a larger stiffness, which results in potentially lower structural deformations.

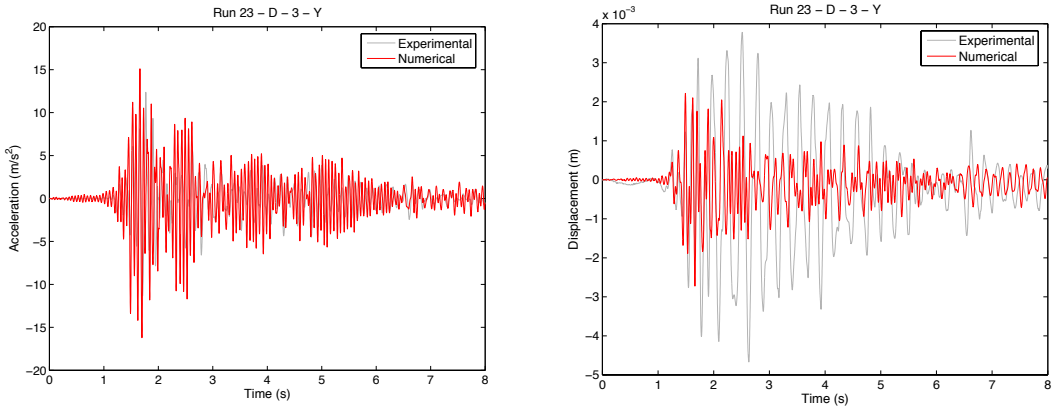

Figure 2.21. History of accelerations and displacements – RUN 23, Y-direction, point D

Finally, Table 2.4 shows the relative error associated with the maximum accelerations and displacements obtained during RUN 9, 19 and 23, determined with the following expression:

$$Error_{Max.} = \frac{max(EDP_{computed}) - max(EDP_{measured})}{max(EDP_{measured})} \tag{2.14}$$

where *EDP* represents the structural accelerations or displacements.

Table 2.4: Relative error associated with the accelerations and displacements measured along X and Y directions during RUN 19

		Acceleration		Displacement	
		X	Y	X	Y
RUN 9	Point B	1.73	1.05	0.83	1.25
	Point D	1.02	2.14	0.16	0.60
RUN 19	Point B	0.42	0.36	-0.19	-0.49
	Point D	0.23	0.05	-0.43	-0.33
RUN 23	Point B	0.27	0.54	-0.40	-0.49
	Point D	0.00	0.31	-0.05	-0.42

Based on the results presented in the previous table, it is clear that the accuracy of the response evaluated at point B and D varies along the different runs and directions. These observations suggest that, the dynamic properties of the numerical model (namely its torsional component), may present some deviations with respect to the structure tested on the shake table.

2.6.4 Discussion on the use of simplified wide-column models

The displacements and accelerations computed by the model under low seismic intensity present non-negligible deviations when compared with the experimental results. These differences may be associated to an eventual dispersion of material properties and to the simplifications related with the use of a wide-column model, namely regarding the definition of the slab, connections between adjacent walls and the contribution of shear deformations.

Furthermore, it was verified that under strong seismic motions, the structural displacements were consistently underestimated. It is believed that the additional flexibility (base rotation) resulting from the separation between the RC wall and the foundation during the experimental test contributed greatly to the difference observed. In addition, it is important to note that important numerical convergence difficulties precluded the consideration of alternative modelling solutions that, in the authors' opinion, would render more accurate response parameters. It is recalled that the numerical model does not account for strain penetration effects, while the shear mechanism associated with the response of structural RC walls was modelled with linear shear springs, which represents an extremely simplified approach. Moreover, the use of FB elements, possibly including the nonlinear shear behaviour [Correia *et al.*, 2015], together with better estimates of the material properties, tension stiffening effects, etc., could also contribute to improve the numerical simulation of the experimental test.

2.7 SUMMARY

This chapter presented a summary of some relevant modelling options for nonlinear seismic analysis of RC structures with distributed plasticity frame elements. Supported on a detailed literature review of the underlying theoretical principles, each option is discussed in detail. From such review it became apparent that the level of sophistication shown by the distinct material constitutive models and time-domain integration algorithms reflect highly consolidated stages of development.

On the other hand, it also became clear that conventional strategies considered to model structural damping have a limited relation with the actual energy dissipation mechanisms. In view of the popularity of EVD models among structural engineers, the different variants of this approach (namely stiffness and mass proportional) are explored in some

detail in the following chapter, highlighting the main benefits and limitations of each approach.

For what respects the simulation of the local response of RC members, several researchers along the last years have proposed different solution to deal with localization issues and strain penetration effects. Despite some encouraging results in these fronts, it is apparent that additional modelling efforts are still required. The development of accurate, yet not too computationally demanding, models for engineering applications is needed.

A final conclusion of the present chapter is that despite the limitations associated to the use of beam-column elements to simulate the response of RC walls, the application of wide-column models can be a reliable and acceptably accurate option. Naturally, the consideration of more advanced models featuring detailed meshes are expected to render more accurate simulations for these type of structures.

3. SENSITIVITY ANALYSIS CONSIDERING PAST BLIND PREDICTION CONTESTS

In this chapter, three different structures tested in two international blind prediction challenges were selected to perform a sensitivity study. The goodness-of-fit for each approach is assessed in terms of lateral displacements, as well as accelerations when available, following two post-processing strategies: a more conventional one based on the error associated to the peak values measured during each record, and another using the frequency content characteristics of the entire response history. Sensitivity parameters included equivalent viscous damping, element formulation and discretization scheme, strain penetration effects, material models, numerical time-domain integration and time-step. The conclusions, which are interpreted in the light of state-of-the-practice recommendations and established theoretical framework, address fundamental modelling decisions for engineers and researchers.

3.1 CASE STUDIES

3.1.1 Structure 1

The first structure to be analysed is a full-scale RC bridge column used in the 'Concrete Column Blind Prediction Contest 2010', sponsored by the *Pacific Earthquake Engineering Research Center* (PEER) and the *Network for Earthquake Engineering Simulation* (NEES). The specimen was tested on the *NEES Large High-Performance Outdoor Shake Table* located at UCSD's *Englekirk Structural Engineering Center*. Detailed description of the experimental test can be found in Terzic *et al.* [2015] and Schoettler *et al.* [2015].

The structure is a cantilevered column with a height of about 7.3 m from the face of the foundation up to the centre of gravity of the top RC block with 230 tons representing the superstructure mass, as shown in Figure 3.1. The circular cross-section has a diameter of approximately 1.2 m.

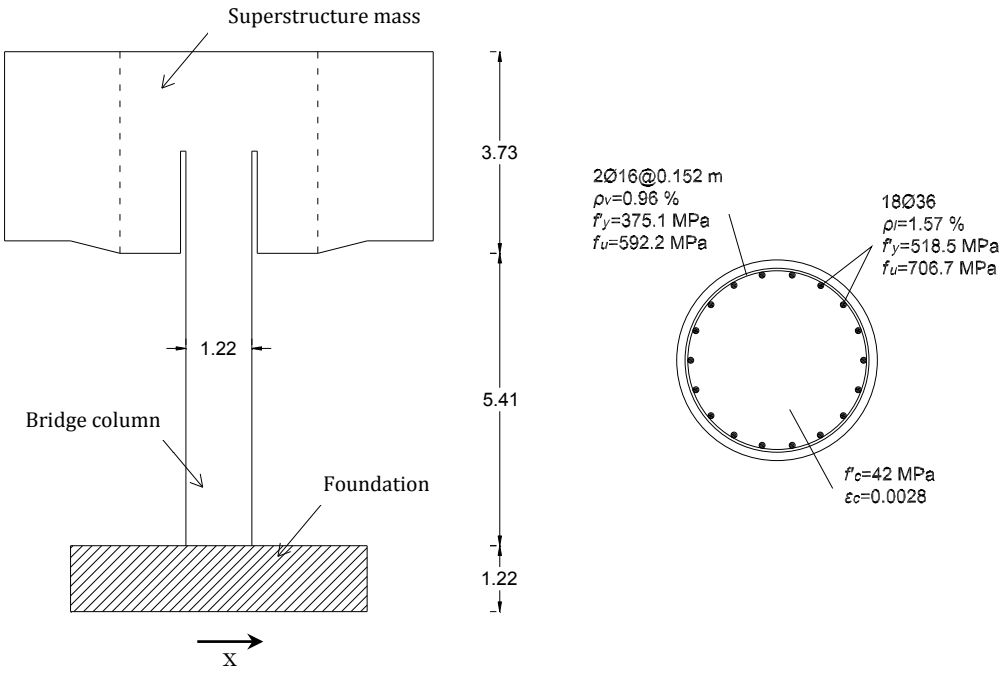

Figure 3.1. Structure 1: Elevation view (left) and cross-section details (right)

The modal properties of the bridge column identified through eigenvalue analysis evidence that the response is essentially governed by the 1st translational mode (X-direction in this case). Table 3.1 and Figure 3.2 presents a summary of the modal properties together with the modal shapes associated with the first and second modes of vibration.

Table 3.1. Modal properties of Structure 1

Mode	Period (s)	Effective modal mass (%)					
		X	Y	Y	R-X	R-Y	R-Z
1	0.78	84.8	0.0	0.0	0.0	15.0	0.0
2	0.14	11.8	0.0	0.0	0.0	54.5	0.0
3	0.04	0.0	0.0	96.5	0.0	0.0	0.0

Nevertheless, the concrete block on the top of the column introduces additionally a significant rotational inertia that governs the second mode of vibration (T_2 = 0.14 s) and

partially affects the fundamental mode (the effective modal masses for the 1st mode equal 85% and 15% for the transversal and rotational component respectively). Finally, the third mode reflects the axial movement and occurs for a very low period of vibration.

Figure 3.2. 1st (left) and 2nd (right) modal shapes of Structure 1

Numerical simulation results indicate that, despite the post-yield hardening behaviour of the sectional response, the global force-displacement curve shows a noteworthy softening behaviour that reflects the important influence of second-order effects (Figure 3.3).

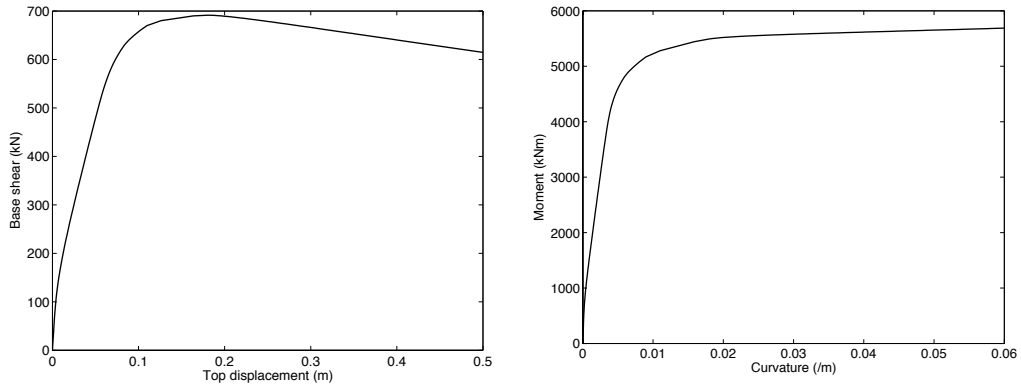

Figure 3.3. Lateral load-displacement (left) and moment-curvature (right) response of Structure 1

The experimental campaign consisted of six consecutive ground motions of varying intensity. The test protocol included historical ground motions such as those of Loma Prieta (1989) and Kobe (1995) earthquakes. Figure 3.4 illustrates the set of records considered in the experimental test.

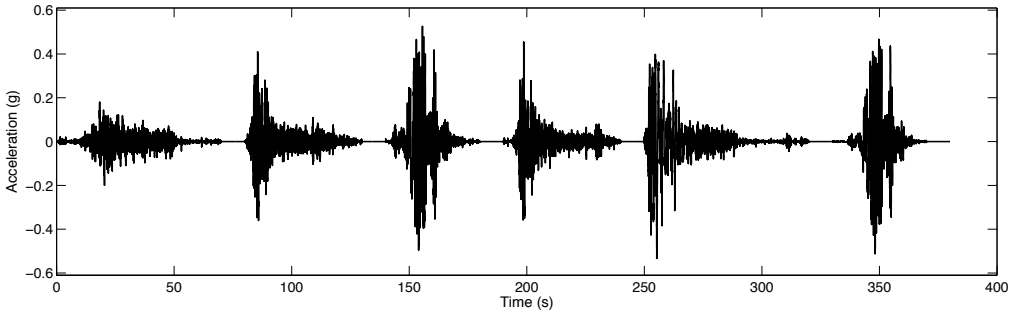

Figure 3.4. Series of applied acceleration records to Structure 1

3.1.2 Structure 2 and Structure 3

The second group of structures considered in this study are two 3D RC frames with identical geometrical dimensions (Figure 3.5), but different reinforcement detailing. Both structures were tested at Lisbon's LNEC (*National Laboratory for Civil Engineering*) 3D shake table, which can impose simultaneously movements in the three translational directions whilst passively restraining the three rotations [Campos Costa *et al.*, 1996]. The experiments were carried out under the initiative 'Blind Test Challenge' included in the 15th World Conference on Earthquake Engineering.

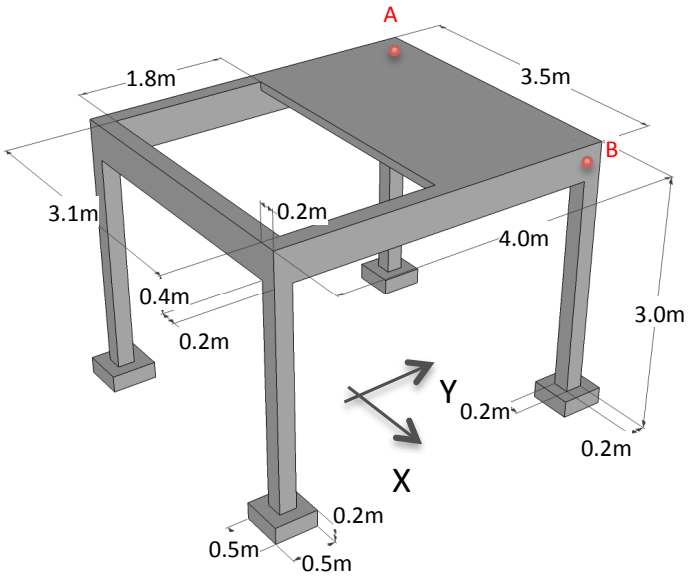

Figure 3.5. Structures 2 and 3: General dimensions of the mock-up

As stated before, the two structures differ only with regards to reinforcement details, see Table 3.2. Structure 2 was designed without capacity design considerations, while Structure 3 was detailed in order to develop an appropriate seismic behaviour with a ductile response (Figure 3.6). In addition to the self-weight of the mock-up, a set of nine additional masses of around 1200 kg each were placed eccentrically on top of the slab [Costa *et al.*, 2012].

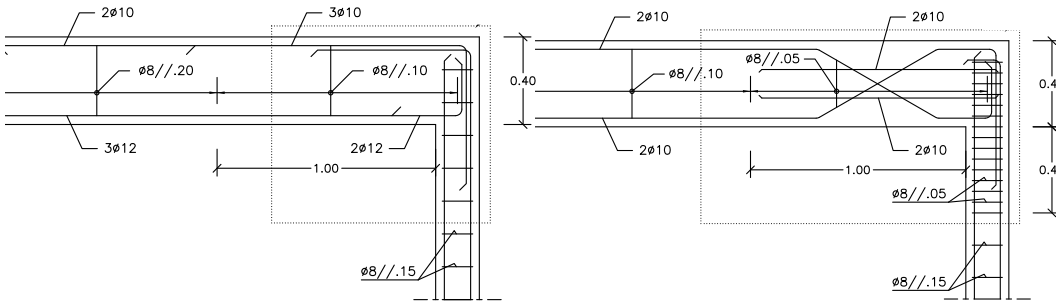

Figure 3.6. Beam/column joint reinforcement details of Structure 2 (left) and Structure 3 (right)

Table 3.2. Structures 2 and 3: Section and material details

	Columns		Beams	
	Long. Rebars (ρl)	Transv. Rebars (ρv)	Long. Rebars (ρl)	Transv. Rebars (ρv)
Structure 2	8Ø10 (1.57%)	Ø8@0.15m (0.57%)	2Ø10 + 3Ø12 (0.62%)	Ø8@0.1m (0.63%)
Structure 3		Ø8@0.05m (1.71%)	4Ø10 (0.39%)	Ø8@0.05m (1.26%)

ρl - Longitudinal reinforcement ratio
ρv - Volumetric ratio of transverse reinforcement

	$f'y$ (MPa)	fu (MPa)	$f'c$, columns (MPa)	$f'c$, beams (MPa)
Ø 8	560	653		
Ø 10	559	632	30	35.6
Ø 12	566	631		

$f'c$ - Concrete compressive strength
$f'y$ - Yield strength of steel
fu - Steel ultimate stress

Considering that the geometric properties of both structures are identical, it is not surprising that the modal (elastic) properties of Structure 3 are similar to those of Structure 2. The behaviour of the two structures is essentially governed by the two first modes of vibration along the orthogonal horizontal reference axes (T_1 = 0.31 s along X and T_2 = 0.28 s along Y); the third mode (T_3 = 0.17 s) represents the vertical flexibility of the slab. A fourth mode of vibration (T_4 = 0.15 s), reflecting a rotation around the vertical axis, contributes significantly to the torsional response of the structure. The corresponding modal shapes associated with the main modes are depicted in Figure 3.7.

Table 3.3. Modal properties of Structure 2

Mode	Period (s)	Effective modal mass (%)					
		X	Y	Z	R-X	R-Y	R-Z
1	0.31	97.0	0.0	0.0	0.0	0.6	3.5
2	0.28	0.0	99.9	0.0	0.8	0.0	0.0
3	0.17	0.0	0.1	40.5	3.1	0.0	0.0
4	0.15	2.6	0.0	0.0	0.0	0.0	95.8

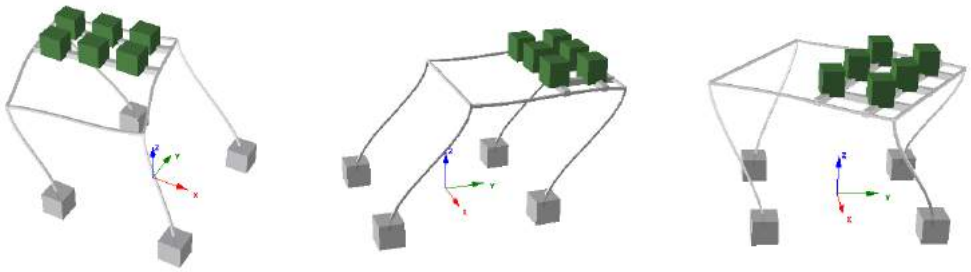

Figure 3.7. 1st (left), 2nd (centre) and 4th (right) modal shapes of Structure 2

Pushover analyses along the X and Y directions show that the two structures exhibit a softening response at the global level that is a combination of second-order effects and material softening at the column's cross-sections (Figure 3.8 and Figure 3.9).

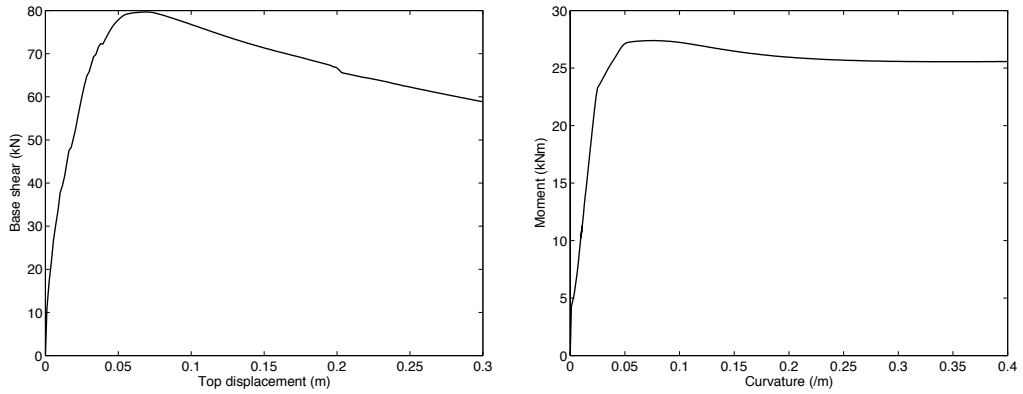

Figure 3.8. Lateral load-displacement (left) and moment-curvature (right) response of Structure 2 along Y direction

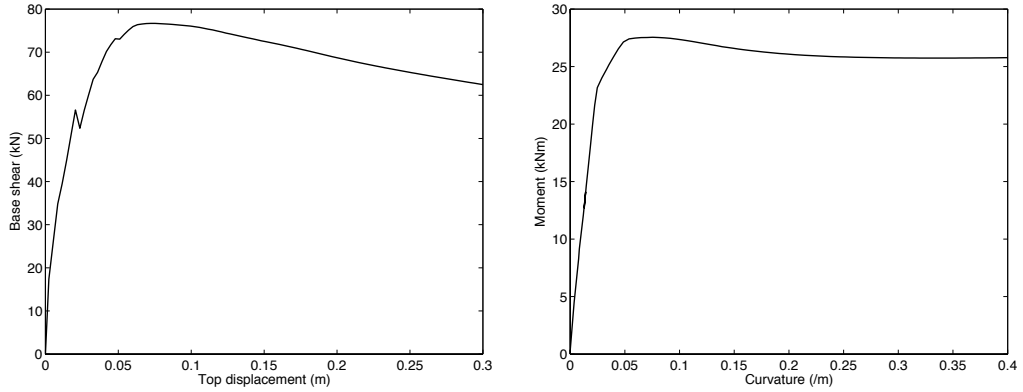

Figure 3.9. Lateral load-displacement (left) and moment-curvature (right) response of Structure 3 along Y direction

Both structures were subjected to four ground motions of increasing intensity applied simultaneously in the two horizontal directions. The input signals were synthetically generated based on a time segment of two horizontal orthogonal components of a real strong motion accelerogram registered during the 2011 March 11 Great East Japan (Tohoku) earthquake. Figure 3.10 represents the input time-history of Structure 2 in the longitudinal (*Y*) direction.

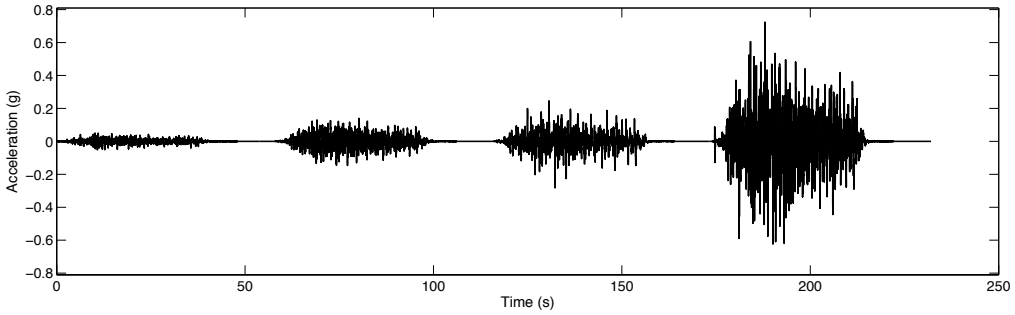

Figure 3.10. Series of applied acceleration records on Structure 2 in the longitudinal direction

3.2 SENSITIVITY PARAMETERS

Taking into account the considerations of Chapter 2, the present study analyses the following sensitivity parameters:

- Equivalent Viscous Damping

Four different models are considered: no damping, initial stiffness-proportional damping (ISPD), tangent stiffness-proportional damping (TSPD), and mass-proportional damping (MPD). Additionally, varying percentages of critical damping, ranging from 0% to 5%, were assigned to the fundamental period of vibration.

- Element Discretization

The FB approach was used to simulate the column response, to the detriment of the DB counterpart, since it verifies equilibrium along the element length in an exact way. The number of IPs was defined such that the weighted length of the IPs at the extremities of the members corresponds to either the total *equivalent* plastic hinge length (L_P) or to one-half of that value, as determined using the expression proposed by [Priestley et al. 2007]:

$$L_P = kL_C + L_{SP} \geq 2L_{SP} \tag{3.1}$$

where

$$k = 0.2\left(\frac{f_u}{f_y} - 1\right) \leq 0.08 \tag{3.2}$$

accounts for the strain-hardening steel properties, L_C is the shear span of the element, f_y and f_u are the yielding and ultimate strength of the longitudinal rebars, and L_{SP} is the

strain penetration length determined by Equation (2.10). In addition, a model featuring 10 IPs, representative of a highly refined integration scheme, is also considered.

It is important to recall that the *equivalent* plastic hinge length is a fictitious quantity from which inelastic member deformations can be computed based on the assumption of a constant (or nearly constant) inelastic curvature profile. It is distinct from (and smaller than) the *real* plastic hinge, taken as a physical length wherein damage concentrates [Almeida et al., 2014]. Some recent expressions are available in the literature to estimate the *real* plastic hinge length, such as those of [Bae and Bayrak, 2008; Pam and Ho, 2009; Mortezaei and Ronagh, 2011]. Unfortunately, such proposals output a wide range of results, presented in Table 3.4, which further expose the current difficulty in distinguishing estimates for the *equivalent* and *real* plastic hinge lengths. Note that in the following table the estimations according to the expressions proposed by [Bae and Bayrak 2008] and [Pam and Ho 2009] does not account for the strain penetration contribution.

Table 3.4. Estimations of plastic hinge length for the different structures

	equivalent plastic hinge length (m)	*real* plastic hinge length(m)		
	Priestley *et al.* [2007]	Bae and Bayrak [2008]	Pam and Ho [2009]	Mortezaei and Ronagh [2011]
Structure 1	0.53+0.41=0.94	0.3 (L_p only)	1.2 (L_p only)	0.72 (far fault)
Structures 2 & 3	0.04+0.12=0.16	0.05 (L_p only)	0.21 (L_p only)	0.12 (far fault)

While additional research is not available to resolve this apparent conflict, the *equivalent* plastic hinge length of Equation (3.1) - which appears to be a somewhat average value in between those presented in Table 3.4 - was assumed as equal to the *real* plastic hinge length and hence was used to define the various element discretization schemes. Following the theoretical considerations presented in Section 2.2.3, the models with a number of IPs such that the weighted length of each IP at the extremities corresponds to this assumed plastic hinge length are herein taken as reference.

Table 3.5 summarises the mesh and number of IPs considered for the modelling of the columns in each structure. The number of elements used to model the beams of Structure 2 and Structure 3 vary depending on the reinforcement details along the member. Due to space limitations and the fact that beam discretization did not greatly affect the results, no further details are herein provided on that regard. However, each FB sub-element comprised a minimum of 3 IPs as discussed in Section 2.2.1.

Table 3.5. Element discretization scheme adopted for the different structures

	End IP ≈ L_p			End IP ≈ 0.5 L_p			10 IPs		
	No elem.	No IPs	Wgt. lgt. (m)	No elem.	No IPs	Wgt. lgt. (m)	No elem.	No IPs	Wgt. lgt. (m)
Structure 1	2	3 + 3	1	2	4 + 3	0.5	1	10	0.08
Structures 2 & 3	1	4	0.23	1	6	0.09	1	10	0.03

- Strain Penetration

Three alternative SP modelling approaches were studied: (i) base spring with constant rotational stiffness, (ii) element elongated by the strain penetration length, and (iii) strain penetration effects neglected. For the first approach, the column rotational stiffnesses were determined with Equation (2.12), resulting in the following values: K_θ = 2610x10^3 kNm/rad, K_θ = 7000 kNm/rad and K_θ = 7450 kNm/rad for Structure 1, 2, and 3 respectively. For the elongated element approach, the strain penetration length was determined based on Equation (2.10), which yielded the following values: L_{sp} = 0.41 m for Structure 1 and L_{sp} = 0.12 m for Structures 2 and 3. Despite the approximate double bending response of columns in Structures 2 and 3 under lateral loads, the members were elongated of only L_{sp} (and not of 2× L_{sp}), corresponding to the deformations taking place at the base of the columns. It was hence considered that the strain penetration effects at the beam-column joints are somehow accounted for in the numerical model by connecting the columns with the beams at the geometric centre of the joint, i.e., by disregarding the so-called *rigid offsets*.

- Material model

The numerical analyses feature eight different uniaxial stress-strain relations, as discussed in Section 2.4. The concrete models adopted are the ones proposed by Mander *et al.* [1988] (with and without tensile strength), Madas and Elnashai [1992], and Kappos and Konstantinidis [1999].

Regarding the reinforcement rebars, the model proposed by Menegotto and Pinto [1973] is adopted considering two values for A2 = 0.15, in the reference model and A2 = 0.075, that results in smoother transition curves. In addition, the model from Monti and Nuti [1992] together with the simple bi-linear approach are also considered.

- Integration algorithm and time-step

The well-known Newmark and Hilber-Hughes-Taylor integration algorithms were adopted in the sensitivity study. In addition the analyses comprised the use of three different time-step: (i) the original time-step of the records ($\Delta t_{,Structure1}$ = 0.0042 s and $\Delta t_{,Structure2,3}$ = 0.005 s), (ii) one tenth of the fundamental period of vibration of the structures ($\Delta t_{,Structure1}$ = 0.078 s and $\Delta t_{,Structure2,3}$ = 0.03 s) and (iii) a time-step of 0.02 s. The two latter values represent customary boundaries consider to ensure numerical accuracy, ensuring, at the same time, a smooth transition along the earthquakes records, as described in Section 2.5.

Table 3.6 sums up the sensitivity parameters and associated properties considered in the present analysis. The properties highlighted in bold correspond to state-of-the-practice options which were taken as reference (i.e., model properties that were kept constant while varying those associated to the sensitivity parameter under analysis). The EVD properties to be used as reference were not evident *a priori*, and hence those producing the best results in the initial evaluation of Section 3.4.1 were selected. All the analyses were carried out with the structural analysis software *SeismoStruct* [Seismosoft, 2013].

Simple initial estimations of the shear span ratios for all the analysed structural columns vary between 6 (Structure 1) and 7.5 (Structures 2 and 3), indicating that shear deformations are negligible [Almeida *et al.*, 2014]. Unsurprisingly, the shear capacity as computed by Priestley *et al.* [2007] is roughly between five (Structures 2 and 3) and seven (Structure 1) times larger than the member shear that is in equilibrium with the bending capacities at the member extremities (assuming a cantilever response for Structure 1 and double fixed bending for columns in Structures 2 and 3).

Table 3.6. Sensitivity parameters considered in the parametric study

Sensitivity Parameters	Properties	
Damping model	TSPD ISPD MPD	0% 0.5% 1% 1.5% 2% 5%
Element discretization scheme	10 IPs End IPs ≈ 0.5 L_p **End IPs ≈ L_p**	
Strain penetration	No strain penetration Longer element **Base Spring**	
Material model	Concrete	**Mander et al.** No tensile strength Madas and Elnashai Kappos and Konstantinidis
	Steel	**Menegotto-Pinto (A2=0.15)** Menegotto-Pinto (A2=0.075) Monti-Nuti Bilinear
Integration algorithm	**Hilber-Hughes-Taylor** Newmark	**$\Delta t=\Delta t,eqk$** Δt=0.1T Δt=0.02

In bold: options corresponding to the reference model

3.3 GOODNESS-OF-FIT EVALUATION

The goodness-of-fit resulting from sensitivity analyses is expressed for EDPs that are judged representative of the structural response, and it should be computed with methodologies that compare experimental and numerical results in an efficient and unbiased way.

3.3.1 Response Engineering Demand Parameters

Lateral displacements and accelerations were chosen as the EDPs to be assessed in this study since they are internationally accepted indicators of structural response [Krawinkler, 2006] and are also part of typically available data from experimental campaigns. Accelerations were only experimentally measured for Structure 1 and hence the goodness-of-fit evaluation of Structures 2 and 3 comprises only the comparisons with respect to structural displacements.

Although local response EDPs such as concrete and rebar strains can better and more directly relate to structural damage [Berry *et al.*, 2008], their experimental monitoring during the blind prediction tests was not carried out and thus they are not herein considered. It is noted that most recent experimental campaigns place a very significant emphasis on the use of advanced instrumentation allowing for the monitoring of local-level EDPs, followed by corresponding efforts of numerical simulation [Goodnight *et al.*, 2012; Almeida *et al.*, 2015].

3.3.2 Response error

In order to assess the accuracy of each model with respect to the experimental results, two distinct relative error measures were used: *Cumulative Error* and *Peak Error*. The former compares the specific EDP over the entire range of the dynamic response, considering both phase and amplitude changes. On the other hand, the latter error measure compares absolute maximum values at discrete instants, which represents a more commonly used approach.

3.3.2.1 *Cumulative Error*

The *Cumulative Error* evaluates the variations in magnitude of a specific quantity and is defined as an 'averaged' error (herein taken as the *Root Mean Square Error*, RMSE) normalized by the *Root Mean Square* (RMS_M) of the magnitudes of the measured (subscript index *M*) signal. This error measure can be computed in the time (*t*) and frequency (*f*) domains:

$$Cumulative\ Error = \frac{RMSE}{RMS_M} = \frac{\sqrt{\frac{1}{n}\sum_n \left(x_{M,i}(t) - x_{C,i}(t)\right)^2}}{\sqrt{\frac{1}{n}\sum_n \left(x_{M,i}(t)\right)^2}} =$$

$$= \frac{\sqrt{\frac{1}{n^2}\sum_n \left|X_{M,i}(f) - X_{C,i}(f)\right|^2}}{\sqrt{\frac{1}{n^2}\sum_n \left|X_{M,i}(f)\right|^2}} \quad (3.3)$$

where $x_{M,i}$ *(t)* and $x_{c,i}$ *(t)* are the measured (subscript index *M*) and calculated (subscript index *C*) time series with *n* discrete time *(t)* samples and $X_{M,i}$ *(f)* and $X_{c,i}$ *(f)* are the Fourier transform of the corresponding time series, as a function of the frequency *(f)*. The advantage of using Equation (10) in the frequency domain is that it allows for the determination of the error associated with the amplitude and phase independently. In this context, the signals are separated into their real and imaginary components, where the amplitudes are the lengths of the vectors in the Argand diagram and the phases are the angles between those vectors and the real axis at a specific frequency *i* (Figure 3.11). The previous equation can thus be rewritten as:

$$Cumulative\ Error = \frac{\sqrt{\frac{1}{n^2}\sum_n \left|X_{M,i}(f) - X_{C,i}(f)\right|^2}}{\sqrt{\frac{1}{n^2}\sum_n \left|X_{M,i}(f)\right|^2}} =$$

$$= \frac{\sqrt{\frac{1}{n^2}\sum_n \left[\left(R_{M,i} - R_{C,i}\right)^2 + \left(I_{M,i} - I_{C,i}\right)^2\right]}}{\sqrt{\frac{1}{n^2}\sum_n \left[{R_{M,i}}^2 + {I_{M,i}}^2\right]}} \quad (3.4)$$

where R_{Mi}, I_{Mi} and R_{Ci}, I_{Ci} are the real and the imaginary components of the measured and calculated responses at frequency *i*, while *n* is the number of frequency samples of the Fourier transform.

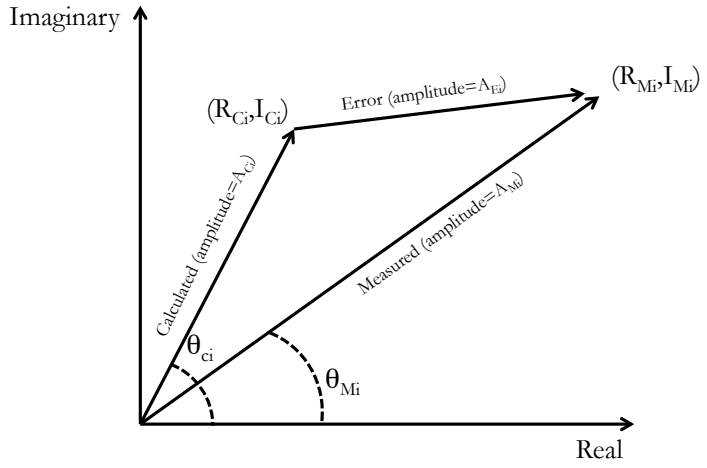

Figure 3.11. Graphical representation of the real and imaginary components of the calculated and measured quantities in the frequency domain

Noting that the frequency resolution (Δf) of the Fourier transform is given by $1/(n\times\Delta t)$, (Δt defines the sampling interval), the interval defined by f_1 and f_2 should encompass the most relevant frequency content of the analysed signals. Thus, in order to account for the higher-mode effects and period elongation under nonlinear response, f_1 and f_2 are defined as function of the fundamental period of the structures: $1/(4T_1)$ and $1/(0.1T_1)$, respectively [Lepage *et al.*, 2008]. Possible spurious amplitudes at irrelevant frequencies (from the structural viewpoint) are therefore somehow filtered out from the computed error.

The amplitude component of the *Cumulative Error* can be determined as:

$$Cumulative\ Amp.Error = \frac{\sqrt{\frac{1}{n^2}\sum_{i=f1}^{f2}\left[\left(R_{M,i}+I_{M,i}\right)^2-\left(R_{c,i}+I_{Ci}\right)^2\right]}}{\sqrt{\frac{1}{n^2}\sum_{i=f1}^{f2}\left[{R_{M,i}}^2+{I_{M,i}}^2\right]}} \quad (3.5)$$

while the *Cumulative Phase Error* can then be determined by subtracting the amplitude component (Equation (3.5)) from the total *Cumulative Error* (Equation (3.4)).

It is underlined that this error measure determined with from Equation (3.4) and (3.5) produces values that vary between 0 and infinite: 0 indicates a perfect match; if the two signals are 180° out-of-phase, an error of 2 is obtained. Increasing values of the *Cumulative*

Error reflect larger differences between the signals in terms of amplitude and/or phase and hence a poorer match. Alternative normalization methods, such as the Theil's inequality coefficient [Theil, 1961], have been used in other recent studies as goodness-of-fit measures [Babazadeh *et al.*, 2015].

3.3.2.2 *Peak Error*

The second error measure represents a more commonly used approach, which determines the maximum relative error of the considered EDP (displacement or acceleration), for each record separately. The main disadvantage of this error measure is that it is sensitive to the magnitude of the experimental data, and in particular when the latter tends to zero it is of little use. The error is computed for both positive "+" and negative "-" values in each direction, as described by Equation (3.6).

$$Peak\ Error_j^{+} = \frac{max\left(EDP_{computed,j}\right) - max\left(EDP_{measured,j}\right)}{max\left(EDP_{measured,j}\right)}$$
$$Peak\ Error_j^{-} = \frac{min\left(EDP_{computed,j}\right) - min\left(EDP_{measured,j}\right)}{min\left(EDP_{measured,j}\right)} \quad (3.6)$$

In the previous equation, the index *j* indicates each individual record within the full set. It should be noted that the time instant where the maximum (or minimum) of the measured signal occurs does not necessarily coincide with the time instant corresponding to the maximum (or minimum) of the computed response.

3.4 APPLICATIONS

The present section presents the results of the sensitivity study carried out using nonlinear dynamic analyses, an outline of which is depicted in Figure 3.12.

In the plots of the following sub-sections the *Peak Error* computed for each individual record is illustrated with filled and empty markers for the positive and negative loading directions respectively. In addition, the black circles with the associated error bars represent the mean value plus/minus the standard deviation computed for the records in each set. Due to space limitations, and given that the plots follow essentially the same format, the legend is presented only for the first figure. For the *Cumulative Error* the distinction between negative and positive directions is not applicable and an empty marker is hence used to identify each record. Regarding this latter error measure, prevalence is given to the amplitude component (which will henceforth be simply referred as *Cumulative Error*), as it appears more representative of the EDP variations. At the right-hand side of each plot, is presented the denominator of the associated error.

This secondary plot, representing the measured component of the error, allows getting a perspective of the relative importance of the error values presented in the main plots.

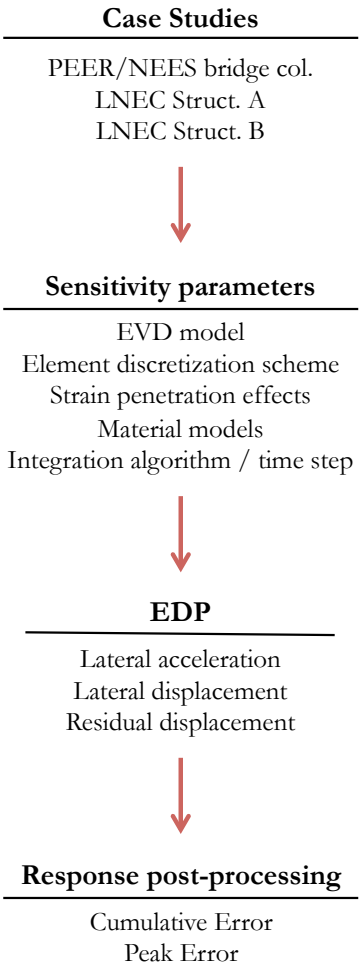

Figure 3.12. Outline of the parametric study

3.4.1 Equivalent Viscous Damping

The following paragraphs present the results of the sensitivity analyses for the Equivalent Viscous Damping.

Figure 3.13 and Figure 3.14 evidence that the numerical models simulate more accurately the experimental results for EVD models with low percentages of critical damping

(roughly between 0.5% and 2%, depending on the structure). For such range of values the damping forces developed are small and therefore it is not straightforward to assess the differences between MPD or SPD models by looking at this response parameters. Yet, it is clear that as the percentage of critical damping increases the error associated with the ISPD augment with respect to the TSPD and MPD counterparts. On the other hand, the use of 0% damping produces an increase of the error, noticeable even in comparison with the case of 0.5% of critical damping, which is associated with an overestimation of the simulated displacements.

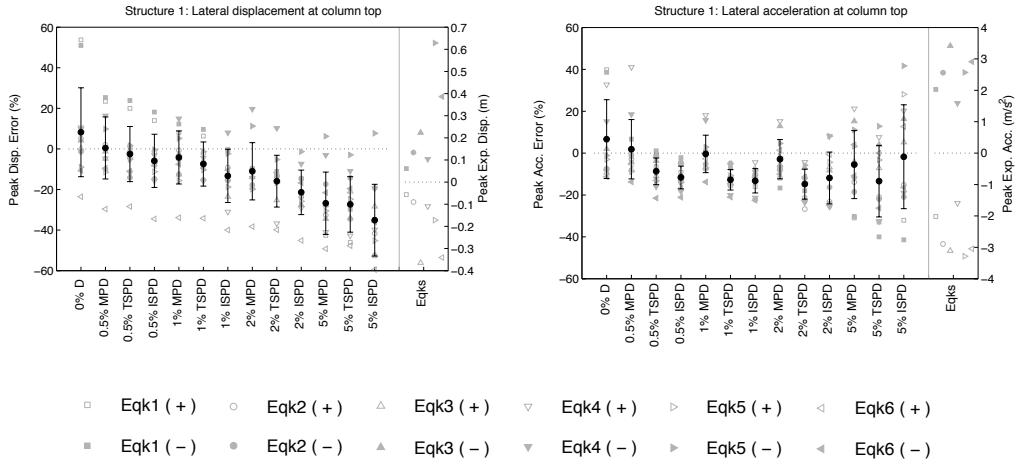

Figure 3.13. Peak displacement (left) and acceleration (right) error for Structure 1 considering different EVD models

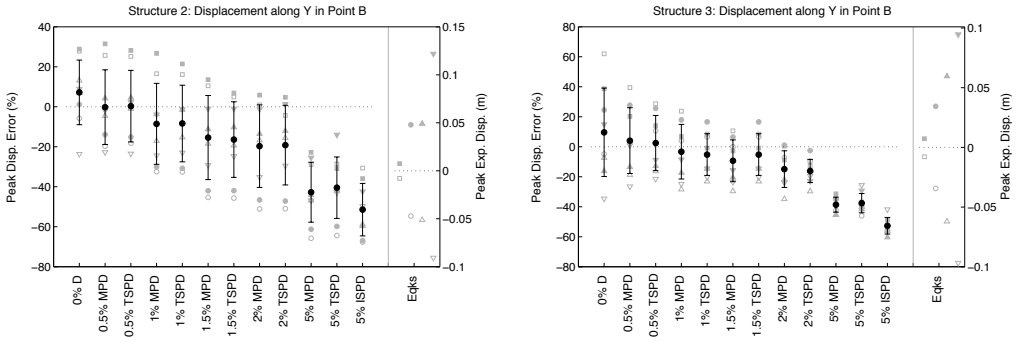

Figure 3.14. Peak displacement error for Structures 2 (left) and 3 (right) considering different EVD models

The right-side plot of Figure 3.13 shows the relative error associated with the measured accelerations of Structure 1. It is interesting to observe that the averaged maximum accelerations are generally better estimated with MPD models independently of the percentage of critical damping, although the corresponding variance in the results is also larger. In order to clarify the reasons of such peculiar behaviour, the left and right plots in Figure 3.15 depict the variation of the transverse and rotational accelerations at the top of the pier considering both MPD and TSPD with 0.5% of critical damping.

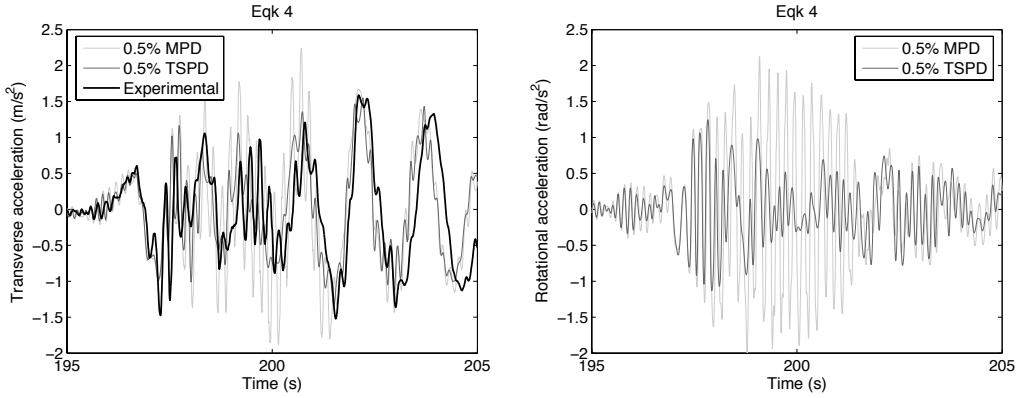

Figure 3.15. Transverse (left) and rotational (right) history of accelerations measured in Structure 1 during Eqk 4 considering 0.5% MPD and 0.5% TSPD

The left plot shows a significant difference in the transverse accelerations computed with both damping models around the time instant $t = 200$ s. After this point, both models produce similar values, close to the experimental ones. This localized effect appears to be connected with the way in which SPD and MPD models deal with the contribution of higher-mode effects (second mode, in this case). In the right side plot, the high-frequency rotational accelerations - response parameter associated with the second mode of vibration - exhibit also larger differences at around $t = 200$ s. In this case the values computed with MPD are about four times larger than the ones obtained with the TSPD model (even considering only 0.5 % of critical damping). This is due to the fact that while damping forces increase for the higher modes using SPD models, in the MPD case the higher modes tend to become more important as they are always less damped than the fundamental mode of vibration.

Considering the similarities obtained in terms of displacements by TSPD and MPD for the same percentage of critical damping, it is difficult to select the most accurate one. However, the accelerations computed with MPD are more prone to present amplified response accelerations, and thus inertial and member forces, associated with higher

modes. On the other hand, as shown in Correia *et al.*, [2013], SPD models tend to produce more significant damping forces that strongly influence member and joint equilibrium. In the following sections, only the damping models showing the best approximation to the experimental results are considered. Hence, critical damping values of 0.5 % (for Structures 1 and 2) and 1 % (Structures 1 and 3) were considered for MPD and TSPD.

3.4.2 Element Discretization

In the following, the results of the parametric tests related to the discretization options indicated in Table 3.5 are evaluated for the most accurate damping models identified in the previous section. The moment-curvature curve of Structure 1 (Figure 3.3) shows a fully hardening post-yield behaviour. Such observation implies that localization issues, as described in Section 2.2.2, are not expected and hence, the most refined approach (corresponding to the use of 10 IPs) should minimize the error, see also Section 2.2.1. However, Figure 3.16 shows a large variability for both the displacements and accelerations errors computed for this bridge pier, making it difficult to identify one discretization scheme that clearly stands with respect to another.

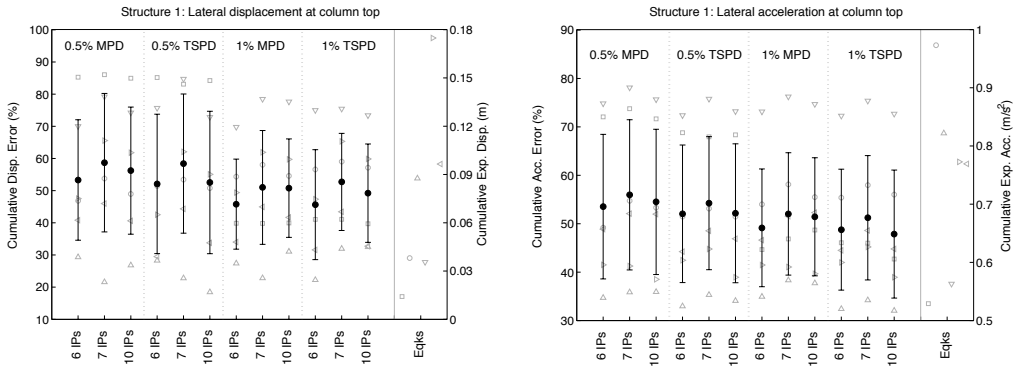

Figure 3.16. Cumulative displacement (left) and acceleration (right) error for Structure 1 considering different discretization schemes

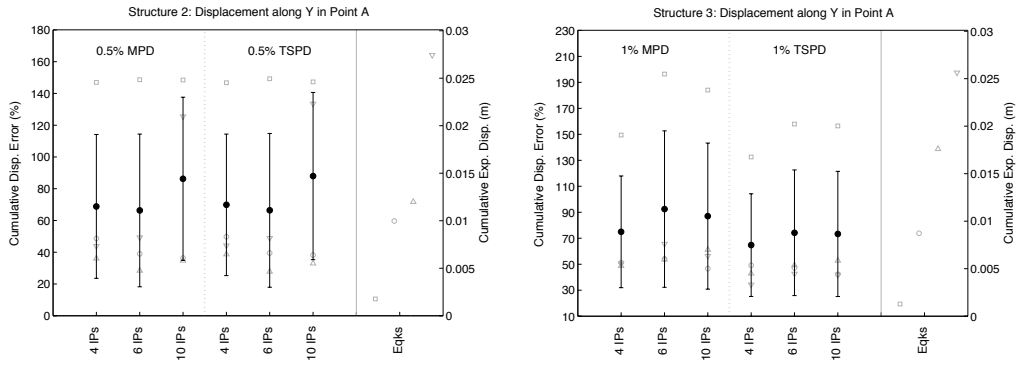

Figure 3.17. Cumulative displacement error for Structures 2 (left) and 3 (Right), considering different discretization schemes

Regarding Structures 2 and 3, the columns' moment-curvature curves exhibit a very slight softening branch after the peak (Figure 3.8 and Figure 3.9, respectively), which is attained at a curvature of around 0.1 m^{-1}. However, as depicted in Figure 3.18, this value is barely reached during the nonlinear dynamic time history. Once again, the most refined approach should thus minimize the error.

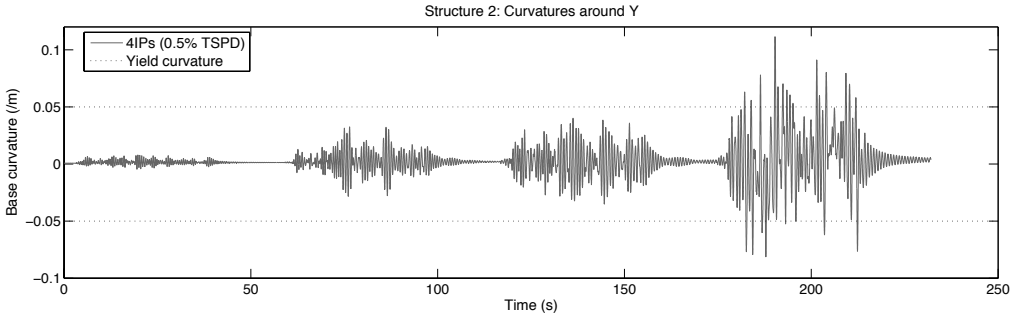

Figure 3.18. History of curvatures measured at the column base below Point B of Structure 2 considering 0.5% TSPD and 4 IPs per column

Nevertheless, similarly to Structure 1, Figure 3.17 does not confirm the previous expectation and instead it appears that the use of a discretization scheme such that the integration weight of the extreme IP approaches the plastic hinge length (i.e., when '4 IPs' are employed) produce improved simulations. The reason behind this discrepancy between the theoretical considerations of Section 2.2.1 and the experimental results are related with the limitations of Euler-Bernoulli theory. In fact, recent experimental findings [Goodnight *et al.*, 2014] indicate that plastic curvatures always follow an approximately linear distribution in the plastic hinge region (and show that the height at

which this distribution intersects the elastic curvature profile increases for higher imposed ductility levels) due to tension-shift effects. This is unlike what an exact (or refined) solution of an Euler-Bernoulli beam element predicts, since the latter is not able to simulate the aforementioned physical phenomena. The use of a reduced number of integration points in a FB element, for which the bottom IP integration weight somehow simulates this length along which the plastic curvatures are linear, hence seems to serve as a workaround that allows for a better match against experimental results. In other words, the need to 'regularize' the response in the pre-peak branch and not just for the post-peak phase of behaviour appears to be required. Some recent modelling efforts have proposed methods to incorporate such observations in the context of Euler-Bernoulli FB approaches [Feng *et al.*, 2014].

Related to the above, and despite the absence of base curvature detailed measurements during the experimental tests herein analysed, the present case studies confirm that the numerical estimation of this local-level EDP is very sensitive to the adopted discretization. Figure 3.19 shows the variation of the base curvatures in Structure 1 during Eqk 1 (on the left) and 3 (on the right). As expected, while the pier responded essentially in the linear range (Eqk 1), the base curvatures simulated by two different models (taken as '10 IPs' and '6 IPs') are very similar; however, during large nonlinear excursions (Eqk 3), the base curvatures predicted with 10 IPs reach values that are more than two times larger than those obtained with 6 IPs.

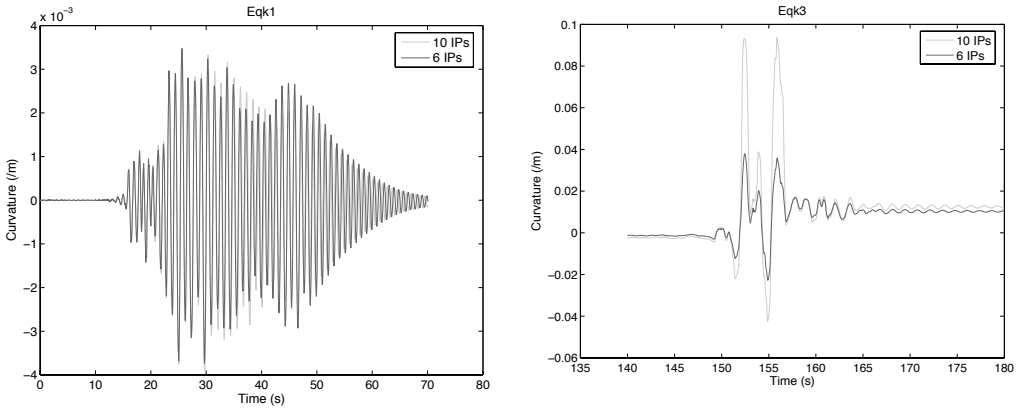

Figure 3.19. Predicted curvatures at base IP for Structure 1 during Eqk 1 and Eqk 3

As a final observation, it is noted that the *Cumulative Error* is very sensitive to small variations in the amplitude of the signals under comparison. For instance, the history of measured and computed displacements for Structure 1 assuming MPD with 0.5 % of critical damping with 6 IPs, for which the calculated error is approximately 30 % for

Eqk 3, is presented in Figure 3.20; the reader can thus visually observe that extremely good matches between the experimental and the numerically simulated signals can still produce relatively large values of the *Cumulative Error*.

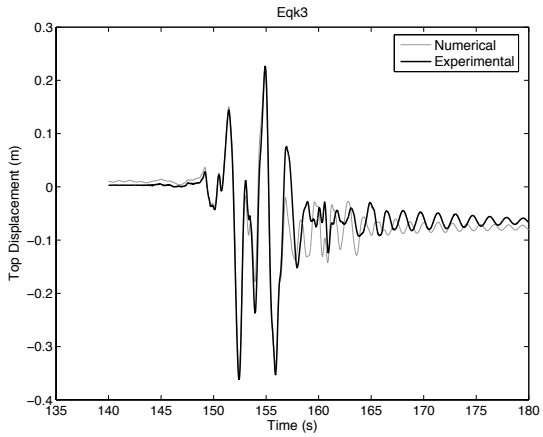

Figure 3.20. Comparison between measured and simulated displacement time-histories in Structure 1, considering 0.5 % MPD with 6 IPs during Eqk 3

3.4.3 Strain penetration

The results illustrated in Figure 3.21, Figure 3.22 and Figure 3.23 indicate that, in general, the consideration of a rotational spring or an artificially elongated element to model strain penetration effects improve the estimations with respect to the case where the additional SP flexibility is neglected. Furthermore, the use of elongated elements appears to provide more accurate EDPs than the use of a rotational spring at the base of the columns.

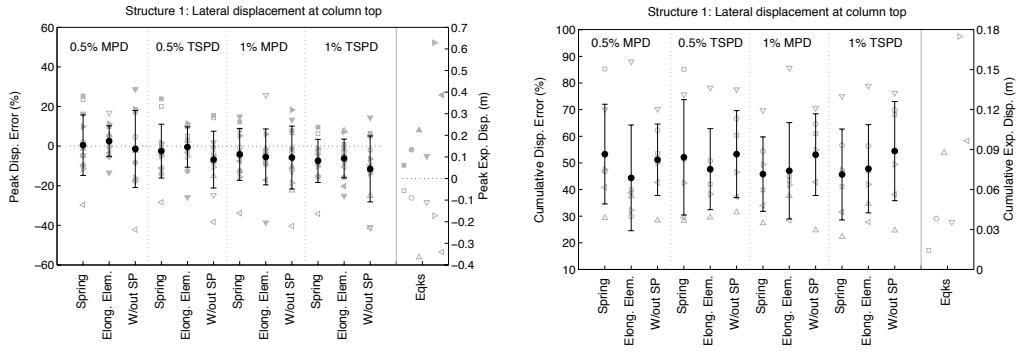

Figure 3.21. Peak (left) and cumulative (right) displacement error for Structure 1, considering different SP models

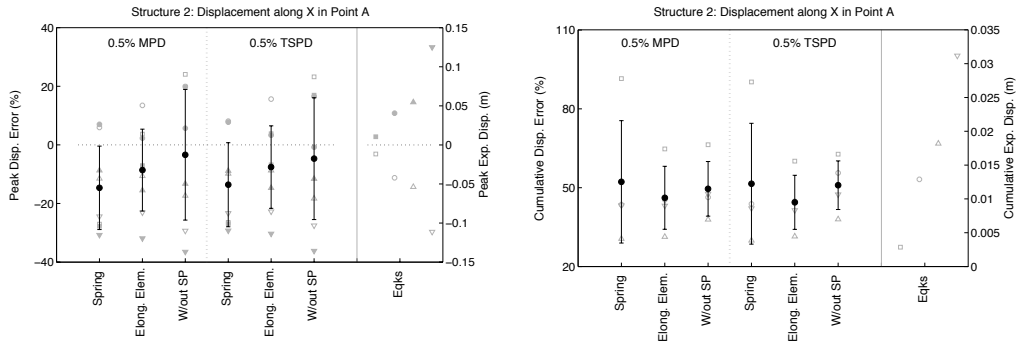

Figure 3.22. Peak (left) and cumulative (right) displacement error for Structure 2, considering different SP models

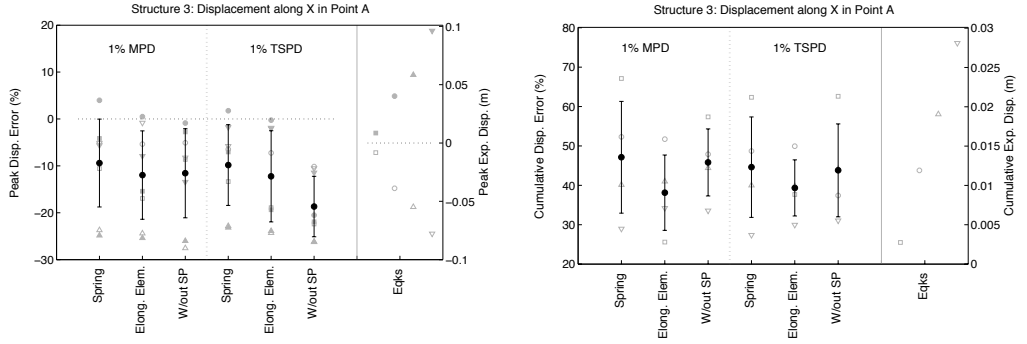

Figure 3.23. Peak (left) and cumulative (right) displacement error for Structure 3, considering different SP models

It is noted that the simulation improvements observed for larger seismic intensity demands bring about significant differences in the structural response at lower intensity excitations. In fact, each simplified SP modelling option affects the elastic dynamic structural properties through an (unrealistic) increase in member flexibility; it is recalled that the elongation of the members by the strain penetration length or the consideration of an elastic spring are calculated from the assumption that the longitudinal rebars have yielded. This point is illustrated in Table 3.7, which summarises the elastic periods of vibration of Structure 2 with the different SP modelling options. It is clear that the models of Structure 2 with elongated elements have a period of vibration that compare very satisfactorily with the experimental ones. The increased flexibility of this modelling option turns out to reproduce more accurately the flexibility of the coupled system (specimen + shake table) than the use of a fixed-base model with no consideration for SP effects. Note that the modal properties determined including the specimen and the shake

table accounts also for the shake table DOF and hence, the system becomes more flexible than when the test specimen is analysed isolated.

Table 3.7. Elastic vibration periods of Structure 2 for different SP modelling options

Modes	Experimental		Numerical		
	Specimen	Specimen + shake table	No SP	Elong. elem.	Base spring
T1_X (s)	0.277	0.333	0.311	0.326	0.365
T2_Y (s)	0.256	0.303	0.285	0.300	0.337
T3_RZ (s)	0.129	0.154	0.146	0.154	0.170

To further illustrate the abovementioned differences, Figure 3.24 compares the history of simulated and experimental displacements in Structure 2 at point A along direction *X*, for Eqk 1 and Eqk 3. Particular attention is given to the elastic response during the first record, between $t = 5$ s and $t = 10$ s.

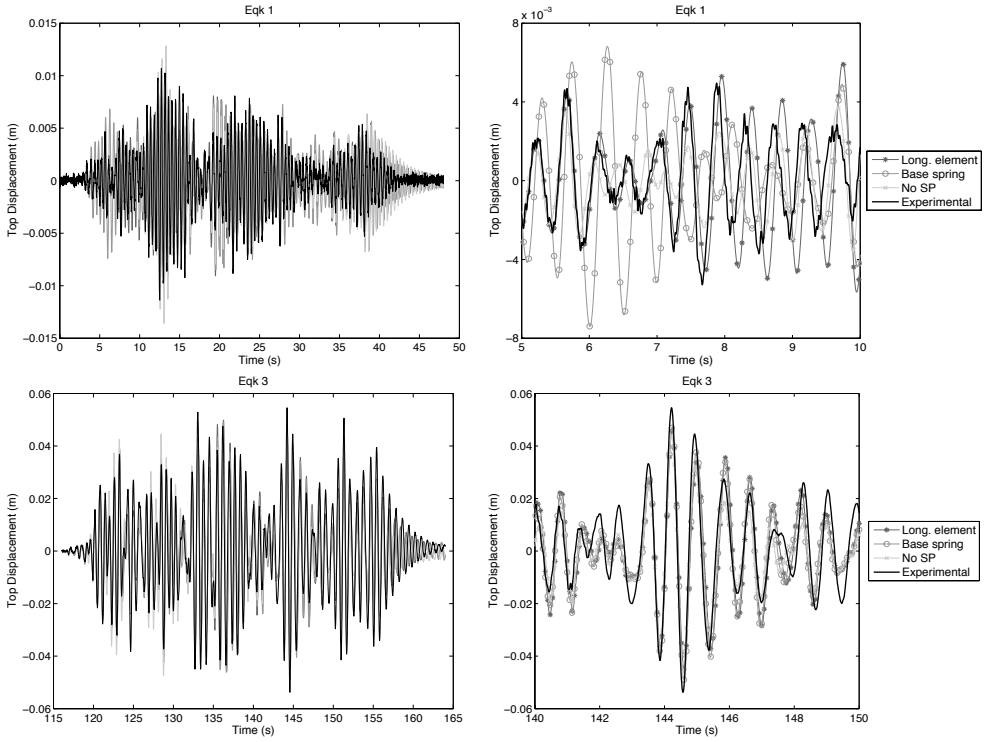

Figure 3.24. Time-history of measured displacements in Structure 2 (point A, direction *X*) *vs* displacements computed with different SP models, during Eqk 1 and Eqk 3

A visual assessment of this series of plots reinforces the conclusion that the use of longer vertical elements produces better estimations when compared with the use of a rotational spring. Moreover, as it only requires the calculation of a strain penetration length estimate, it is simpler to implement than an equivalent spring stiffness and further it seems to more adequately reproduce the elastic modal properties (see Table 3.7). On the other hand, for framed structures with multiple storeys and/or bays, geometrical incompatibilities will arise due to likely different strain penetration lengths for parallel members and lastly the shear demands will be slightly underestimated given the increased shear span of the elements.

3.4.4 Material Stress-Strain Models

3.4.4.1 *Concrete*

The concrete models considered in this study differ primarily with respect to the approaches used to simulate the confinement effects on the cross-section core: in particular, the definition of the post-peak response may differ significantly as illustrated in Figure 2.11. Figure 3.25 and Figure 3.26 show that for the analysed cases only marginal deviations in the global structural response were observed. This can be partially attributed to the relatively small concrete compressive strain demands, as discussed below in more detail. The model proposed by Kappos and Konstantinidis [1999], which was calibrated for concrete strengths larger than 50 MPa (hence larger than those of the analysed structures), offered results in terms of displacement and acceleration predictions which are in line with those of the reference model [Mander *et al.*, 1988]. On the other hand, despite the encouraging results for Structure 1, the model proposed by Madas and Elnashai [1992] showed numerical instability issues for Structures 2 and 3 which prevented the completion of the analyses for the full set of records.

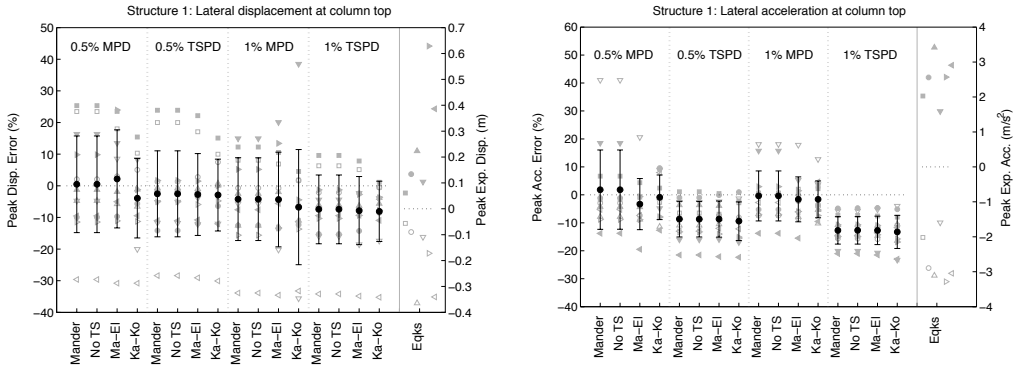

Figure 3.25. Peak displacement error (left) and acceleration (right) error for Structure 1 considering different concrete models

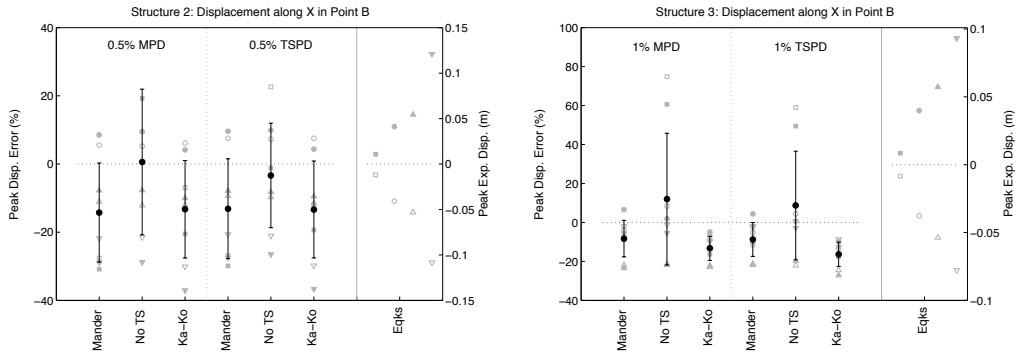

Figure 3.26. Peak displacement error for Structure 2 (left) and 3 (right) considering different concrete models

In addition, while Figure 3.25 shows that neglecting the concrete tensile strength for Structure 1 does not seem to adversely affect the match, for Structures 2 and 3 this parameter plays an important role in the response. Considering the low intensity of Eqk 1, both Structures 2 and 3 respond essentially in the elastic regime during this ground motion. Hence, it is not surprising that the displacements obtained neglecting the tensile response are overestimated since the stiffness of the structure is significantly underestimated (Figure 3.26). For larger intensities, however, the numerically simulated displacements are essentially similar with or without consideration of the concrete tensile strength. This effect can be appreciated in more detail in Figure 3.27, which depicts the history of displacements of Structure 3 under elastic (left) and inelastic (right) response.

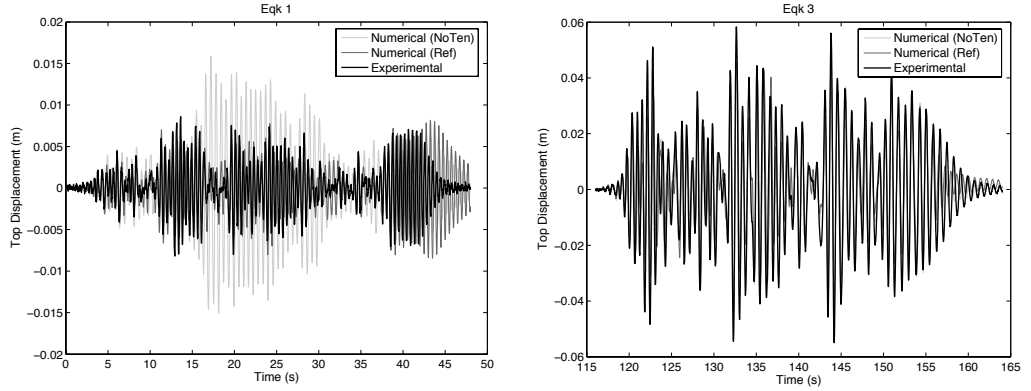

Figure 3.27. Time-history of simulated displacements in Structure 3 (point A, direction *X*) considering Mander's concrete model with and without tensile strength

As mentioned above, the structural response was not significantly affected by the alternative constitutive relation considered, notwithstanding the significant number of nonlinear cycles imposed by successive records. It could be expected *a priori* that the highly distinct post-peak branches would influence the results. However, that did not turn up to be the case, which can be essentially attributed to the concrete compressive strains seldom exceeding the strain at peak stress, as illustrated in Figure 3.28**.** It shows the strain history at diametrically opposed fibres in the base cross-section of Structure 1, corresponding to the most strained fibres of the confined concrete (the dashed line indicates the strain at peak compressive stress).

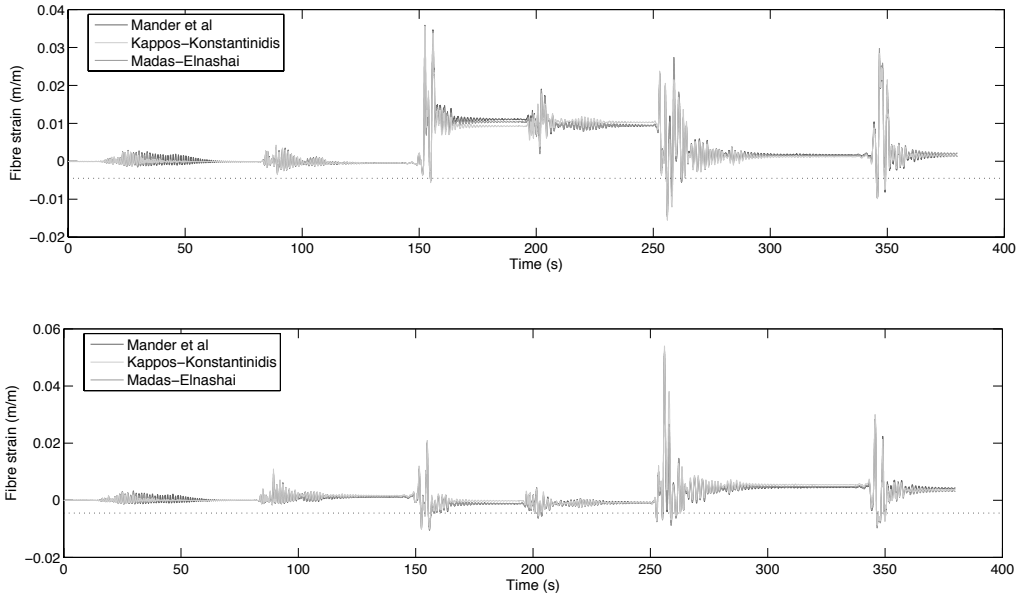

Figure 3.28. History of simulated strains in Structure 1 at diametrically opposed fibres of the base section compressed core, for the entire set of records and considering alternative concrete models

It is apparent that when the concrete is subjected to large compressive strain demands under flexure, the opposite side of the cross-section experiences much larger (absolute) tensile strains producing large equilibrating forces in the reinforcement. Hence, during cyclic loading, the outmost rebars tend to elongate alternatively on both sides of the cross-section and to accumulate permanent residual tensile strains. This well-known phenomenon progressively limits the occurrence of large compressive strains in the concrete to shorter periods of very strong seismic demand.

Moreover, based on the previous figure and the stress-strain response presented in Figure 3.29, it is possible to verify that the maximum strains at the base of the element are not sensitive to the adopted concrete constitutive relation.

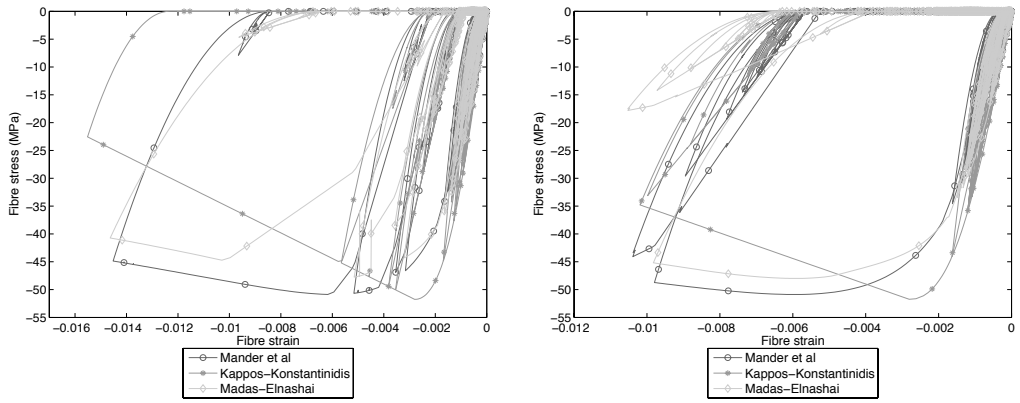

Figure 3.29. Simulated stress-strain response in Structure 1 at diametrically opposed fibres of the base section, for the entire set of records and considering alternative concrete models

3.4.4.2 *Reinforcing steel*

The present section examines the effect of four different reinforcing steel constitutive models: the well-known Menegotto-Pinto [Menegotto and Pinto, 1973] (using two different transition curves), the model proposed by Monti-Nuti [Monti and Nuti, 1992] to account for buckling of the longitudinal rebars, and the simple bilinear approximation. Figure 3.30 and Figure 3.31 confirm that, as expected and noted by others [Blandon, 2012], the computed error measures are significantly more sensitive to the adopted constitutive steel model than to concrete's.

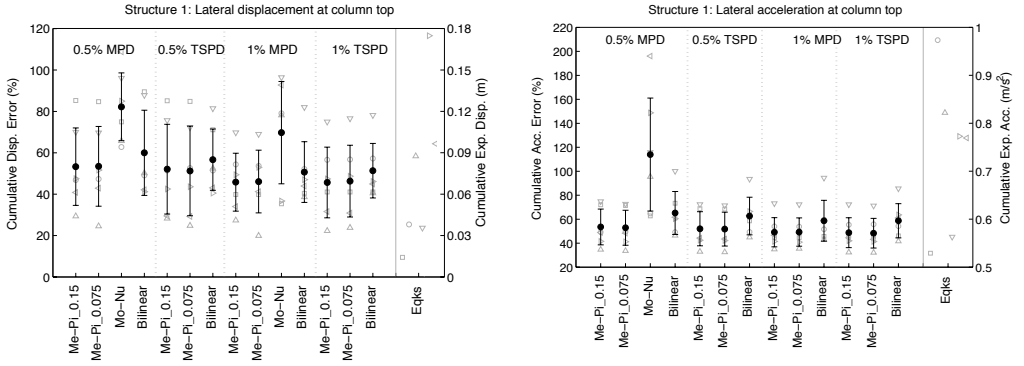

Figure 3.30. Cumulative displacement (left) and acceleration (right) error for Structure 1 considering different steel models

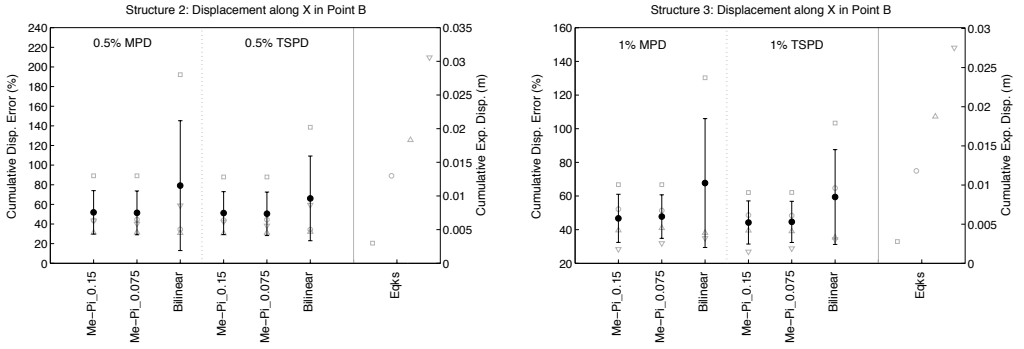

Figure 3.31. Cumulative displacement error for Structure 2 (left) and 3 (right) considering different steel models

Regarding the simple bilinear model, one can confirm the expected increase in the computed mean error values and standard deviation. Bearing in mind that all steel models assume the same loading and unloading stiffness, it becomes evident that the hysteresis loop shape, i.e., unloading and reloading curves, impact significantly the overall response simulation. The results presented in the top plots of Figure 3.32 demonstrate that the strain demands when the bilinear model is employed may differ significantly from both approaches featuring the Menegotto-Pinto model. Moreover, the history of curvatures presented in the bottom part of the same figure shows important deviations during Eqks 3, 4 and 6.

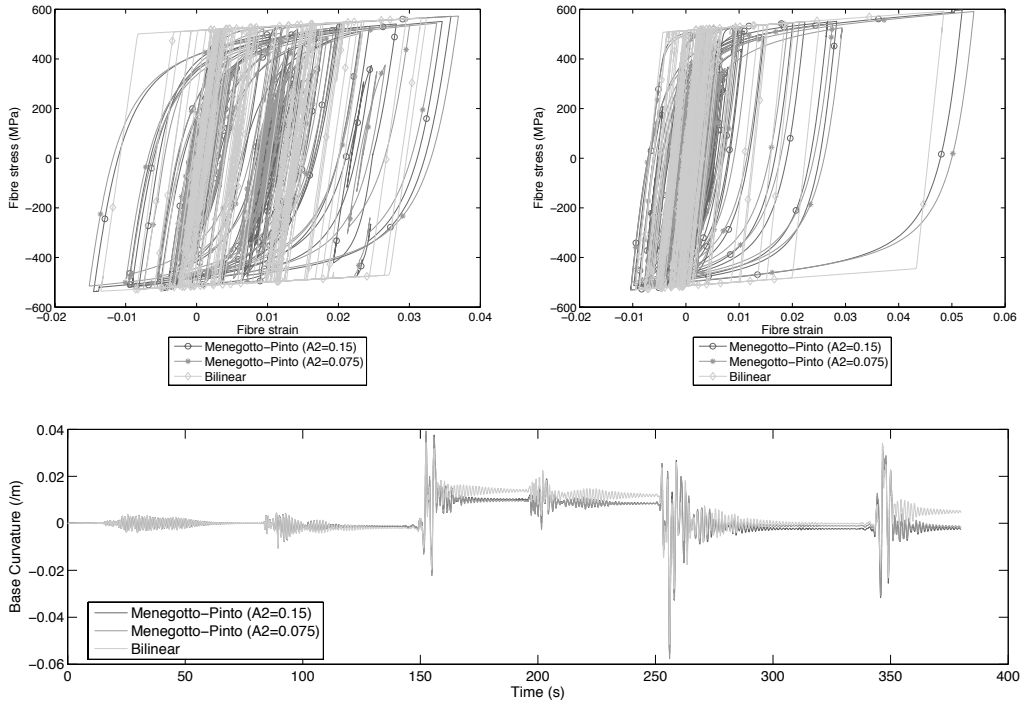

Figure 3.32. Stress-strain response at diametrically opposed fibres of the base section (top) and history of simulated curvatures (bottom) in Structure 1 for the entire set of records considering alternative steel models

The previous observations emphasize the importance of the Bauschinger's effect in obtaining an accurate representation of the reinforcement behaviour and therefore a better estimation of the structural response. Based on the overall set of computed errors and the stability of the analyses, one may conclude that the Menegotto-Pinto's steel model exhibits the better performance. The use of different transition curve parameters (A2 = 0.15 *versus* A2 = 0.075), on the other hand, is seen to have a limited influence.

3.4.5 Numerical Integration and Time-Step

3.4.5.1 *Integration Algorithms*

This section addresses the effect of considering two well-known integration algorithms: Newmark (in the constant average acceleration variant) and Hilber-Hughes-Taylor. Figure 3.33 presents the error measures associated with the lateral displacements computed for Structure 1. The results reveal that, for the original time-step (Δt = 0.0042 s), the response computed with the two algorithms converge to an identical numerical solution. This observation is valid both in terms of *Peak Error* and *Cumulative Error*.

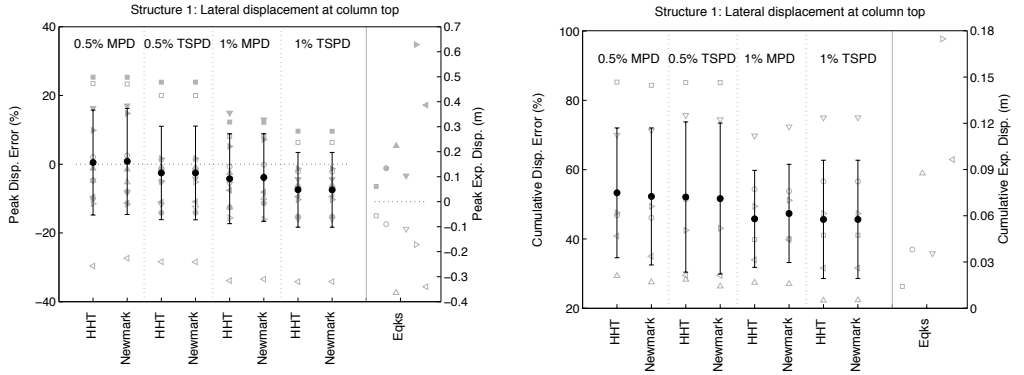

Figure 3.33. Peak (left) and cumulative (right) displacement error for Structure 1 considering different integration algorithms

Similar results were obtained for Structure 2 and Structure 3, whose results are presented in Figure 3.36 and Figure 3.35, respectively. In the latter case, the results corresponding to the use of Newmark method with 0.5 % MPD are not presented due to convergence difficulties to complete the analysis.

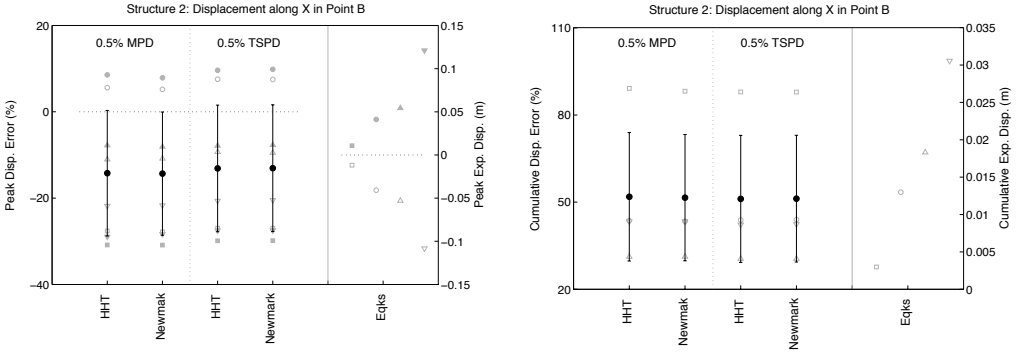

Figure 3.34. Peak (left) and cumulative (right) displacement error for Structure 2 considering different integration algorithms

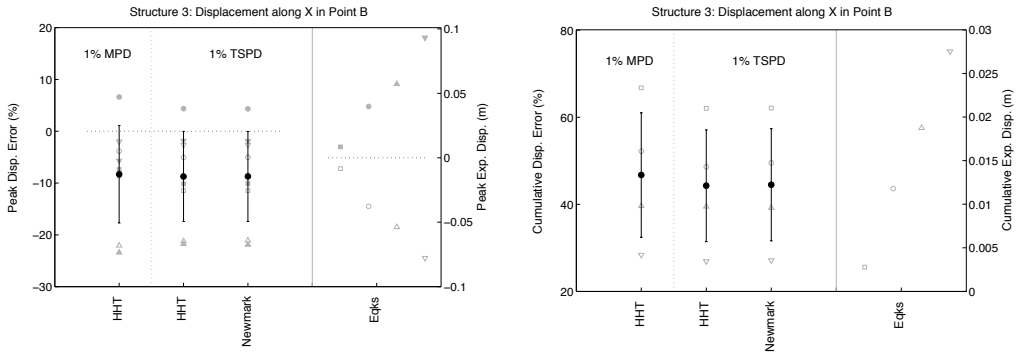

Figure 3.35. Peak (left) and cumulative (right) displacement error for Structure 3 considering different integration algorithms

However, when analysing the computed accelerations at Structure 1, it is possible to observe that the response determined with both methods is not identical. For the models considering the Newmark method together with mass proportional damping, the error increases substantially, in particular for Eqk 4, where the structural accelerations are minimal (Figure 3.36).

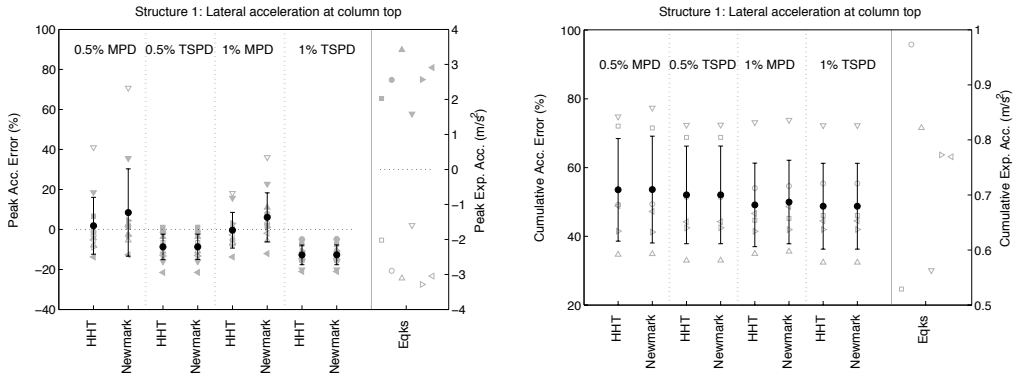

Figure 3.36. Peak (left) and cumulative (right) acceleration error for Structure 1 considering different integration algorithms

The results presented before indicate that the analysis performed with the Hilber-Hughes-Taylor and Newmark's integration algorithm produce identical results in terms of displacements. Nevertheless, the accelerations computed with Newmark's method tend to exhibit larger errors when used with mass proportional damping models. This effect seems to be associated with the spurious contribution of higher dynamic modes. As

described in Section 2.5, the main advantage of the HHT approach lies on the incorporation of numerical damping for higher frequencies, filtering the dynamic response and limiting potential spurious responses. At the same time it should be recalled that, contrarily to what occurs with stiffness proportional damping (SPD), the use of mass proportional damping (MPD) implies that the fundamental mode is always more damped than the higher modes (see Figure 2.8).

It is thus apparent that the employment of the Newmark method together with MPD may produces less accurate analyses, which are more prone to exhibit spurious responses and potential numerical instability. In light of these problems, the following section assesses the influence of varying the time-step on the computed response.

3.4.5.2 *Time-step*

The performance of nonlinear dynamic analysis on large structures is often conditioned by time constraints. In order to reduce the computational time it is common to increase the time-step. Hence, it seems important to appraise the limits beyond which the accuracy of the analysis may become compromised. Thus, in addition to the original time-step of the original record, time-steps of $\Delta t = 0.02$ s and $\Delta t = 0.1T_1$ are considered.

The results presented in Figure 3.37, representing the *Peak Displacement Error* for both HHT and Newmark method, reveal that the computed displacements are not relevantly affected as far as the time-step is lower than 0.02 s. For larger values, such as $\Delta t = 0.078$ s for the present case, the error increases, in particularly for the models featuring MPD.

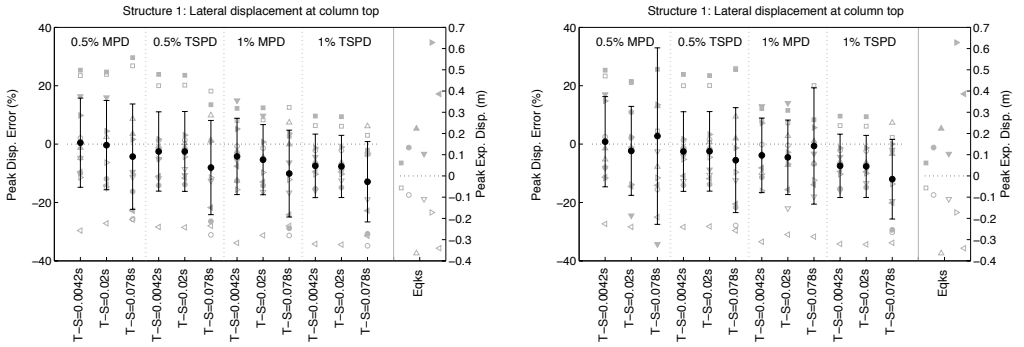

Figure 3.37. Peak displacements error for Structure 1 considering different time-steps with HHT (left) and Newmark (right) integration algorithms

Similarly to what was observed in the previous section, the results illustrated in Figure 3.38 indicate that the accelerations are more sensitive to variations of the time-step. Once again, it is possible to observe that the models featuring Newmark algorithm together with MPD model are more sensitive to the increase in time-step.

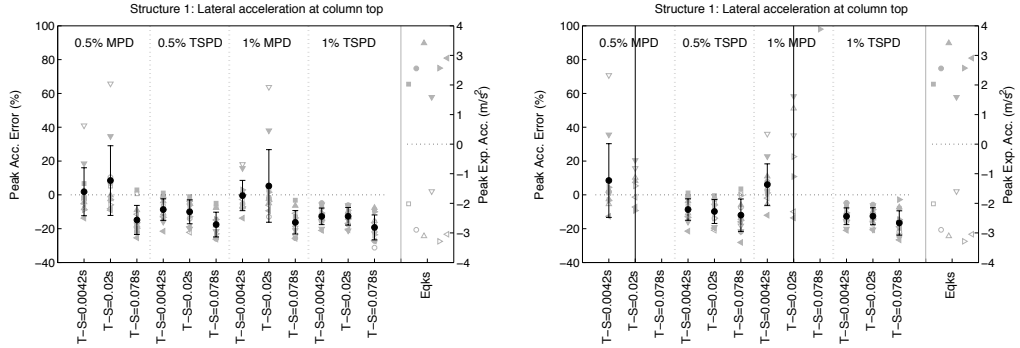

Figure 3.38. Peak acceleration error for Structure 1 considering different time-steps, with HHT (left) and Newmark (right) integration algorithms

The previous conclusions can be analysed in more detail in Figure 3.39, which shows the time-history of accelerations at the top of Structure 1 determined with both integration algorithms and increasing time-step.

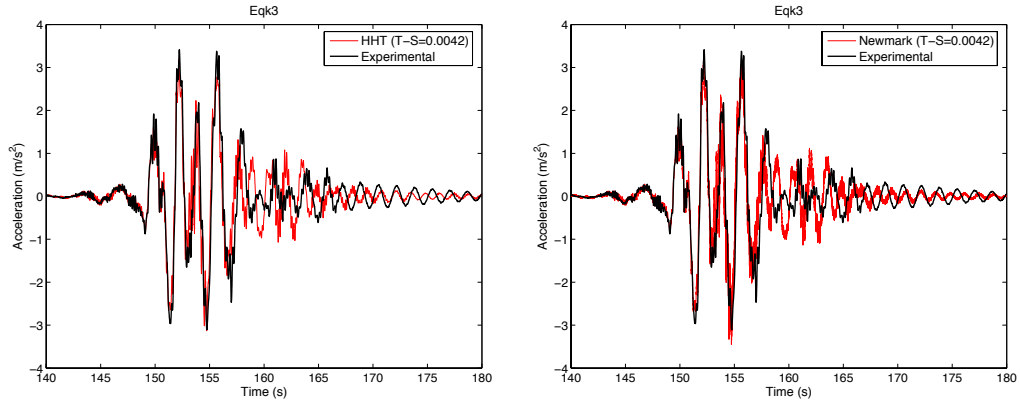

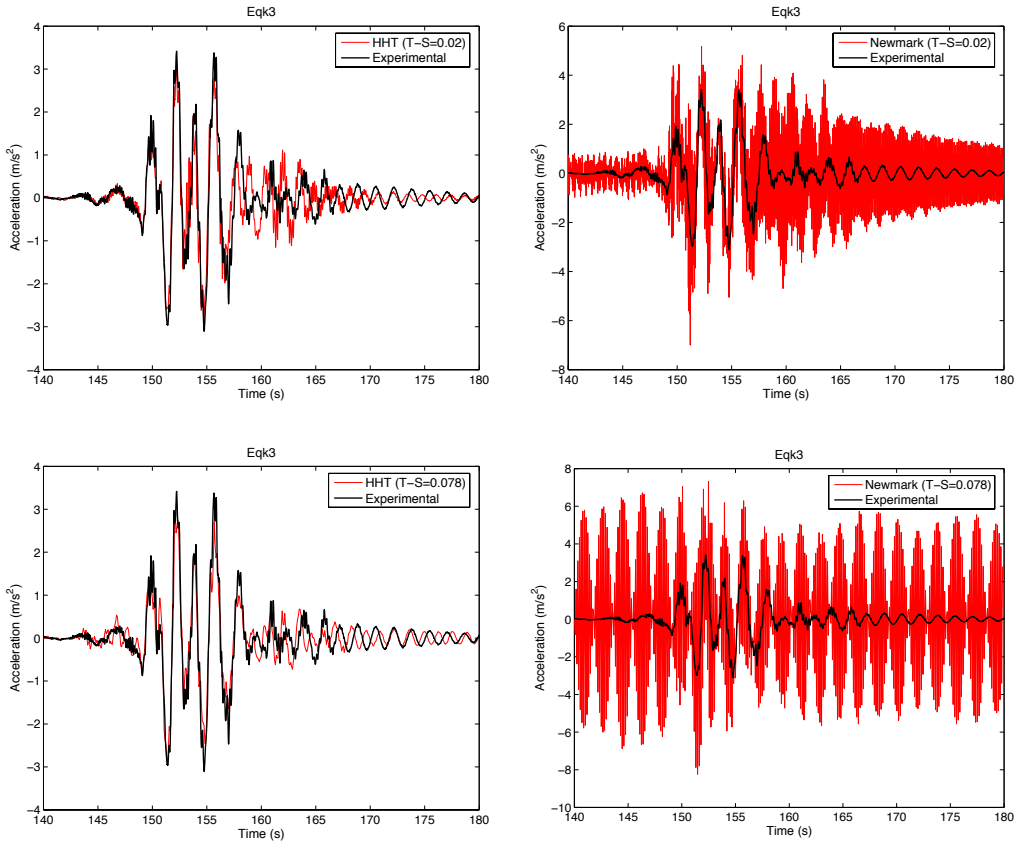

Figure 3.39. Time-history of transversal accelerations measured in Structure 1 *vs* transversal accelerations computed with HHT (left) and Newmark (right) integration algorithm and increasing time-step (top to bottom), during Eqk 3

From the figure above, it is clear that for the case of Newmark method, as the time-step increases, the accelerations oscillates at very high frequencies, reaching, in some cases, important amplitude variations.

The error associated with the displacements of Structure 2 and Structure 3 is presented in Figure 3.40 and Figure 3.41, respectively.

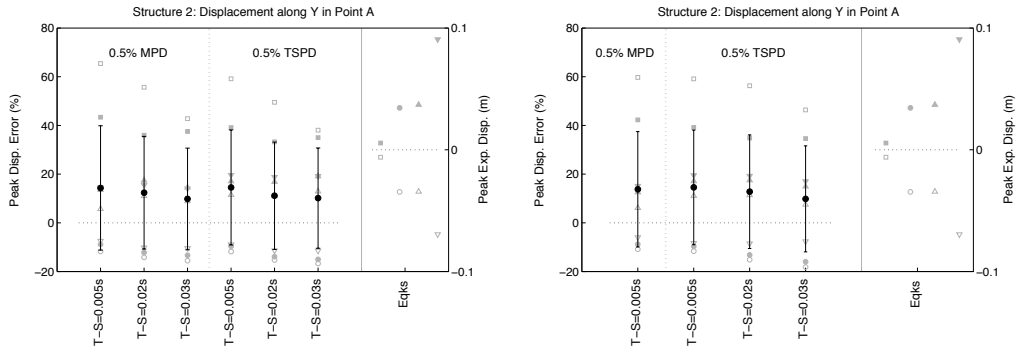

Figure 3.40. Peak acceleration error for Structure 2 considering different time-steps, with HHT (left) and Newmark (right) integration algorithms

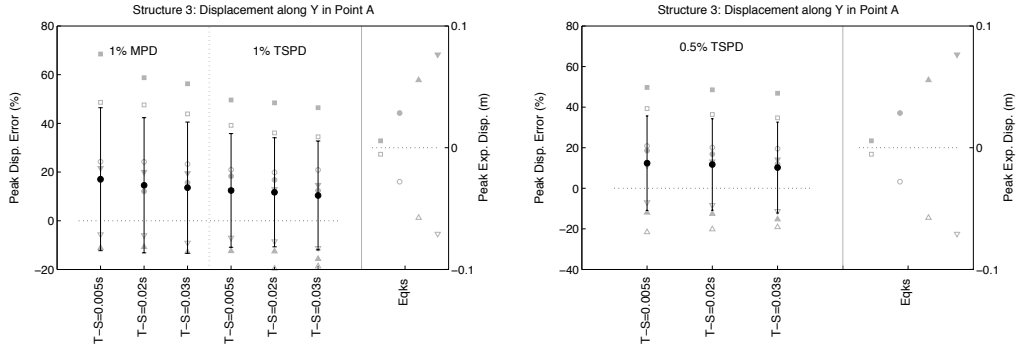

Figure 3.41. Peak acceleration error for Structure 3 considering different time-steps, with HHT (left) and Newmark (right) integration algorithms

As for the previous case, the displacements are in general less sensitive to the use of increased time-step. Nonetheless, the models featuring Newmark's approach with MPD exhibited relevant convergence difficulties making it difficult to complete some of the analysis. For this reason, the corresponding results are not illustrated in the previous figures.

3.5 SUMMARY

Motivated by the successful participation in recent blind prediction challenges, it was decided to undertake a critical review on the simulation options available to engineers and researchers that use fibre-based beam models to numerically estimate the nonlinear dynamic behaviour of RC framed structures. Based on a review of past studies, five modelling options were selected to be analysed in detail: equivalent viscous damping,

element discretization, simulation of strain penetration effects, material constitutive models (concrete and steel) and integration algorithm and time-step. The three structures tested in the abovementioned challenges were used as case-studies. The goodness-of-fit was evaluated with a newly developed proposal for a *Cumulative Error* measure and a more traditional *Peak Error* measure. They were applied to the engineering demand parameters that were measured experimentally, namely displacements and accelerations. Together with a qualitative comparison of the time-history responses, the following main conclusions were obtained from this study:

- In nonlinear dynamic analysis of bare RC structures with distributed plasticity elements, most of the energy dissipation mechanisms are explicitly modelled and hence equivalent damping models should be carefully employed. Based on the analyses carried out, enhanced performance was obtained with values of critical damping ranging from 0.5 % to 2 %. Numerical analyses with larger levels of EVD tend to underestimate the structural response, whilst considering no damping results in a small overestimation of the response parameters. The study also reviewed and analysed the specific limitations of both mass proportional damping and tangent stiffness proportional damping, highlighting the difficulty to advocate one model with respect to the other. However, for the recommended small values of critical damping such differences become limited.
- The definition of a number of integration points per element such that the weighted length associated with the extremity IP matches the expected plastic hinge length seems to produce somewhat more accurate results. This was not an anticipated result from theoretical considerations since for all the analysed structures no localization issues took place and hence the most refined solution should have produced the most accurate results. This discrepancy can be attributed to the presence of tension-shift effects – as demonstrated by other recent experimental findings, which cannot be simulated by Euler-Bernoulli beam theory. The need to develop, calibrate and apply appropriate 'regularization' techniques for fully hardening post-yield moment-curvature relations is hence confirmed from the present study.
- Two simple modelling approaches were considered to account for strain penetration effects, and both contributed to reduce the estimated response errors, particularly for larger inelastic demands. The elongation of the member length by a strain penetration length tends to produce better results than the use of a linear rotational spring. Nonetheless, it should be acknowledged that both approaches have drawbacks, namely: (i) the modification of the elastic dynamic properties of the initially undamaged structure, which can be particularly relevant when a base spring is considered; (ii) the slight underestimation of the member shear demand associated to the use of an artificially elongated element. The development of more accurate (while computationally light) strain penetration models should deserve particular attention from researchers. This issue is addressed in more detail in the following chapters of

this thesis.

- Amongst the limited sample of concrete models analysed, those proposed by Mander *et al.*, [1988] and Kappos and Konstantinidis [1999] provided similar estimations of the global-level structural response. Moreover, it was shown that neglecting the tensile strength of the concrete does not impact the structural response during its nonlinear phase. However, if one is interested in the linear phase of behaviour, the consideration of the tensile strength is advised despite the increased potential for numerical convergence issues.
- Regarding the steel models, the present study indicates that the well-known Menegotto and Pinto [1973] model combines both accuracy and stability. Furthermore, it was verified that the definition of different transition curves in the unloading and reloading branches, through parameters A2 = 0.15 and A2 = 0.075, produced negligible differences in global response error measures. On the other hand, the more theoretically advanced model proposed by Monti and Nuti [1992] did not translate in improved results, essentially due to overshooting problems. As for the bilinear elastoplastic model, disregarding the Bauschinger effect appears to influence substantially the global structural response as the errors computed with this model are consistently larger than the ones obtained with both variants of the Menegotto-Pinto steel model.
- The results obtained in the current parametric study demonstrate that the Hilber-Hughes-Taylor (HHT) integration algorithm is in general more accurate and numerically more stable than the more conventional Newmark's method. Despite the considered structures being relatively simple, and hence with relatively well "defined" modes of vibration, the analysis featuring Newmark integration algorithm are very sensitive to the contribution of higher modes, and often result in spurious response. This observation tends to be amplified when considering increasing time-step and when MPD model are employed. Despite the displacements computed with HHT being relatively insensitive to the EVD and time-step, the error associated with the computed accelerations (and consequently the members forces) tend to increase with higher time-step.

4.STRAIN PENETRATION IN RC MEMBERS

The results presented in the previous chapter exposed the limitations associated with the use of simplified numerical models to account for strain penetration (SP) effects in the seismic modelling of RC structures.

After a through literature review, the present chapter introduces a detailed overview of the different mechanisms associated with the strain penetration effects in RC structures, together with an assessment of the main features of alternative numerical models.

The analysis of the most relevant parameters impacting the SP behaviour, together with the main limitations identified in current numerical models, are described in the following sections and represent, thus, the basis for the new bond-slip model presented in Chapter 5.

4.1 IMPORTANCE AND EFFECTS IN THE SEISMIC RESPONSE OF RC STRUCTURES

Since the incorporation of reinforcement in concrete, back from the mid-19th century, bond between steel and concrete has been the subject of numerous studies. One of the major breakthroughs occurred in the early years of the 20th century with the introduction of deformed surface rebars in substitution of, at that time, conventional plain rebars. This innovation improved the adhesion between the two materials and, consequently, reduced the embedment length (L_e) required to anchor the axial load developed at a given rebar.

Despite the substantial increase in bond resistance provided by deformed rebars, the design of reinforced concrete structures still requires the consideration of a sufficiently long embedment length, along which, the axial load at the rebar can be transferred to the surrounding concrete. The length required to anchor a given force is usually referred to as development length (L_d), i.e., the length along which the rebar force gradually reduces to zero. Ideally, the embedment length provided should be sufficiently large to guarantee that, under the maximum load supported by the rebar, the contact surface around the reinforcement is able to transfer the axial load to the surrounding concrete. This is the underlying idea present in the expressions prescribed by RC codes. Whenever the embedment length is insufficient, the rebar experiences an important increase of slip,

leading to a large increase of the element's base rotation or even failure of the anchorage system (Figure 4.1).

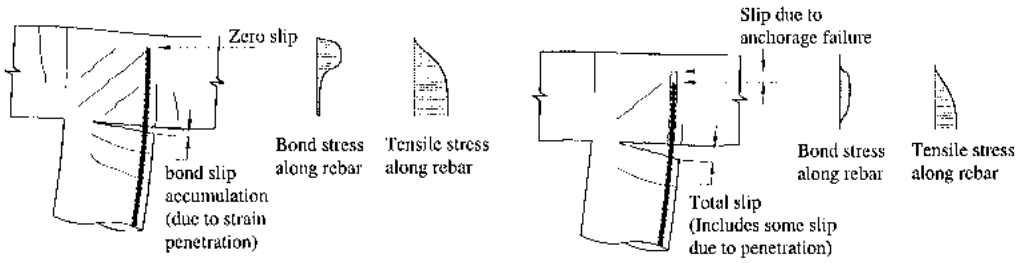

Figure 4.1. Behaviour of anchorage region with adequate (left) and limited (right) embedment length (adapted from Sritharan *et al.* [2000])

Considering that the rebar forces are gradually transmitted to the surrounding concrete, the reinforcement experiences strain variations along the development length. The 'penetration' of steel stresses and strains along the anchorage zone is generally referred to as *Strain Penetration (SP) Effects*.

From a structural engineering viewpoint, these effects are particularly relevant as they can result in significant fixed-end displacements and rotations if a given RC member undergoes important seismic loads. When subjected to tensile forces, the embedment region of the rebar elongates, which is reflected in an increase of the members' end flexibility. Under the assumption that the concrete in the anchorage zone remains essentially undeformed, i.e., neglecting the deformations in concrete, the slip of each rebar represents the relative displacement between the steel and the surrounding concrete. In other words, for a rebar with sufficient embedment length, L_e, the slip at the members' end represents the integral of steel strains ranging from the loaded-end to the point where the force is zero. However, the location at which the rebar force drops to zero does not necessarily correspond to having zero slip of the rebar of the embedment length is insufficient. In these cases, it is important to note that if $L_d = L_e$ the slip measured at the loaded-end is no longer equal to the integral of the strains, but also includes a component corresponding to a global sliding of the rebar.

Despite the previous considerations, in most engineering applications it is common practice to consider that the reinforcing bars are perfectly bonded to the surrounding concrete, i.e., the relative slip deformations, occurring essentially at the connection to foundations systems and at beam-column joints, are neglected. This option reflects an erroneous perception that most of the deformations (being within the linear or nonlinear

range) in RC members are essentially dictated by the deformation occurring along the members' clear span.

However, experimental campaigns conducted on RC columns have shown a significant contribution of strain penetration deformations to the overall lateral deformation of RC members. For instance Sezen and Moehle [2004] concluded that up to 40 % of the total lateral displacement can be due to longitudinal rebar slip. This order of magnitude is in line with the results obtained by Goodnight et al. [2015b], considering several circular bridge RC columns. Based on the results presented in Figure 4.2 it is possible to verify that the displacement component attributed to strain penetration effects (blue bars) represents about 30 % - 40 % of the overall member deformation. Moreover, for increasing levels of ductility, it is apparent that this component increases in an identical proportion with respect to the deformations along the length of plastic hinge region (red bars). Finally, it is important to highlight the notorious relevancy of the SP deformations with respect to the ones resulting from all other elastic mechanisms, including shear deformations.

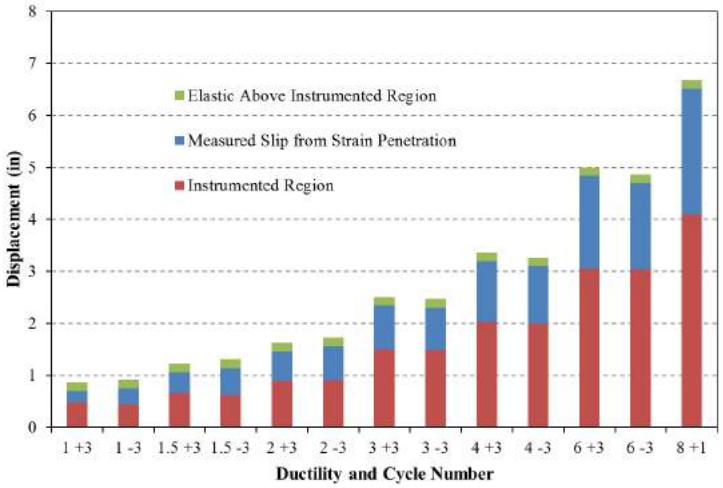

Figure 4.2. Lateral displacement components measured in a circular RC column (Test 9) [Goodnight *et al.*, 2015a]

Identical values were also reported by Saatcioglu *et al.* [1992]. However, according to this study the SP deformations tend to be more relevant before yielding of the rebars. The authors found that at yielding, the member-end rotations accounted for about 50 % of the top displacement – for larger ductility range, the relative importance seems to decrease to values in the order of the ones reported by Sezen and Moehle [2004]. Similar results were also reported by Popov [1984] and Filippou *et al.* [1983] in experimental tests

conducted on beam-joints connections. The latter argued that these effects are the cornerstone of any hysteretic behaviour of RC joints.

In this context, particular attention to this phenomenon should be paid in the assessment of RC structures built essentially in the first half of the 20th century, given that most of these structures were built with plain rebars. In such cases, the consideration of SP effects becomes even more critical - experimental tests conducted on both RC columns [Verderame *et al.*, 2008] and beam-column joints [Melo *et al.*, 2011], reveal that this mechanism may contribute to nearly 90 % of the overall member deformation at failure.

4.2 BOND MECHANICS AND FAILURE MODES

Data resulting from previous research programs, conducted over the last decades, allows the scientific community to have, in the present days, a though understanding of the bond-slip behaviour at anchorage regions. In what regards the transference of rebar forces to the surrounding concrete, it is now evident that it occurs essentially through three main mechanisms, which vary according to the anchorage properties and loading demand:

1. Chemical adhesion between steel and concrete
2. Frictional forces at the interface between both materials
3. Bearing force of the ribs against the surrounding concrete

In addition to the different forces involved in the resisting mechanism, Figure 4.3 shows also the damage induced in the concrete through crack opening and concrete crushing in the vicinity of the ribs.

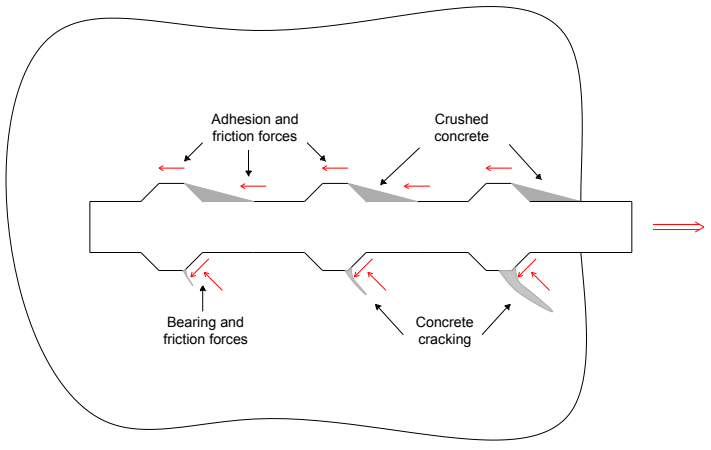

Figure 4.3. Bond mechanisms at the anchorage region of a RC member

According to fib [2000], the transfer mechanism between the rebars and the surrounding concrete can be divided in 4 main stages:

1. At low loading demand, the concrete remains essentially uncracked and bond is mostly ensured by chemical adhesion.
2. As the load increases, the chemical adhesion breaks and the lugs induce large bearing stresses in the concrete and transverse micro cracks at the tips of the lugs allowing the rebar to slip. The wedging action of the lugs remains limited and there is no concrete splitting. After cracking and loss of adhesion, the stiffness suffers an important reduction.
3. As the bond stresses increase, the bond strength is ensured by bearing action in front of the lugs, while longitudinal (splitting) cracks start to spread radially. This restraining action is naturally dependent on the confinement level of the surrounding concrete. Hence, in case of light transverse reinforcement this stage ends as soon as the concrete splitting reaches the outer surface of the member. In relatively short anchorages with moderate confinement a pullout failure is more prone to occur, despite the possibility of developing moderate splitting cracks along the bond length. In cases of large confinement through transverse reinforcement or thick concrete cover, splitting is prevented and the failure mode corresponds to pullout. At this stage, all possible contributions to confinement are mobilized. The magnitude of the different forces are dependent on the existing concrete cover thickness, spacing between rebars, amount of transverse reinforcement and its layout, transverse pressure and cracking cohesion.
4. With larger load levels, the development of longitudinal splitting cracks leads to a softening of the bond strength. After a peak value, the response is essentially dependent on the amount of confinement provided. For light-to-medium transverse reinforcement quantities, the longitudinal cracks spread out through the entire concrete cover thickness or rebar spacing and bond strength can reduce abruptly. On the other hand, the presence of an adequate amount of transverse reinforcement can ensure the development of large slip values (in the order of 5 % of the rebar diameter) with a smooth softening transition.

The variation in bond strength with the anchorage properties described above can be interpreted in a graphical manner in the bond stress-slip plot presented in Figure 4.4.

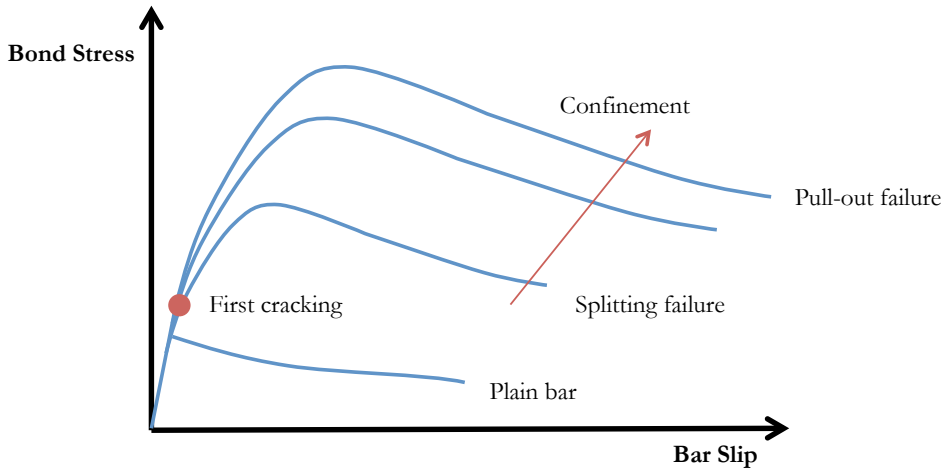

Figure 4.4. Influence of different transfer mechanisms in the bond-slip relations (adapted from fib [2000]

As previously mentioned and illustrated in the figure above, the type of failure is essentially dependent on the level of (passive or active) confinement provided to the system. If the concrete cover, rebar spacing, or transverse reinforcement are sufficient to prevent or delay a splitting failure (Figure 4.5, left), the system can develop larger bond stresses and will potentially fail by shearing (pullout) along the surface of the rebars (Figure 4.5, right). Moreover, if the anchorage within the concrete is adequate, the stress in the reinforcement may become large enough to reach yield and possibly even strain harden the rebar.

On the other hand, in bond splitting failures the peak bond stress is essentially dependent on the tensile strength and fracture energy of the concrete. As described with more detail in Section 4.3.3, concrete specimens exhibiting larger fracture energies result in improved bond capacities, even if the tensile strengths are similar.

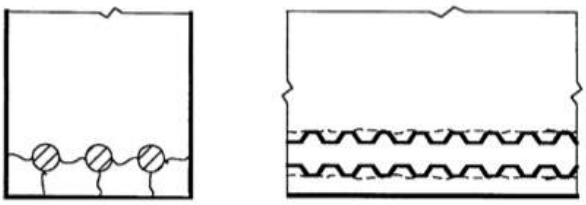

Figure 4.5. Different typologies of anchorage failure: splitting (left) and pullout (shearing) failure of anchorage systems [ACI, 2003]

Taking into account the large strength and ductility capacity of a pullout type of failure with respect to a splitting failure, current design expressions attempt to guarantee that the anchorage zones are detailed with appropriate confinement or, under limited confinement conditions, the anchorage length is sufficiently large to avoid potentially more brittle splitting failures. For instance, Eurocode 2 [CEN, 2004b] defines a minimum embedment length of 10 rebar diameters (d_b). However, in most common applications, code requirements can easily reach 15 d_b or more, depending on the anchorage properties, namely the level of (active or passive) confinement. Conventional "rule of thumb" suggests the use of more conservative values, in the order of 30 d_b. Values of this order of magnitude can be easily found from simple equilibrium considerations at the anchorage region (Equation (4.1)), under the assumption of an average bond stress at the interface between the concrete and the reinforcement in the order of $\tau \approx \sqrt{f_c}$ [MPa]. The following equation can be easily interpreted through the illustrative example presented in Figure 4.28.

$$F_{bond} = F_{bar}$$

$$\sqrt{f_c} \times P_b \times L_e = f_y \times A_b \tag{4.1}$$

In the previous equation P_b, A_b and F_y are the perimeter, area and yield stress of the reinforcing bar, respectively.

Notwithstanding the adequate level of confinement, for systems with insufficient anchorage length or subjected to severe cyclic loading, the demand may exceed the bond capacity, resulting in localized damage and significant sliding between the reinforcing steel and the surrounding concrete.

4.3 ANCHORAGE PROPERTIES AFFECTING STRAIN PENETRATION

The previous section reported the main bond mechanisms and the different types of failures. It was observed that the type of failure is essentially dictated by the level of confinement present around the anchorage region of the rebars. However, even (and especially) under pullout failure conditions, the level of bond stress developed along the rebar can be significantly influenced by geometric, material and loading properties.

These properties are usually determined from experimental tests performed with rebars anchored in concrete blocks with relatively short embedment length ($\approx 5d_b$). Short embedment lengths are generally adopted so that the bond stresses developed can be considered constant along the length of the rebar, in order to produce general bond-slip laws. In addition, it is customary to adopt an unbonded length close to the loaded-end of the rebar in order to achieve the desired stress state, without unrealistic compressive (confinement) forces around the rebar due to the force application apparatus (Figure 4.6).

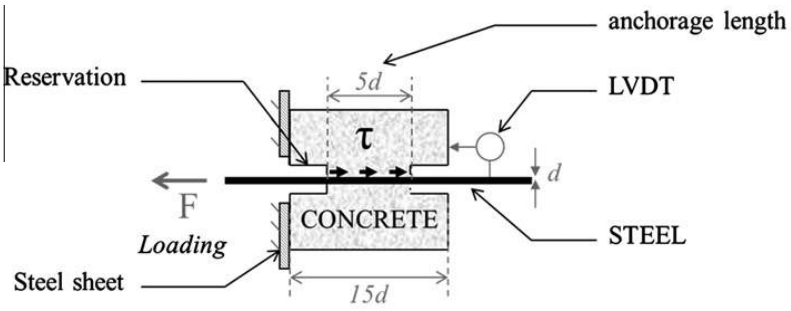

Figure 4.6. Example of a pullout test setup [Casanova *et al.*, 2013]

Under these conditions, the anchorage force is generally lower than the rebar capacity. Hence, the importance of rebar yielding, as well as the evaluation of the different response parameters along more realistic anchorage lengths, requires the use of larger embedment lengths.

The present section presents a review of past experimental tests conducted in order to identify and quantify the parameters that have a larger influence on the bond-slip response. The comprehension of this constitutive relation is of primary importance as it represents the basis of most numerical tools developed for modelling anchorage regions. For convenience, the parameters presented hereafter are divided into 4 main groups: confinement, reinforcement, concrete and loading properties.

4.3.1 Passive and Active Confinement

Confinement in reinforced concrete members may be provided passively or actively. The first one reflects the confining radial forces provided by sufficiently large rebar cover or transverse reinforcement hoops surrounding a given concrete anchorage block. Similarly, the active confinement produces an identical benefit but, in this case, the restraining action is achieved through the application of a compressive pressure.

Results form previous experimental tests indicate that once the concrete cover thickness is sufficient to avoid a splitting failure, the rate of bond stress increase with increasing concrete cover is progressively reduced. This effect is evident in a recent study from Casanova *et al.* [2013] and presented in Figure 4.7, depicting the evolution of the ratio between the maximum bond stress and the concrete tensile strength against the ratio between the cover thickness and the rebar diameter, for different transverse pressures.

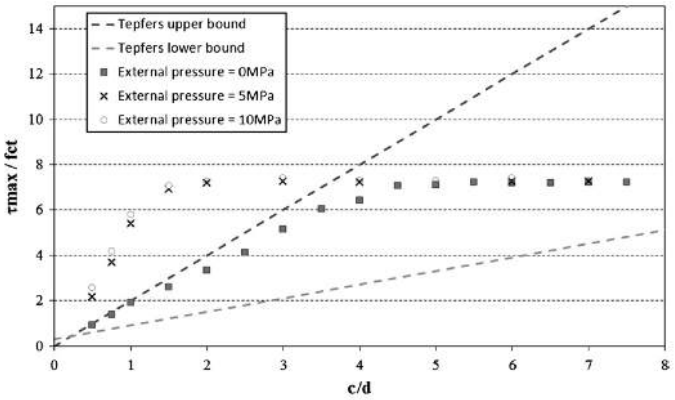

Figure 4.7. Evolution of bond strength with the concrete cover for different transverse pressure [Casanova *et al.*, 2013]

Similarly to an adequate concrete cover thickness, the employment of transverse reinforcement hoops for confinement helps to limit the progression of splitting cracks, thus increasing the bond efficiency both for conventional anchorage systems and for lap splices. However, as illustrated in Figure 4.8, additional transverse reinforcement beyond the amount needed to cause the transition from a splitting to a pullout failure becomes progressively less effective, providing only a marginal increase in bond strength [Orangun *et al.*, 1977; Eligehausen *et al.*, 1983]. The following figure shows the variation in bond stress for different ratios of the area of transverse reinforcement with respect to the area of the longitudinal rebar.

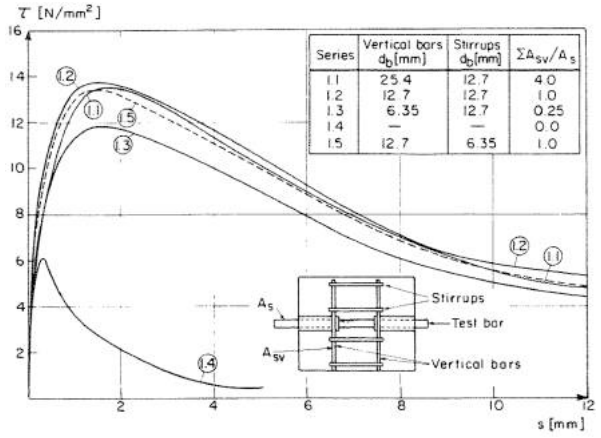

Figure 4.8. Bond stress-slip relation under different passive confinement conditions [Eligehausen *et al.*, 1983]

Regarding the active confinement effects, Malvar [1991] analysed the influence of increasing transverse loading during different loading stages. He concluded that the transverse pressure is particularly important when the adhesion is lost. After this stage, the presence of transverse loading increases the bearing and friction forces while prevents the increase/development of splitting cracks. This is evident in the results of an identical specimen subjected to increasing transverse pressure, present in Figure 4.9. Naturally, if the transverse load is a tensile one, favoring the opening of concrete cracks, it is expected a reduction of the bond strength, and the anchored rebar become more prone to exhibit a splitting failure.

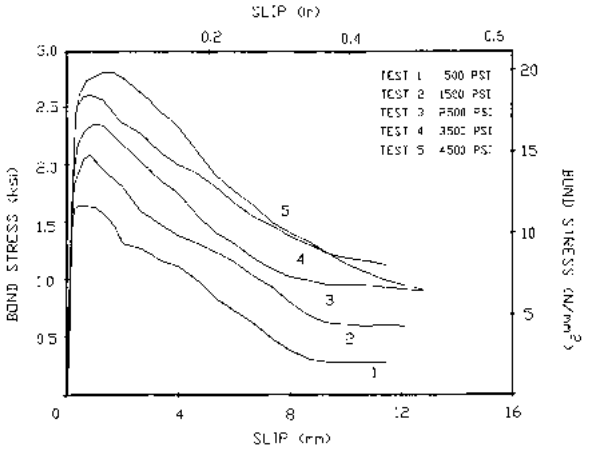

Figure 4.9. Bond stress-slip response under different transverse pressure [Malvar, 1991]

For low values of pressure, the bond stress seems to increases almost linearly with the confining pressure. However, once the bond stress reaches its peak, the decay is relatively steep. This is attributed to the faster degradation resulting from the large confinement and strain energy density. This seems to indicate the existence of a limiting value of the confining stress beyond which bond behaviour is not improved [Malvar, 1991]. This observation is in line with the bond factors derived by Eligehausen *et al.* [1983] for different levels of transverse reinforcement (Figure 4.10). Regarding the figure below, it is also important to verify that the factors derived by different authors evidence important deviations between them.

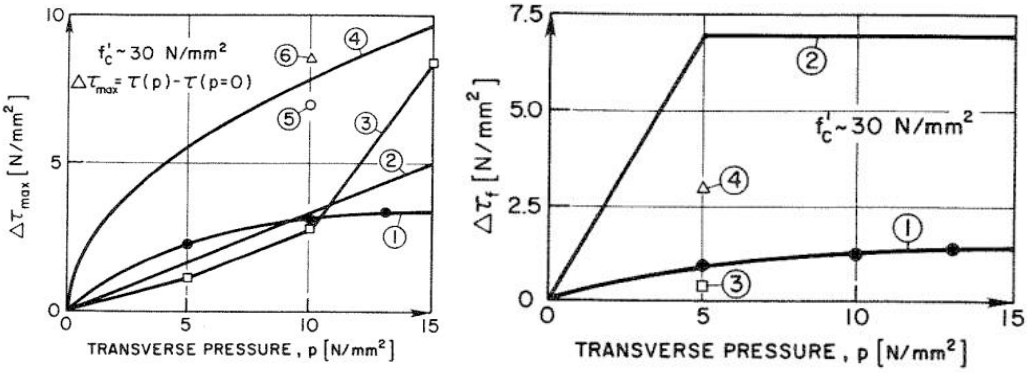

1 – Eligehausen *et al.* [1983]
2 – Tassios [1979]
3 – Dorr [1978]
4 – Untrauer and Henry [1965]
5 – Viwathanatepa *et al.* [1979]
6 – Cowel *et al.* [1982]

1 – Eligehausen *et al.* [1983]
2 – Tassios [1979]
3 – Viwathanatepa *et al.* [1979]
4 – Cowel *et al.* [1982]

Figure 4.10. Evolution of maximum (left) and frictional (right) bond stress components with transverse pressure from different studies presented by Eligehausen *et al.* [1983]

4.3.2 Reinforcement Properties

The present section provides a review on some reinforcement properties that were object of analysis considering their potential effect on the bond strength.

With the development and production of deformed rebars, it became clear that these rebars were able to attain higher bond resistance than plain (smooth) rebars [Abrams, 1913]. Since then, different studies suggest that the surface deformation pattern may have a significant effect on bond response. The outcome from the study of different surface parameters (e.g., rib height, spacing or depth) was, nevertheless, inconclusive, as it becomes difficult to establish bond factors for the different properties. Over time, however, these effects became progressively clearer. And it was demonstrated that the bond-slip response is essentially independent of any specific combination of rib height and spacing but, instead, can be related through a general index. The so-called bond index (f_r) or relative rib area (R_r), reflect a combination of the rib height, rib spacing (S_R) and rebar diameter (d_b), and is generally used to evaluate the importance of the surface deformation pattern in rebars:

$$f_r = R_r = \frac{A_R}{\pi d_b S_R} \tag{4.2}$$

where A_R is the area of the projection of a single rib (consisting often of 2 lugs) on the cross-section of a rebar.

Darwin and Graham [1993] studied the effect of the surface deformation pattern on bond strength using beam-end specimens. The results indicate that increased relative rib area results in increased bond stiffness and strength for specimens that do not exhibit a splitting bond failure. If the rebar is tested under relatively low confinement the bond strength is governed by a splitting failure in the concrete. The plots presented in Figure 4.11 show a consistent increase in bond strength for increasing relative rib area, as long as appropriate confinement is provided. It should be noted, however, that after a certain point, the increase in R_r has only marginal effect in the bond properties.

Based on the analysis of different studies, Lowes [1999] concluded that the increase in the rib bearing area may increase the bond capacity by as much as 70 percent.

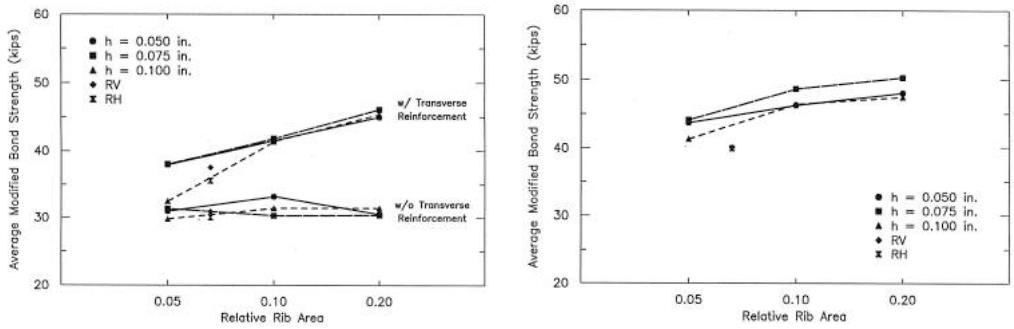

Figure 4.11. Evolution of bond stress with relative rib area with and without transverse reinforcement (left) and with different spacing (h) of transverse reinforcement (right) [Darwin and Graham, 1993] (1 kips = 4448.2 N / 1 in = 0.0254 m)

In what respects the establishment of reference values of relative rib area, [Clark, 1946] recommended a minimum value of R_r equal to 0.1, which, interestingly, is not much different from Abrams' [1913] recommendations. Nonetheless, these later recommendations are not subscribed by US standards [ACI 2003], where typical values of relative rib area for rebars currently used range between 0.057 and 0.087 [Choi *et al.*, 1990]. In Europe, at the turn-of-the-past-century these values were about 0.06 [Fardis, 2009]. In a recent study conducted by Louro [2014], it was found that the values in current practice are identical to the ones observed in US, varying between 0.06 and 0.08, were the rebars with larger diameter typically present increased values of R_r. According to

fib [2000], values between 0.05 and 0.1 are generally good indicators and cover the range of values commonly provided by manufactures.

For the same embedment length, a rebar with larger diameter has larger splitting or pullout failure strength, due to its increased area of contact surface. However, the rebar perimeter increases slower than the rebar area, which means that, under identical anchorage conditions, longer embedment length is generally needed for larger rebars.

The results obtained by Eligehausen *et al.* [1983] identify a reduction in bond stress with an increase in rebar diameter (Figure 4.12).

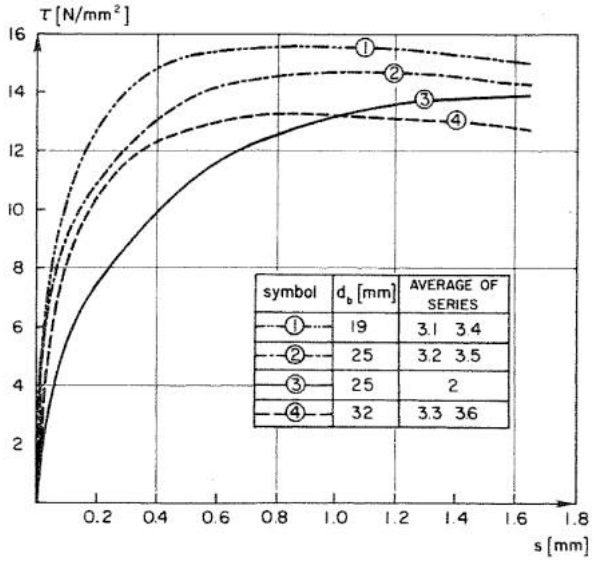

Figure 4.12. Variation in the bond-slip response for different rebar diameter [Eligehausen et al. 1983]

Care should be taken while analyzing these results, since different rebars have different relative rib areas. Therefore, the analysis of the results is biased: while the rebars identified with "1" and "2" have similar R_r values (0.1 and 0.11, respectively), the rebars "3" and "4" have R_r values of 0.066 and 0.16, respectively. While for cases "1" and "2" the bond reduction is relatively modest, the results for case "4" present an important reduction, especially taking into account that the relative rib area is significantly higher.

In a different experimental campaign, Bigaj [1995] also analysed the importance of the rebar diameter (d_b = 16 mm and 20 mm) concluding, however, that the effect is not significant. Identical results were obtained by Viwathanatepa *et al.* [1979], for d_b = 19 mm to 31 mm.

The conclusions of the different studies may indicate that the larger forces supported by larger rebars may induce a more severe degradation in the surrounding concrete. In these cases, longer embedment lengths and eventually additional confinement measures should be adopted in order to prevent an important reduction in bond strength. On the other hand, under low slip demand, the stiffness appears to be independent of the rebar diameter and governed by the value of R_r.

Finally, regarding the reinforcing bar surface conditions, it is not surprising that the presence of corrosion, mud, oil, and other nonmetallic coatings potentially reduce friction forces developed between the reinforcing steel and concrete as shown by Yalciner *et al.* [2012]. The interest reader can find additional information in ACI [2003].

4.3.3 Concrete Properties

A number of concrete properties affect bond strength, such as: compressive strength, fracture energy, aggregate type and quantity, the use of admixtures, concrete slump or the use of fibre reinforcement. Given their relative importance, this section presents a brief summary on the influence of concrete strength, fracture energy, aggregate type and casting position. Additional details on the influence of other concrete properties can be found in ACI [2003].

It is a well-known fact that bond strength increases with the increase in concrete compressive strength. The way these two parameters are related is, however, less clear and has been the subject of different studies over the years. In this respect, the ACI [2003] report provides a summary of the main findings.

Among the different proposals, it is relatively consensual that the bond stress (τ) follows a power law of this sort:

$$\tau = f_c^p \tag{4.3}$$

where the value of p varies with the proposal.

Using a large number of tests, Darwin *et al.* [1996] observed that a best fit with existing data was obtained considering p = ¼ for both development (pullout) and splice strength. The uncertainty in this correlation is depicted in Figure 4.13, comparing the results of 171 test specimens not confined by transverse reinforcement. The two best-fit lines show the test-prediction ratios versus f_c, considering p = ½ and p = ¼. Despite the use of p = ¼ produces a ratio close to one for a wide range of concrete strengths, the results present a large dispersion making the identification of the exponent parameter extremely difficult.

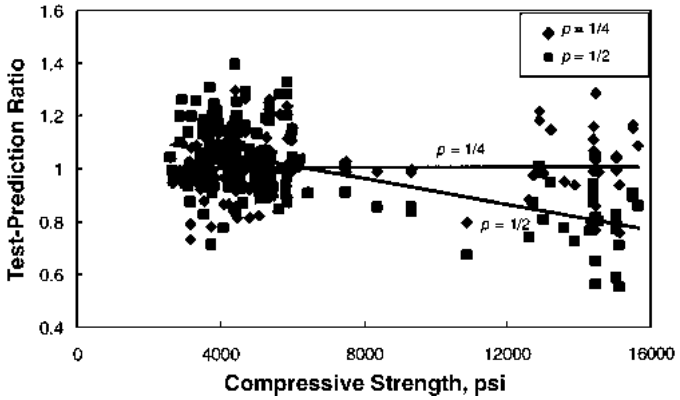

Figure 4.13. Best-fit correlation of parameter p to describe the bond stress as a function of the concrete strength for unconfined rebars [ACI, 2003] (1 psi = 0.00689 MPa)

However, for rebars properly confined with transverse reinforcement, Zuo and Darwin [2000] found that $p = ¼$ significantly underestimates the effect of concrete strength. Instead, the results presented in Figure 4.14 shows that that $p = ¾$ provides a better representation of the influence of compressive strength on bond strength, when such confinement is considered.

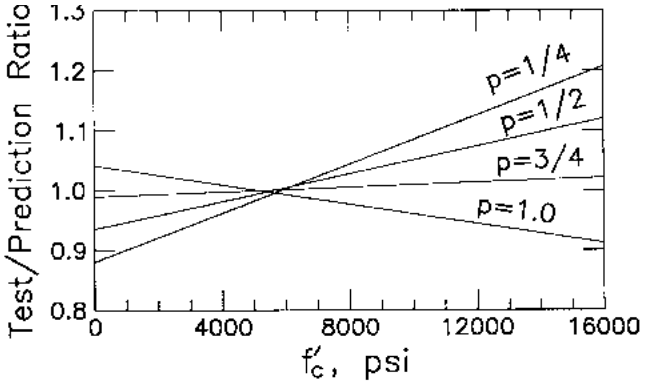

Figure 4.14. Best-fit correlation of parameter p to describe the bond stress as a function of the concrete strength for properly confined rebars [Zuo and Darwin, 2000]. (1 psi = 0.00689 MPa)

This value has proven to be adequate as long as concrete strengths do not exceed 55 MPa. For higher-strength concrete, the average bond strength at failure, normalized with respect to the concrete strength , decreases with an increase in compressive strength

ACI [2003]. Identical conclusions were reported by Bigaj [1995], who has shown that larger bond strength and stiffness are observed for high-strength concrete than for normal-strength concrete. However, when the bond strength is normalized with respect to the square root of the concrete strength, about 25 % lower values are obtained for high-strength concrete.

The recent Model Code 2010 [fib, 2011], adopted the use of the traditional square root relation when pullout failures are expected, while $p = ¼$ is used to represent the response of splitting failures, which are associated with the absence of appropriate confinement.

Moreover, the addition of reinforcement fibres or different aggregates (e.g., containing basalt) can increase more the fracture energy in proportion to the compressive strength. The resulting higher fracture energy increases the resistance to crack propagation, which delays splitting failure and increases bond strength [Zuo and Darwin, 2000; Chao *et al.*, 2009]. Overall, as the concrete compressive strength increases, bond strength increases at a progressively lower rate, while the failure mode becomes more brittle. This effect can be somehow controlled providing high-strength fibres, increasing the fracture energy, and consequently the bond strength of the reinforcement. On the other hand, the use of lightweight concrete may reduce the bond strength to about 65 % of the values obtained with normal-weight concrete [ACI, 2003].

Finally, the rebar position during concrete casting may also influence the bond strength between concrete and reinforcing steel. Rebars placed near the upper surface of casting tend to have lower bond strengths than rebars placed lower in a member [Orangun *et al.*, 1977]. This is essentially because the greater the depth of concrete below a given rebar, the greater will be the settlement and the accumulation of bleed water near the rebar.

4.3.4 Loading

The previous sections addressed the influence of different material and mechanical parameters in the response of an anchorage region subjected to monotonic loading. Under seismic action, the anchored rebar is subjected to repeated cyclic loading with several excursions of variable amplitude. Considering the oscillatory nature of seismic loading, it is critical to understand how the bond-slip behaviour degrades with the number and magnitude of the different cycles.

In addition, modern seismic design philosophies, namely the ones using performance-based and capacity design principles, rely on the capacity of some of the seismic resisting elements in the structure to experience important nonlinear response without significant strength degradation. Therefore, it is also important to understand how the yielding of the longitudinal rebars impacts on the bond strength of the anchorage region.

Until now, bond properties were discussed under the assumption of elastic behaviour of the reinforcement. However, under severe seismic loading, it is expected to observe yielding in the rebars of some RC members. It is thus critical to understand how the yielding of the rebars affects the bond strength of an anchorage region.

Some experimental studies on RC members, e.g., [Shima et al., 1987a; Bigaj, 1995; Ashtiani *et al.*, 2013], indicate that local bond strength is reduced upon yielding of the reinforcement in tension and increased for reinforcement yielding in compression. This behaviour is partly explained on the basis of the familiar Poisson's effect, which causes the diameter of the reinforcing bar to shrink once tensile yielding occurs (Figure 4.15). On the other hand, once compressive yielding occurs the reinforcing bar expands, improving the wedging effect of the ribs (Hoyer's effect) and, therefore, the bond strength [Fernandes Ruiz *et al.*, 2007].

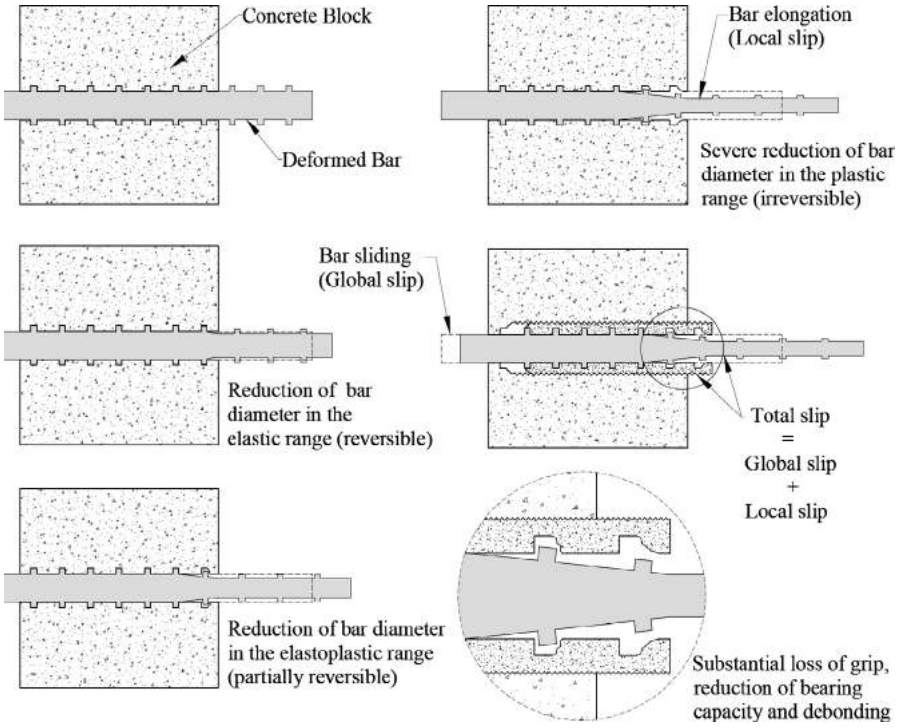

Figure 4.15. Local bond-slip behaviour for yielded rebars [Ashtiani *et al.*, 2013]

The influence of rebar yielding in the bond stress was firstly addressed by Viwathanatepa *et al.* [1979] and analysed in more detail by Shima *et al.* [1987a]. These tests were performed on specimens with larger embedment length (usually in the order of 50 d_b) in order to guaranty that the anchorage strength is higher than the rebar one.

The evolution of the strains at the different strain gauges attached along the embedment length of the rebar, allows the determination of the slip (through integration of strains) as well as rebar stresses/forces (from steel constitutive relation). The bond stress profile along the rebar can then be determined based on the force difference between adjacent strain gauges. The experimental results obtained by Shima *et al.* [1987a] reveal that, in the region were the rebars have yielded, the slip increases greatly at the same time that the bond stress is drastically reduced (up to 20 % of the elastic one). Identical conclusions were observed later by Bigaj [1995] – see Figure 4.16. The authors noticed that, along the portion of the rebar reaching plastic strains just beyond the yield strain a sudden drop in the bond stress takes place. Identical response was observed for the different tests performed during the experimental campaign. However, for models with high-strength concrete it was observed a more pronounced drop after the yielding point. Notice that the results reported in Figure 4.16 refers to normal strength concrete.

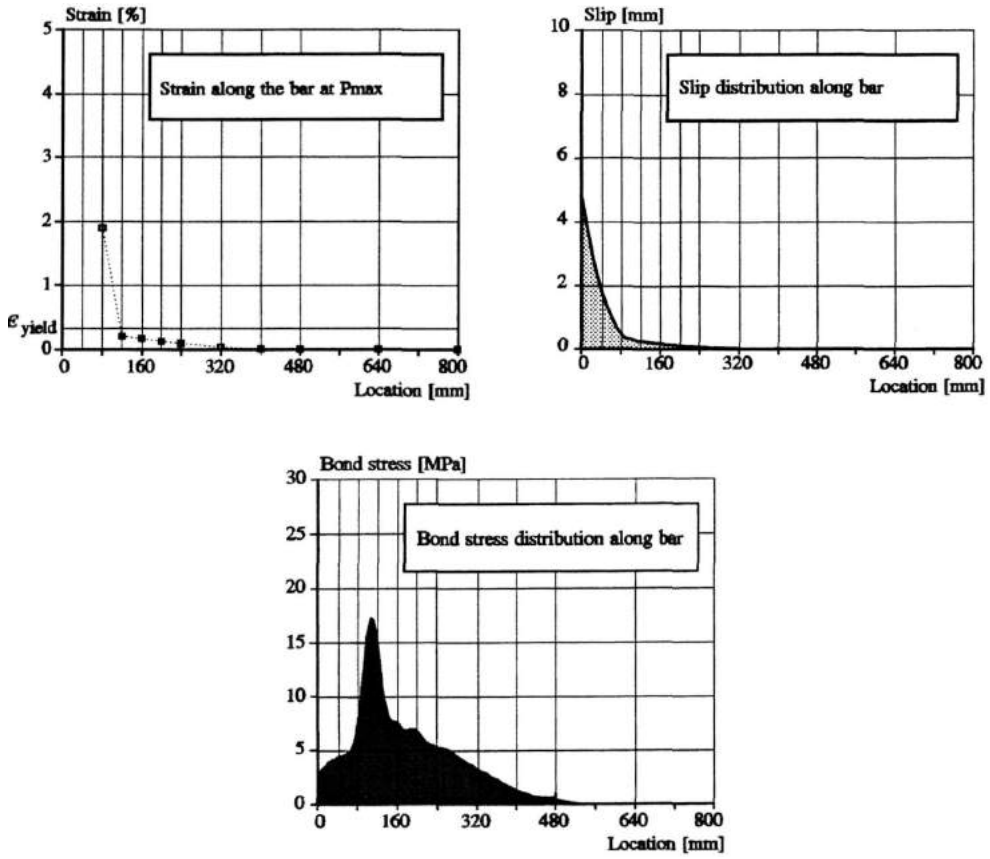

Figure 4.16. Strain, Slip and bond distribution along the embedment length of the rebar reported by Bigaj [1995]

In order to account for such effect, Eurocode 8 (EC8) - Part 1 [CEN, 2004a] specifies that for structures designed for high ductility (DCH in EC8), the anchorage length of beams or column rebars anchored in beam-column joints shall be measured from a point on the rebar at a distance 5 d_b inside the face of the joint, in order to take into account the yield penetration due to cyclic post-elastic deformations.

Based on the limited experimental data available, in particular in what regards the behaviour in compression, Lowes [1999] proposed a parameter that reduces the (elastic) bond stress based on the local strains experienced by the rebar. The evolution of the reduction factor with the reinforcement strains is illustrated in Figure 4.17. A similar relation is proposed by Model Code 2010 [fib, 2011] for yielding in tension. However, no reference is made for yielding in compression.

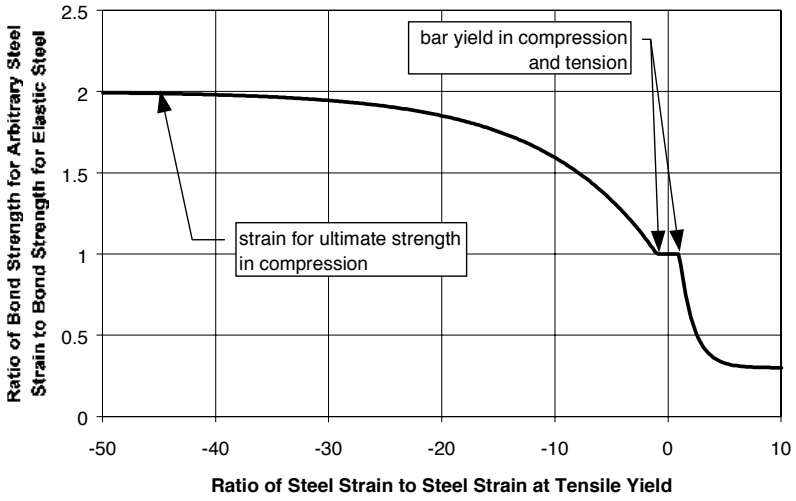

Figure 4.17 Influence of rebar yielding on bond strength [Lowes, 1999].

Another relevant issue on the bond response of reinforcing bars regards the cyclic degradation under earthquake loading. Being a reference in this subject, the study conducted by Eligehausen *et al.* [1983] considered an extensive number of cyclic tests conducted under different conditions. It is well known that the bond strength degrades under cyclic loading, nonetheless, it is essential to understand which are the most relevant parameters, and how do they contribute for the overall degradation.

A first important aspect regards the observation of an identical bond-slip response under tensile and compressive load, as illustrate in Figure 4.18.

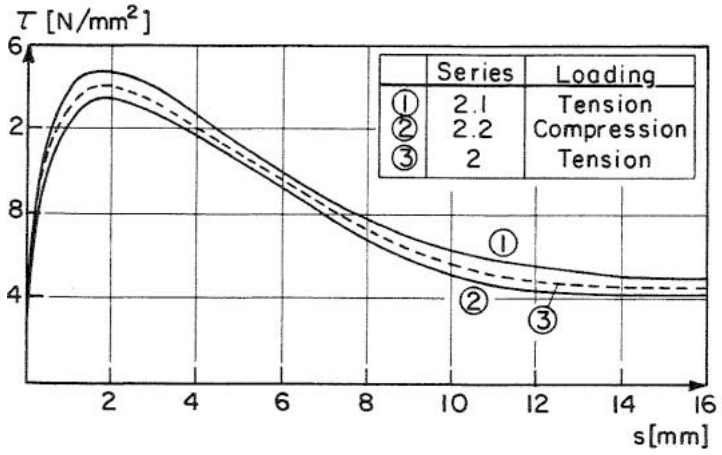

Figure 4.18. Bond stress-slip relation under tensile and compression loading [Eligehausen *et al.*, 1983]

In addition to the direction of loading, past tests also investigate the behaviour under different loading rates. Figure 4.19 presents the variation of maximum bond stress with the loading rate obtained by different authors. The results indicate that the bond stress tends to increase with an increase in loading rate. Nonetheless, according to the presented results, an increase in loading rate by a factor of 100 results in a bond strength increase only of about 15 %.

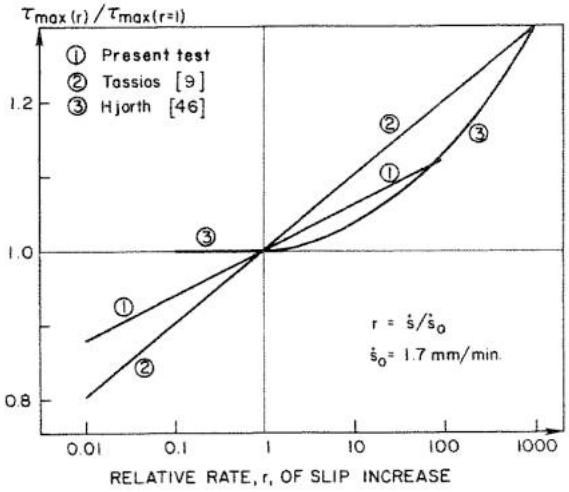

Figure 4.19. Influence of load relative rate in maximum bond stress according to different authors [Eligehausen *et al.*, 1983]

When subjected to cyclic loads, the concrete between the lugs of the rebar is progressively damaged on both sides of the ribs. This effect is described in Figure 4.20, reflecting the progressive damage due to concrete crushing and crack opening in both directions.

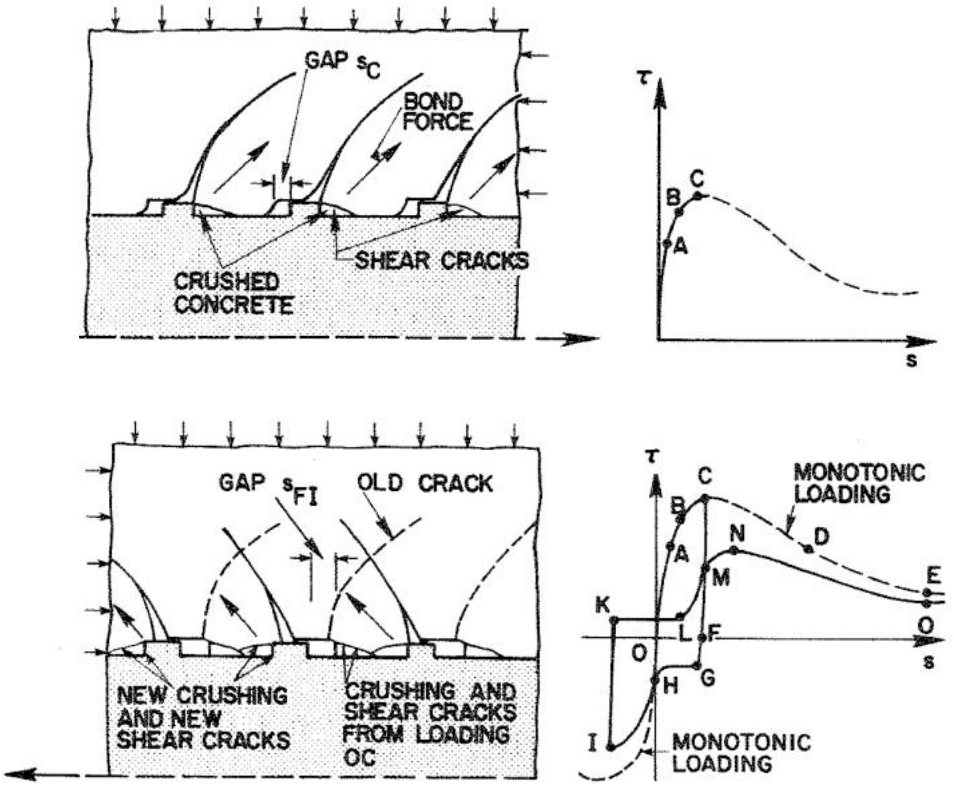

Figure 4.20. Bond mechanisms under cyclic loading: loading (top) and reloading (bottom). (adapted from Eligehausen *et al.* [1983])

As illustrated in Figure 4.21, the bond capacities achieved during unloading and reloading directions are highly dependent on the amplitude of the previous cycles. Under the same number of loading cycles, the bond degradation becomes more pronounced as the amplitude of the cycles increase. If the reinforcement was subjected to large slip demand in previous cycles, the bond stress is highly reduced with respect to the monotonic case.

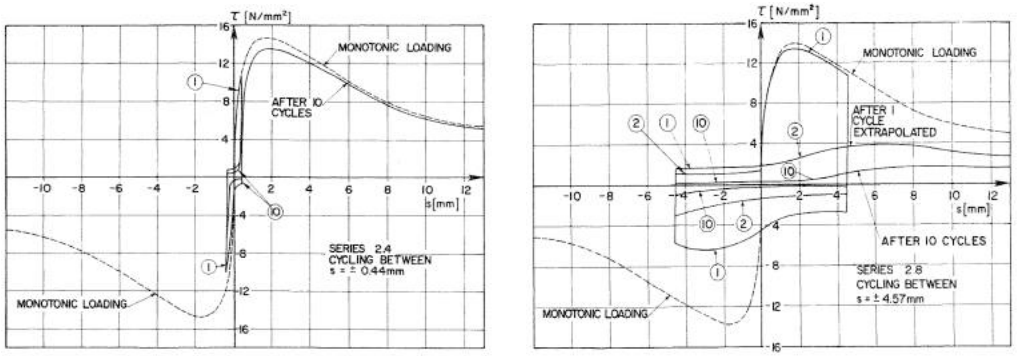

Figure 4.21. Bond-slip cyclic response under the same number of cycles for low (left) and large (right) slip amplitude demand (adapted from Eligehausen *et al.* [1983])

Based on the previous results, the author concluded that if the bond stress does not exceed 70 - 80 % of the maximum bond under monotonic loading, the bond strength is not significantly affected. On the other hand, if the loading exceeds the slip related to the maximum bond stress, then the degradation is more pronounced, even for a reduced number of cycles. This observation is also valid for the bond stresses in the reverse direction as observed in the right plot of Figure 4.21. On the other hand, it is interesting to note that after being loaded up to an arbitrary load and then unloaded to a force close to zero, the bond strength is essentially recovered, independently of the amplitude of the different cycles (Figure 4.22).

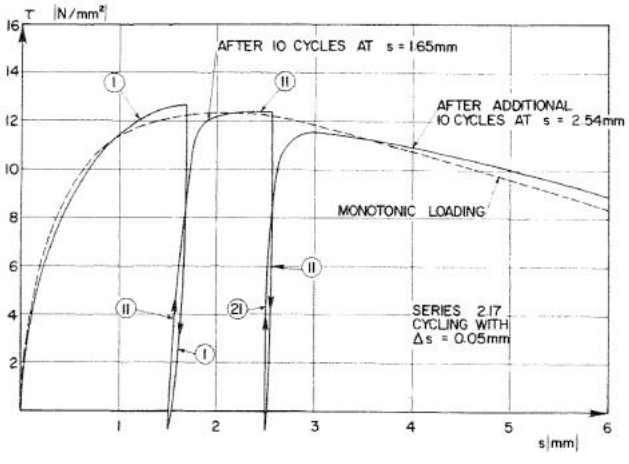

Figure 4.22. Bond-slip response under unload and reload, without slip reversal [Eligehausen *et al.*, 1983]

It is, thus, apparent that the loading excursion in one direction affects essentially the bond strength in the opposite direction. When the rebar is unloaded down to zero force, only a small portion of the slip is reversed and, hence, there is essentially no degradation of the bond resistance during the unloading stage. If the slip reversal is insufficient to transfer the bond forces to the undamaged concrete then the bond strength remains essentially at its monotonic characteristic value.

In addition to the slip amplitudes, the number of load reversals impacts also in the bond degradation. Figure 4.23 shows that with an increase in the number of slip reversals the bond stress is progressively reduced, but in an asymptotic manner. After a significant reduction at the firsts load reversals, the bond degradation factor shows a smoother evolution for increased number of cycles.

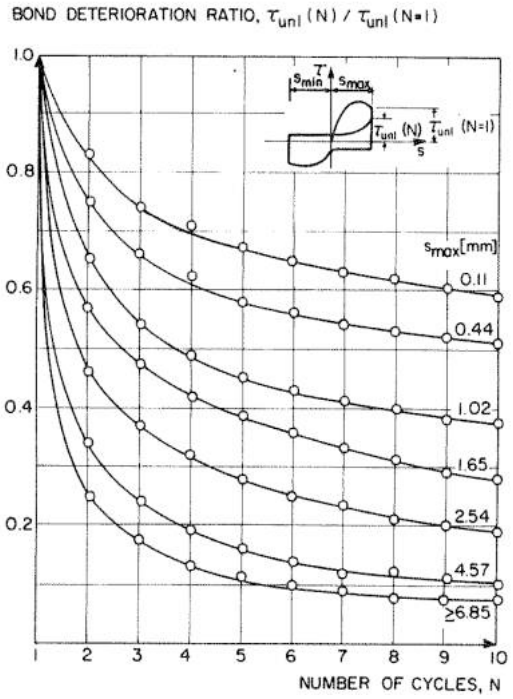

Figure 4.23. Bond degradation ratio with number of cycles and slip amplitude [Eligehausen *et al.*, 1983]

The study conducted by Eligehausen *et al.* [1983] also reveals that the abovementioned bond stress reduction is highly dependent on the amplitude of the slip reversal. For the same number of cycles, the specimens subjected to full slip reversal present bond strengths that are about half the ones obtained when the slip reverses to zero only (Figure 4.24).

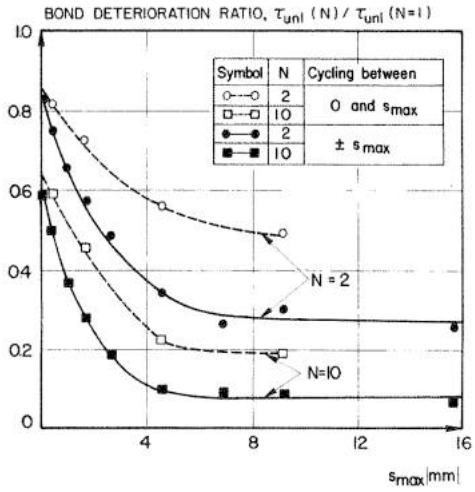

Figure 4.24. Comparison of bond degradation ratio considering full and half slip cyclic reversals [Eligehausen *et al.*, 1983]

Finally, the work addressed also the variation of the unloading stiffness. Based on the results presented in Figure 4.25, it is apparent that, after an initial reduction, the unloading/reloading stiffness remains essentially unchanged and is essentially dependent on the concrete strength. Nonetheless, the results also show an important dispersion in the obtained results.

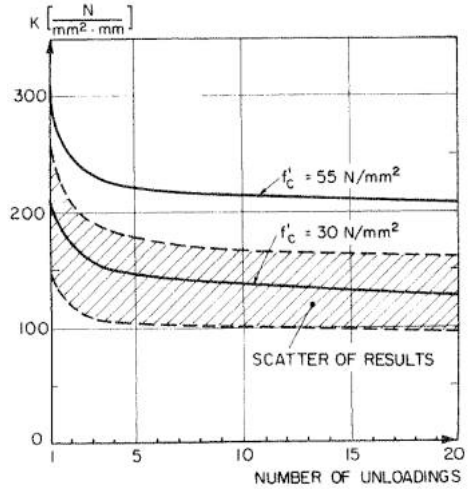

Figure 4.25. Variation of unloading stiffness with concrete strength and number of unloadings [Eligehausen *et al.*, 1983]

After this analysis of the existing experimental results associated with the cyclic bond-slip behaviour, it becomes clear that the establishment of a constitutive model that attempts to capture all the characteristic behaviours presented above would become cumbersome. However, one of the most interesting findings of Eligehausen *et al.* [1983] is that the bond degradation can be described as a function of the combined effect of the number and amplitude of the cycles, namely through a dimensionless cumulative energy dissipation factor. Briefly, this factor is determined by the ratio of the cumulative energy dissipated during the cyclic response with respect to the amount of work associated with the monotonic envelope (Figure 4.26).

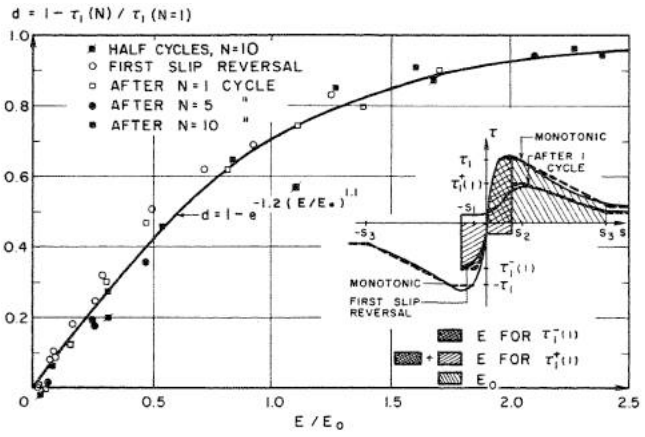

Figure 4.26. Damage factor for reduced bond envelope based on hysteretic energy dissipation [Eligehausen *et al.*, 1983]

Based on the main findings from the experimental campaign, Ciampi *et al.* [1981] and Eligehausen *et al.* [1983] proposed an analytical model for bond stress-slip that accounts also for cyclic degradation. Despite being developed over 30 years ago, this model is still a reference for more recent and general models. A thorough description of this model is presented in Section 5.2.

4.4 CURRENT NUMERICAL TOOLS TO MODEL SP EFFECTS

Despite the recognised importance of strain penetration effects on the response of RC structures (see Section 4.1), the consideration of such effects in numerical models is still limited or through very simplified models. The main reason behind this observation lies on the lack of suitable models in most conventional numerical packages. In the following, the most relevant of the existing numerical models are presented, pointing out their main features and limitations.

The use of advanced bond-slip models within detailed FE, capable of simulating continuous domains with highly discretized meshes, has witnessed great advances over recent years, evidencing encouraging results (e.g., [Lowes, 1999; Salem and Maekawa, 2004; Jendele and Cervenka, 2006; Casanova *et al.*, 2012; Mendes and Castro, 2013]).

This type of models allow the adoption of either a perfect adhesion between the reinforcement and surrounding concrete or by assigning different bond-slip constitutive laws for the relation between the bond stress and the slip occurring at the concrete/rebar interface (Figure 4.27). Although the promising results achieved with these models, this type of modelling approach is computationally very demanding, turning the seismic (nonlinear) analysis of structures with these models unfeasible for most practical applications.

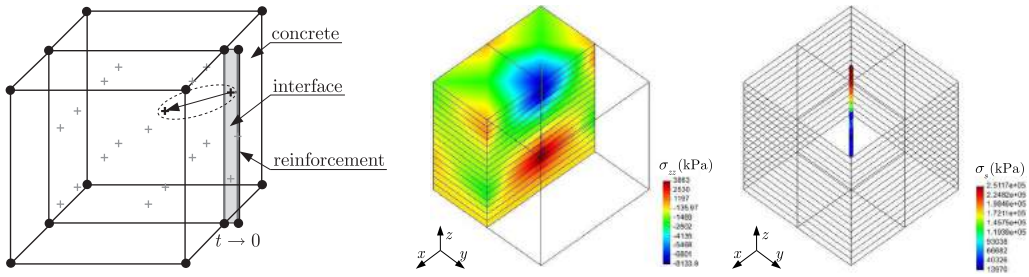

Figure 4.27. Illustration of generic bond-slip model in detailed FE packages (adapted from Mendes and Castro [2013])

Alternatively, the use of beam-column elements, featuring lumped or distributed plasticity, represents a more efficient option, producing equally accurate results for conventional RC framed structures. However, for this latter case, it is not possible to explicitly describe the interface between the reinforcement and the surrounding concrete along the embedment length of the rebar. Therefore, the solution for the problem in hands has traditionally been solved through simplified formulations based on (essentially) empirical relations.

One of the simplest approaches to the problem involves the consideration of a constant (or sets of constant) averaged bond stress along the development length of the reinforcing bar [Otani and Sozen, 1972; Alsiwat and Saatcioglu, 1992; Sezen and Setzler, 2008]. In these cases, for a given imposed force, it is possible to determine the development length required to satisfy the equilibrium at the anchorage region.

Given that the force (and therefore, the strain) distribution corresponds to the integral of the bond stress, the slip at the loaded-end can easily be determined as the integral of the strains, corresponding to the rebar force, along the development length. The slip at the loaded-end is thus obtained by integrating the bond stresses twice (Figure 4.28).

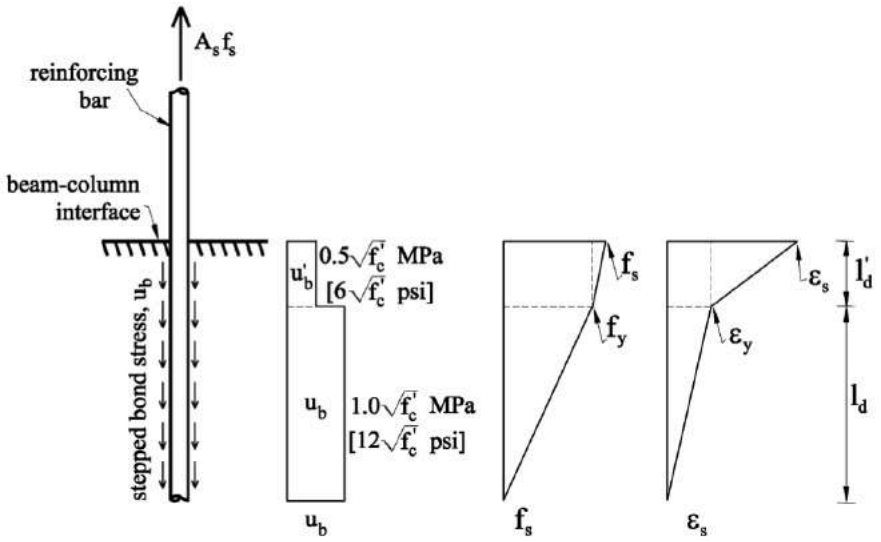

Figure 4.28. Schematic representation of the reinforcement slip model proposed by Sezen and Setzler [2008]

Despite being an extremely efficient procedure, this approach is based on the simplifying, yet erroneous, assumption that the bond stress is constant along the embedment region. As noted in Section 4.3, the bond properties along the rebar may vary significantly depending of the anchorage properties and loading demand. As such, it becomes extremely difficult to establish a constant averaged bond stress *a priori*.

A completely different approach was proposed by Zhao and Sritharan [2007]. In this case, the authors introduced a rebar stress-slip hysteretic model, show in Figure 4.29, that can be integrated into fibre-based analysis of concrete structures using a zero-length element.

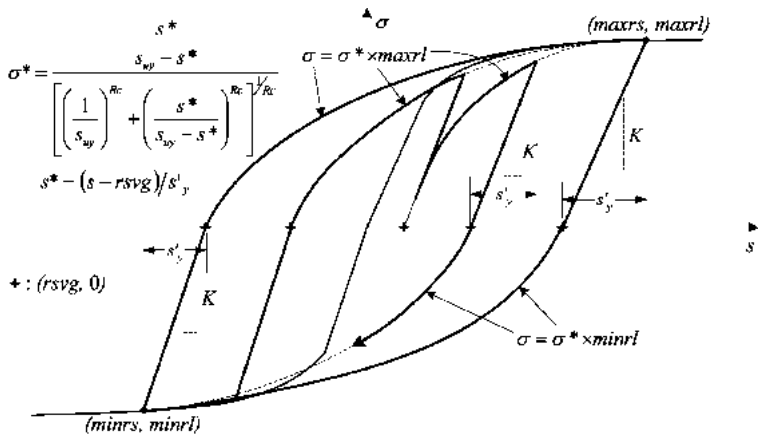

Figure 4.29. Reinforcing bar stress-slip hysteretic relation proposed by Zhao and Sritharan [2007]

The relation, presented in the previous figure, was derived based on a compilation of 16 experimental tests featuring a minimum pre-established anchorage length. After an initial linear slope, the response becomes softer once the slip at yielding is reached. This latter value is determined through an expression also derived from a linear regression of the experimental tests results. The hysteretic rules of this model are very convenient as they allow a direct determination of the rebar slip uniquely based on the stress at the loaded-end of the rebar.

The model, implemented in OpenSEES [McKenna *et al.*, 2000], makes use of fibre-based elements were the axial response of each reinforcement fibre is determined with the rules of the bond-slip model. The contribution of all sectional fibres (concrete and reinforcement) is then integrated within a zero-length element in order to determine the member-end generalized displacements associated with the strain penetration effects.

An interesting feature of this approach is that it manages manage to directly translate the rebar's stress into rebar slip, and not strain as it generally occurs in fibre-based models. However, considering that the adopted hysteretic relation is purely empirical, a significant calibration effort may be required for adjusting the different parameters in order to accommodate alternative anchorage conditions, namely the consideration of a reduced embedment length or the presence of plain rebars, as noted by Melo *et al.* [2011].

Finally, Monti and Spacone [2000] proposed a RC beam finite element that explicitly accounts for the slip between the reinforcing bars and the surrounding concrete, merging the bond-slip formulation proposed by Monti *et al.* [1997] into a force-based fibre element (Figure 4.30).

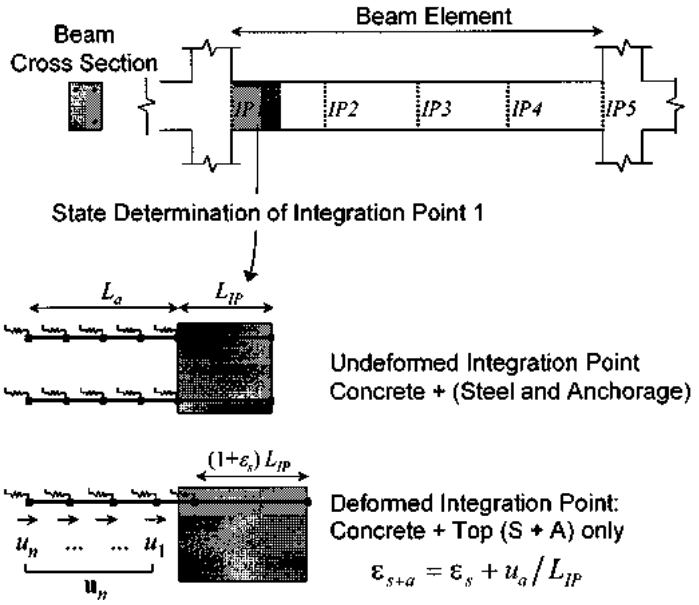

Figure 4.30. Model of beam element with rebar slip proposed by Monti and Spacone [2000]

The model uses essentially the same principles of the flexibility method of analysis (see discussion in Section 2.2) to determine the moment-rotation relation at the zero-length strain penetration element. The member end-section retains the plane section assumption, but the steel fibre strains are computed as the sum of two contributions: the rebar deformation and the anchorage slip. The latter is modelled through a series of additional FB elements representing the embedment length of the rebars. The definition of several elements with different IPs along the embedment length is a very interesting strategy, bypassing the limitations of simpler models as the ones described before.

Despite making use of a powerful framework, the employment of a FB formulation to model the bond-slip behaviour does not render the exact solution as obtained for traditional FB beam-column elements. The reason for this is because the assumed linear interpolation function of bond stress between adjacent IPs is not exact, and the actual bond distribution can only be achieved at the expense of considering a substantial number of elements. This observation is particularly relevant considering that the development length at each load step is not fixed, i.e., the active length of the elements depends on the history and amplitude of the loading demand. Moreover, as observed in Section 4.3.4, the distribution of bond stresses may vary significantly under cyclic loading or when considering the (localized) bond stress reduction in the yielded regions of the rebars.

4.5 EQUATIONS GOVERNING BOND-SLIP BEHAVIOUR

Considering the limitations identified in current bond-slip models, and before entering into the description of the formulation of the new model proposed in this thesis, it is essential to understand with some detail the mechanics of the problem.

When subjected to an external axial load, the force in an anchored rebar is progressively transferred to the surrounding concrete until the force in the rebar is reduced to zero. The rate of this decrease is essentially dependent on the bond strength between the two materials, which, in turn, is depending on its anchorage conditions.

Hence, for a generic rebar embedded in a concrete block subjected to a given applied load (F_0), the equilibrium equation that governs the bond-slip response is given by:

$$F_0 = \int_0^{L_d} \tau \, dL \, P_b \tag{4.4}$$

where P_b is the perimeter of the rebar, τ is the bond stress and L_d is the development length, i.e., the length required for the rebar force at the rebar to reduce to zero.

At the same time, the slip at the loaded-end of the rebar (S_0) reflects the sum of the strains (ε_s) developed at the rebar along the development length. In addition, whenever the strains penetrate through the entire embedded length (L_e), a rigid-body displacement of the entire rebar occurs, as illustrated in Figure 4.1.

In this case, the displacement at the free-end of the rebar (S_{Le}), is different from zero while the strain, and hence the force, will necessarily drop to zero at that location. The compatibility equation that represents a generic anchorage region is given by:

$$S_0 = \begin{cases} \int_0^{L_d} \varepsilon_s \, dL & , L_d < L_e \\ \int_0^{L_e} \varepsilon_s \, dL + S_{Le} & , L_d = L_e \end{cases} \tag{4.5}$$

Past experimental studies [Shima *et al.*, 1987b; Bigaj ,1995] made reference to the so-called "unique strain distribution" along the embedment length (Figure 4.31). In other words, it

was observed that the shape of the strain distribution remains essentially unchanged for a monotonically increasing load demand and can be determined from a simple parallel translation:

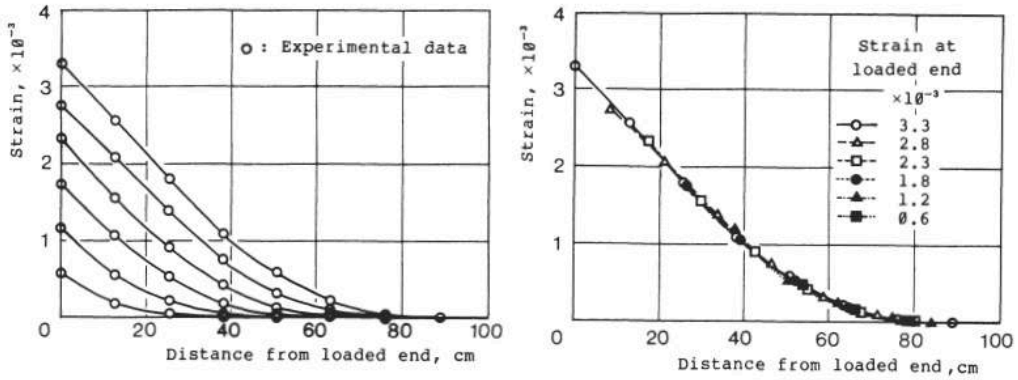

Figure 4.31. Experimental strain distribution for one specimen and the corresponding unique strain distribution derived by parallel translation [Shima *et al.*, 1987b]

Based on the observed strain distributions it is possible to derive equations relating the anchorage force with the slip at the loaded-end of the rebar, for a particular anchorage system. Nonetheless, as described in Section 4.3, recent studies showed that the bond stress can vary significantly with the anchorage conditions and the level of load demand. Hence, the identification of a generic expression should, somehow, be able to account for the variation in bond stress observed under different conditions.

A possible strategy for determining a closed-form solution must include the determination of the values of the integrals in Equation (4.4) and Equation (4.5). To this end, it is essential to establish predefined profiles of both strain and bond stress distributions along the embedment length.

The results presented in Figure 4.31 indicate that strain distributions follow approximately a parabolic shape. Under these observations, one can assume that the bond stress distribution along the rebar follows a generic quadratic function of order "*x*" on the depth z (Equation (4.6)). Given that the force (and hence the stress and strain) distributions corresponds to the integral of the bond stress, one can state that the stress and strain distribution along the rebar will follow a distribution of order "*x+1*" (Equation (4.7)). In addition, given that the slip along the rebar is nothing more than the integral of the rebar stains, the slip distribution will follow a power function of order "*x+2*" (Equation (4.8)). A schematic representation of the different curves is presented in Figure 4.32.

$$\tau(z) = f\tau(z^x) \tag{4.6}$$

$$\varepsilon_s(z) \propto \sigma(z) \propto F(z) = \int \tau(z) = f\varepsilon_s(z^{x+1}) \tag{4.7}$$

$$S(z) = \int \varepsilon_s(z) = fS(z^{x+2}) \tag{4.8}$$

By inverting Equation (4.8), one verifies that z follows a power function of S with exponent $1/(x+2)$. Combining Equation (4.6) with Equation (4.8), and solving for τ, it is thus possible to determine the equation that defines the bond as a function of slip:

$$\tau(S) = f\left(\left(S^{1/x+2}\right)^x\right) = f\left(S^{x/x+2}\right) \tag{4.9}$$

This expression is particularly relevant as it mimics the format of common bond stress-slip constitutive relations, i.e., the bond stress (τ) as a function of slip (S). The underlying idea is to develop a closed-form expression that provides the fundamental anchorage response parameters (slip and anchorage force) simply as a function of the bond stress-slip constitutive relation considered and the load applied to the rebar.

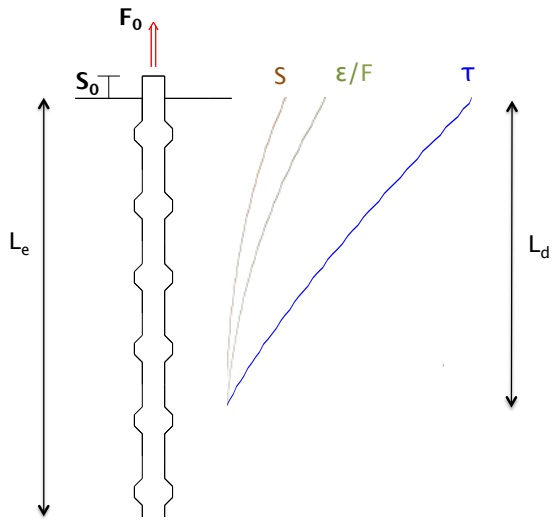

Figure 4.32. Schematic representation of bond stress, slip and strain distributions along the development length

Once the order of the power laws that define the distribution of the different response parameters along the rebar is defined, and taking into account the scale invariance property of the power laws, these integrals can be easily computed based on the area enclosed by the different power distributions (Equation (4.10) and Equation (4.11)).

$$F_0 = \int_0^{L_d} \tau(z)dz\, P_b = \frac{\tau(S_0)\times L_d}{x+1}\times P_b \tag{4.10}$$

$$S_0 = \int_0^{L_d} \varepsilon_s(z)dz = \frac{\varepsilon_{s0}\times L_d}{x+2} \tag{4.11}$$

Let us now consider the constitutive model proposed in Model Code 2010 [fib, 2011], and presented in detail in Section 5.2. According to this constitutive law, the bond stress-slip backbone curve can be divided into four regions limited by different slip (S) limits:

- $0 \leq S \leq S_1$:

$$\tau(S) = \tau_{max}\left(\frac{S}{S_1}\right)^{\alpha} \tag{4.12}$$

- $S1 \leq S \leq S2$:

$$\tau(S) = \tau_{max} \tag{4.13}$$

- $S2 \leq S \leq S3$:

$$\tau(S) = \tau_{max} - \left(\tau_{max} - \tau_f\right)\times\frac{(S - S_2)}{(S_3 - S_2)} \tag{4.14}$$

- $S > S3$:

$$\tau(S) = \tau_f \tag{4.15}$$

A qualitative description of the evolution of the bond stresses with the slip values along the different branches is presented in Figure 4.33.

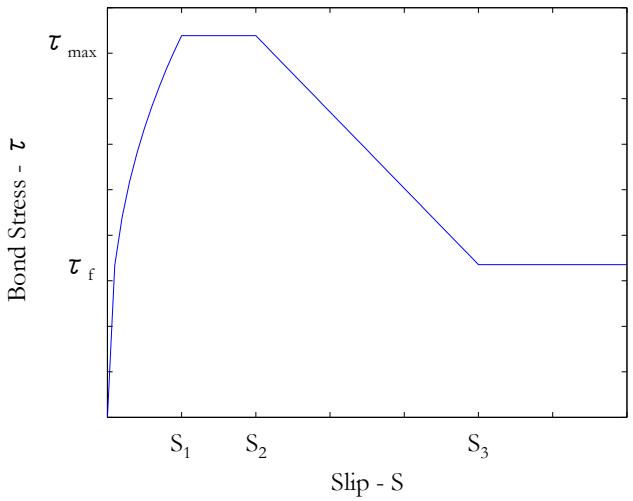

Figure 4.33. Generic bond stress-slip constitutive model

For demonstration purposes, let us consider the equation represents the bond stress - slip response at the initial branch, i.e., for $S \leq S_1$. In addition, it is assumed that: (i) the steel strain remains always under elastic conditions, and (ii) the embedment length of the rebar is sufficiently long in order to guarantee that no slip occurs at the free-end.

If the constants (τ_{max} and S_1) in the Equation (4.12) are considered, both Equation (4.9) and Equation (4.12) are of the same form. Therefore, for a given α value prescribed by a bond stress-slip constitutive relation, one can determine the value of x:

$$\frac{x}{x+2} = \alpha \quad \rightarrow \quad x = \frac{-2\alpha}{\alpha - 1} \tag{4.16}$$

For instance, for $\alpha = 0.4$, as recommended by Model Code 2010 for deformed rebars under normal bond conditions, $x = 4/3$. Recovering both equilibrium and compatibility equations and considering the properties of the bond-slip law, it is possible to derive an equation that directly relates the slip at the loaded-end of the rebar based on the imposed load (in the form of the rebar force or strain, in this case).

Based on the compatibility requirements (Equation (4.11)), the development length (L_d) can be expressed as:

$$L_d = \frac{S_0 \times (x+2)}{\varepsilon_{s0}} \tag{4.17}$$

Substituting the previous equation in the equilibrium equation (Equation (4.10)), one obtains:

$$F_0 = \varepsilon_{s0} \times E_s \times A_b = \frac{\tau(S_0) \times P_b}{x+1} \times \frac{S_0 \times (x+2)}{\varepsilon_{s0}} \tag{4.18}$$

Substituting the bond stress ($\tau(S_0)$) by the constitutive relation provided by the Model Code 2010 (Equation (4.12)):

$$F_0 = \varepsilon_{s0} \times E_s \times A_b = \frac{\tau_{max} \times \left(\frac{S_0}{S_1}\right)^{\alpha} \times P_b \times S_0}{\varepsilon_{s0}} \times \frac{(x+2)}{(x+1)} \tag{4.19}$$

Solving now the equation for S_0:

$${S_0}^{\alpha+1} = \frac{{\varepsilon_{s0}}^2 \times E_s \times A_b}{\frac{\tau_{max} \times P_b}{{S_1}^{\alpha}}} \times \frac{(x+1)}{(x+2)} \tag{4.20}$$

Rearranging and simplifying the previous expression, one obtains the slip (S_0) as a function of the strain (directly proportional to the force) at the loaded-end of the rebar:

$$S_0 = \left(\frac{E_s \times d_b \times {S_1}^{\alpha} \times (\alpha+1)}{8\tau_{max}} \times {\varepsilon_{s0}}^2 \right)^{\frac{1}{(\alpha+1)}} \tag{4.21}$$

where E_s and ε_{s0} are the modulus of elasticity and the rebar strain at the loaded-end, ϕ is the diameter of the rebar, τ_{max}, S_1 and α are parameters that can be obtained form a reliable bond stress-slip constitutive relation. It is important to note that the previous equation is simply a function of the material, bond properties and the imposed load (in this case in the form of ε_{s0}), and that it does not consider any generic calibration factor or parameter. Once the slip (S_0) is determined from the previous expression, the development length (L_d) required to anchor the imposed load can be directly determined with Equation (4.17).

For the sake of completeness, based on the computed boundary conditions, it is possible to determine the exact distribution of the different response parameters along the

development length of the rebars. To this end, let us consider a general equation describing a power function of order *i*:

$$F(z) = a(h - z)^i + k \tag{4.22}$$

where *z* represents the length along the embedded region of the rebar (z = 0 at the loaded-end), the pair (*h*,*k*) defines the inflection point of the function with $h = L_d$ and $k = 0$ – which, in this case represents the location where the force is reduced to zero (L_d) – and the coefficient "*a*" can be determined based on the value of the desired response parameter at the loaded-end of the rebar.

The value of *i* can be determined following the reasoning associated with the definition of the exponents in Equation (4.6), Equation (4.7) and Equation (4.8). For instance, considering $i=4/3$ for the bond distribution (see derivation of Equation (4.16)), the equations that describe the distribution of bond stress, rebar strain and slip are given by Equation (4.23), Equation (4.24) and Equation (4.25). Note that the force distribution is directly proportional to the strain one, since these variables can be related with each other by a factor equal to the rebar area times the modulus of elasticity of the rebar.

$$\tau(z) = a(L_d - z)^{4/3} \tag{4.23}$$

$$\varepsilon_s(z) = a(L_d - z)^{7/3} \tag{4.24}$$

$$S(z) = a(L_d - z)^{10/3} \tag{4.25}$$

The coefficient "*a*" can, thus, be determined based on the boundary conditions previously determined with Equation (4.19) and Equation (4.21):

$$a(\tau) = \frac{\tau(S_0)}{{L_d}^{4/3}} \tag{4.26}$$

$$a(\varepsilon_s) = \frac{\varepsilon_{s0}}{{L_d}^{7/3}} \tag{4.27}$$

$$a(S) = \frac{S_0}{{L_d}^{10/3}} \tag{4.28}$$

Once the value of *a* is determined, the distribution of the different response parameters becomes:

$$\tau(z) = \frac{\tau(S_0)}{L_d{}^{4/3}}(L_d - z)^{4/3} \tag{4.29}$$

$$\varepsilon_s(z) = \frac{\varepsilon_{s0}}{L_d{}^{7/3}}(L_d - z)^{7/3} \tag{4.30}$$

$$S(z) = \frac{S_0}{L_d{}^{10/3}}(L_d - z)^{10/3} \tag{4.31}$$

The graphical illustration of the evolution of the abovementioned parameters along the embedment length of the rebars can be appraised in Section 6.2.1, where this analytical solution will be used to evaluate the accuracy of the results obtained with the new bond-slip model proposed in this work.

Assuming that the imposed load is sufficiently large to produce a rebar slippage larger than S_1 (slip limit of the first branch of the Model Code 2010 bond constitutive model), then the previous expressions are no longer valid since the distributions of the different parameters in this region will follow a different trend. Hence, if one is interested in determining the behaviour for such slip demand, it is necessary to first compute the embedment length along the rebar which is associated with the different slip limits. For the illustrative case presented above, when S_0=S_1 the strains $\varepsilon_{s0,S1}$, embedment length L_{d,S_1} and force F_{0,S_1} can be determined by replacing S_0 by S_1 in Equation (4.21), Equation (4.17) and Equation (4.19), respectively:

$$\varepsilon_{s0,S_1} = \sqrt{\frac{S_1{}^{(\alpha+1)} \times 8 \times \tau_{max}}{E_s \times d_b \times S_1{}^{\alpha} \times (\alpha+1)}} = \sqrt{\frac{S_1 \times 8 \times \tau_{max}}{E_s \times d_b \times (\alpha+1)}} \tag{4.32}$$

$$L_{d,S_1} = \frac{S_1 \times (x+2)}{\varepsilon_{s0,S_1}} \tag{4.33}$$

$$F_{0,S_1} = \frac{\varepsilon_{s0,S_1} \times E_s \times \pi \times d_b{}^2}{4} \tag{4.34}$$

Once these values are determined, the response for an increased loading demand ($S > S_1$), can be computed by adding the values from the previous slip limit to the ones corresponding to the current loading condition. Naturally, the new expressions should reflect the changes in the bond constitutive model for the different slip limits.

On the other hand, despite the previous equations can be extended to account for different effects, namely increased values of slip, rebar yielding effects (both at the rebar strain and at the bond stress-slip relation), insufficient anchorage length or cyclic degradation, the consideration of the possible combinations at every location along the rebar turns out to be extremely complex and inefficient. Hence, and despite the benefits associated with the use of a closed-form solution, it seems more convenient to explore an alternative strategy built on a finite element approach.

4.6 SUMMARY

Past experimental studies revealed that the slip of reinforcing bars due to strain penetration effects can contribute to about 40 % of the total deformation of RC members. In older RC structures, featuring plain rebars, these effects are magnified, reaching values of the order of 80 % - 90 %.

The relative importance of strain penetration effects is naturally dependent on the anchorage properties. After a detailed analysis of several experimental test results it was possible to identify the parameters that have a larger impact on the bond resistance. Among others, it is apparent that the concrete strength, the geometry of the rebar surface, the embedment length, the yielding of the rebars and the cyclic degradation assume a particular relevancy.

Regarding the numerical simulation of the bond-slip behaviour, in the present there are numerical packages featuring detailed finite elements capable of accurately reproducing strain penetration effects. However, in software featuring fibre-based beam-column elements, the models available present important limitations as they are generally based on simplified empirical constitutive relations.

Alternatively, a closed-form solution was proposed where the response at the loaded-end of an anchored rebar can be accurately determined. This procedure is extremely efficient under simplified loading action but becomes relatively complex as rebar yielding and cyclic degradation effects are incorporated into the formulation.

Considering the importance of the strain penetration effects in RC structure together with the current limitations in accurately simulating these effects in numerical tools, a new fibre-based bond-slip model is proposed in the following chapter.

5. A NEW BOND-SLIP MODEL FOR RC FIBRE-BASED NONLINEAR BEAM-COLUMN ELEMENTS

5.1 GENERAL DESCRIPTION OF THE PROPOSED BOND-SLIP MODEL

As demonstrated in Section 4.4, it is nowadays possible to explicitly describe strain penetration effects through bond-slip models implemented in finite element (FE) software. These effects are generally represented through contact elements located at the interface between the concrete and reinforcing bar along the anchorage region. The application of such strategy is, nonetheless, limited to software packages featuring FE implementations with highly discretized solid elements, such as the ones described in Lowes [1999] or Louro [2014].

On the other hand, in numerical packages using simpler beam-column elements, which are significantly more efficient for framed RC structures, the strain penetration models currently available are still somewhat limited. In these cases, the solution usually lies on the use of empirical constitutive relations (e.g., Zhao and Sritharan [2007]), which are necessarily limited in their range of application. Alternatively, and despite the improvements observed in the simulated responses, the employment of simplified approaches such as the use of linear springs at the members' ends, elongated elements or reduced reinforcement elastic modulus, exhibit important drawbacks as demonstrated in Section 2.3 and Section 3.4.3.

As an attempt to overcome the foregoing limitations, a study was conducted in order to develop a comprehensible bond-slip model that can be used with fibre-based beam-column elements. The model presented herein intends to quantify the additional flexibility resulting from strain penetration effects occurring at the connection between RC members. To this end, priority was given to developing a tool that can be as general as possible, being capable of accurately reproducing the physical phenomena associated with strain penetration effects for a wide variety of anchorage conditions.

Based on the literature review carried out in Chapter 4, it was apparent that the numerical tool should be able to account for the following mechanical properties and physical phenomena:

- Type of failure (pullout or splitting)
- Concrete strength
- Embedment length
- Cyclic degradation
- Amplitude of steel strains (rebar yielding)
- Rebar properties (plain or ribbed rebars)
- Transverse pressure
- Level of confinement
- Bond conditions (reinforcement surface conditions, casting position)
- General bond stress-slip constitutive relations

Considering the number and diversity of the different properties and phenomena involved, it becomes clear that the simulation of the anchorage region of a given RC member cannot be based on simple pre-established empirical relations. However, as described in detail in the following section, most of these phenomena can be directly accounted for through appropriate bond-slip local constitutive relations, which describe the magnitude of bond stresses at the interface between the rebars and the surrounding concrete for a given history of slip values.

In order to use these constitutive models to determine the bond-slip response of a reinforcing bar, it is essential to accurately describe how the different response parameters, namely the slip, vary along the embedment length of the rebar. Furthermore, in order to account for the bond degradation due to cyclic loading and rebar yielding, it is necessary to monitor both slip and strain histories at different locations along every rebar of the cross-section of interest. For the latter parameters, it is also essential to have a constitutive model that can be treated independently at the different points along the embedment length of a given rebar.

As demonstrated in Section 4.5, under complex loading demand (as the seismic one) it becomes extremely difficult and inefficient to accurately anticipate how the different response parameters evolve along the embedment length of the rebars. Therefore, in order to satisfy the previous requirements for an adequate constitutive model, it is essential to define a series of monitoring points to keep track of all the response parameters along the rebar. Naturally, this implies developing a consistent and robust formulation to guarantee that both equilibrium and compatibility are respected within the model's framework.

In this way, the resulting strain penetration deformations become directly dependent on the bond constitutive relation adopted, which, in turn, reflects the anchorage properties of the system under analysis. This represents a great advantage with respect to conventional empirical models, as the analyst can make use of state-of-the-art local constitutive models that realistically reflect the anchorage conditions.

In addition to the previous guiding principles, it is important to guarantee the simplicity and efficiency of the model so that both researchers and practitioners can apply it in their applications with an acceptable computational effort. As such, the proposed model was developed as a zero-length element, to be located at the extremity of structural members, which simulates the behaviour of the rebars' anchorage zone adjacent to a RC frame member. The end-section of the frame element of interest is thus replicated and a set of auxiliary integration points (IPs) is defined along the actual (yet, not explicitly modelled) embedment length of all rebars of the cross-section. A schematic representation of the model components is presented in Figure 5.1, where, for better comprehensibility, the number of rebars represented in the numerical model was reduced with respect to the actual RC member.

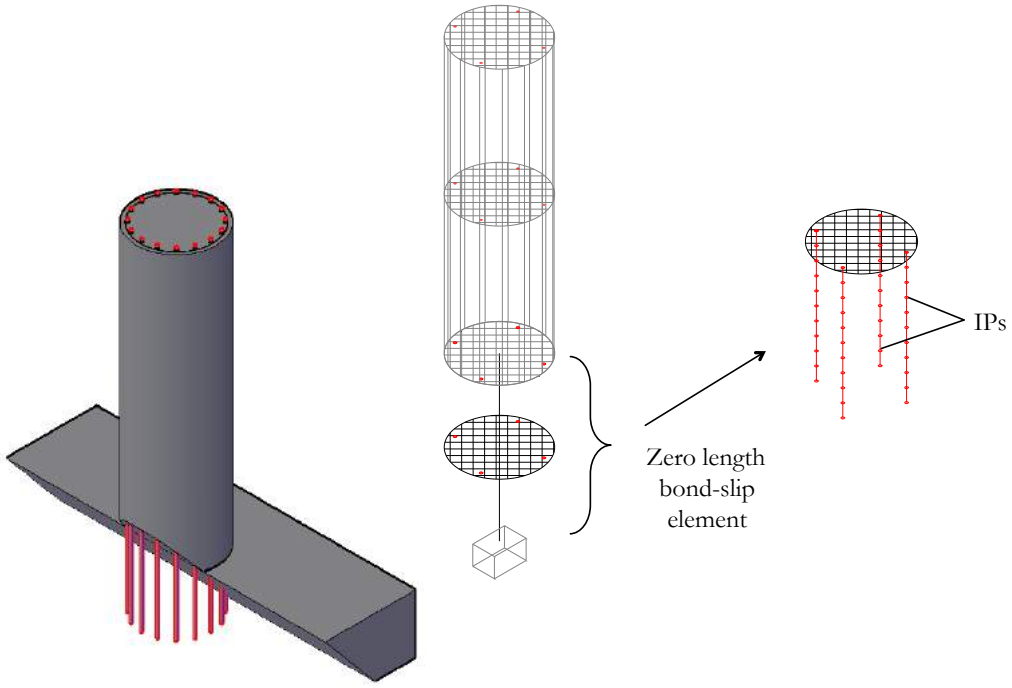

Figure 5.1. Schematic representation of the different components of the proposed bond-slip model

The features of the proposed bond-slip element can be interpreted in light of the comparison between lumped versus distributed plasticity beam-column elements. Similarly to the latter case, the new bond-slip model only requires the definition of the geometric properties and appropriate constitutive relations for reinforcement and bond stress-slip response, as well as for the concrete fibres.

In the proposed formulation, the reinforcement is modelled through a simple bilinear relation whilst the bond stress-slip curve adopted is the one prescribed in the recent Model Code 2010 [fib, 2010], whose main characteristics are presented in Section 5.2. Regarding the fibres assigned with concrete material, the response is determined following the concrete model adopted for the adjacent member or any other found appropriate.

Briefly, in order to simulate the anchorage behaviour of a given RC member, the zero-length element replicates the member's cross-section and generates a series of IPs along the anchorage length of the rebars. Starting from an imposed pair of axial load and flexural moment (resulting from the analysis at the level of the structure), the slip at each rebar is computed assuming the hypothesis of plane sections remain plane adopted in the Euler-Bernoulli beam theory.

The anchorage force at the loaded-end of each rebar is then determined through the integration of the different response parameters at each IP along the rebar. This process makes use of an iterative procedure in which both equilibrium and compatibility are enforced at every point along the rebar – with each IP featuring independent constitutive models. The contribution of the different fibres of the cross-section is thus summed up in order to compute the member-end forces (axial force and flexural moments in the two orthogonal directions). A simplified flowchart describing the main steps of the proposed bond-slip model is presented in Figure 5.2.

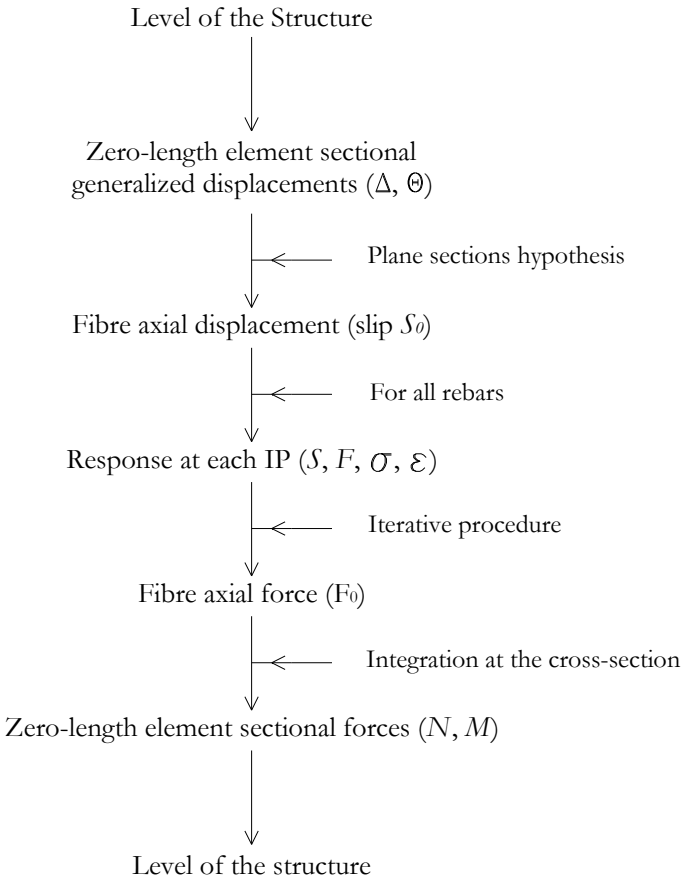

Figure 5.2. Simplified flowchart of the proposed bond-slip model

For simplicity, the previous flowchart makes reference only to the contribution of the rebars given that they represent the source of strain penetration deformations. Naturally, the computed sectional response takes also into account the concrete fibres. A detailed description and the formulation behind the above procedure is presented in Section 5.3.

The choice of adopting the plane section's hypothesis requires some discussion. This choice implies that the slip at every rebar and the strain at every concrete fibre are related through kinematics to the sectional deformations. The latter, in turn, have to respect equilibrium with the nodal forces. With this assumption, the stresses in the rebars and concrete fibres within the zero-length element will, in general, be different from the ones computed at the adjacent beam-column cross-sections due to the allowance for rebar slippage. This should not be considered a downfall of the approach, since the stress-

resultants at the beam-column cross-section represent the response of a given length along the beam-column associated to the integration point corresponding to the cross-section, and thus, the corresponding material stresses in the fibres do not need to coincide with the stresses at the bond-slip zero-length element. Nevertheless, the stress-resultants will coincide in both cross-sections.

Alternatively, one could have chosen to not respect the plane sections' hypothesis, with the sectional deformation resulting from averaging the slips and strains at the different fibres. In such case, one would have to impose the equality between the material stresses in the fibres of the cross-section of the zero-length element and the corresponding ones at the extremity cross-section of the beam-column element. Such interdependence would require another iterative level in order to have the same stresses in both cross-sections of both elements, thus implying additional computational time and convergence difficulties. For these reasons the first approach was adopted.

The proposed model requires several input parameters that, in essence, can be divided into three groups: geometric, material and bond properties. The first group comprises the dimensions of the cross-section under analysis, the embedment length of the anchored rebars and an influence length. The latter represents the length along which the concrete compressive strains in the anchorage region are expected to develop – additional details on this parameter are given in Section 5.3.3. The second group represents conventional material properties that, in general, should coincide with the ones considered for the adjacent RC element (beam or column). Finally, the last group reflects the properties defining the bond stress-slip constitutive model and can be found in reference publications.

In summary, the structure of the proposed element can be divided into four main groups: (i) detailed bond stress-slip constitutive relations (ii) response along the embedment length, (iii) rebar force-slip response at the loaded-end, and (iv) sectional response. A detailed description of the different procedures, together with the implementation strategy within a distributed plasticity beam element with FB formulation is presented in the following sections.

Table 5.1. List of input parameters for the proposed bond-slip numerical model

Geometric properties	
RC cross-section	Shape and dimensions
Embedment length	L_e
Influence length	L_i
Rebar diameter	d_b
Material properties	
Concrete comp. stress	f_c
Steel yield stress	f_y
Ultimate steel stress	f_u
Modulus of elasticity	Es
Strain hardening parameter	r
Bond properties	
Characteristic slip limits	S_1, S_2, S_3
Maximum bond stress	τ_{max}
Bond stress parameter	α
Friction bond stress	τ_f

5.2 BOND STRESS-SLIP CONSTITUTIVE RELATION

Over the past three decades, several bond stress-slip constitutive relations have been proposed taking into account the influence of several material properties, geometric characteristics and loading conditions (e.g., [Ciampi *et al.*, 1981; Eligehausen *et al.* 1983; Bigaj, 1995]). These models provide a comprehensive characterization of the bond-slip response and are able to emulate a number of different phenomena.

The characteristics of the bond-slip model presented hereafter are usually defined on the basis of experimental tests devised to simulate a uniform distribution of the bond stresses along a single rebar, under the assumption that it represents a statistically acceptable average local bond-slip relation, for short anchorage lengths [fib, 2011]. Such tests are generally performed using specimens with very short embedment lengths, $l_d < 6\ d_b$ [Louro, 2014]. This type of tests allows the extrapolation of the results obtained with

short anchorage lengths to more realistic ones where the embedment lengths are typically larger.

The constitutive model adopted in the proposed bond-slip model follows essentially the one prescribed by Model Code 2010 [fib, 2011], which, in turn, represents the results of the most relevant research works, and is based on contributions from over 800 tests. The bond stress-slip parameters of the present model are statistically valid for mean concrete compressive strengths between 15 MPa and 110 MPa and for rebars with a relative rib area (f_r according with Equation (4.2)) within the range 0.05 - 0.14. The rationale underpinning its rules are available in the technical report "Bond and Anchorage of Embedded Reinforcement: Background to the fib Model Code for Concrete Structures 2010" [fib, 2014].

As mentioned previously, an important feature of this model lies on its ability to represent the bond stress-slip response for several different anchorage conditions and properties. However, as noted by different researchers (e.g., [Eligehausen *et al.*, 1983; Verderame *et al.*, 2009]) it is important to keep in mind that this type of constitutive relations invariably exhibit large scatter, as shown in Figure 5.3, representing the comparison between alternative constitutive models proposed by different authors for deformed rebars [Eligehausen *et al.*, 1983].

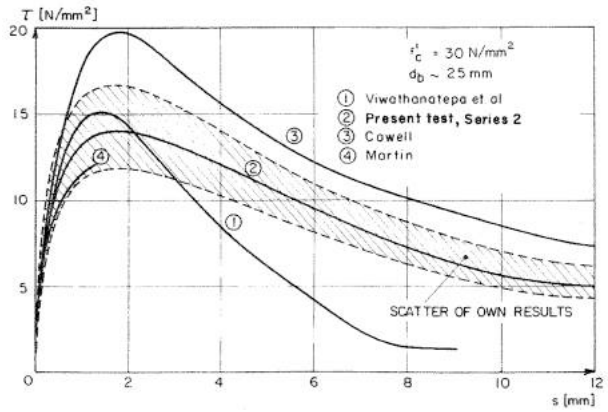

Figure 5.3. Comparison between different bond stress-slip relations [Eligehausen *et al.*, 1983]

Past research efforts indicate that much of the scatter results from differences in concrete properties (such as fracture energy), reinforcing bar geometry (relative rib area, diameter) [ACI, 2003], different measuring techniques or different loading and deformation velocities [fib, 2011]. In addition, it is important to note that the simple pullout test (the most common experimental test adopted to derive these models) is the least realistic one.

Its main criticism is that the concrete surrounding the reinforcing bar is generally under compression due to the load application technics (with the development of compressive struts near the loading-end region), whilst in most of real cases the concrete in this location is under tension. For such reason, it is expected that bond stresses determined with this simple experimental setup may be overestimated. In order to avoid the previous condition, it is costmary to define an unbonded length near the loaded-end(s) of the rebar, as illustrated in Figure 4.6. Alternatively, more representative tests models, such as the ones described in ACI [2003], can be considered.

According to Model Code 2010 [fib, 2011], the backbone of the generalized bond stress-slip relation can be divided into four main braches, defined through characteristic slip (S) limits. The following equations were introduced in Section 4.5 and are repeated here for convenience:

- $0 \leq S \leq S_1$:

$$\tau_i(S) = \tau_{max}\left(\frac{S}{S_1}\right)^{\alpha} \tag{5.1}$$

- $S_1 \leq S \leq S_2$:

$$\tau_i(S) = \tau_{max} \tag{5.2}$$

- $S_2 \leq S \leq S_3$:

$$\tau_i(S) = \tau_{max} - (\tau_{max} - \tau_f) \times \frac{(S - S_2)}{(S_3 - S_2)} \tag{5.3}$$

- $S > S_3$:

$$\tau_i(S) = \tau_f \tag{5.4}$$

The expressions presented above are standard relations that apply to general anchorage systems. However, the generic bond stress (τ_i) is a function of several parameters (τ_{max}, S_1, S_2, S_3, α and τ_f) that can be used to define the shape and magnitude of a particular bond stress-slip model, according with the properties of a given anchorage system. Moreover, as described in more detail in Section 5.2.4, this generic bond stress can be modified by different parameters influencing the bond stress.

As described in more detail hereafter, the specific values of the characteristic slip limits (S_1, S_2, S_3), maximum bond stress (τ_{max}), frictional bond stress (τ_f) and the exponent α,

depend on several factors, namely: type of failure, bond conditions, concrete strength, surface properties of the reinforcing steel, or level of confinement.

5.2.1 Bond stress-slip parameters for pullout and splitting failure

According to the rules proposed by Model Code 2010, a first distinction should be made based on the expected failure mode. For instance, for rebars with small cover thicknesses and low levels of confinement the anchorage system is more prone to exhibit a splitting failure. On the other hand, well confined regions can guarantee the integrity of the surrounding concrete under larger loading demand, allowing the development of higher bond stresses at the interface between the rebar and the surrounding concrete. According to the above mentioned document, the latter failure mode, the pullout failure, is expected to occur in anchorage regions with well confined concrete (concrete cover ≥ 5 Ø, clear spacing between rebars ≥ 10 Ø) and with ribbed reinforcement with a relative rib area (determined with Equation (4.2)) that satisfies the minimum defined in general international standards (usually in the order of 0.05 - 0.07).

Typical values for the parameters associated with the pullout type of failure for different bond conditions are presented in Table 5.2.

Table 5.2. Parameters defining the bond-slip relation for deformed rebars under expected pullout failure (adapted from [fib, 2011])

	Good bond cond.	Other bond cond.
τ_{max}	$2.5\sqrt{f_{cm}}$	$1.25\sqrt{f_{cm}}$
S_1	0.001	0.0018
S_2	0.002	0.0036
S_3	C_{clear}	C_{clear}
α	0.4	0.4
τ_f	$0.4\ \tau_{max}$	$0.4\ \tau_{max}$

In the previous table, f_{cm} is the mean value of concrete compressive strength in MPa, whilst C_{clear} represents the clear spacing between the reinforcement ribs - rib spacings higher than 5 mm are commonly found in conventional reinforcing bars. This value assumes a particular relevance as it defines the limit beyond which the bearing action is lost and the bond resistance mobilized results only from friction.

A generic bond stress-slip response corresponding to a pullout failure is presented in Figure 5.4. The presented monotonic envelope, corresponds to f_{cm} = 25 MPa and C_{clear} = 0.005 m.

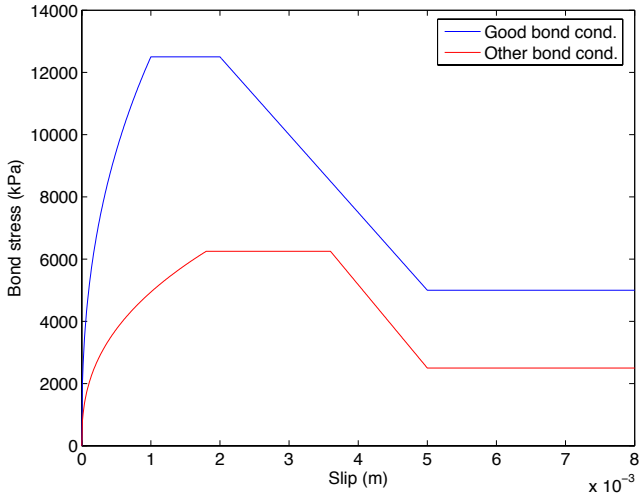

Figure 5.4. Bond-slip relations for deformed rebars under expected pullout failure

It is interesting to note that, although it may be sometimes difficult to be adequately defined, the bond conditions play an important role, especially in what concerns the maximum bond strength. According to Model Code 2010, good bond conditions are obtained whenever the rebars are positioned with an inclination of 45° to 90° with respect to the horizontal during concrete pouring and casting operations. For rebars with an inclination less than 45°, good bond conditions can also be considered if they are located at the bottom 250 mm or at a depth larger than 300 mm from the top of the concrete layer during pouring and casting.

In what respects the behaviour under an expected splitting failure, the values presented in Table 5.3 reflect a significant reduction in the overall bond stresses, in comparison with the values presented above. In addition to the differences associated with the bond conditions, in this case, the bond strength also depends on the level of confinement. It should be noted that the envelope associated with the pullout failure does not depend on the level of confinement, given that this failure type is observed only in the presence of an adequate level of confinement.

Table 5.3. Parameters defining the bond-slip relation for deformed rebars under expected splitting failure (adapted from fib [2011])

	Good bond cond.		Other bond cond.	
	Unconfined	Stirrups	Unconfined	Stirrups
τ_{max}	$7\left(\frac{fcm}{25}\right)^{0.25}$	$8\left(\frac{fcm}{25}\right)^{0.25}$	$5\left(\frac{fcm}{25}\right)^{0.25}$	$5.5\left(\frac{fcm}{25}\right)^{0.25}$
s_1	$s\ (\tau_{max})$	$s\ (\tau_{max})$	$s\ (\tau_{max})$	$s\ (\tau_{max})$
s_2	s_1	s_1	s_1	s_1
s_3	$1.2\ s_1$	$0.5\ C_{clear}$	$1.2\ s_1$	$0.5\ C_{clear}$
α	0.4	0.4	0.4	0.4
τ_f	0	$0.4\ \tau_{max}$	0	$0.4\ \tau_{max}$

The parameters in the previous table were derived for $\emptyset \leq 20$ mm, $c_{max}/c_{min} = 2.0$, $c_{min} = \emptyset$ and $K_{tr} = 2$ % in case of stirrups. The values of c_{max} and c_{min} can be easily computed through the following equations:

$$c_{max} = \max\left(\frac{c_s}{2}, c_x\right)$$
$$c_{min} = \min\left(\frac{c_s}{2}, c_x, c_y\right) \tag{5.5}$$

where c_x, c_y and c_s can be determined based on the sketch presented in Figure 5.5:

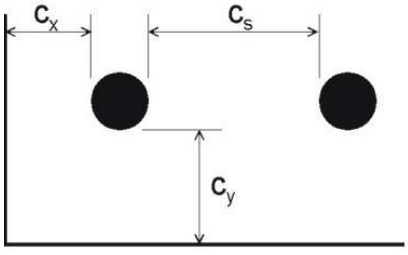

Figure 5.5. Rebar spacing and cover parameters

In addition, K_{tr} can be computed with the following equation:

$$K_{tr} = \frac{n_t \, A_{st}}{n_b \, \emptyset \, s_t} \leq 0.05 \tag{5.6}$$

where n_t is the number of stirrup legs crossing a potential splitting failure, A_{st} is the cross sectional area of one leg of a confining rebar, s_t is the longitudinal spacing of confining reinforcement and n_b is the number of anchored rebars or pairs of lapped rebars in the potential splitting surface.

Moreover, it is possible to observe that in this case, the value of S_1 is not a fixed value. Instead, its value should be computed with Equation (5.1), replacing τ_i by τ_{max} corresponding to a splitting failure, for the conditions under analysis:

$$S_{1,split} = S_{1,pull-out} \left(\frac{\tau_{max,split}}{\tau_{max,pull-out}} \right)^{\frac{1}{\alpha}} \tag{5.7}$$

The differences in bond stresses and slip limits for splitting failure under varying bond and confinement conditions can be appraised in Figure 5.6. Under expected splitting failure, the bond stresses present a rising branch similar to the case of pullout failure, but exhibit a sudden drop after the maximum bond stress is reached. This response reflects the loss of bond strength when large cracks open in the concrete surrounding the rebars - this effect is naturally magnified whenever the anchorage region is unconfined. Similarly to the pullout case, the initial part of the response curve is less steep and reaches a lower bond strength if the bond conditions are not appropriate.

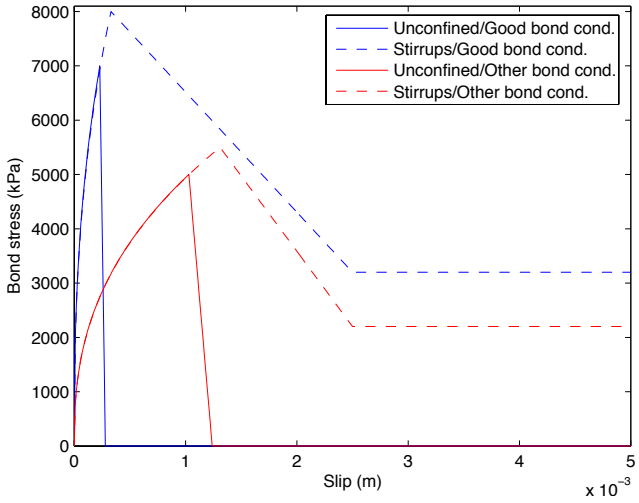

Figure 5.6. Bond-slip relations for deformed rebars under expected splitting failure

5.2.2 Bond-slip parameters for plain rebars

The parameters described in the previous paragraphs are appropriate for ribbed rebars. Taking into consideration that, in the absence of ribs, the bearing action between the rebar and the concrete is limited, a significant reduction in the bond strength for plain rebars is expected, as shown in Table 5.4.

Table 5.4. Parameters defining the bond-slip relation for plain rebars (adapted from fib [2011])

	Cold drawn wire		Hot rolled rebars	
	Good bond cond.	Other bond cond.	Good bond cond.	Other bond cond.
τ_{max}	$0.1\sqrt{f_{cm}}$	$0.05\sqrt{f_{cm}}$	$0.3\sqrt{f_{cm}}$	$0.15\sqrt{f_{cm}}$
s_1	0.00001	0.00001	0.0001	0.0001
s_2	0.00001	0.00001	0.0001	0.0001
s_3	0.00001	0.00001	0.0001	0.0001
α	0.5	0.5	0.5	0.5
τ_f	τ_{max}	τ_{max}	τ_{max}	τ_{max}

Regardless of the bond conditions and the manufacturing process, both slip and bond stress exhibit a severe reduction in their reference parameters when compared with the values defined for deformed rebars. This reduction is clearly observed when comparing the plots from Figure 5.4 and Figure 5.6 with the ones presented in Figure 5.7. Moreover, it is pointed out that the maximum bond stress is equal to the frictional bond stress, consistently with the anchorage mechanism described beforehand.

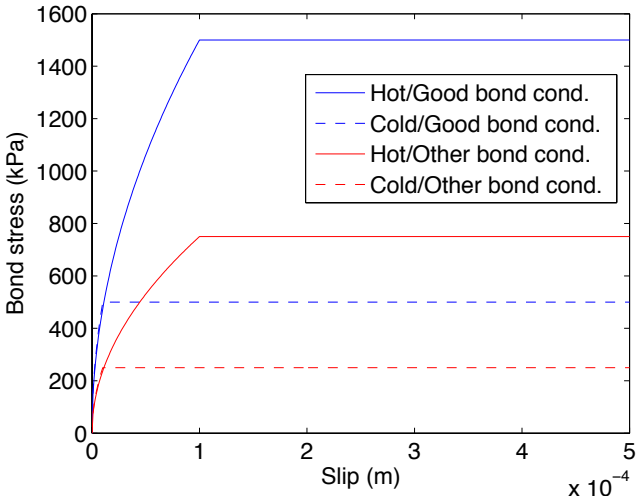

Figure 5.7. Bond-slip relations for plain rebars

5.2.3 Response under cyclic loading

All generic constitutive models presented so far define different parameters reflecting the initial anchorage conditions and considering the monotonic response under positive slip and bond stresses for a tensile loading case. Nevertheless, strain penetration-related deformations occur both under tensile and compressive loading. It is therefore essential, and the objective of this work, to explore also the behaviour under cyclic loading.

The cyclic rules proposed by Model Code 2010 assume that the unloading and reloading branches have a constant slope corresponding to the secant stiffness at s = 0.01 mm, as indicated in Equation (5.8) and Equation (5.9). Naturally, the values of τ_{max}, s_1 and α correspond to the values associated with the monotonic envelope of the anchorage system. In general, the unloading/reloading stiffness is of the order of $K_{unl/rel}$ = 200 N / mm ^{3}. Considering the low slip value used to determine the secant stiffness (s = 0.01 mm), this means that residual deformations are expected to exist from very low loading demand.

- Linear unload/reload branch (for small load reversals):

$$K_{unl/rel} = \frac{\tau(S)}{S}\bigg|_{S = 0.01mm} \tag{5.8}$$

where

$$\tau(S) = \tau_{max}\left(\frac{S}{S_1}\right)^{\alpha}\bigg|_{S = 0.01mm} \tag{5.9}$$

In addition to this linear branch, once the bond stress reaches the friction bond value coming from a load reversal point with a bond stress having opposite sign to the current load point, the unloading/reloading response becomes perfectly plastic (Equation (5.10)).

- Constant stress unload/reload branch (for large load reversals):

$$\tau(S) = \tau_f \tag{5.10}$$

The bond stress will remain constant until the maximum slip already attained in previous inelastic excursions is reached. After that point, the linear unload/reload branch is retrieved until the bond stress reaches the envelope curve, as illustrated in Figure 5.8. These rules are valid for load reversals in both directions.

As further developed in the following sections, the frictional bond stress, for both positive and negative stress values, may vary with the cyclic degradation and/or yielding of the rebar during the analyses.

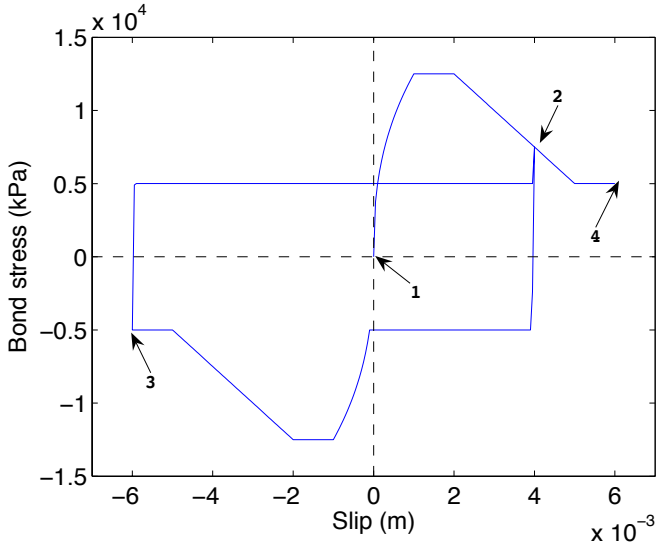

Figure 5.8. Cyclic response for the adopted bond stress-slip model

5.2.4 Parameters Influencing Bond Stress

In addition to the bond-slip response described by the parameters previously introduced, the behaviour of an anchorage region is also influenced by other factors (see Chapter 4). In order to widen the range of application of the proposed model, the values of bond stress (τ_i) defined above, should be updated according to the following expression:

$$\tau_m = \tau_i \ \Omega_{p,tr}\, \Omega_{cr}\, \Omega_y\, \Omega_{cyc} \tag{5.11}$$

where τ_m, is the bond stress after being modified by the different Ω factors. These values are associated with the yielding of the rebar (Ω_y), presence of transverse pressure ($\Omega_{p,tr}$), longitudinal cracking (Ω_{cr}) or due to cyclic degradation (Ω_{cyc}).

For convenience, in the present document, the four factors are arranged in two groups: "Transverse Pressure and Longitudinal Cracking" and "Rebar Yielding and Cyclic Degradation". The two groups differ on the way the bond stresses are affected by the corresponding parameters and how they evolve during the numerical analysis.

In the first case, the factors are defined as initial input and remain constant throughout the analysis. Ideally, these factors would be updated during the analysis in order to reflect the opening of concrete cracks and possible changes in the transverse force equilibrium in anchorage regions, especially for structural joints (as in the connection between beams and columns).

However, given that the proposed model was developed as a zero-length element within the framework of a fibre-based distributed plasticity software, it becomes extremely difficult to monitor the evolution of these quantities along the numerical analysis. On the other hand, the yielding of the rebar and the cyclic loading are effects that can be monitored directly by the bond-slip model. In addition, and contrarily to the previous group, these factors modify the bond stress for different values of slip and level of loading demand.

The following sections describe in more detail the quantification of the different Ω factors and how they affect the bond stress along the development length of the rebars.

5.2.4.1 *Transverse Pressure and Longitudinal Cracking*

The first phenomenon analysed refers to the presence of a transverse pressure around the anchorage region. Naturally, if the concrete surrounding the rebar is subjected to confining compressive forces, the bearing and frictional bond resistance will be magnified.

On the other hand, if the embedment zone is subjected to tensile forces, the anchorage mechanisms are weakened. Moreover, if the tensile stress applied reaches the tensile strength of the concrete, cracks will appear and the anchorage strength will be compromised. The following expressions reflect the reduction of bond stress, uniformly along the development length, with the evolution of transverse pressure.

- $f_{ctm} \geq P_{tr} \geq 0$

$$\Omega_{p,tr} = 1 - \frac{0.3P_{tr}}{f_{ctm}} \tag{5.12}$$

- $P_{tr} \leq 0$

$$\Omega_{p,tr} = 1 - \tanh\left(\frac{0.2P_{tr}}{0.1f_{cm}}\right) \tag{5.13}$$

Where, f_{cm} and f_{ctm} are the mean compressive and tensile concrete stress. Note that positive P_{tr} values indicate tensile load while negative indicate compressive stresses. A graphical representation of the previous equations is given in Figure 5.9.

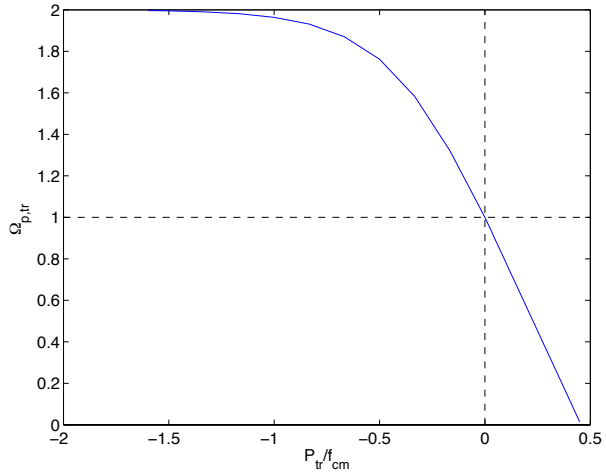

Figure 5.9. Variation of transverse pressure parameter with transverse pressure

Regarding the behaviour under tensile forces it is observed that the bond strength decreases linearly with a tensile transverse load. In the presence of compressive forces, the relation shows an almost linear increase in $\Omega_{p,tr}$ for relatively moderate transverse loading. After reaching transverse pressure values similar to the concrete compressive strength, the effect on the bond stress tends to stabilize, which is consistent with the results obtained by Malvar [1991].

As for the tensile transverse pressure, the presence of longitudinal cracks around the anchorage region reduces the bond stresses. In the following expressions, the bond stress is determined as a function of the crack width:

- Uncracked concrete:

$$\Omega_{cr} = 1 \tag{5.14}$$

- Cracked concrete:

$$\Omega_{cr} = 1 - 1.2 w_{cr} \quad (w_{cr} \; in \; mm) \tag{5.15}$$

Where w_{cr} is the crack width parallel to the rebar axis in mm. In addition, the expressions are valid only for cracks up to 0.5 mm, whose value is identified in Figure 5.10 by a red circle. For wider cracks the expression above is no longer valid and the anchorage strength is eventually compromised.

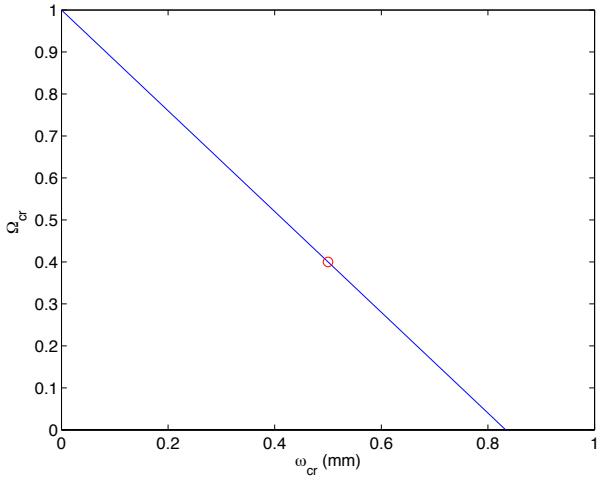

Figure 5.10. Variation of longitudinal cracking parameter with crack width

It should be recalled that, in the proposed model, the effects described in this section are assumed to be defined at the beginning of the analysis and produce a uniform increase or decrease of the bond stresses, independently of the slip demand. Moreover, the resulting constitutive model is adopted for all integration points defined along the embedment length of the rebars.

5.2.4.2 *Rebar Yielding and Cyclic Degradation*

As reported in Section 4.3, the quantification of the effects due to rebar yielding has been object of study by different authors. Despite the different opinions in this matter, the idea that the bond stresses decrease significantly along the rebar length when it exhibits inelastic deformations seems to gather a large consensus.

Once a rebar reaches its yield strength, the strains tend to increase rapidly for an identical level of force, resulting in a more pronounced increase in the rebar slip. At the same time, as the tensile strains increase, the cross section starts to shrink due to the necking effect (similar to Poisson effect but in the inelastic domain). This reduction of the rebar cross-section reduces the bearing and friction actions between the rebar and the concrete, leading to a decrease in bond stresses.

According to the recommendation from Model Code 2010, this reduction can be determined as a function of the rebar strain, based on the following expressions:

- $\varepsilon_s \leq \varepsilon_{s,y}$

$$\Omega_y = 1 \tag{5.16}$$

- $\varepsilon_{s,y} < \varepsilon_s \leq \varepsilon_{s,u}$

$$\Omega_y = 1 - 0.85\left(1 - e^{-5a^b}\right) \tag{5.17}$$

where *a* and *b* are given by:

$$a = \frac{\varepsilon_s - \varepsilon_{s,y}}{\varepsilon_{s,u} - \varepsilon_{s,y}} \tag{5.18}$$

$$b = \left(2 - \frac{f_{um}}{f_{ym}}\right)^2 \tag{5.19}$$

with f_{um} and f_{ym} the mean values of the concrete tensile and steel yield strengths, respectively.

As illustrated in Figure 5.11, the bond factor Ω_y decreases abruptly once the rebar enters the inelastic region – for instance, for a strain ductility of 2, the bond stress is reduced to almost half the initial value. For increased levels of ductility, the bond stress at the locations where the rebar yielded is further decreased, but in a less pronounced manner.

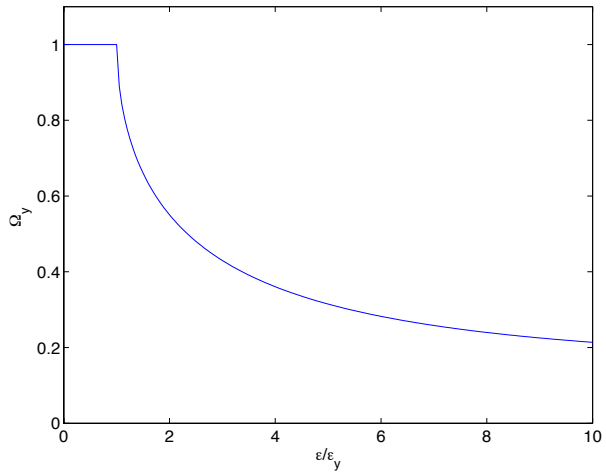

Figure 5.11. Variation of rebar yielding parameter with rebar strain

Naturally the opposite effect is expected if the rebar yields in compression. In this case, the rebar expand its nominal diameter, maximizing the bond strength of the rebar. However, the rules adopted for the present bond-slip model do not account for such beneficial effect because there is little information in this regard (see discussion in Section 4.3). Furthermore, in typical RC sections subjected to cyclic bending action, it is not frequent to observe yielding of rebars under compression, given the contribution of concrete in compression.

For a generic anchorage system, Figure 5.12 shows that the bond stresses can be greatly reduced once the rebar experiences nonlinear tensile deformations. Under compressive loads, the bond stress-slip model remains unchanged.

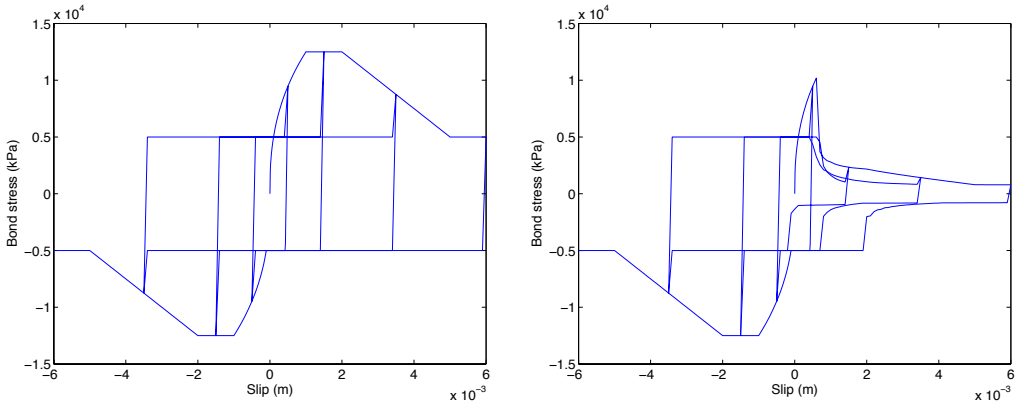

Figure 5.12. Generic bond stress-slip model with (right) and without (left) yielding degradation

Focusing now the attention on the bond degradation due to cyclic loading, the rules adopted in the proposed bond-slip model and recommended by Model Code 2010 follow essentially the ones proposed in the work developed by Ciampi *et al.* [1981]. In this case, the reduction in bond stresses is determined based on the cumulative dissipated energy from the previous cycles, as illustrated in Figure 5.13.

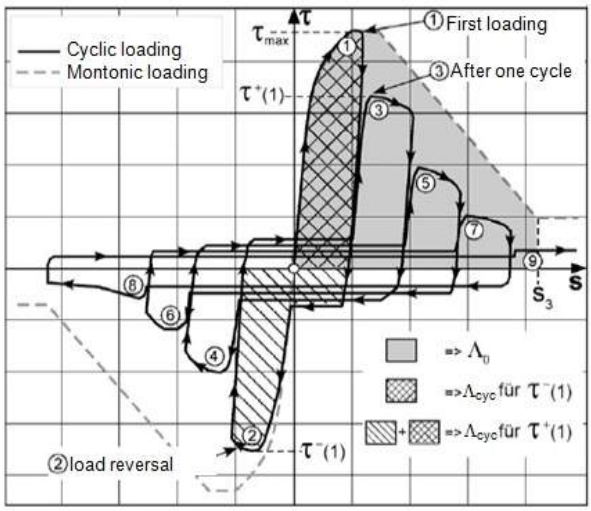

Figure 5.13. Bond stress reduction due to cyclic degradation [fib ,2011]

Hence, during the first loading in one direction, the bond stresses remain unchanged with respect to the initial monotonic envelope curve. When the load reverses, the bond stresses are reduced based on the energy dissipated previously. This process is successively updated, with the bond stresses being determined through the cumulative dissipated energy up to the last load reversal. Such dissipated energy corresponds to the area enclosed by the bond stress-slip curve during each cycle. The computation of this area in the proposed numerical model also takes into account the fact that only a fraction of the dissipated energy between peak slip values is related to damage in the bond-slip mechanism, while the remainder is related to overcoming the frictional resistance and is transformed into heat. This is taken into consideration by accounting half of the dissipated energy corresponding to the friction mechanism, as suggested by Eligehausen *et al.* [1983].

The quantification of the bond stress reduction, Ω_{cyc}, is therefore determined using Equation (5.20):

$$\Omega_{cyc} = e^{\left[-1.2\left(\frac{A_{cyc}}{A_0}\right)^{1.1}\right]} \tag{5.20}$$

where A_{cyc} represents the cumulative summation of the cyclic hysteretic areas and A_0 reflects a reference value defined by the area of the initial bond stress-slip monotonic curve up to S_3 (slip limit before the constant bond stress branch).

The evolution of Ω_{cyc} with the ratio A_{cyc}/A_0 can be appraised in Figure 5.14.

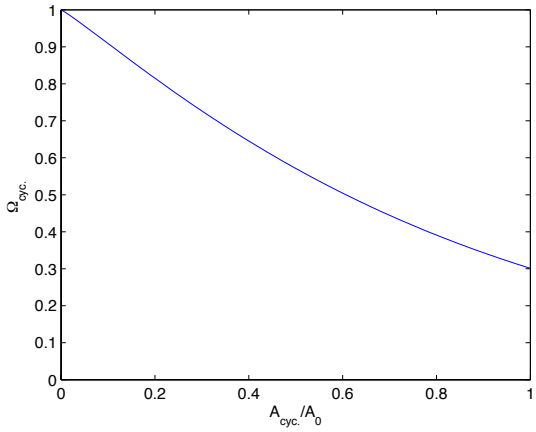

Figure 5.14. Variation of cyclic degradation parameter with the energy dissipated under cyclic loading

The loading rate effect is neglected in the present model since, under seismic loading, it is difficult to establish an effective loading rate. Moreover, it is expected that an increase in the loading rate results in an increase in the bond strength at the anchorage region.

Figure 5.15 presents a graphical comparison of considering or not the reduction in bond stresses due to cyclic degradation. It is possible to observe an important reduction in the bond stresses, especially for larger slip demand. Nonetheless, the reduction seems to be less pronounced than the one observed due to rebar yielding. On the other hand, in this case, the reduction also occurs when the rebar is subjected to negative slip values.

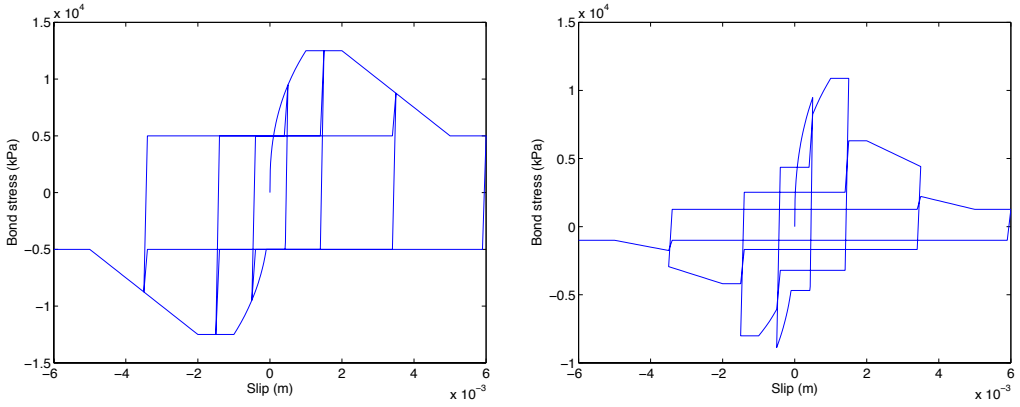

Figure 5.15. Generic bond stress-slip model with (right) and without (left) cyclic degradation

Finally, in order to assess the influence of these two factors combined, Figure 5.16 represents the superposition of a generic bond constitutive model with the one resulting from the combination of the two stress degradation factors. From this comparison it is possible to evaluate the potential negative effects that this degradation has on the anchorage capacity of RC elements subjected to seismic loading.

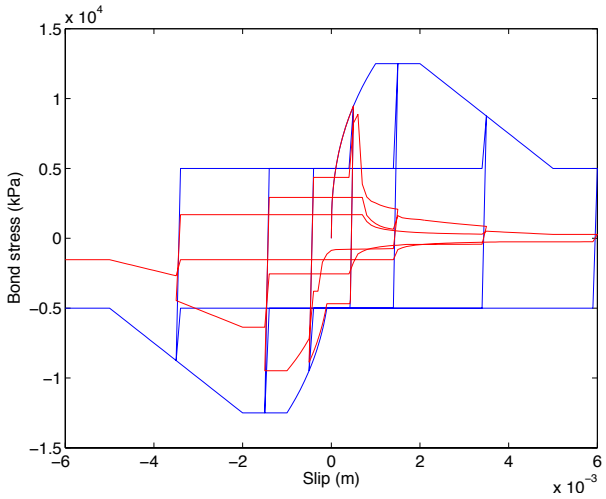

Figure 5.16. Comparison between a generic bond stress-slip model (blue) with the same model reduced by the yielding and cyclic degradation parameters (red)

5.2.4.3 *Hooked rebars*

Regarding the presence of hooked rebars, no particular modification is adopted for the bond constitutive model. However, following the recommendations from Ueda *et al.* [1986], the embedment length should be corrected by considering an equivalent straight embedment length (L_{eq})determined according to the following expression:

$$L_{eq} = L_s + D_{hook} + d_b \tag{5.21}$$

where L_q is the straight rebar lead in length to the hook and D_{hook} is the diameter of the hook for a rebar with a diameter d_b.

5.3 ELEMENT FORMULATION

Similarly to a traditional FE, the formulation of the present bond-slip element is built-up on the equilibrium and compatibility conditions, coupled with appropriate (concrete, reinforcement and bond) constitutive relations. The proposed model presents, however, some specificities that require the adoption of unconventional methods. Hence, for a clearer interpretation, the different procedures can be separated into four main groups.

Ordered by increasing scale of the problem, these comprise, the (i) definition of the different response parameters along the embedment length of one rebar, (ii) determination of the rebar anchorage force associated with the applied displacement, (iii) determination of the bond-slip sectional response and (iv) determination of the associated tangent stiffness. The description of each of the different components is described in detail in the following sections.

5.3.1 Strain Penetration Effects Along the Embedment Length

Taking into consideration that the present model was designed to be implemented in general structural analysis software, it is important that the procedures adopted follow the basic principles commonly adopted in FE methodologies. Hence, the primary goal for the proposed bond–slip model consists in determining the anchorage force (F_0) associated to a given applied slip (S_0) at the loaded-end of a reinforcing bar defined in the cross-section of the zero-length element (equal to the adjacent RC member). To do that, it is critical to understand how the force- and deformation-related parameters evolve along the embedment length of the rebar. Figure 5.17 presents how the different constitutive relations are assigned to the different IPs, together with a possible distribution of the different response parameters along the rebar.

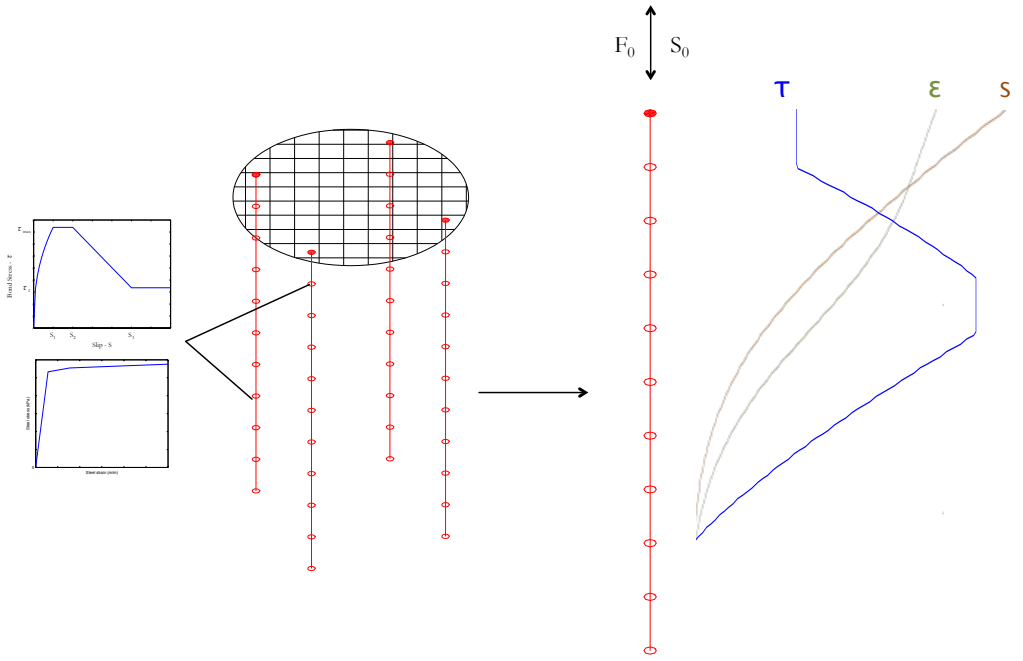

Figure 5.17. Schematic representation of the contribution of the different response parameters for the determination of SP effects in a rebar

Noting that the equilibrium equation that governs the bond slip mechanisms is given by the following expression:

$$F_0 = \int_0^{L_d} \tau(z)\, P_b\, dz \tag{5.22}$$

and that the compatibility equation is given by:

$$S_0 = \int_0^{L_d} \varepsilon_s(z)\, dz \tag{5.23}$$

it becomes evident that the determination of the slip (S_0) and force (F_0) at the loaded-end of a rebar requires the accurate estimation of the bond stresses ($\tau(z)$) and reinforcement strains ($\varepsilon(z)$) along the embedment length. In the previous equations P_b is the perimeter of the rebar, and L_d is the development length. Note that the latter length is always lower or equal to the embedment length.

One of the basic principles of the finite element (FE) method involves the subdivision of a large "problem" into smaller and simpler parts. A possible strategy to fulfil the previous requisite passes through the assumption of an interpolation function that approaches the shape of a desired displacement- or force-related parameter (as in the model proposed by Monti and Spacone [2000]). This type of approach allows the use of advanced numerical integration algorithms based on the family of Gauss quadrature methods – schemes commonly employed due to their recognized accuracy and efficiency. Nonetheless, these parameters may vary significantly with the anchorage properties and/or loading history, as illustrated in the previous chapter. Moreover, the development length, i.e., the length of the element that is "mobilized" for a given applied load, is not known *a priori*, being determined only at the end of each converged solution. In this regard, it is important to highlight that the proposed rules should recognize that the development length at a given load stage does not necessarily correspond to the embedment length.

Considering the previous limitations, the employment of simplified one-step methods for numerical integration appears a more convenient solution, where the different response parameters at each IP along the rebar can be progressively determined considering small length intervals. In the following, the application of two alternative numerical methods is explored: the (explicit) forward-Euler and the (implicit) Crank-Nicholson method. Following a brief description of both methods, the advantages and disadvantages of each procedure are evaluated in order to determine the most convenient to be considered in the proposed numerical tool.

5.3.1.1 *Forward-Euler Method*

The family of Euler Methods represents one of the simplest procedures used to approximate the solution of ordinary differential equations. This method is known to be numerically unstable, as it usually requires small step sizes, which leads to a large number of integration points. Generically, the properties at a given location of a domain can be determined as:

$$u(z+h) = u(z) + \int_{z}^{z+h} f\big(\xi, u(\xi)\big)\, d\xi \tag{5.24}$$

where z represents the location of the different IPs, h is the length of the step, u is the solution to be approximated and f represents the derivative of the function u. Given that the solution of the integral is a function of the solution to be determined, the integral cannot be solved explicitly. However, starting with an initial value at one extremity of the domain of interest, it is possible to approximate the solution at the subsequent points using the principles of an explicit integration method.

For the problem in hand, the equilibrium equation can be rewritten as:

$$F_n = F_{n-1} - \int_{z}^{z+\Delta z} \tau(z)\, dz\; P_b = F_{n-1} - \tau_{n-1}\, L_{IP}\, P_b \tag{5.25}$$

where F_n is the force at the integration point n, z is the distance of each IP from the loaded-end, L_{IP} is the distance between the different IPs and $\tau(z)$ is the bond stress at each location along the rebar. Similarly, the compatibility equation is given by:

$$S_n = S_{n-1} - \int_{z}^{z+\Delta z} \varepsilon_s(z)\; dz = S_{n-1} - \varepsilon_{s,n-1}\, L_{IP} \tag{5.26}$$

where S and ε_s are the slip and the strain along the length of the rebar.

It should be noted that the previous variables could be related at each IP through different constitutive relations - $\varepsilon_s(z)$ is a function of $F(z)$, while $\tau(z)$ is function of $S(z)$. The previous relations can be easily interpreted in Figure 5.18, where the grey rectangles represent the assumed variation of the rebar strain and the bond stress, while the red line represents the variations in force and slip.

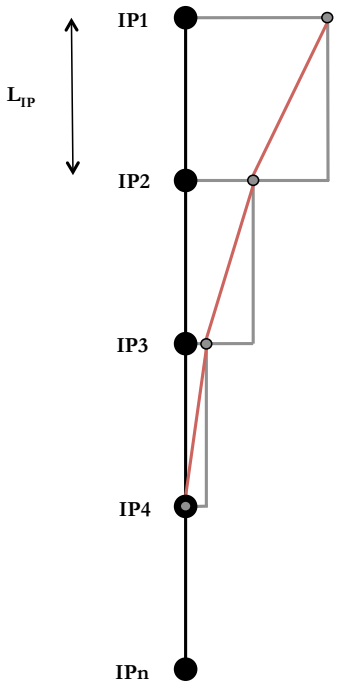

Figure 5.18. Schematic representation of response parameters distribution along the embedment length of the rebar following the forward-Euler method

The rectangular or stepwise evolution of ε_s and τ are consistent with the explicit nature of this integration method. Accordingly, the response parameters at each IP are computed solely based on the values already determined for the closest (previous) IP. This procedure is illustrated in a simplified manner in Figure 5.19.

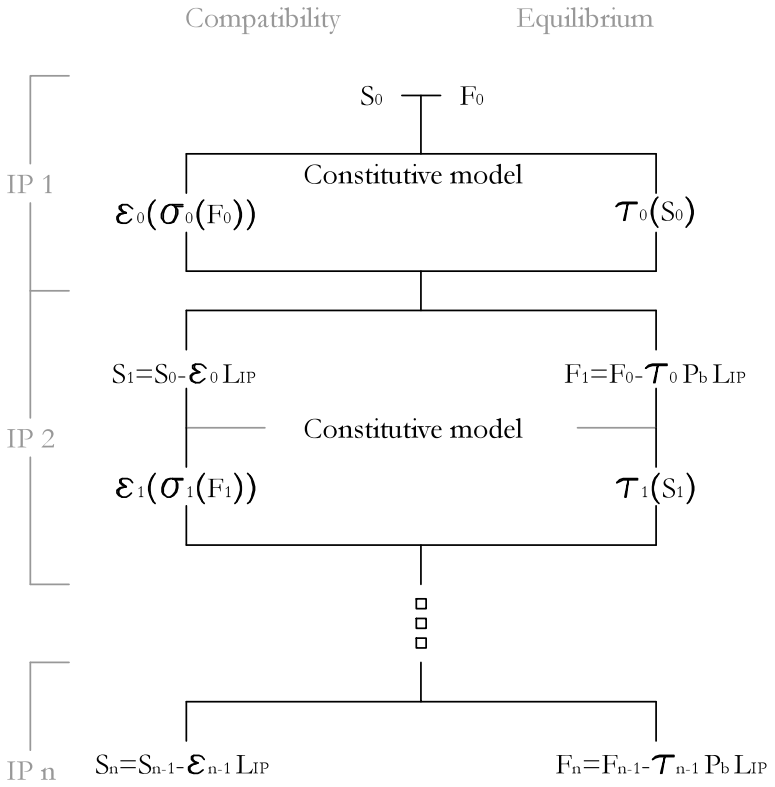

Figure 5.19. Flowchart describing the formulation used to determine the different response parameters along the embedment length following the forward Euler method

5.3.1.2 *Crank-Nicholson Method*

The Crank-Nicholson method is based on the trapezoidal rule of numerical integration and results from the combination of both forward- and backward-Euler methods. Contrarily to these, it is a second-order convergence method, exhibiting superior convergence and stability. On the other hand, being an implicit method, it requires the solution of nonlinear equations along the procedure.

Figure 5.20 expresses, in a graphical manner, how the previous concepts can be applied to the current problem. In this case, and contrarily to what was observed for the Euler method (Figure 5.18), the variation in slip or force is dependent on the response of two successive IPs: the current and the previous one.

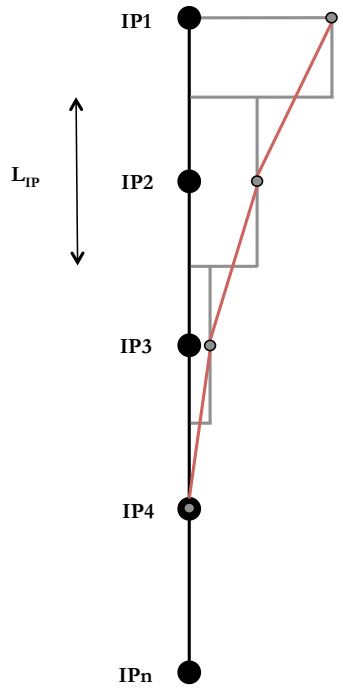

Figure 5.20. Schematic representation of response parameters distribution along the embedment length of the rebar following the Crank-Nicholson method

The equilibrium and compatibility equations can, thus, be expressed by:

$$F_n = F_{n-1} - \int_{z}^{z+\Delta z} \tau(z)\, dz\ P_b = F_{n-1} - \frac{L_{IP}}{2}\left(\tau_{n-1} + \tau_n\right) P_b \tag{5.27}$$

$$S_n = S_{n-1} - \int_{z}^{z+\Delta z} \varepsilon_s(z)\, dz = S_{n-1} - \frac{L_{IP}}{2}\left(\varepsilon_{s,n-1} + \varepsilon_{s,n}\right) \tag{5.28}$$

From the previous equations, it is possible to verify that the variables at a given IP_n are not only dependent on the response at the previous IP (IP_{n-1}) but also on the response parameters at the IP under analysis (IP_n). Hence, the solution cannot be determined directly.

Recalling that both the bond stress and the steel strain should respect their respective constitutive model, let us first assume that the reinforcement responds in the elastic range. In this case, the steel strains at a given IP ($\varepsilon_{s,n}$), can be described as:

$$\varepsilon_{s,n} = \frac{F_n}{E_s\, A_b} \tag{5.29}$$

where E_s is the modulus of elasticity of the reinforcement and A_b represents the cross-sectional area of the rebar. Replacing now Equation (5.29) in the bond-slip model's compatibility equation, one obtains that:

$$S_n = S_{n-1} - \frac{L_{IP}}{2}\left(\varepsilon_{s,n-1} + \frac{F_n}{E_s\, A_b}\right) \tag{5.30}$$

The force (F_n) at IP_n, can now be replaced by the corresponding equilibrium equation, resulting in the following expression:

$$S_n = S_{n-1} - \left(\frac{\varepsilon_{s,n-1} + \left(F_{n-1} - \dfrac{\frac{\tau_{n-1} + \tau_n}{2}\, L_{IP}\, P_b}{E_s\, A_b} \right)}{2} L_{IP} \right) \tag{5.31}$$

Noting that the bond stress (τ) is a function of the slip demand at a given IP, it can be replaced by its force counterpart considering any suitable bond constitutive model. Considering the rules presented in 5.2, and assuming that the applied slip (S) is lower than S_1, the bond stress can be determined with Equation (5.32). It should be noted that any other expressions from alternative constitutive relations or different slip values can be used.

- $0 \leq S \leq S_1$:

$$\tau_n(S) = \tau_{max}\left(\frac{S_n}{S_1}\right)^{\alpha} \tag{5.32}$$

Finally, replacing Equation (5.32) into Equation (5.31), it is possible to verify that the slip at a given integration point (S_n) can be related to quantities previously evaluated at the integration point above (IP_{i-1}):

$$S_n = S_{n-1} - \left(\frac{\varepsilon_{s,n-1} + \left(F_{n-1} - \frac{\tau_{n-1} + \tau_{max} \left(\frac{S_n}{S_1} \right)^{\alpha}}{2} L_{IP} \, P_b \right)}{E_s \, A_b} }{2} L_{IP} \right) \tag{5.33}$$

Despite being possible to express the slip at the point of interest (S_n) as a function of quantities from the previous point, S_n is present on both sides of the equation and cannot be isolated. Hence, in order to find the solution of the previous equation, it is necessary to adopt an iterative algorithm.

Once the slip value is determined, the corresponding bond stress can be easily found through the bond constitutive model, and the associated force can be computed directly from the equation of equilibrium, given by Equation (5.27). The solution for the different IPs defined along the embedment length of the rebar can then be determined following a procedure similar to the one described in Figure 5.19.

5.3.1.3 *Advantages and Limitations of Forward Euler and Crank-Nicholson Methods*

In the previous sections, two alternative approaches were devised for determining different response parameters along the embedment length of a rebar. It is now important to evaluate which of those alternatives offers a better performance in terms of accuracy and efficiency. In the present context it is also important to evaluate how discretized should the embedment length of the rebar be and how fast the numerical response converges to the exact solution.

Based on the description presented in the two previous sections, it seems clear that the Forward Euler method, as a first-order one, requires a higher discretization of the embedment length to produce identical results to the Crank-Nicholson method, which is a second-order convergence method. On the other hand, the Crank-Nicholson method is an implicit method, meaning that an additional iterative level is required to determine the solution at each IP.

In order to evaluate the performance of both methods, a study was conducted considering the generic anchorage and bond properties that are detailed in Table 5.5.

Table 5.5. Properties considered for the comparative study

Anchorage properties	
d_b (m)	0.02
L_e (m)	0.80
f_c (MPa)	30
f_y (MPa)	550
f_u (MPa)	687.5
E_s (GPa)	190
$E_{s,p}$ (GPa)	1
C_{clear} (m)	0.005
Bond-slip parameters considered	
S_1 (m)	0.001
S_2 (m)	0.002
S_3 (m)	0.005
τ_{max} (MPa)	$2.5\sqrt{f_c}$
τ_f (MPa)	$0.4\ \tau_{max}$

The performance of both approaches was evaluated for different discretization schemes. The adopted spacing between IPs, together with the corresponding number of IPs is presented in Table 5.6.

Table 5.6. IP spacing and corresponding number of IPs

IP spacing (m)	0.200	0.100	0.050	0.016	0.010	0.005
Number of IPs	5	9	17	51	81	161

The comparison between both numerical approaches was conducted for an applied slip of S_0 = 0.5 mm. The computed anchorage force and development length were compared against the theoretical value determined with the procedure described in Section 4.5. In this study, all other parameters were kept constant except the number of IPs along the

rebar. The force at the loaded-end was determined following an iterative procedure that is described in detail in the subsequent section. Figure 5.21 presents the comparison of the anchorage force and development length for an increasing number of IPs.

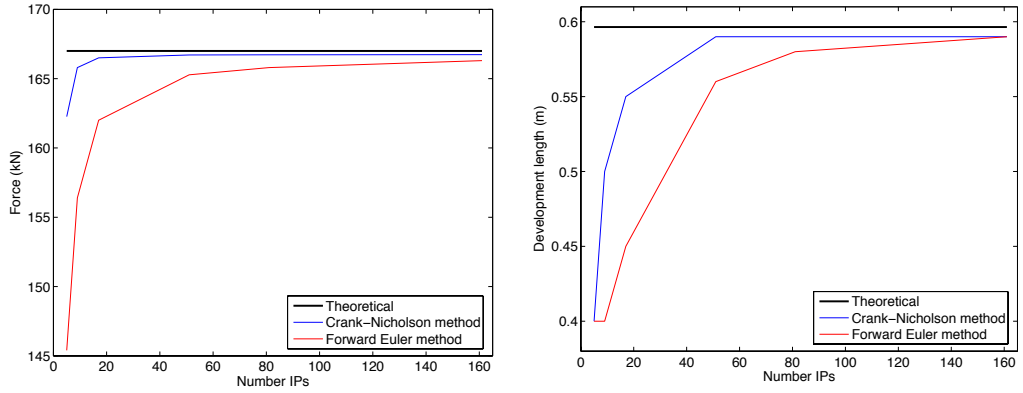

Figure 5.21. Convergence rate for anchorage force and development length, depending on the number of IPs

From the previous plots it is clear that the Crank-Nicholson method requires a significantly smaller number of IPs to converge to the theoretical solution – with 17 IPs (spacing of 5 cm) the anchorage force is predicted with appreciable accuracy. However, in this case, the development length is still significantly underpredicted, which may become a relevant issue in cases where the entire embedment length is "active". On the other hand, the Forward Euler method requires 81 IPs (spacing of 1 cm) to produce a reasonable approach to the theoretical solution in terms of anchorage force.

However, and despite requiring about 5 times more IPs (81 *vs* 17 IPs) to produce an identical solution, the use of the Forward Euler method turns out to be significantly more efficient, since its computing time is about 3 times lower than with the Crank-Nicholson method. The reason for this difference in computing speed is because the latter requires the use of an additional iterative level to solve a nonlinear equation at every IP.

For completeness, Figure 5.22 presents the evolution of the predicted strain profiles with both methods for an increasing number of IPs. The evolution of strains allows for an adequate interpretation of the performance of the element as it reflects somehow the evolution of both force- and deformation-related parameters.

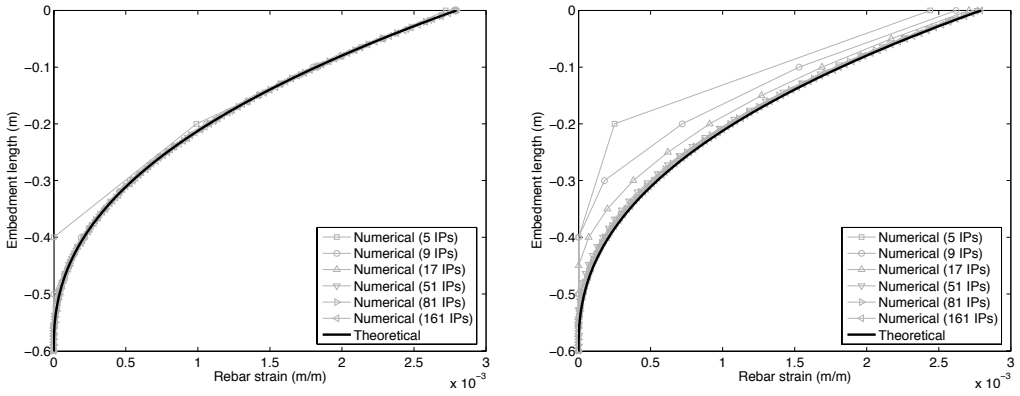

Figure 5.22. Comparison between theoretical and numerical strain distribution, for different number of IPs, considering Crank-Nicholson (left) and Forward Euler (right) methods

Once again, the results demonstrate that the Crank-Nicholson method converges faster to the theoretical solution – with 9 IPs the profile diverges only marginally at an embedment length around 0.5 m, whilst with the Forward Euler approach, an identical profile is only observed with at least 51 IPs. Despite the distinct velocity of convergence, it is clear that, with a suitable discretization, both methods manage to accurately reproduce the actual strain distribution along the embedment length of the rebar.

Based on the results obtained, the implementation of the Forward Euler method seems favourable as far as the spacing between IPs is in the order of one centimetre. The consideration of shorter values seems irrational given the difficulty to observe such precision during the construction of the structures. On the other hand, using larger intervals between IPs difficults the identification of the precise evolution of some response parameters along the rebar (such as rebar yielding, for instance). Moreover, the use of larger values will result in on inaccurate estimation of the actual development length, which will necessarily affect the remaining response parameters.

As illustrated in Figure 5.23, the adoption of the Forward Euler method with 1 cm spacing between IPs manages to reproduce the theoretical solution with remarkable accuracy for the different response parameters along the rebar.

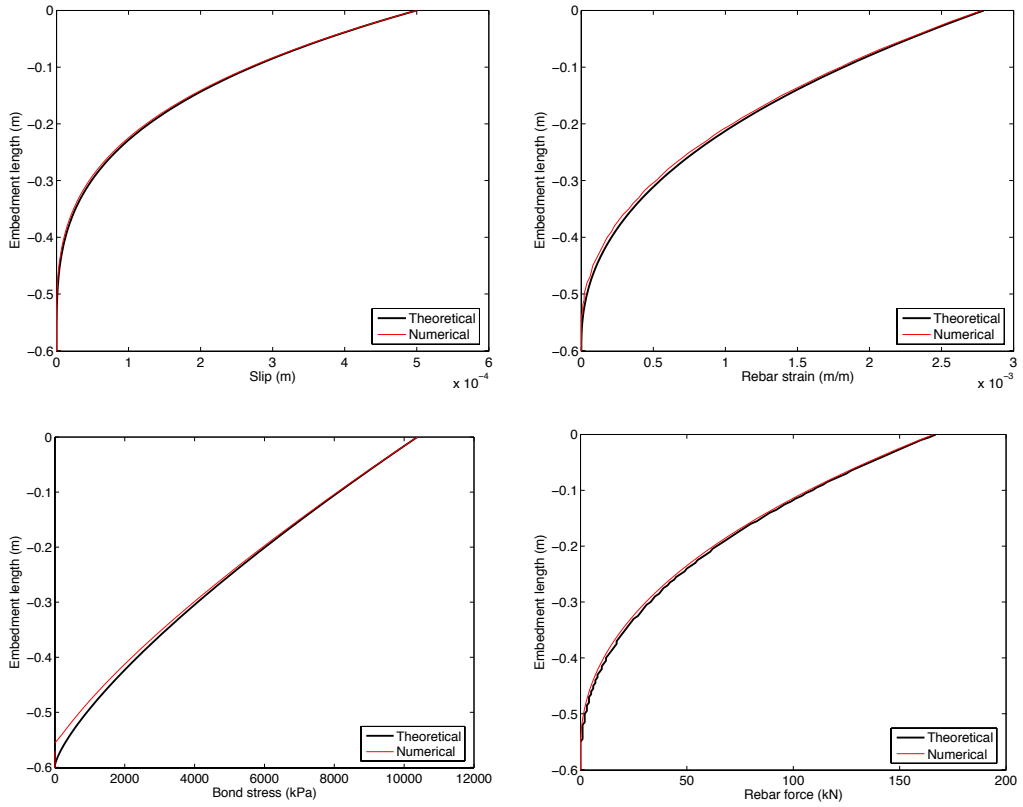

Figure 5.23. Response parameters distribution along the development length of the rebar, considering the Forward Euler method with a step size of 1 cm

The previous results reveal a small divergence in the bond stress close to the equilibrium point. This observation is associated with the steep increase in bond stress for very low values of slip demand as described by the bond stress-slip constitutive relation (see section 5.2). Nevertheless, it should be pointed out that, at this region, the different response parameters assume very low values with negligible influence in the overall bond-slip response.

In summary, and considering the above discussion, the selection of the Forward Euler method to incorporate the proposed bond-slip model seems favourable for two main reasons: (i) it requires about ⅓ of the computational cost to produce results with identical accuracy and (ii) the use of 1 cm spacing between IPs turns out to be advantageous because it allows a better representation of different effects along the rebar (e.g., rebar yielding) and a more precise estimation of the actual development length.

5.3.2 Rebar Force-Slip Response at the Loaded-End

The procedure described in the previous section allows the determination of the response along the embedment length of the rebar for a given pair (S_0 / F_0) applied at the loaded-end of the rebar (see Figure 5.17). However, one of the response parameters at the loaded-end of the rebar, either S_0 or F_0, is usually not known during the state determination analysis. In conventional FE formulation, it is customary to determine the force component that is associated with a given prescribed displacement. Hence, and despite the present formulation can be solved for either of the variables, it is the conventional approach that is described in the following since it is the one of interest for incorporation within general structural analysis software packages.

The proposed iterative procedure is thus used to determine the axial load that is consistent with a given applied slip at the loaded-end of each rebar, and it uses the same principles as the well-known bisection method. In its original formulation, this numerical method consists in delimiting progressively narrower intervals that approach the root of a given function. Considering a function f, continuous in the interval $I_n = [\, a\, ,\, b\,]$, such that $f(a)$ and $f(b)$ have opposite signs, then there is at least one zero within the interval. Starting from pre-established values of a and b that satisfies the previous requisite, the interval is then repeatedly bisected, computing the midpoint $c = (\, a + b\,) / 2$, until the interval becomes as smaller as desired. By examining the sign of $f(c)$, the new interval $I_{n+1} = [\, a\, ,\ c\,]$ or $I_{n+1} = [\, c\, ,\, b\,]$ is defined such that the extremities of the interval remain with opposite signs. Taking $I_0 = [\, a\, ,\, b\,]$, as the starting interval and ε_F the prescribed error admitted, the number of iterations required (n) until convergence can be determined with the following equation [Pina, 1995]:

$$n = \frac{\ln\left(\frac{|a-b|}{\varepsilon_F}\right)}{\ln 2} \tag{5.34}$$

Being categorized as a global convergence method, i.e., it does not require a sufficiently close approximation of the solution, the convergence tends to be slow (linear rate of convergence). On the other hand, considering that the approximation to the solution does not require any information from the previously converged solution, the method is very stable and is not susceptible to the well-known convergence issues associated with Newton's family of methods. The employment of the latter methods is also difficult as the computation of the bond-slip tangent stiffness is not trivial, as further developed in section 5.3.4.

In order to apply this method it is necessary to establish an interval ($I = [\, a\, ,\, b\,]$, as defined previously) that guarantees the existence of the solution within it. For this case, the limits a and b, here renamed as F^+ and F^-, can be easily established by using the maximum resisting force that each rebar can support:

$$F^+ = -F^- = +F_u = +A_b\, f_u \tag{5.35}$$

where A_b and f_u are the area and ultimate stress of the rebar. Independently of the anchorage properties, this condition is universal, considering that the load carried by the rebars will never exceed this limit neither in tension nor in compression. Once these limits are established, it is required to develop a procedure that guaranties the convergence to an anchorage force consistent with the applied slip.

After analysing carefully the behaviour of the different response parameters along the embedment length (with a detailed description presented in the previous sections), it was possible to observe that the distributions of the different parameters follow distinct behaviours whether the force is under- or overestimated. For instance, if a trial tensile force is larger than the theoretical one, the slip decreases faster (due to larger rebar strains) and, as the slip changes sign to negative values, the bond stress will tend to change the sign, leading to an increase of the bond force values. Consequently, the force will tend to move away from zero, instead of being progressively reduced. In the same way, whenever the trial force is underestimated, the inverse behaviour is observed. Moreover, it should be noted that the previous rules are valid independently of the slip value (being positive, negative or zero) and sign of the trial force.

The abovementioned behaviour can be easily interpreted with the plots presented in Figure 5.24 where, for an imposed slip of 0.45 mm, the response along the rebar is plotted for the cases were the trial force is lower (blue line), equal (black line) and higher (red line) than the exact one. In addition to the previously described conditions, the following plots also show that both force and slip converge to zero at the same integration point (equilibrium IP) when the trial force converges to the exact solution.

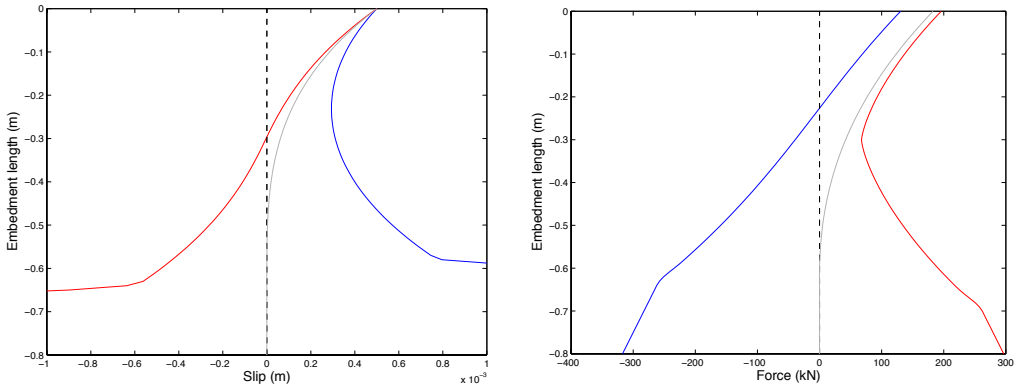

Figure 5.24. Slip (left) and force (right) distribution for different trial forces

Taking into account the previous effects, it is possible to establish simple rules that guarantee the convergence of the method to the desired solution. Hence, if the force at the free-end of the rebar ($F_{IP,n}$) is positive, this means that the approximation to the loaded-end force ($F_{0,trial}$) was overestimated. In this case, the upper bound of the interval should be updated with the current $F_{0,trial}$. If, instead, the trial force at the free-end is negative the lower-bound of the interval is replaced by the corresponding $F_{0,trial}$. In order to progressively decrease the amplitude of the interval within the current step, the trial force at every iterations is given by the mean value of the interval.

Thus, considering an initial interval given by:

$$I_i = [F^-, F^+] \tag{5.36}$$

where *i* represents the current step of a given analysis and F^+ and F^- are the initial limits of the interval, determined with the following equations:

$$F^- = -A_b\, f_u \quad \text{and} \quad F^+ = A_b\, f_u \tag{5.37}$$

Hence, the initial trial force at the loaded-end of the rebar is given by:

$$F_{0,trial} = \frac{F^+ + F^+}{2} \tag{5.38}$$

At this stage, the response along all the IPs is determined through the Forward Euler procedure (Section 5.3.1.1), taking the trial force ($F_{0,trial}$) and the slip demand (S_0) at the loaded-end as input parameters. Once, the response at the free-end is determined, the following condition is tested:

- If ($F_{IP,n}$) ≤ 0 :

$$I_{i+1} = \left[F_{0,trial}, F^{+}\right] \tag{5.39}$$

- If ($F_{IP,n}$) > 0 :

$$I_{i+1} = \left[F^{-}, F_{0,trial}\right] \tag{5.40}$$

The process is then repeated until the amplitude of the interval is smaller than a prescribed error. In addition, it should be pointed out that even when the full length of the rebar is mobilized (resulting in an additional overall slip of the rebar), the force at the free-end will necessarily be zero and, hence, this method is still valid.

Once the converged force and, therefor, the position of the equilibrium IP (IP_{eq}) is determined, the force and slip at the subsequent IPs are set to zero and the bond stress and steel strain are determined according to the corresponding bond and steel constitutive models. During the iterative procedure all the response parameters assigned to each IP are referred as trial values. Whenever the converged solution is found, these values are saved and the trial ones are initialized for the following step.

The solution algorithm for the proposed model is illustrated in the flowchart of Figure 5.25. Note that the procedure describing the response along the length of the rebars is presented in grey.

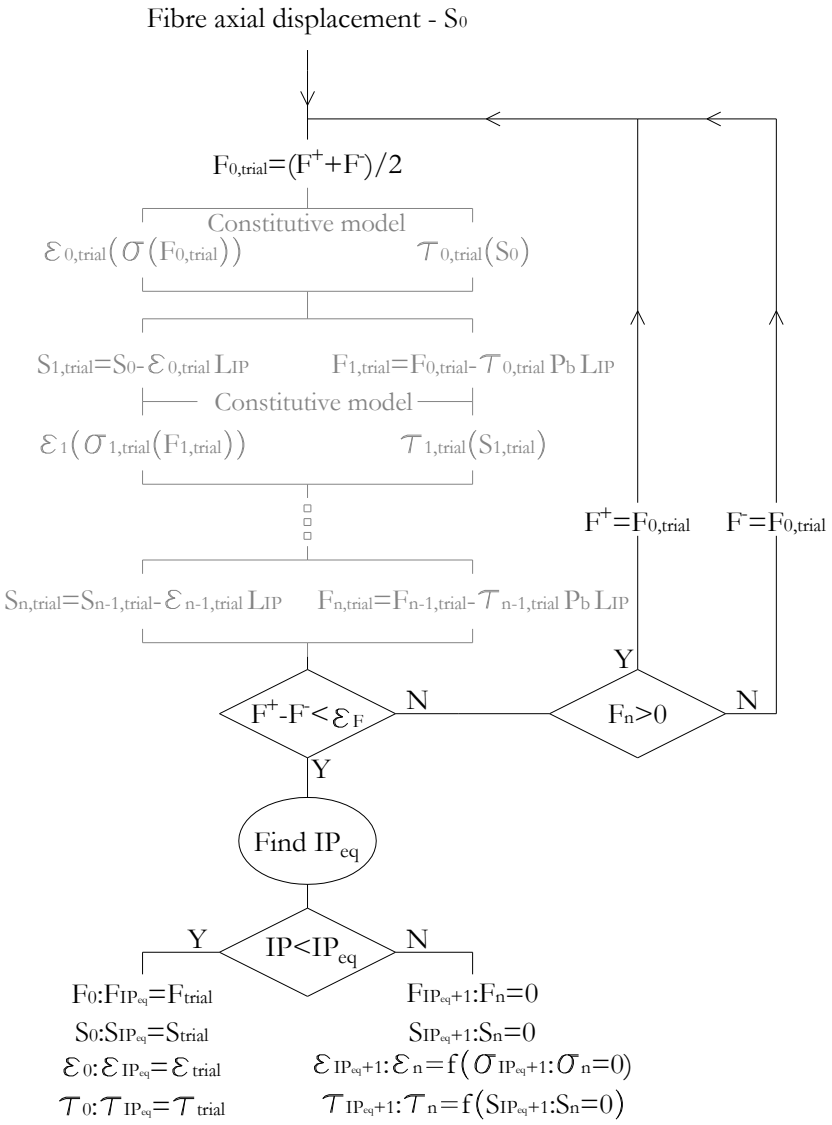

Figure 5.25. Flowchart describing the application of the bisection procedure within the proposed bond-slip model

For demonstrative purposes let us consider a ϕ22 rebar with f_y = 550 MPa (f_u = 687 MPa) and an admitted convergence error of 1 N. From Equation (5.34) it is possible to verify that the procedure requires 19 iterations. The evolution of the trial force ($F_{0,trial}$) for an increment of slip from 0.4 and 0.5 mm is presented in Figure 5.26.

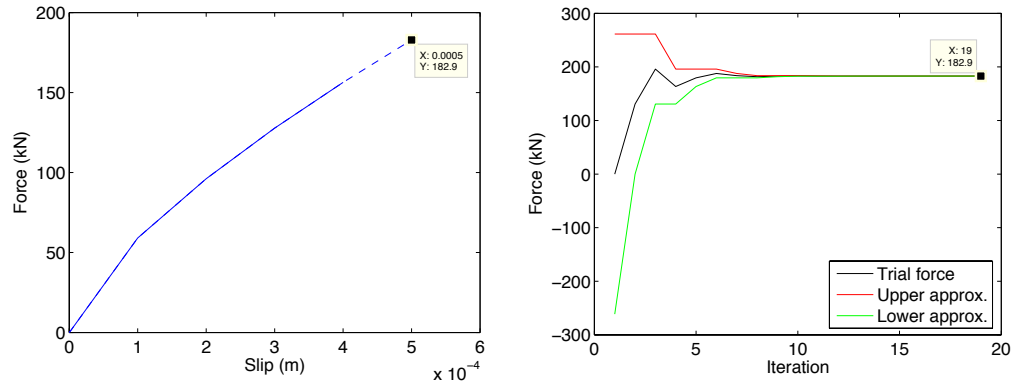

Figure 5.26. Progression of force convergence for increasing number of iterations considering the bisection approach

Based on the evolution of the trial force presented in the right plot of the previous figure, it is apparent that beyond the 10th iteration, the precision of the computed force is only marginally improved. This effect is also evident in Figure 5.27 that depicts the slip and force distributions along the rebar for the first 18 iterations (grey lines) and the converged solution (red line).

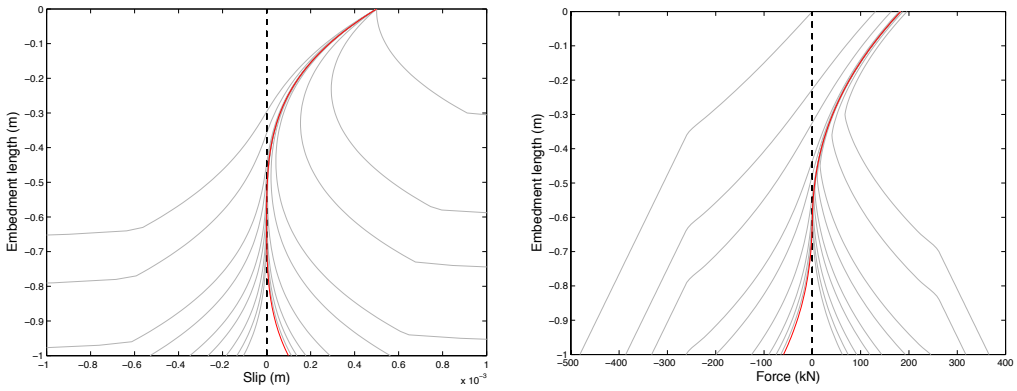

Figure 5.27. Slip and force profiles along the embedment length at each iteration - line in red represents the profiles associated with the converged solution

As expected, the previous plots also show that the force and slip distributions at the converged solution approach zero approximately at the same location. Nonetheless, it is evident that, for both cases, the red curves starts to diverge from zero at deeper regions of the rebar due to tolerance errors beyond the equilibrium IP. This is the reason why once the equilibrium IP is found (IP where both force and slip approach to zero) the force and slip values at deeper regions are set to zero (not depicted in the plots).

Note that the response parameters beyond the IP_{eq} have no contribution to the actual response of the rebar. The correction at these points is required only to guarantee the accuracy at subsequent loading steps where longer development lengths might be required. In such conditions, these points may become active and therefore it is important that they follow the appropriate cyclic rules for both bond and reinforcement constitutive models.

Alternatively, one can decrease the value of the convergence error admitted, enforcing the analysis to approach the anchorage force with higher precision. As illustrated in the following plots (Figure 5.28), it is possible to observe that both slip and force converge to zero even at the IPs located far beyond the development length. Naturally, such optimized solution is determined at the expense of a considerably larger number of iterations (19 and 53, respectively).

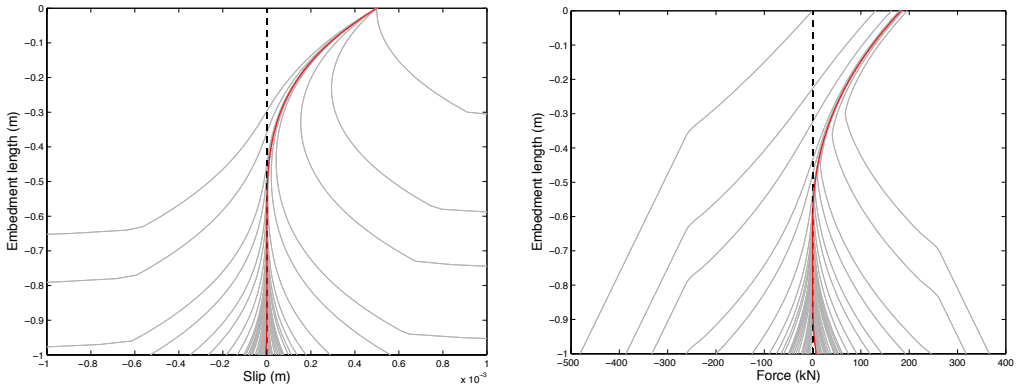

Figure 5.28. Slip and force profiles along the embedment length at each iteration considering a reduce convergence tolerance - line in red represents the profiles associated with the converged solution

Nevertheless, it is important to highlight that, for both cases under comparison, the force determined at the loaded-end - ultimately, the value of interest - remains essentially the same. Considering the degree of precision generally required in earthquake engineering analyses, the variation observed in the results (182.884 kN *vs* 182.883 kN) is negligible. Eventually, the use of larger convergence criteria (e.g., 0.5 kN) may be considered for most common applications, reducing the number of iterations required to about half the value previously considered.

The convergence strategy adopted can be considered reliable because the solution of both equilibrium and compatibility equations along the rebar are convergent regardless of the loading demand and response parameters at each step. In order to illustrate the validity of the method, the rebar used in the previous demonstrative example is now subjected to a

load reversal as illustrated in Figure 5.29. (load reversal with dashed line; the numbers indicate the loading sequence).

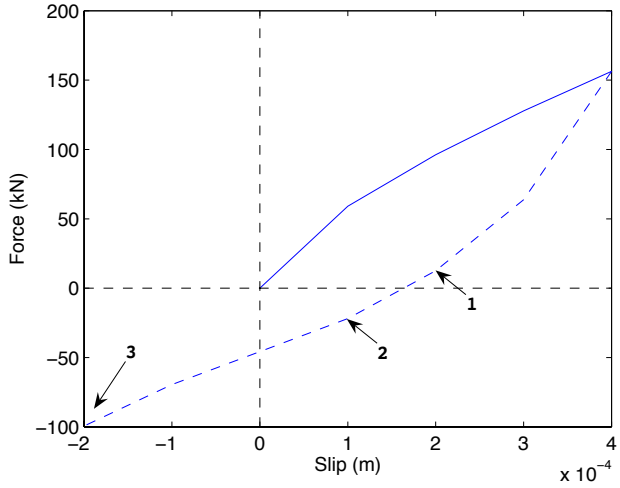

Figure 5.29. Force-slip demand at the loaded-end of the rebar

The response is then analysed for three distinct conditions: (i) both slip and force are positive, (ii) a transition zone where the force is negative but the slip is still positive and (iii) both slip and force are negative. The evolution of the distributions of slip and force along the embedment length of the rebar is presented in Figure 5.30.

i:

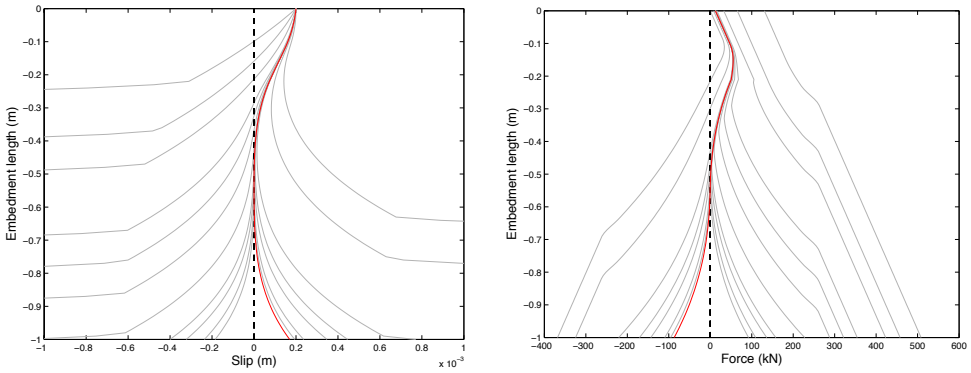

ii:

iii:

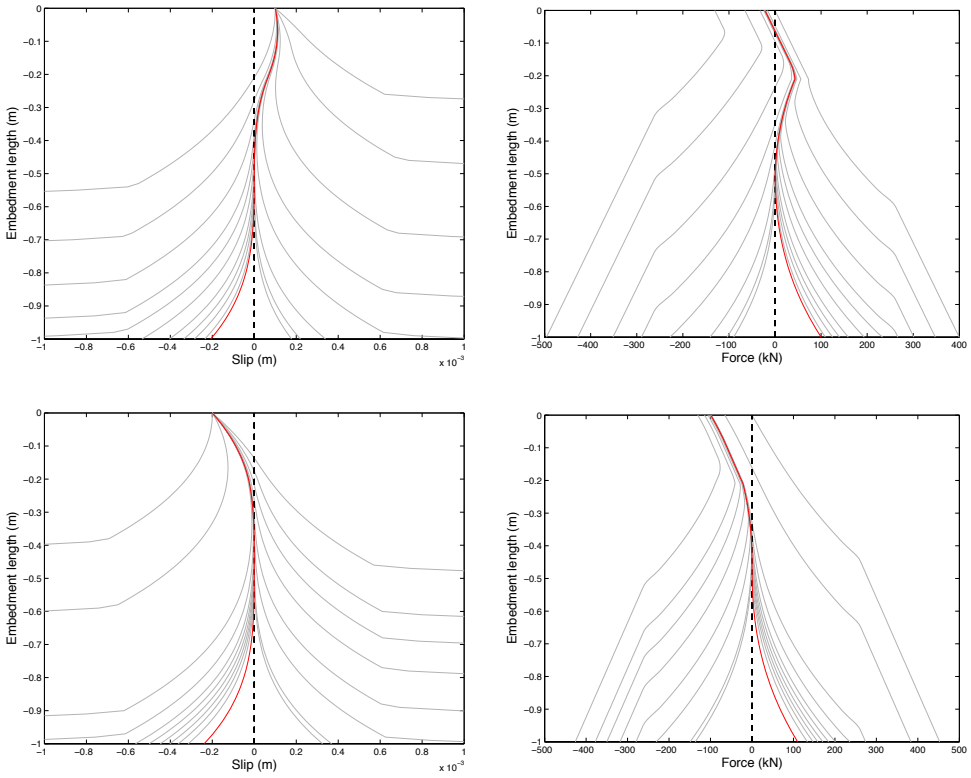

Figure 5.30. Slip and force profiles along the embedment length at each iteration for load reversal (top to bottom) - the line in red represents the profiles associated with the converged solution

5.3.3 Member-End Response due to SP Deformations

The proposed model was designed to behave as a zero-length element to be applied at the extremities of RC fibre-based elements. The previous sections describe the methodologies developed to determine the strain penetration response parameters associated with a single rebar subjected to an imposed slip. In most common structural applications, however, the RC members comprise several rebars per cross-section. Hence, in order to integrate the previous methodology into a general structural analysis package, the contribution of all cross-section fibres (reinforcement and concrete) needs to be integrated at the cross-sectional level in order to reproduce the corresponding sectional deformations. Figure 5.31 illustrates how the proposed model is incorporated into a general purpose RC frame model.

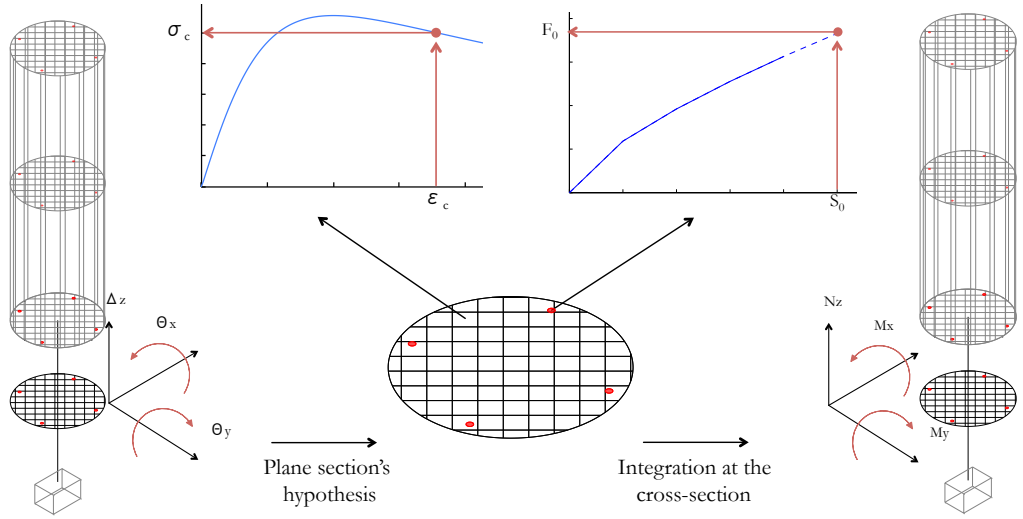

Figure 5.31. Schematic representation of the bond-slip model: determination of sectional forces based on prescribed displacements

If the response of the reinforcing bars (anchorage force and slip) can be used directly to determine the moment-rotation response of the cross-section, the incorporation of the component associated with the concrete fibres is not straightforward. In fact, since concrete constitutive laws are defined in terms of stress-strain response (and not in force-displacement as for the bond-slip model), it is necessary to define an "influence length" associated to all concrete fibres in order to convert the concrete displacements into concrete strains. These strains are then used to determine the concrete stresses using any appropriate concrete constitutive model. The force contribution of each concrete fibre can then be easily determined multiplying the concrete stress by the area of the corresponding fibre.

The definition of the influence length (L_i) is the most subjective parameter in the proposed model. Actually, the definition of a length along which the concrete strains are assumed to be constant may vary depending on the anchorage region that is to be modelled. Taking a foundation region as example, it seems consensual that the compressive forces applied at the base of the column are fully transmitted to the base of the foundation. In such cases, it would be intuitive to assume an L_i equal to the foundation depth. However, given that the foundation area is significantly larger than that of the column's cross-section, the concrete strains and stresses tend to decrease for deeper regions of the foundation, due to a "fan" effect. In such cases, and despite not having a physical meaning, it seems more appropriate to assume a larger value of L_i – eventually twice the foundation depth or even higher in order for the computed stress in

the concrete fibres of the model to be similar to the one existing in reality. On the other hand, in structural joints, the use of the actual height of the joint appears more reasonable. Nonetheless, one should take into account that the compressive struts developed in these regions may present different characteristics depending on the strength/stiffness relation between the different adjacent members.

The issue described above represents a classical localization problem and, as for most of the cases where this numerical problem arises, it is not possible to establish a single solution that is valid for any generic condition. Instead, an adequate engineering judgement is eventually required. Nonetheless, the definition of an influence length that varies between one and twice the depth of the anchorage regions should provide a good estimation for most typical conditions.

Once the fibre forces are determined, the axial force and bending moment associated with the bond-slip cross-section can be easily determined by integrating the contributions from all concrete and reinforcement fibres as defined by the following equations. Note that, in this element, and contrarily to conventional zero-length elements, the axial force and the bending moments in the two directions are coupled.

$$N = \sum_{1}^{m} F_{fibre,m} \tag{5.41}$$

$$M_{y/x} = \sum_{1}^{m} \left(F_{fibre,m} \, d_{x/y} \right) \tag{5.42}$$

In the previous equations, m represents the different fibres of the section and $d_{x/y}$ is the distance of each fibre to the centre of mass of the cross-section along the X- or Y-axis. Note that the forces attributed to the reinforcement fibres correspond to the anchorage force to be determined as described in the previous section. On the other hand, the axial force attributed to the concrete fibres is simply given by:

$$F_{fibre,conc.} = \sigma_c \, A_c \tag{5.43}$$

where A_c is the area of the concrete fibre and σ_c is the concrete stress determined from corresponding concrete constitutive model.

Once, the element generalized forces are computed, the equilibrium between the bond-slip element and the adjacent RC member is verified at the upper (structural) iterative level, as for any other element of the structure. The following Figure 5.32 describes succinctly the main steps considered in the proposed formulation, and how it was integrated in the structural analysis software, *SeismoStruct* [Seismosoft, 2013].

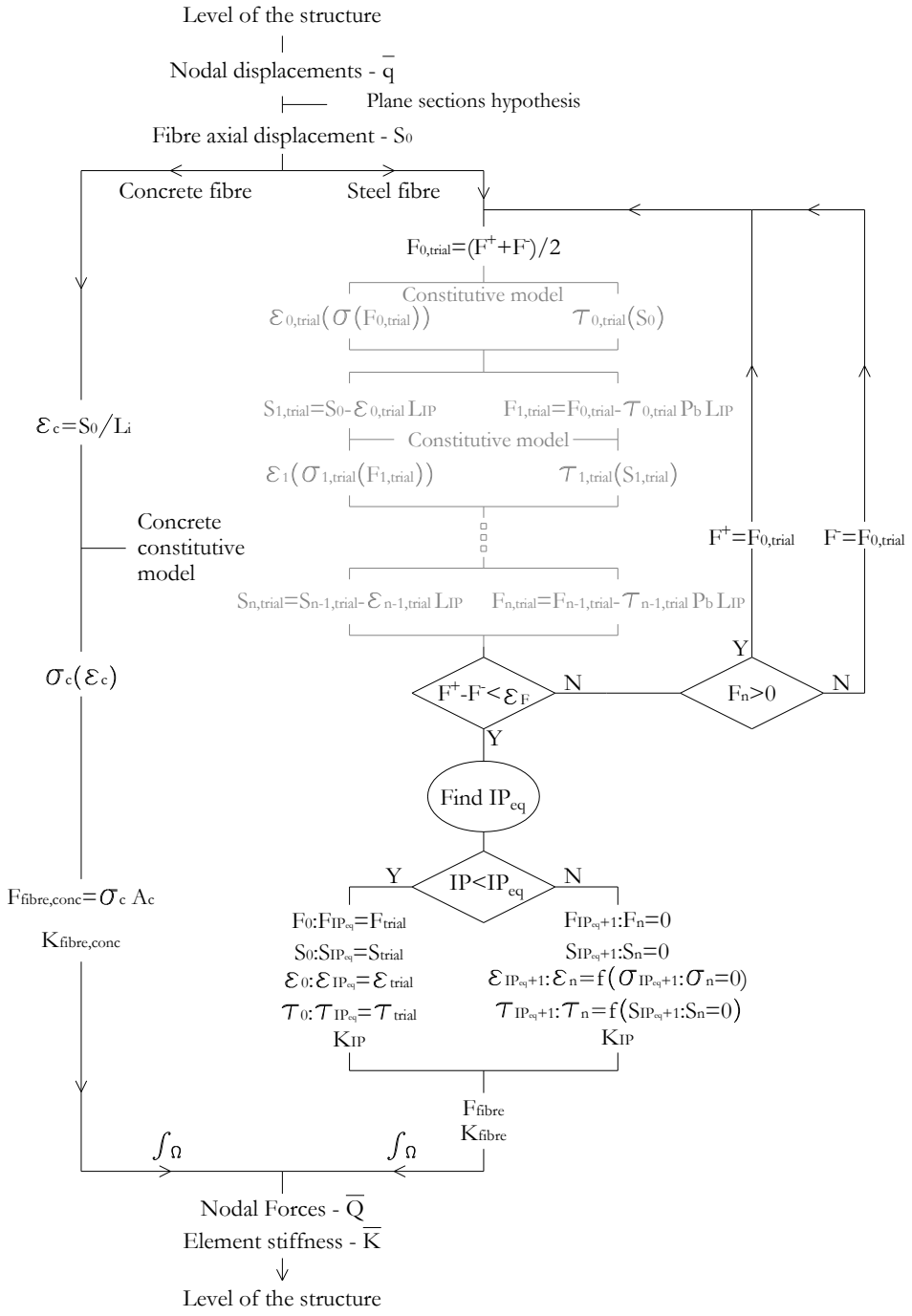

Figure 5.32. Global flowchart of the proposed bond-slip numerical model

As noted before, the iterative procedure adopted does not require the determination of the tangent stiffness. However, in order to implement this procedure in conventional fibre-based structural software, it is necessary to compute the element tangent stiffness in order to build-up the structures' tangent stiffness matrix, required in upper iterative levels. Considering the peculiarities of the proposed model, the procedure to determine the bond-slip tangent stiffness is described in the following sections.

5.3.4 Determination of tangent stiffness

In the following sections, the process adopted to determine the tangent stiffnesses associated to the different levels of the bond-slip formulation is described, starting with the formulation associated with each IP along the embedment length and progressively extended until the element's tangent stiffness.

5.3.4.1 *IP Tangent stiffness*

Similarly to a regular material constitutive model, the tangent stiffness associated to each IP (K_{Tan}^{IP}) can be determined as the first derivative of the bond stress-slip constitutive model. Such derivative will naturally depend on which branch of the model the current loading point is (Figure 5.33).

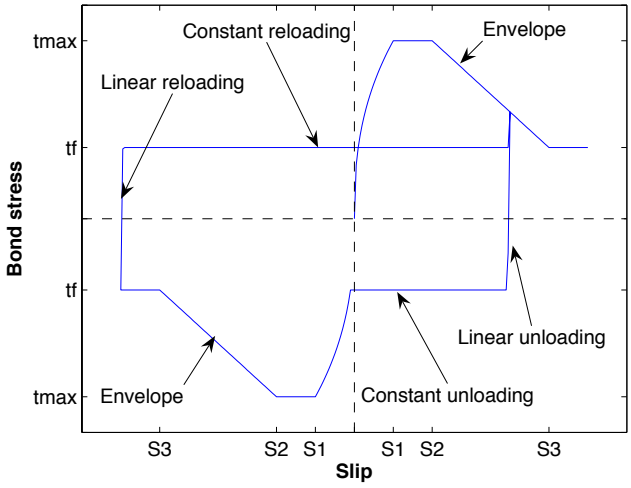

Figure 5.33. Main braches of the cyclic bond-slip model

If the current loading point is on the envelope curve, the tangent stiffness at a given IP can be determined as by the equations below, which depend on the current demand. Note that these equations are nothing more than the derivatives of the expressions that

define the different branches of the bond-slip model adopted and presented in Section 5.2.

- $0 \leq S \leq S_1$:

$$k_{tan}{}^{IP} = \frac{d\tau}{dS} = \frac{d\left[\tau_{max}\left(\frac{S}{S_1}\right)^{\alpha}\,\Omega_y\,\Omega_{cyc.}\,\Omega_{p,tr}\,\Omega_{cr}\right]}{dS} =$$

$$= \alpha\tau_{max}\frac{S^{\alpha-1}}{S_1{}^{\alpha}}\Omega_y\,\Omega_{cyc.}\,\Omega_{p,tr}\,\Omega_{cr} \tag{5.44}$$

- $S_1 \leq S \leq S_2$:

$$k_{tan}{}^{IP} = \frac{d\tau}{dS} = \frac{d\left[\tau_{max}\,\Omega_y\,\Omega_{cyc.}\,\Omega_{p,tr}\,\Omega_{cr}\right]}{dS} = 0 \tag{5.45}$$

- $S_2 \leq S \leq S_3$:

$$k_{tan}{}^{IP} = \frac{d\tau}{dS} = \frac{d\left[\tau_{max} - (\tau_{max} - \tau_f)\times\frac{(S - S_2)}{(S_3 - S_2)}\,\Omega_y\,\Omega_{cyc.}\,\Omega_{p,tr}\,\Omega_{cr}\right]}{dS} =$$

$$= -\frac{(\tau_{max} - \tau_f)}{(S_3 - S_2)}\,\Omega_y\,\Omega_{cyc.}\,\Omega_{p,tr}\,\Omega_{cr} \tag{5.46}$$

- $S > S_3$:

$$k_{tan}{}^{IP} = \frac{d\tau}{dS} = \frac{d\left[\tau_f\,\Omega_y\,\Omega_{cyc.}\,\Omega_{p,tr}\,\Omega_{cr}\right]}{dS} = 0 \tag{5.47}$$

Similarly, the tangent stiffness along the unloading and reloading branches can be determined using the following expressions:

- Linear unload/reload branch (for small load reversals):

$$k_{tan}{}^{IP} = \frac{\tau_{max}\left(\frac{S}{S_1}\right)^{\alpha}}{S} \qquad \text{with } S\text{=0.01mm} \tag{5.48}$$

- Constant stress unload/reload branch (for large load reversals):

$$k_{tan}{}^{IP} = 0 \tag{5.49}$$

5.3.4.2 *Element tangent stiffness*

Considering that the proposed model is based on a zero-length element, the element tangent stiffness corresponds to a sectional stiffness that relates the axial force with the axial displacements and the bending moments with the associated rotations. It should be noted, however, that contrarily to conventional fibre-based elements the response at the sectional level in the bond-slip model is defined in terms of forces and displacements, instead of forces and deformations.

Hence, the sectional stiffness can be computed as the summation of the axial stiffness of all the fibres (concrete and reinforcement/bond-slip), similarly to the procedure used to compute the sectional forces. Thus, the tangent stiffens associated with the axial ($K_{tan,N}$) and the two rotational ($K_{tan,Mx/y}$) degrees of freedom (DOF), can be determined as:

$$K_{tan,N} = \sum_{1}^{m} K_{fibre,m} \tag{5.50}$$

$$K_{tan,Mx/y} = \sum_{1}^{m} \left(K_{fibre,m}\, d_{x/y}{}^{2} \right) \tag{5.51}$$

where m represents the different fibres of the cross-section and $d_{x/y}$ is the distance of each fibre to the centre of mass of the cross-section along the X- or Y-axis. The axial stiffness attributed to the concrete fibres can simply computed as:

$$K_{fibre,conc.} = E_c \frac{A_c}{L_i} \tag{5.52}$$

where A_c is the area of the concrete fibre.

However, given that neither the slip nor the force distribution along the rebar are known at each step of the analysis, the rebar stiffness cannot be determined with convectional methods, as used for the concrete fibres. Instead, the determination of the bond-slip tangent stiffness follows an alternative procedure.

Bearing in mind that the tangent stiffness of the rebar is nothing more than the derivative of the anchorage force with respect to the slip at the loaded-end, one can write that:

$$k_{tan}{}^{bar} = \frac{dF_0}{dS_0} = \int_0^{L_d} \frac{d\tau(S(S_0,z))}{dS_0} P_b \, dz \tag{5.53}$$

where the fraction inside the integral can be expressed by:

$$k_{tan}{}^{bar} = \int_0^{L_d} \frac{d\tau(S)}{dS} \frac{dS(S_0,z)}{dS_0} P_b \, dz \tag{5.54}$$

While the first member of the integral represents the slope of the bond stress-slip constitutive relation, and hence can be easily estimated, the second member reflects the variation in slip along the rebar which is not known *a priori*.

Let us, thus, explore the compatibility equation associated with the procedure described in 5.3.1.2 derived for the determination of the response along the rebar:

$$S(S_0,z) = S_0 - \int_0^{z} \varepsilon\,(S_0,u)\; du \tag{5.55}$$

If both sides of the equation are divided by the derivative of S_0, we obtain the following expression:

$$\frac{dS(S_0,z)}{dS_0} = 1 - \int_0^{z} \frac{d\varepsilon\,(S_0,u)}{dS_0}\; du \tag{5.56}$$

The member inside the integral can then be decomposed in:

$$\frac{d\varepsilon\,(S_0,u)}{dS_0} = \frac{d\varepsilon}{d\sigma}\,\frac{d\sigma}{dF}\,\frac{dF}{dS_0} = \frac{1}{E_s\,A_b}\,\frac{dF(S_0,z)}{dS_0} \tag{5.57}$$

Given that the equilibrium equation is given by:

$$F(S_0, z) = \int_z^{L_d} \tau(S(S_0, u))\, P_b\, du \tag{5.58}$$

the derivative of F in order to S_0 becomes:

$$\frac{dF(S_0, z)}{dS_0} = \int_z^{L_d} \frac{d\tau(S(S_0, z))}{dS_0}\, P_b\, du = \int_z^{L_d} \frac{d\tau(S)}{dS}\, \frac{dS(S_0, z)}{dS_0}\, P_b\, du \tag{5.59}$$

At this stage we can rearrange the equations and write Equation (5.56) as:

$$\frac{dS(S_0, z)}{dS_0} = 1 - \int_0^z \frac{1}{E_s\, A_b} \int_z^{L_d} \frac{d\tau(S)}{dS}\, \frac{dS(S_0, z)}{dS_0}\, P_b\, dv\, du \tag{5.60}$$

Finally, it is possible to write that the equation that defines the tangent stiffness associated to each rebar is given by:

$$k_{tan}{}^{bar} = \int_0^{L_d} \frac{d\tau(S)}{dS}\, \frac{dS(S_0, z)}{dS_0} P_b\, dz =$$

$$= \int_0^{L_d} \frac{d\tau(S)}{dS}\, P_b\, dz - \frac{{P_b}^2}{A_b} \int_0^{L_d} \frac{d\tau(S)}{dS} \left\{ \int_0^z \frac{1}{E_s} \left[\int_u^{L_d} \frac{d\tau(S)}{dS} \frac{dS(S_0, v)}{dS_0} dv \right] du \right\}\, dz \tag{5.61}$$

Once again, part of the equation depends on the derivative of S in order of S_0, which is not known and, according to Equation (5.60), is related to the quantity that is inside the curly brackets:

$$\frac{dS(S_0, v)}{dS_0} = 1 - \int_0^z \frac{d\varepsilon\ (S_0, w)}{dS_0}\, dw$$

where

$$\frac{d\varepsilon\ (S_0, u)}{dS_0} = \frac{1}{E_s}\left[\int_u^{L_d} \frac{d\tau(S)}{dS}\frac{dS(S_0, v)}{dS_0}dv\right]$$

Hence, in order to be consistent with the Forward Euler method adopted in the remaining formulation, $\frac{d\varepsilon\ (S_0,u)}{dS_0}$ will be computed using the values from the previous converged step. At the initial step, this derivative will be taken as zero.

5.4 SUMMARY

This chapter describes the formulation developed for the proposed zero-length bond-slip element. The model makes use of an advance bond-slip constitutive relation, capable of describing the physical phenomena associated with strain penetration effects for a wide variety of anchorage conditions, such as concrete strength, embedment length, rebar surface properties, rebar yielding or cyclic degradation, among others. This represents an important advantage with respect to conventional empirical models, as the analyst can make use of state-of-the-art constitutive models to reflect alternative anchorage conditions.

The anchorage region replicates the cross-section of the adjacent RC member and preserves the plane section's hypothesis. Each of the cross-section's rebars is represented through a number of integration points (IPs) distributed along its anchorage length. Using the Forward Euler method, the response at each IP is determined enforcing both equilibrium and compatibility requirements. Despite requiring small (spatial) step sizes, this option presents some advantages with respect to more conventional approaches, as the response along the embedment region of the rebar can be accurately determined, regardless of the boundary conditions and without the need to define an approximated interpolation function representative of the actual distribution of a given parameter (bond stress, rebar strains or slip).

Finally, the bond-slip response at each cross-section rebar is iterated following the bisection method. The axial force and bending moments in the two orthogonal directions are then determined through the integral of the contribution of the cross-sectional fibres (concrete and reinforcement). The element tangent stiffness is derived directly from the bond stress-slip constitutive relation and is used solely to compute the global tangent stiffness required in iterative procedures at the level of the structure.

6. SENSITIVITY ANALYSIS AND VALIDATION OF THE NEW BOND-SLIP MODEL

After performing the required validation tests, the proposed bond-slip model was implemented in *SeismoStruct* [Seismosoft, 2013], an advanced structural analysis software specialized in nonlinear seismic analysis and featuring distributed plasticity elements with fibre-discretized cross-sections. By integrating the proposed formulation into a robust nonlinear fibre-based software, it was possible to assess in great detail the performance of the new element, as well as to evaluate the contribution of strain penetration effects in the response of different RC structures.

6.1 SENSITIVITY ANALYSIS ON DIFFERENT MODEL PARAMETERS

The purpose of this section is to analyse and quantify how some of the different parameters considered in the proposed model, namely the bond stress-slip constitutive model, as well as the rebar and sectional parameters, influence the response of RC members. This study was carried out on a circular RC column (Test 19) that was experimentally tested in the framework of a study carried out by Goodnight *et al.* [2015b]. The main geometric characteristics, together with the most relevant mechanical and material properties of the tested structure are presented in Figure 6.1 and Table 6.1.

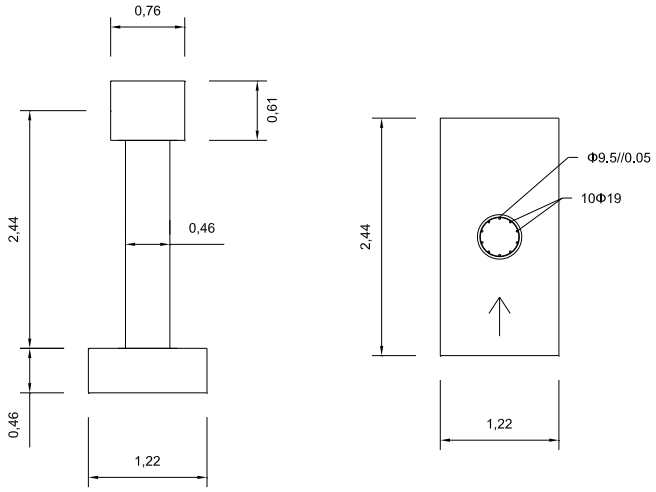

Figure 6.1.Geometric characteristics of the Test 19 specimen (in m)

Table 6.1. Mechanical and material properties of the Test 19 specimen, as well as numerical parameters adopted for the reference model

Anchorage Properties	Test 19
Axial Load (kN) - λ_N	640.5 - 10%
H (m)	2.44
D (m)	0.457
Long. reinf. (ρ_l)	10ϕ19 mm (1.7%)
Trans. reinf. (ρ_v)	ϕ9.5 mm//0.05 m (1.3%)
d_b (m)	0.0189
L_e (m)	1.0 *
f_c (MPa)	43.7
f_y (MPa)	470
f_u (MPa)	637
E_s (GPa)	188
$E_{s,p}$ (GPa)	≈1.4
C_{clear} (m)	-
Bond-Slip Parameters	
S_1 (m)	0.001
S_2 (m)	0.002
S_3 (m)	0.01
τ_{max} (MPa)	$2.5\sqrt{f_c}$
τ_f (MPa)	$0.4\,\tau_{max}$

λ_N - Axial load ratio
ρ_l - Longitudinal reinforcement ratio
ρ_v - Volumetric ratio of transverse reinforcement
* Approximate value based on available detailing information

In the original test protocol, the structure was subjected to a symmetric three-cycle-set load history at the column top. In the present parametric study, however, only one cycle per amplitude was considered (Figure 6.2).

The experimental response under the complete loading set is presented in Section 6.2.2, were the numerical results obtained with the present model are validated against the test results.

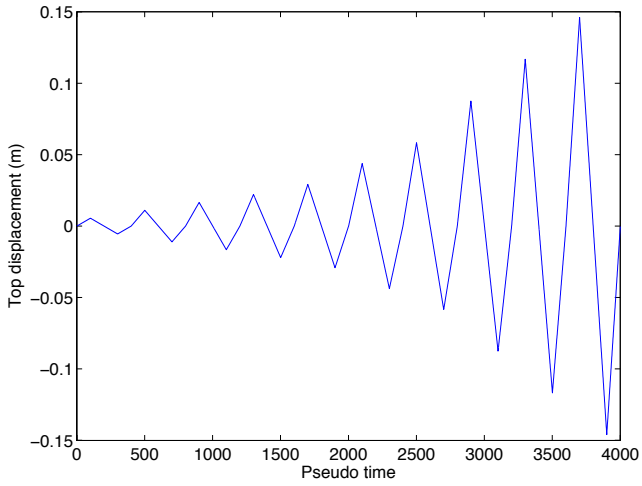

Figure 6.2. History of lateral displacements imposed at the top of the RC column for the numerical simulation

The test sequence comprises 10 cycles of increasing amplitude. The first 4 cycles occur essentially under elastic conditions: ¼ Fy', ½ Fy', ¾ Fy', and Fy', where Fy' represents the analytically predicted force corresponding to the occurrence of the first yielding. After this initial phase, 6 additional cycles are applied at the top of the column, corresponding to multiples of equivalent displacement ductility: 1, 1.5, 2, 3, 4 and 5.

Starting with a set of pre-established parameters, which are taken as the reference set, the response of the column is analysed considering independent variations in the parameters summarised in Table 6.2:

Table 6.2. Parameters and properties considered in the sensitivity analysis

Sensitivity parameters	Properties
Characteristic slip limits	**$S_1 = 1$, $S_2 = 2$, $S_3 = 5$ (mm)**
	$S_1 = 0.5$, $S_2 = 1$, $S_3 = 2.5$ (mm)
	$S_1 = 2$, $S_2 = 4$, $S_3 = 10$ (mm)
Transverse load	**$P_{tr} = 0$**
	$P_{tr} = f_{cm}$
Longitudinal cracking	**$w_{cr} = 0$ mm**
	$w_{cr} = 0.42$ mm
Cyclic degradation	**W/ cyclic degradation**
	W/out cyclic degradation
Rebar surface	**Deformed rebars**
	Plain rebars (W/ cyclic degradation)
	Plain rebars (W/out cyclic degradation)
Embedment length	**$L_e = 1.0$ m**
	$L_e = 0.33$ m
	$L_e = 0.20$ m
Influence length	**$L_i = 0.46$ m**
	$L_i = 0.23$ m
	$L_i = 0.92$ m

In bold: values adopted for the reference model

Following the order established in the previous table for the variation of the parameters, the upcoming sections present the results obtained for the different set of properties. In order to have a visual identification of the effect of each parameter, the results obtained with the reference model are plotted (in black) together with the response for the different parameters considered. For all cases, the response of the bond-slip element is presented through conventional moment-rotation relations, together with the maximum rotations computed at each ductility level. In addition, the anchorage force-slip and the bond stress-slip response at the loaded-end of the most stressed rebar of the cross-section is also evaluated.

6.1.1 Slip limits

As described in Section 5.2, the envelope of the bond stress-slip constitutive law may vary significantly depending on the properties of the anchorage regions. According to the rules proposed by Model Code 2010 [fib, 2011], both bond stress and slip depend on the bond conditions, confinement level and rebar surface conditions. A change by a factor of two with respect to the reference values for the slip limits was adopted for exploring the potential variations in the response of the anchorage system.

The results plotted in Figure 6.3 indicate that the use of different slip limits, despite the significant variation in their magnitude, has only a marginal effect on the cross-sectional response. If, in one hand, the use of larger slip values results in a wider region where the bond stress is larger, on the other, the initial slope (stiffness) of the bond stress-slip relation becomes softer, and vice-versa when lower slip limits are adopted. This effect can be appreciated in the right plot were the use of lower slip limits results in smaller anchorage rotations at the initial load stages. For higher ductility levels, however, this effect is inverted and the drop in bond stress at relatively low slip values is reflected in increased base rotations.

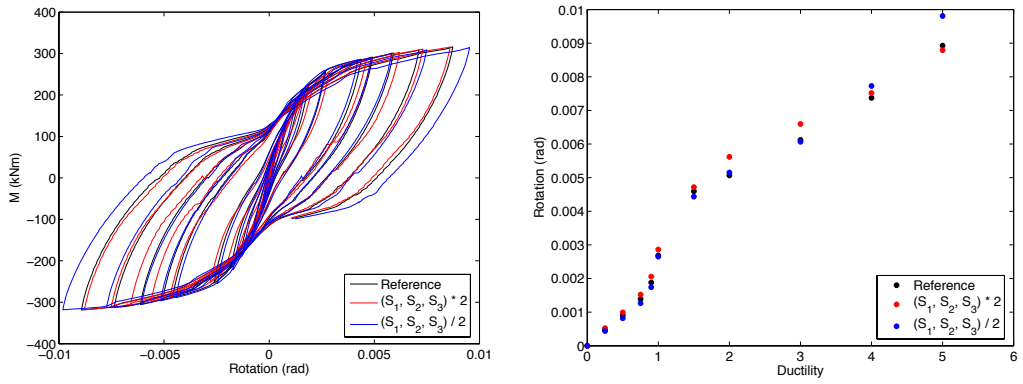

Figure 6.3. Moment-rotation hysteretic behaviour (left) and evolution of maximum rotation for increased ductility demand (right) considering different slip limits

The results shown in Figure 6.4 reflect in more detail the behaviour previously described, in particular the plot representing the bond stress-slip response. Focusing the attention on the bond stress-slip model with half the slip values (plot in blue), it is clear that the bond stresses are larger for lower slip limits, whilst they become lower for larger slip limits. Moreover, one can also notice that the bond stresses in compression tend to exhibit significantly lower values than for the other two cases. This is essentially due to cyclic degradation effects. Given that the ratio between the area of cyclic loading and the monotonic envelope tends to be larger for lower slip limits than for the other two cases

(see Section 5.2.4.2 for additional details), the bond degradation tends to be more pronounced.

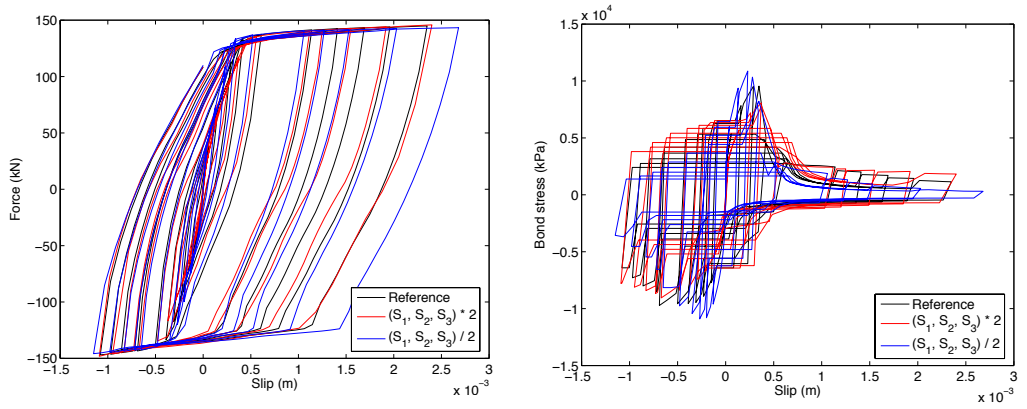

Figure 6.4. Force-slip (left) and bond stress-slip (right) hysteretic behaviour at the loaded-end of the extreme rebar considering different slip limits

In this section, it was thus possible to analyse how the variation of the slip limits established for the bond stress-slip constitutive model, i.e., the definition of a stiffer or softer relation (recall that the maximum bond stress was kept unchanged), affects the different structural response parameters. In summary, it was possible to verify that the variation of S_1 has a marginal effect in the computed SP rotations. Despite the noticeable increase in bond stress at low slip demand at these stages, when the slip limits are reduced, the rotations are low and, thus, the variations have a minor impact at the sectional level response. Nonetheless, reductions in S_2 and/or S_3 result in important reductions of bond stresses at larger slip demand, which turns out to also be reflected in a significant increase in SP rotations for increased ductility levels.

6.1.2 Transverse pressure and longitudinal cracking

The presence of transverse compressive loads at the anchorage region produces a beneficial effect in the anchorage strength of the rebars. On the other hand, when subjected to tensile stresses, with potential development of longitudinal cracks, the bond strength is naturally reduced. The results presented in the following figures provide indications on how the increase or reduction in transverse pressure modifies the response of the anchorage zones. Figure 6.5 and Figure 6.6 present the different responses computed with a compressive stress that equals the mean concrete compressive strength, in comparison with the case where there is no transverse pressure. According to the rules adopted for the bond constitutive model (see Section 5.2.4.1), such compressive pressure increases the bond stresses to nearly twice the ones from the reference model.

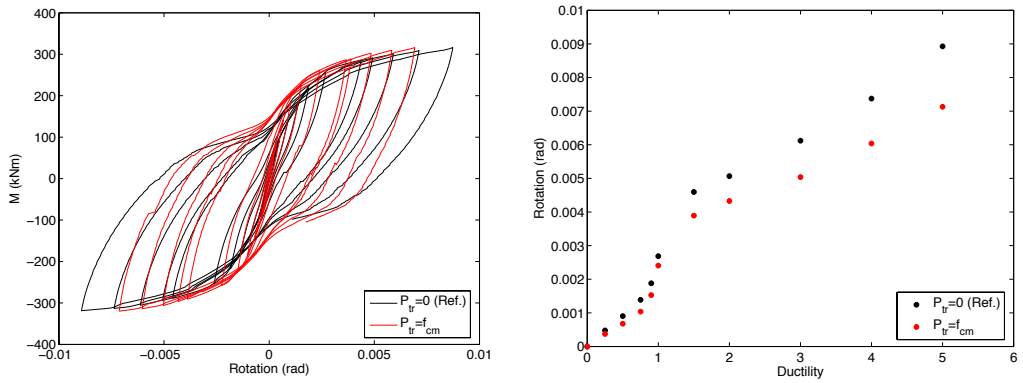

Figure 6.5. Moment-rotation hysteretic behaviour (left) and evolution of maximum rotation for increased ductility demand (right) considering the presence of compressive transverse pressure

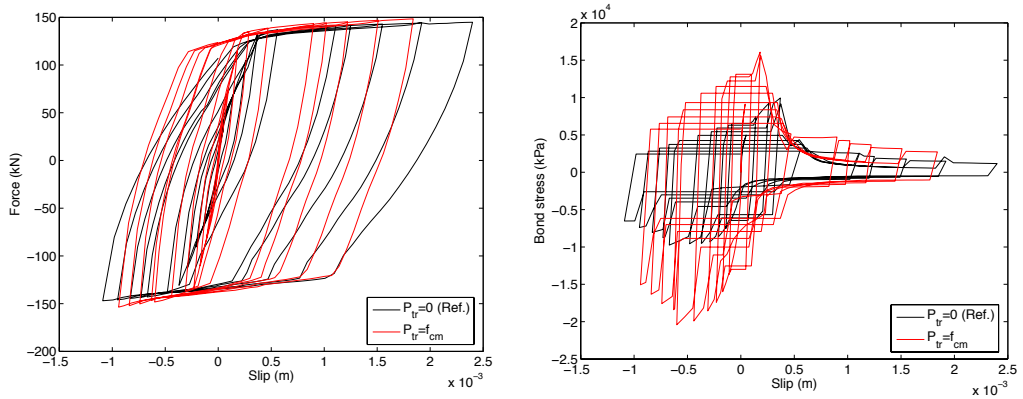

Figure 6.6. Force-slip (left) and bond stress-slip (right) hysteretic behaviour at the loaded-end of the extreme rebar considering the presence of compressive transverse pressure

As expected, the uniform increase in bond stresses results in an important stiffening of the structure's response. This effect is significant at all loading stages. In addition, it is possible to observe a reduction in the pinching effect, especially at the force-slip response of the extreme rebar, indicating a relatively larger ability to sustain reversed loads. This result occurs due to larger bond stresses being reached when the slip approaches zero (Figure 6.6, right), both in the unloading and reloading branches.

Regarding the presence of longitudinal cracks in the anchorage region, the effect is precisely the opposite, i.e., a uniform reduction in the bond stress-slip envelope curve. The results presented in Figure 6.7 and Figure 6.8 were obtained considering a crack width of 0.42 mm. This value was selected in order to produce a bond reduction to about

half the bond strength in the reference model (see Section 5.2.4.1), so that this effect could be adequately compared with the previous case.

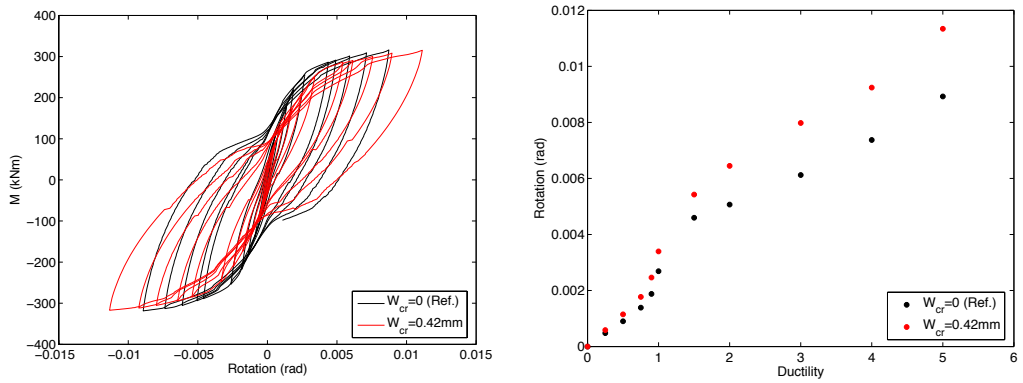

Figure 6.7. Moment-rotation hysteretic behaviour (left) and evolution of maximum rotation for increased ductility demand (right) considering the presence of longitudinal cracks

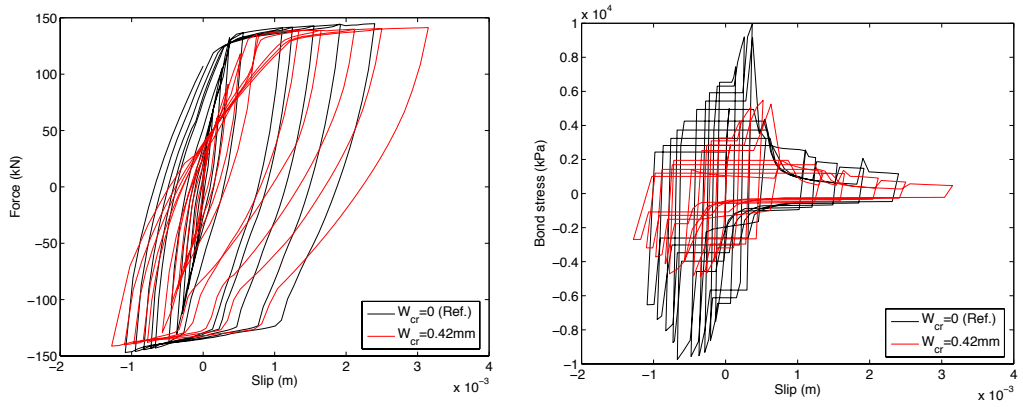

Figure 6.8. Force-slip (left) and bond stress-slip (right) hysteretic behaviour at the loaded-end of the extreme rebar considering the presence of longitudinal cracks

The results presented in the figures above show that the presence of a longitudinal crack results in a significant reduction of the anchorage strength. Contrarily to what was observed in the presence of compressive transverse pressure, in this case the SP rotations increase significantly and in a relatively uniform way throughout the different ductility levels.

Overall, it was observed that the variation in bond strength introduces important variations in the computed response parameters. Naturally, the lower is the bond

strength, more flexible become the SP behaviour. Finally, one should take into consideration that the embedment length provided in this case is significantly larger than the one theoretically required. In case the embedment length was shorter, this reduction in bond strength could result in an abrupt loss of bond properties, as demonstrated in subsequent sections.

6.1.3 Rebar yielding and cyclic degradation

In modern seismic design, namely based on performance and on capacity design principles, it is expected that, under severe seismic loading, some elements will undergo inelastic deformations. Under such circumstances, the reinforcement may experience large nonlinear strains. As described in Section 4.3.4, the effect of rebar yielding in anchorage systems does not gather a generalized consensus. However, the arguments that support the reduction in bond stresses due to rebar yielding - shrinkage of yielded rebars in tension due to Poisson's and necking effects - and the experimental evidence appears to be more convincing.

The results presented in Figure 6.9 reflect a substantial reduction in the computed rotations when the effect of bond stress reduction due to rebar yielding is neglected. The plot on the right hand side illustrates clearly a reduction in base rotation for ductility levels higher than one. As expected, for ductility levels lower than one, no variations are observed given that the reinforcement is still in the elastic range.

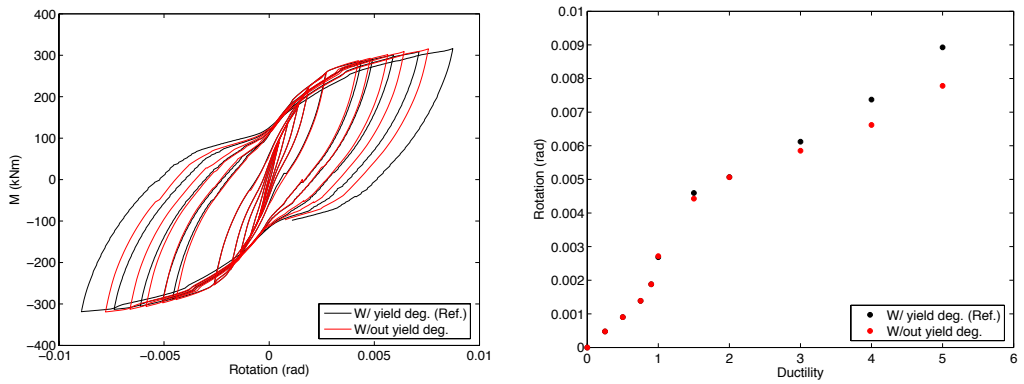

Figure 6.9. Moment-rotation hysteretic behaviour (left) and evolution of maximum rotation for increased ductility demand (right) considering bond stress degradation due to rebar yielding

Focusing the attention on the response of one extreme rebar of the cross-section (Figure 6.10), this effect is particularly evident in the bond-slip response at the loaded-end of the rebar. For slip values higher than 0.5 mm, the bond stresses computed without the

yielding effect reach values much higher than when these effects are accounted for. It should be noted that the results presented represent the response of the most stressed rebar of the cross-section. In the rebars closer to the geometric centre, this effect is necessarily less pronounced and, hence, the global response at the element level is somehow more balanced.

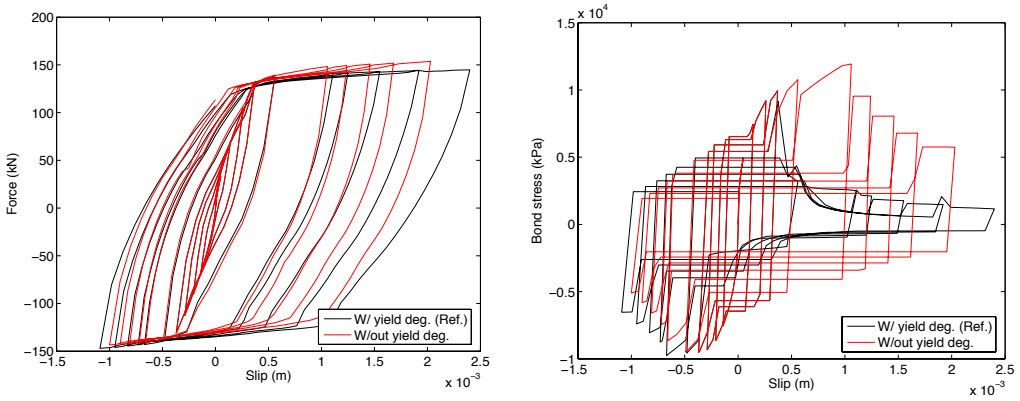

Figure 6.10. Force-slip (left) and bond stress-slip (right) hysteretic behaviour at the loaded-end of the extreme rebar considering, or not, bond stress degradation due to rebar yielding

In addition to potential rebar yielding, under seismic loading, the structural elements are subjected to a large number of load reversals inducing damage in the RC members. Once the adhesion and friction forces are lost, the anchorage strength is essentially developed through bearing action between the ribs and the surrounding concrete. This latter effect produces cracks in the concrete, degrading the bond strength with the increase in amplitude and number of cycles.

When comparing the results presented in Figure 6.9 with the ones representing the effect of cyclic degradation in Figure 6.11, it is clear that the latter has a lower impact in the global sectional response of the element. In the right plot of Figure 6.11 it is possible to verify that the rotations remain essentially unchanged up to a ductility level of 5.

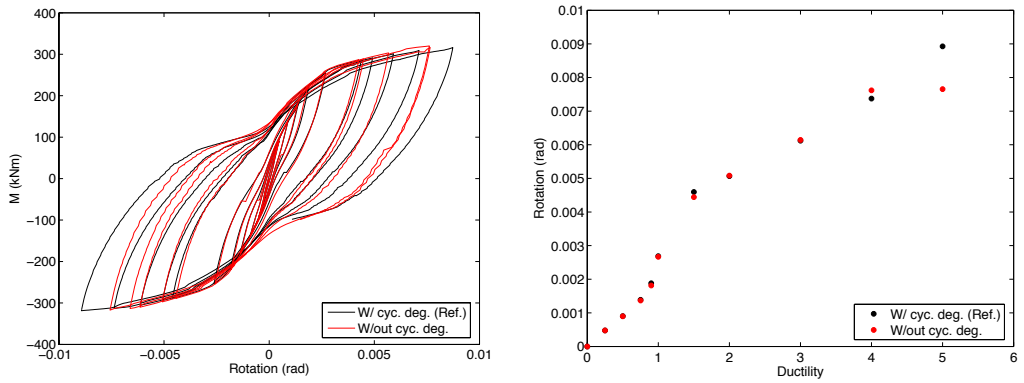

Figure 6.11. Moment-rotation hysteretic behaviour (left) and evolution of maximum rotation for increased ductility demand (right) considering, or not, bond stress degradation due to cyclic loading

As illustrated in Figure 6.12, under tensile load, the bond stresses for both cases do not exhibit significant variations, which indicates that the cyclic degradation parameter has a less pronounced effect on the bond stress than the yielding parameter. Nonetheless, under compression load, the bond stress is significantly reduced. This reduction is naturally translated in increased slip of the rebars, especially for larger ductility levels (left plot). As for the previous parameter, this effect has a larger impact on the extreme fibres of the cross-section, where the rebars are subjected to larger loading demand.

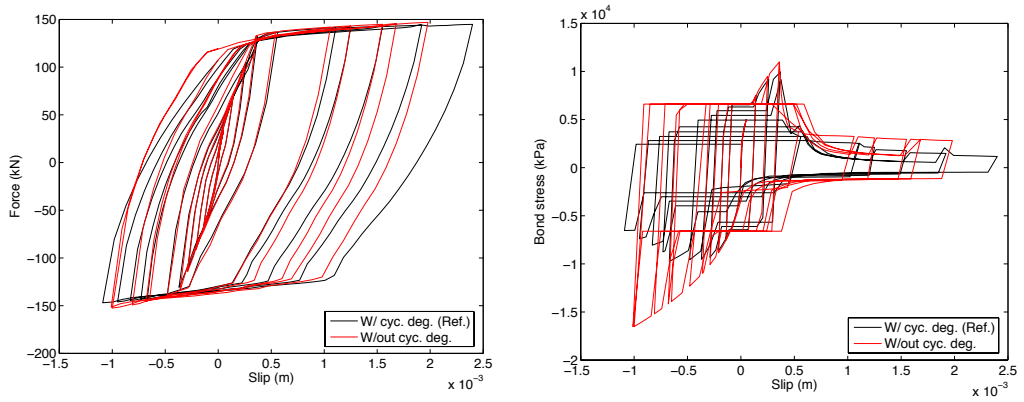

Figure 6.12. Force-slip (left) and bond stress-slip (right) hysteretic behaviour at the loaded-end of the extreme rebar considering bond stress degradation due to cyclic loading

The analyses performed previously, considering the effects of yielding and cyclic degradation independently, indicate that the former has a more pronounced effect in the global response of the elements. In addition, when compared with the cyclic degradation

one (see Sec 5.2.4), it is important to note that it turns out to be indirectly dependent on the yielding degradation. Given that the cyclic degradation is a function of the hysteretic area of the bond-slip model, whenever the rebar strains are beyond the yielding limit, the bond stresses are significantly reduced and, therefore, so is the hysteretic area.

For a clearer interpretation of the impact of both mechanisms, the plots presented in Figure 6.13 and Figure 6.14 compare the response for the cases where both mechanisms are active and inactive.

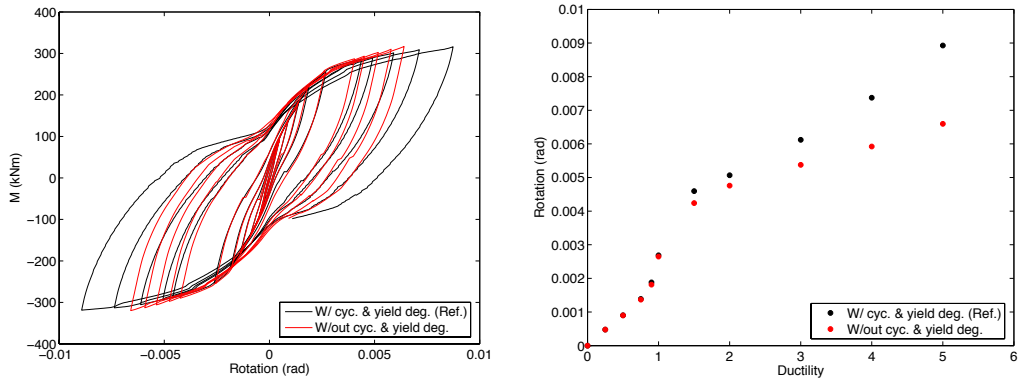

Figure 6.13. Moment-rotation hysteretic behaviour (left) and evolution of maximum rotation for increased ductility demand (right) considering bond degradation due to rebar yielding and cyclic loading

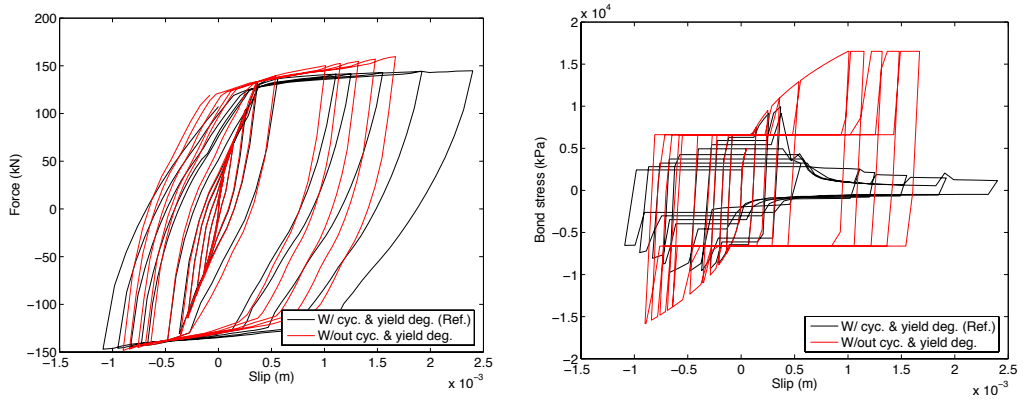

Figure 6.14. Force-slip (left) and bond stress-slip (right) hysteretic behaviour at the loaded-end of the extreme rebar considering bond degradation due to rebar yielding and cyclic loading

The results presented above show that the consideration of both bond reduction mechanisms result in important variations at both local (rebar) and global (section) levels, especially for increased levels of ductility. This evidence becomes even more relevant considering that most of the SP numerical models available for fibre-based RC frame software packages do not offer the ability to explicitly account for these mechanisms.

6.1.4 Rebar surface properties

The contribution of SP deformations to the global behaviour of structures assumes a special importance when dealing with plain rebars, which are often present in old RC structures. Given the absence of ribs at their surface, these rebars cannot sustain large anchorage forces and are, thus, more prone to exhibit larger SP deformations. In the proposed numerical model such effect can be taken into account through the definition of different (lower) slip and bond stress limits in the bond-slip constitutive model.

The results presented hereafter were obtained considering the values recommended for cold-formed plain rebars (see Section 5.2.2). Considering the absence of ribs in the rebars, it is expected that most of the bond force results from adhesion and friction between the reinforcement and the surrounding concrete. Consequently, it is not expected that the anchorage system exhibits meaningful bond degradation due to cyclic loading; at least not at the same degree as observed for deformed rebars.

Taking into account the open questions associated with the previous issue, and given the absence (up to the author's knowledge) of clear indications in the literature, the analysis were performed for the cases where: (i) the cyclic degradation is accounted for and (ii) other where this effect is neglected. It is probable that the solution that best represents the actual behaviour lies somewhere between these two extreme conditions. Figure 6.15 and Figure 6.16 show the results obtained for deformed and plain rebars, neglecting the bond degradation due to cyclic loading.

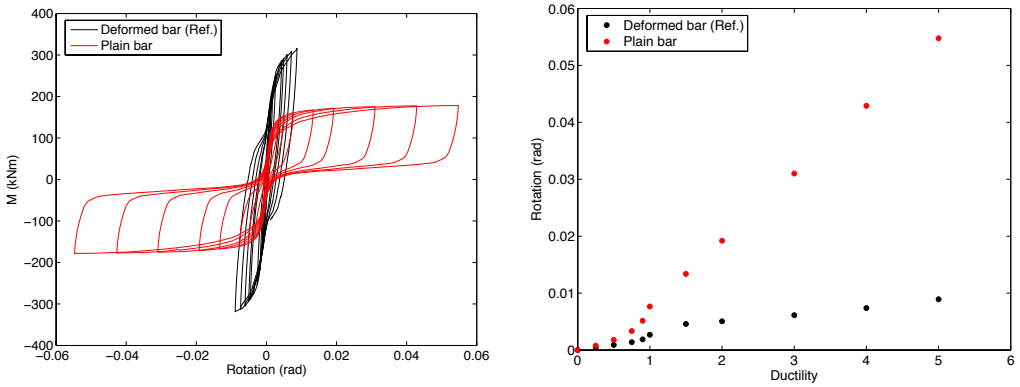

Figure 6.15. Moment-rotation hysteretic behaviour (left) and evolution of maximum rotation for increased ductility demand (right) considering deformed and plain rebars, without cyclic degradation

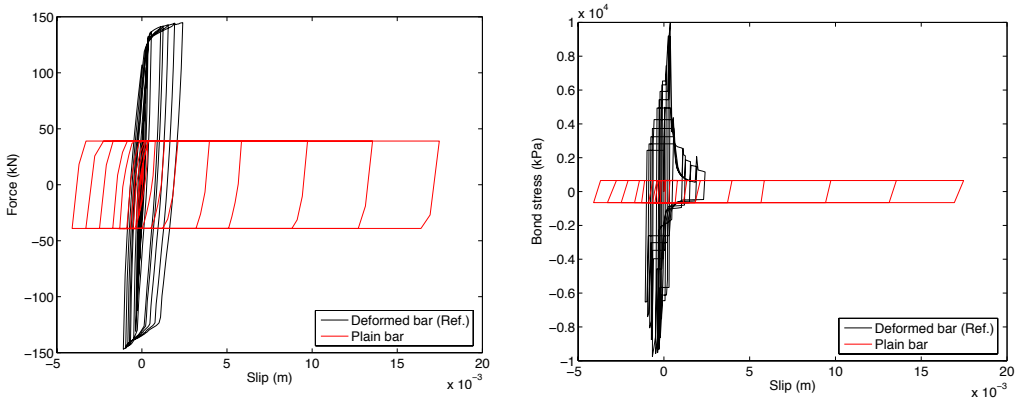

Figure 6.16. Force-slip (left) and bond stress-slip (right) hysteretic behaviour at the loaded-end of the extreme rebar considering deformed and plain rebars, without cyclic degradation

The results obtained with plain rebars at the different structural levels reflect a notorious reduction in the anchorage strength at the same time that the deformations increase significantly. It is important to note that while the end-rotations reach alarming values, the reinforcement is only capable of developing about one-third of its maximum capacity.

Figure 6.17 and Figure 6.18 present the results for the same structural properties but taking into account the cyclic degradation effects. As expected, in this case, the adverse effects of using plain rebars become even more evident. For instance, the bending moment capacity is reduced to almost half the value presented above. Moreover, at large ductility demands, the extreme rebar looses completely its load carrying capacity. For this

reason, the pinching effect already observed in previous cases becomes even more pronounced in this case.

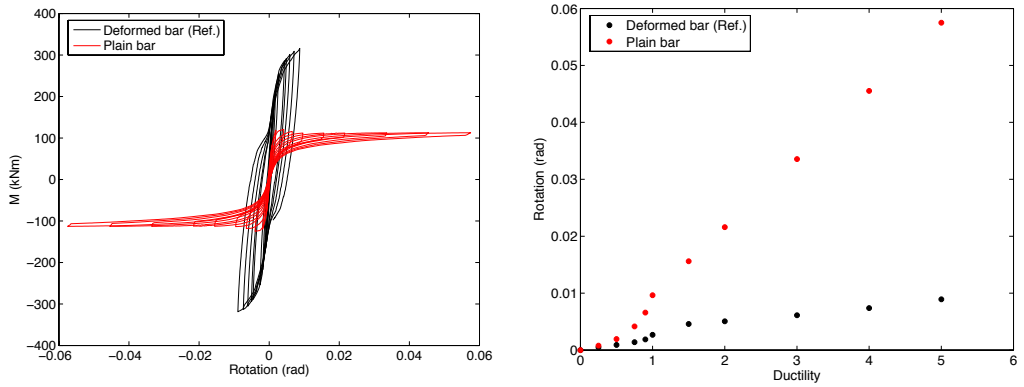

Figure 6.17. Moment-rotation hysteretic behaviour (left) and evolution of maximum rotation for increased ductility demand (right) considering deformed and plain rebars, with cyclic degradation

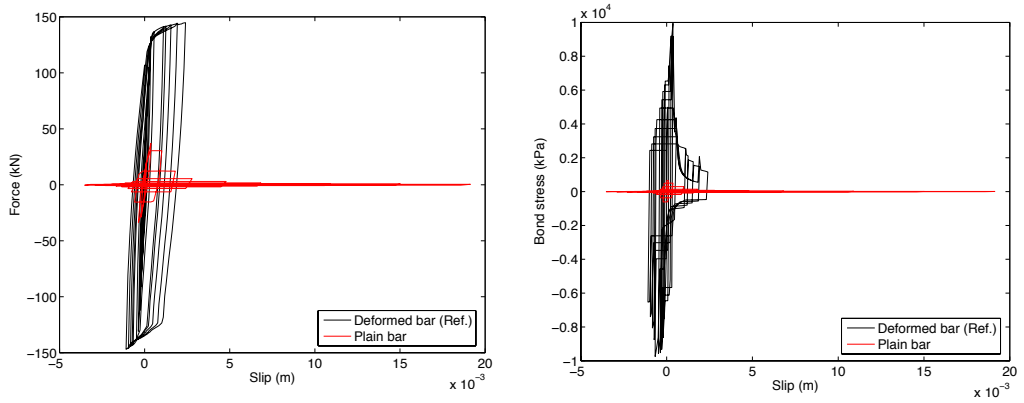

Figure 6.18. Force-slip (left) and bond stress-slip (right) hysteretic behaviour at the loaded-end of the extreme rebar considering deformed and plain rebars, with cyclic degradation

The analysis presented in this section exposes the well-known vulnerabilities associated with the presence of plain rebars in RC members. Most importantly, and despite the possible scatter in the bond-slip model assumed, the results presented demonstrate the ability of the current numerical tool to be easily adjusted to different anchorage conditions.

6.1.5 Embedment length

If a sufficiently large embedment length is provided, the reduction in bond strength in the vicinity of the loaded-end (e.g., due to large slip demand, cyclic degradation or rebar yielding) can be compensated by the transfer of bond stresses to deeper regions. This phenomenon allows the rebar to support increasing forces until, eventually, it reaches its maximum capacity. Naturally, the consideration of embedment lengths longer than the required ones will not translate into increased anchorage capacity; beyond the point where the rebar force is reduced to zero, the region is inactive and, hence, does not contribute with any additional resistance. Given that for the structure under analysis the embedment length provided is almost twice the required one, it is necessary to reduce this value to values lower than 0.5 m in order to evaluate the effects of considering an insufficient embedment length. In this case, the analyses were performed for L_e = 0.33 m and L_e = 0.20 m. The response associated with the cross-sectional behaviour is presented in Figure 6.19.

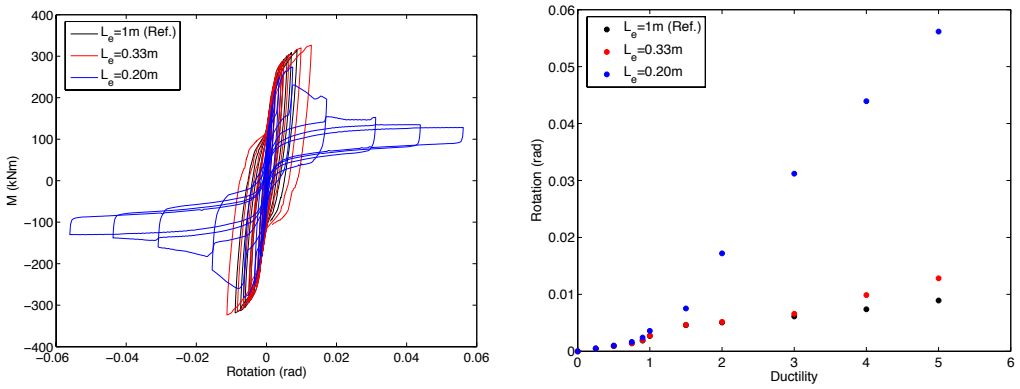

Figure 6.19. Moment-rotation hysteretic behaviour (left) and evolution of maximum rotation for increased ductility demand (right) considering different embedment lengths

As expected, the results show a reduction of the anchorage capacity as the embedment length decreases to values lower than the ones required to transmit the full rebar yield force. Yet, if the reduction is relatively small (L_e = 0.33 m, in this case), the resulting increase in SP rotations becomes apparent only at relatively high ductility levels. On the other hand, if the embedment length provided is very short (L_e = 0.20 m), the cross-sectional rotations start to diverge with respect to the reference model at very early stages, growing rapidly with the increase in ductility demand.

When the development length equals the embedment length, the deformations propagate up to the free-end of the anchorage region, leading to an overall slip of the rebar. Moreover, due to cyclic degradation effects, the bond strength decreases further and eventually becomes insufficient to support the load demand (Figure 6.20).

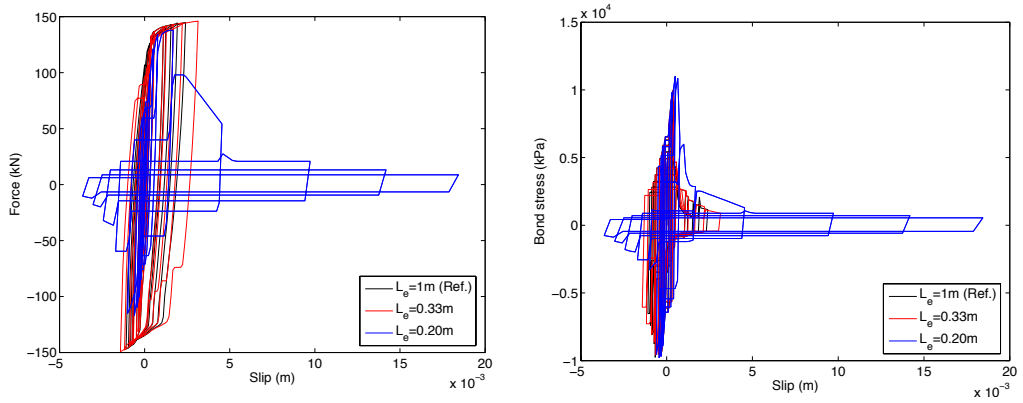

Figure 6.20. Force-slip (left) and bond stress-slip (right) hysteretic behaviour at the loaded-end of the extreme rebar considering different embedment lengths

The previous results reveal a significant degradation of the anchorage resisting mechanism with a decrease of the embedment length. Naturally, the consideration of L_e=0.20m is somehow unrealistic considering the properties of the cross-section under analysis. Nonetheless, the results point out for a negative effect even when a more reasonable length is considered, which may become relevant for structures designed without seismic provisions, where the anchorage lengths provided are typically not long enough.

6.1.6 Influence length

Until this point, the parameters analysed were representing objective structural properties that, with a certain level of confidence, may be replicated numerically. However, as described in Section 5.3.3, the selection of an appropriate influence length may not be a straightforward task and eventually requires some engineering judgment. The present section thus intends to evaluate how the strain penetration effects evolve with the assignment of different influence lengths, L_i. In this case, in addition to the reference value (L_i = 0.46 m), two additional values, corresponding to half and twice the foundation height (L_i = 0.23 m and L_i = 0.92 m, respectively), were considered. The responses computed at both cross-sectional and rebar levels are presented in Figure 6.21 and in Figure 6.22.

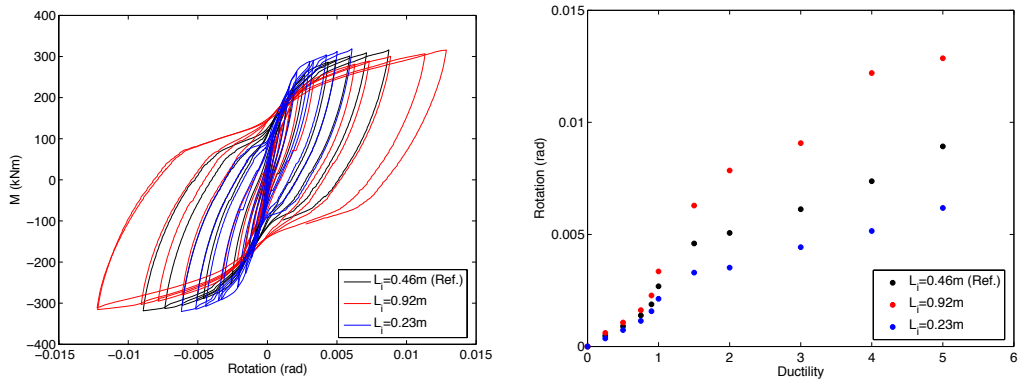

Figure 6.21. Moment-rotation hysteretic behaviour (left) and evolution of maximum rotation for increased ductility demand (right) considering different influence lengths

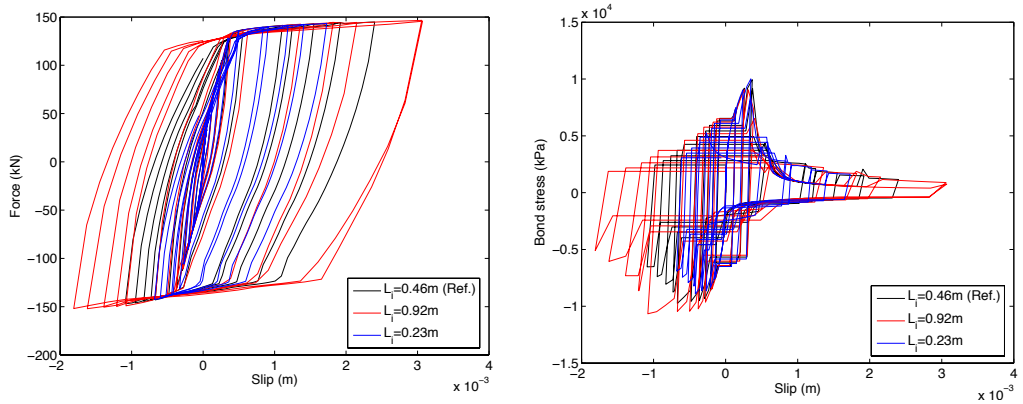

Figure 6.22. Force-slip (left) and bond stress-slip (right) hysteretic behaviour at the loaded-end of the extreme rebar considering different influence lengths

The results presented above show that the definition of different values of L_i introduces important variations in the computed SP rotations. Moreover, it is clear that the computed rotations are correlated with the influence length, i.e., longer values of L_i result in larger rotations and vice-versa. As the influence length increases, the concrete strains in compression decrease, thus resulting in lower stress values. Therefore, in order to find equilibrium at the cross-sectional level, the cross-sectional rotations will tend to increase. On the other hand, this will cause the moment-rotation envelope to become visibly softer (Figure 6.21, left).

Unfortunately, the results confirm the importance of the influence length in the computed rotations, especially considering the inherent subjectivity associated with the choice of this parameter. The effects of the influence length definition are further explored in Section 6.2.2, by confronting the numerical response obtained with different L_i against experimental results.

6.2 COMPARISON WITH EXPERIMENTAL TESTS

In this section, the accuracy of the new bond-slip model is assessed through the comparison of several experimental tests performed in the past against the corresponding numerical results. The selected tests feature different setups in terms of specimen properties and loading protocols, thus allowing a consistent evaluation of the different features of the proposed model. The subsequent sections present the different cases, starting from the simplest one, corresponding to a local behaviour, to more complex ones, representing global structural response.

It is important to point out that standard values were assumed for the bond-slip model in most of the applications, and that no special effort was made to match the numerical values with the experimental ones. Small variations were, however, considered whenever there was a clear evidence that these values are not representative of the experimental observation.

6.2.1 Validation at rebar level

As described earlier, the presented numerical model computes the axial load – slip response at the loaded-end of an anchored rebar through the computation of different response parameters along the embedment length of the rebar. Hence, the evaluation of the accuracy of these parameters is fundamental, as they will necessarily guarantee the accuracy of the global response of an anchored rebar.

The studies performed by Shima *et al.* [1987b] and Bigaj [1995] provide detailed information regarding the evolution of different response parameters along the development length. In addition, the selected tests consider specimens with sufficiently long anchorage length, allowing the rebar to yield when subjected to large axial loads. Despite considering identical test setups (Figure 6.23), the five test specimens selected feature different anchorage properties - the cases selected for validation purposes comprise the use of different steel and concrete strengths, as well as rebar diameter.

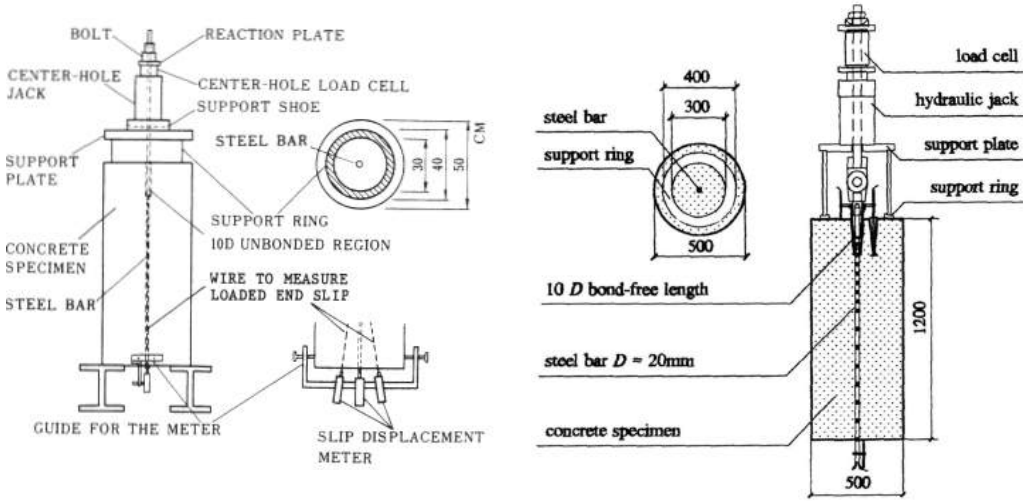

Figure 6.23. Test setup considered by Shima *et al.* [1987b] (left) and Bigaj [1995] (right)

In these experimental tests, the different response parameters were derived from steel strains measured with strain gauges placed at the surface of the rebars along the embedment length. To ensure that yielding took place at the embedded region of the rebars, the tests performed by Bigaj [1995] used taper threaded splicing couplers to connect the embedded rebar with the loading device. A summary of the main properties of the three specimens selected from the study performed by Shima *et al.* [1987b] is presented in Table 6.3.

It should be noted that the three tests were numerically simulated considering the same bond stress-slip constitutive relation, which was defined according to the standard values recommended by Model Code 2010 [fib, 2011]. The results illustrated in Figure 6.24, Figure 6.25 and Figure 6.26 show the distribution of slip, strain, bond stress and rebar stress observed along the embedment length of the rebars for the three different tests.

Table 6.3. Experimental properties and numerical parameters adopted for test SD30, SD50 and SD70, performed by Shima *et al.* [1987b]

Anchorage properties	SD30	SD50	SD70
d_b (m)	0.0195	0.0195	0.0195
L_e (m)	0.97	0.97	0.97
f_c (MPa)	19.6	19.6	19.6
f_y (MPa)	350	610	820
f_u (MPa)	540	800	910
E_s (GPa)	190	190	190
$E_{s,p}$ (GPa)	≈ 3.9	≈ 4.1	≈ 2
C_{clear} (m)	≈ 0.01	≈ 0.01	≈ 0.01
Bond-slip parameters			
α	0.4		
S_1 (m)	0.001		
S_2 (m)	0.002		
S_3 (m)	0.01		
τ_{max} (MPa)	$2.5\sqrt{f_c}$		
τ_f (MPa)	0.4 τ_{max}		

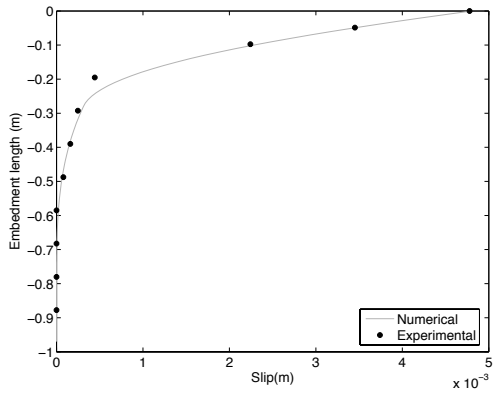

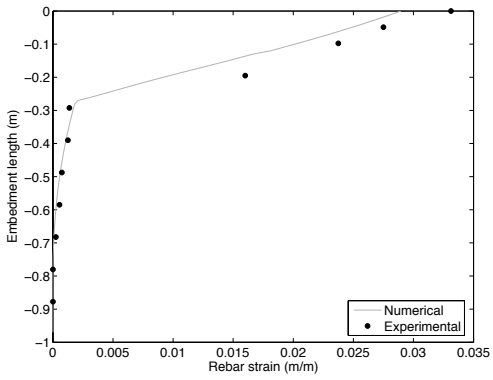

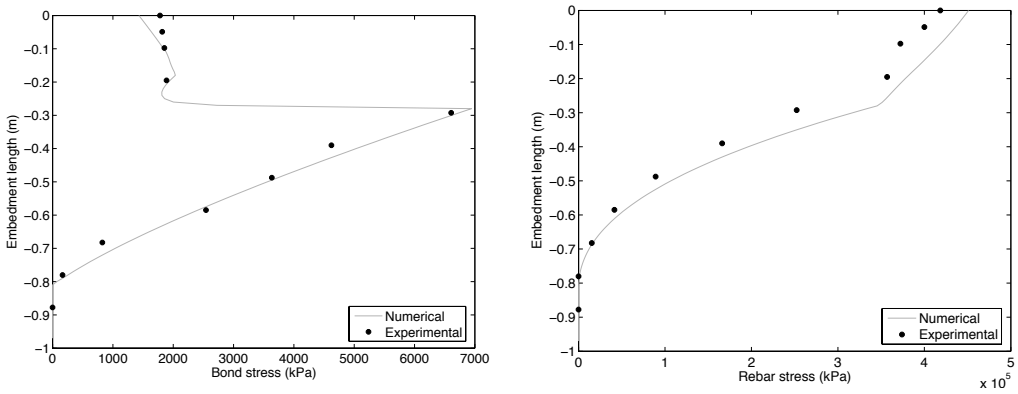

Figure 6.24. Comparison between numerical and experimental results, obtained for test SD30, performed by Shima *et al.* [1987b]

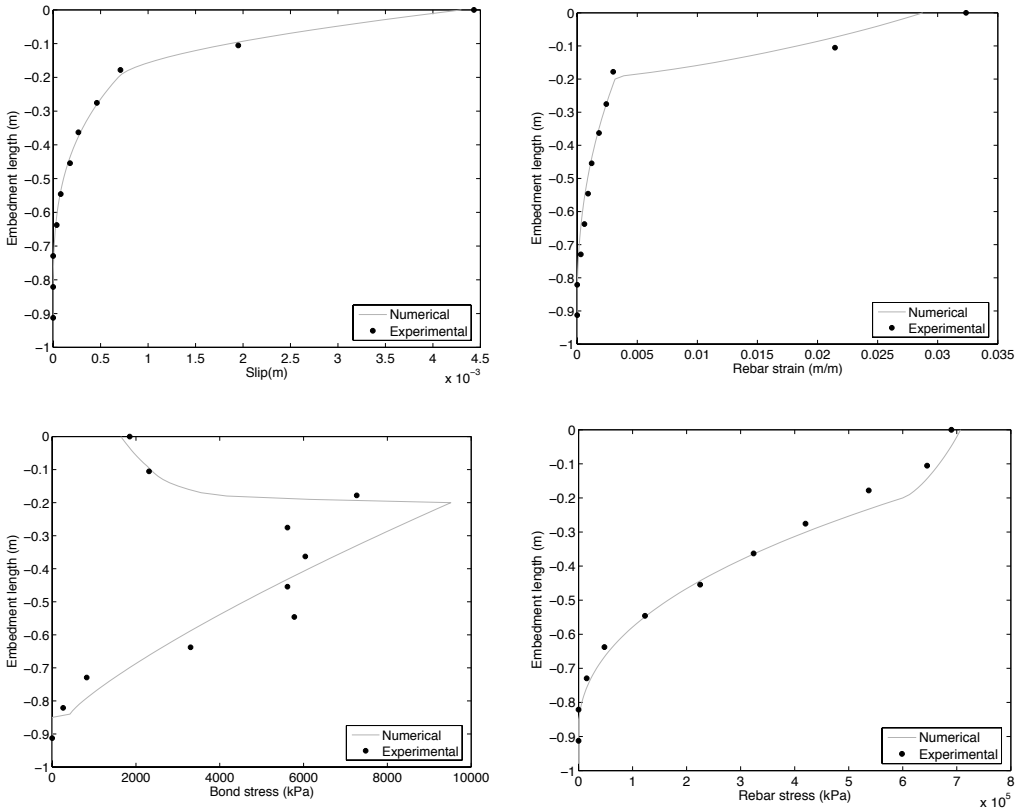

Figure 6.25. Comparison between numerical and experimental results, obtained for test SD50, performed by Shima *et al.* [1987b]

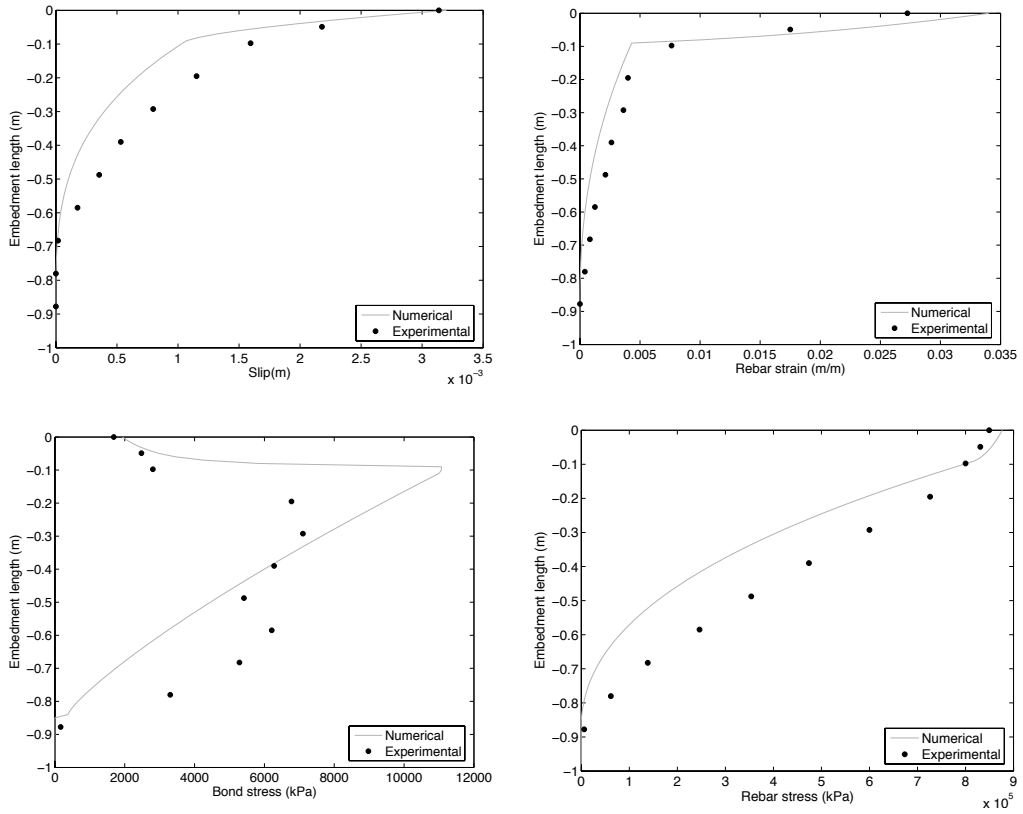

Figure 6.26. Comparison between numerical and experimental results, obtained for test SD70, performed by Shima *et al.* [1987b]

The previous results show a noticeable capacity of the numerical model to reproduce the response of both force- and deformation-related parameters along the embedment length of the rebar. It seems particularly relevant to highlight the model's ability to capture the yielding effect in both steel and bond responses. This effect is reflected in the abrupt loss of bond stress near the loaded-end of the rebar. At the same location, this reduction in bond strength results in a large increase of both strains and slip values. On the other hand, the rebar stresses vary little, as expected, given that the rebar enters in the hardening branch.

Despite the abrupt loss of bond stress associated with the yielding of the rebar being relatively well captured, the maximum bond stress tends to be overestimated and with a very localized peak value, in particular for model SD70, in comparison with the experimental results, which present a wider region with bond stresses close to the maximum value. This observation indicates that the bond-slip constitutive relation used

may not capture accurately the actual bond properties. In this respect, it is important to point out that, despite the important developments observed over the last few years in this subject, the bond-slip constitutive relations available in the literature still present a large dispersion in terms of bond stress and slip limits, as illustrated in Figure 5.3. Naturally, these deviations may result in important changes in the other response parameters along the rebar and, consequently, at the global force-slip response, as demonstrated hereafter. As illustrated in Figure 6.27, the accuracy of the numerical estimations can be further improved if slight changes are introduced to the parameters of the bond stress-slip constitutive model. For the case shown below, the maximum bond stress and the parameter S_1 were multiplied by 0.6 and 0.25, respectively (see Chapter 5.2 for detailed description on the parameters defining the constitutive model adopted).

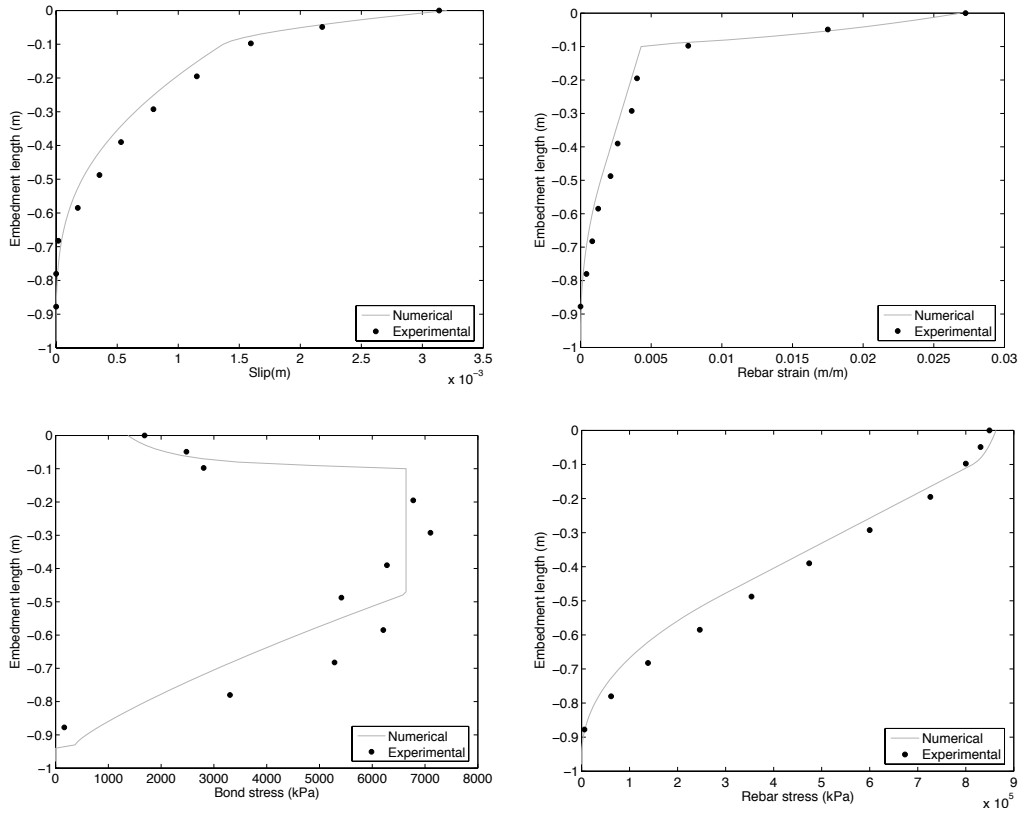

Figure 6.27. Comparison between numerical (with adjusted values for the bond stress-slip parameters) and experimental results, obtained for test SD70, performed by Shima *et al.* [1987b]

These corrections will naturally result in small changes in the global force-slip response of the rebar as illustrated in Figure 6.28. Unfortunately, the corresponding experimental values were not presented and hence, the results cannot be validated.

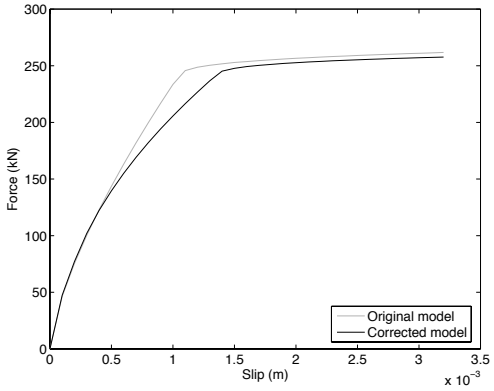

Figure 6.28. Force-Slip response considering the original and corrected bond stress-slip constitutive model

In addition to the distribution of the different response parameters along the embedment length, the results provided by Bigaj [1995] also allows the comparison in terms of anchorage force and slip response at the loaded-end of the rebar for increased levels of loading demand. The main properties of the two specimens analysed are presented in Table 6.4.

Similarly to the previous case, strain gauges were placed along the rebar. However, in this case, the gauges were placed in lugs opened in the rebars in order to preserve the integrity of the gauges during the test. For this reason, the diameter of the rebars considered in the numerical model was corrected to account for the reduction of the rebars' cross-section.

Table 6.4. Experimental properties and numerical parameters adopted for tests P.16.16.2 and P.20.HS.1, performed by Bigaj [1995]

Anchorage properties	P.16.16.2	P.20.HS.1
d_b (m)	0.0149 *	0.0189 *
L_e (m)	0.8	1.0
f_c (MPa)	27.6	94.5
f_y (MPa)	539.67	526.24
f_u (MPa)	624.35	612.87
E_s (GPa)	128.5	150.4
$E_{s,p}$ (GPa)	≈0.76	≈0.8
C_{clear} (m)	-	-
Bond-slip parameters		
α	0.4	
S_1 (m)	0.001	
S_2 (m)	0.002	
S_3 (m)	0.01	
τ_{max} (MPa)	$2.5\sqrt{f_c}$	
τ_f (MPa)	0.4 τ_{max}	

* Diameter modified in order to produce an area equivalent to the prepared rebars

Figure 6.29 presents the comparison between the strain values determined with the proposed numerical model and the ones measured experimentally. The results from the two tests are compared at both yielding (left) and ultimate (right) rebar strength.

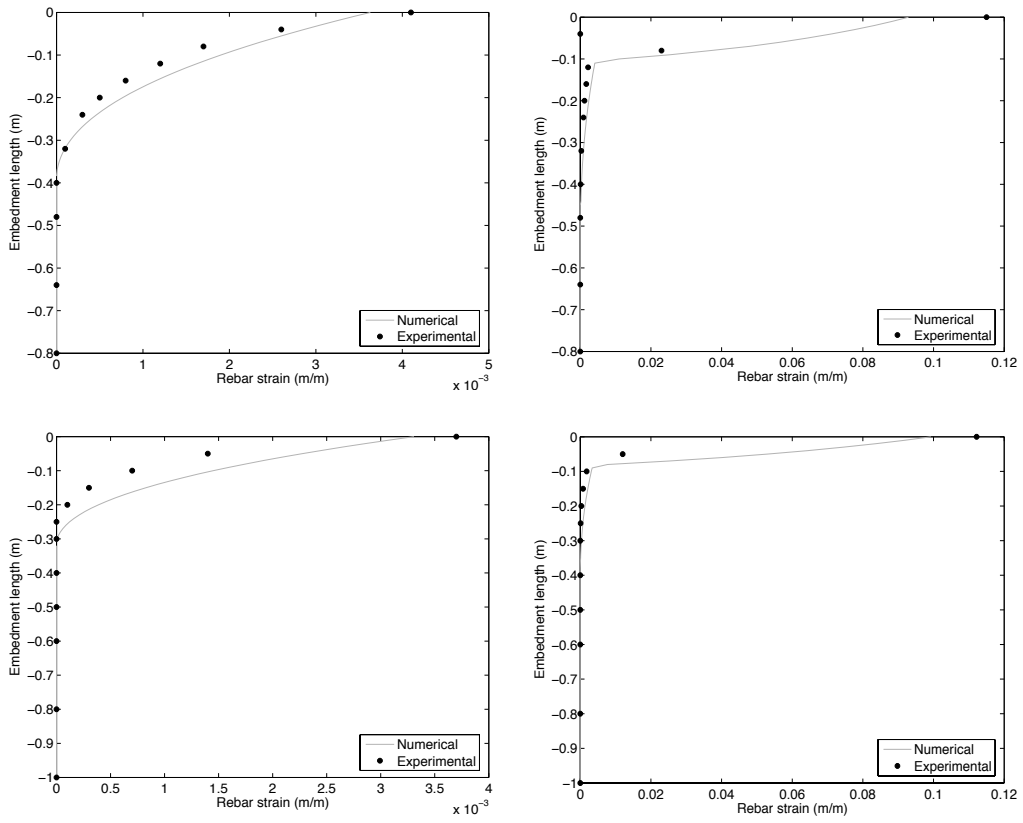

Figure 6.29. Comparison between numerical and experimental strain distribution at yielding (left) and ultimate (right) rebar strain, obtained for tests P.16.16.2 (top) and P.20.HS.1 (bottom), performed by Bigaj [1995]

Once again the response along the rebar is estimated with reasonable precision. In addition, the global response presented in Figure 6.30 indicates that the experimental force-slip response at the loaded-end of the rebars is determined with very good accuracy for increasing slip demand.

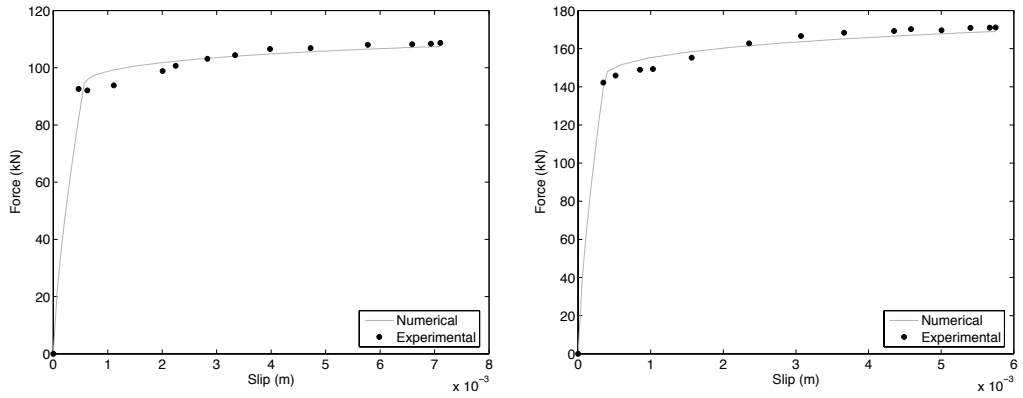

Figure 6.30. Comparison between numerical and experimental force-slip relation at ultimate rebar strain, obtained for tests P.16.16.2 (left) and P.20.HS.1 (right), performed by Bigaj [1995]

In summary, the results presented in this section indicate that the proposed numerical tool predicts with appreciable accuracy the evolution of the different bond parameters along the embedment length as well as the global force-slip response at the loaded-end of the rebars. Moreover, and despite the (natural) dispersion observed in the bond stress-slip constitutive model, these results highlight the need to account for the bond stress decrease due to rebar yielding.

6.2.2 Validation at sectional level

The validation at cross-section level was performed considering the experimental results form two circular RC columns selected from an extensive study carried out by Goodnight *et al.* [2015b] and Feng *et al.* [2015]. Both structures were subjected to cyclic (static) lateral displacements applied at the top of the column up to large ductility levels. Naturally, unlike in the case of a force-controlled test, the loading procedure adopted prevents the explicit evaluation of the increase in flexibility of the columns due to strain penetration deformations at the base of the column. However, these tests represent an important source of information for assessing the performance of the proposed numerical model under simple and controlled loading conditions. In addition, the specimens used in the experimental campaign were thoroughly instrumented, allowing for a detailed analysis of the independent mechanisms contributing to the overall deformation of the columns. The main material properties and numerical parameters' values assumed for the bond-slip model are shown in Table 6.5. Figure 6.31 presents the geometric properties of Test 9, while the main geometric characteristics of Test 19 were already depicted in Figure 6.1.

Table 6.5. Experimental properties and numerical parameters adopted for Test 9 and Test 19 specimens

Anchorage properties	Test 9	Test 19
Axial Load (kN) - λ_N	756 - 5.5%	640.5 - 10%
H (m)	2.44	2.44
D (m)	0.61	0.457
Long. reinf. (ρ_l)	16ϕ19 mm (1.6%)	10ϕ19 mm (1.7%)
Trans. reinf. (ρ_v)	ϕ9.5 mm//0.05 m (1%)	ϕ9.5 mm//0.05 m (1.3%)
d_b (m)	0.0149	0.0189
L_e (m)	1.0 *	1.0 *
f_c (MPa)	47	43.7
f_y (MPa)	470	470
f_u (MPa)	637	637
E_s (GPa)	188	188
$E_{s,p}$ (GPa)	≈1.4	≈1.4
C_{clear} (m)	-	-
Bond-slip parameters		
α	0.4	
S_1 (m)	0.001	
S_2 (m)	0.002	
S_3 (m)	0.01	
τ_{max} (MPa)	$2.5\sqrt{f_c}$	
τ_f (MPa)	0.4 τ_{max}	
L_i (m)	0.46 / 0.92 **	

λ_N - Axial load ratio
ρ_l - Longitudinal reinforcement ratio
ρ_v - Volumetric ratio of transverse reinforcement
* Approximate value based on available detailing information
** Parameter variation in the numerical analysis

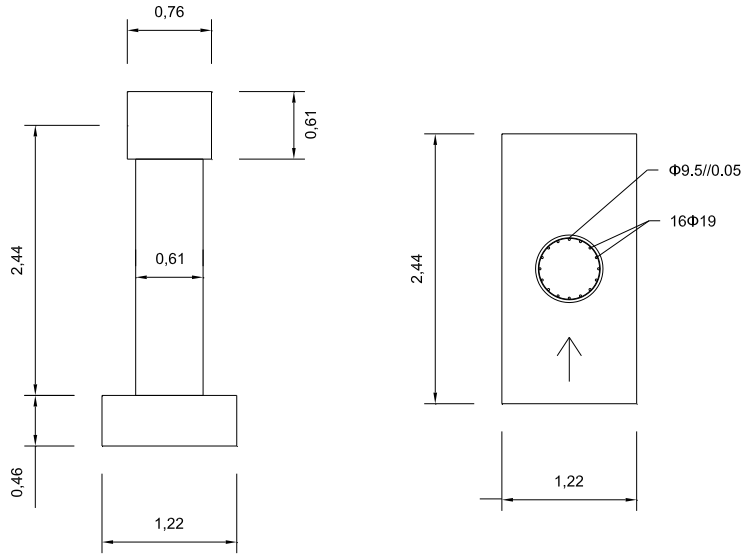

Figure 6.31. Geometric characteristics of the Test 9 specimen (in m)

Both specimens were horizontally loaded at the top of the columns with the application of several cycles of increasing amplitude. After four sets of one-cycle loading with increasing load intensity until the first yielding occurred, the structures were subjected to symmetric three-cycle sets of increasing displacement amplitude, as illustrate in Figure 6.32. It should be noted that in some of the following plots, the response parameters at the last cycles are not presented. This is because for larger displacement demands some of the results, namely the base rotations due to strain penetration effects, could not be measured during the experimental tests.

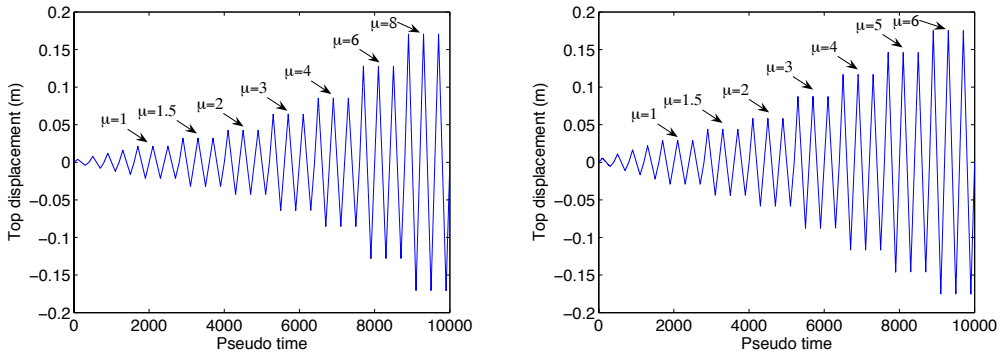

Figure 6.32. History of lateral displacements applied at the top of the column of Test 9 (left) and of Test 19 (right)

In addition to the parameters presented in the table above, special attention was given to the discretization scheme adopted to model the RC column. Given that, for this test protocol, the displacement at the column top is imposed, the evaluation of the strain penetration deformability can only be assessed through the fixed-end rotations and the consequent expected relief in the column's base curvatures. As mentioned before (Section 2.2), the adoption of a different number of integration points along a given RC element may introduce large differences in the computed section curvatures (and consequently at the material strains), in particular for increasing ductility levels.

In order to control the abovementioned numerical strain localization issues, the number of IPs adopted on the beam-column elements was determined on the basis of the observed length of plastic hinge region and the associated shape of nonlinear curvatures distributions. In the referred experimental study, it was found that the plastic curvatures follow essentially a linear distribution (Figure 6.33), which is in line with the observations made by Hines *et al.* [2004]. This observed distribution of curvatures seems to be associated with the so-called tension-shift effects. The interested reader can find further details on this subjects Hines *et al.* [2004] and Goodnight *et al.* [2014].

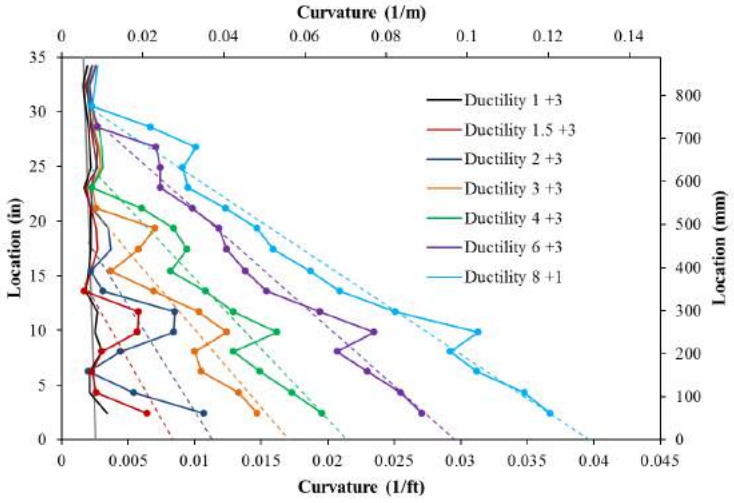

Figure 6.33. – Curvature profiles measured in Test 9 for different ductility levels and number of cycles (values separated by a "+" sign in the legend) [Goodnight *et al.*, 2015b]

Therefore, the number of elements and number of IPs per element in the numerical model was defined so that the weighted length of the integration point at the base of the column, multiplied by the curvature at the IP, approaches the integral of the curvatures along the length of the plastic region. This can be achieved considering an element discretization in which the weighted length of the 1st IP represents half of the

experimental length of the plastic hinge region, in order for the curvature in the numerical model to equal the maximum curvature measured at the base of the column. Noticing that the nonlinear curvatures spread up to about 0.75 m (from the foundation level) at large ductility levels, the RC column was modelled with 2 FB elements (1.25 m and 0.19 m) with 3 IPs each, leading to a weighed length at the base IP of 0.375 m. Without using more sophisticated regularization techniques, such as the ones proposed by Almeida *et al.* [2012], this strategy is expected to reproduce more accurately the curvature profiles at larger ductility levels. At lower ductility levels, the length of plastic hinge region is shorter and, therefore, the curvatures will tend to be underestimated.

In the following, the numerical results obtained with the proposed bond-slip model are, whenever appropriate, compared with more simplified approaches, namely the use of (i) a linear spring at the base, (ii) a longer element or even the (iii) absence of any deformable mechanism at the column-foundation interface. For the first approach, the rotational stiffness's were determined with Equation (2.12), resulting in the following values: K_θ = 324x10^3 kNm/rad and K_θ = 98x10^3 kNm/rad for Test 9 and Test 19, respectively. For the elongated element approach, the strain penetration length was determined based on Equation (2.10). The value obtained for both tests was L_{sp} = 0.2 m. Additional details on the definition of these simplified models can be found in Chapter 2.3.

Figure 6.34 and Figure 6.35 depict the experimental and numerical response in terms of base shear – top displacement obtained for Test 9.

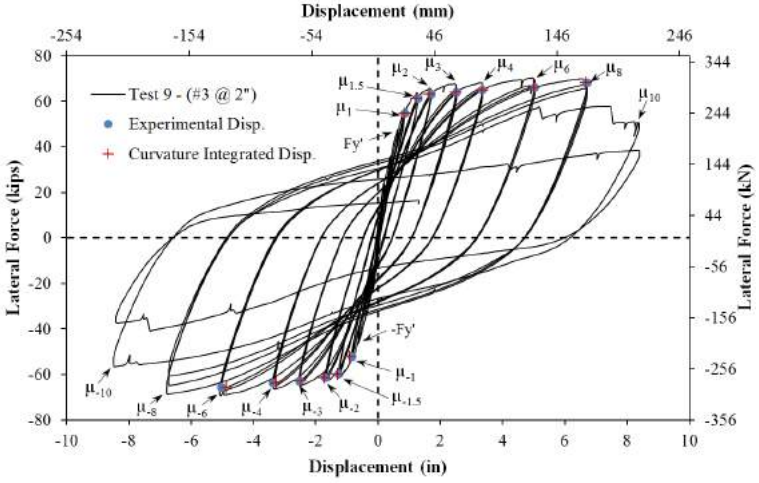

Figure 6.34. Experimental base shear – top displacement relation for Test 9 [Goodnight *et al.*, 2015b]

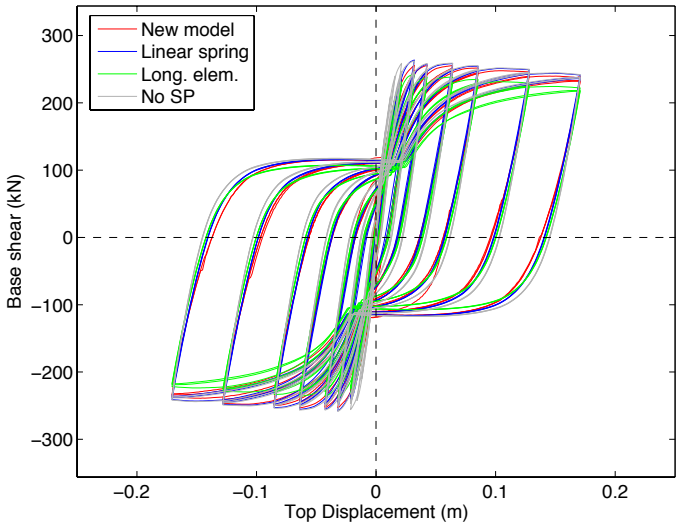

Figure 6.35. Numerical base shear – top displacement relation for Test 9

The comparison between the two plots reveals a good approximation between the experimental and numerical hysteretic behaviour. Nonetheless, the maximum base shear computed is slightly underestimated, which can result from small deviations in the material or geometric properties of the column.

Regarding the hysteretic response with different SP modelling solutions, only small variations are observed at the global scale. This is somehow expected considering that the loading protocol consists in applying prescribed displacements at the top of the column while during most of the loading cycles the column exceeds its yield bending moment capacity. Moreover, given that the foundations were designed to be capacity protected, it is not expected to observe a reduction in the load carrying capacity of the column due to an anchorage failure of any longitudinal rebar.

Nevertheless, it is possible to observe a slightly stiffer response before yielding and a fatter hysteretic loop in the model with fixed base (No SP). Despite the slight pinching effect observed for the other models, the unloading and reloading curves are still slightly steeper than the one measured experimentally. Finally, the previous figure points for one of the limitations associated with the use of an elongated element, which is related with the reduction of the computed base shear. This occurs since, for the same bending moment capacity of the cross-section, the shear span is longer in that particular model and, consequently, the developed base shear will necessarily be reduced in the direct proportion to the increased length of the element.

In the following plot the rotations at the interface between the column and the foundations resulting from strain penetration deformations are compared. The plot presents the experimental values together with the results obtained for the case with a linear spring at the base of the column and the new bond-slip model with two different variants: influence length (L_i) equal to 0.46 m and to 0.92 m. The lower value corresponds to the height of the foundation, whilst the latter is twice this value. It should be recalled that L_i is a parameter that has no influence in the slip computed for each longitudinal rebar. Instead, it is used to convert the shortening displacement at each concrete fibre, arising from the zero-length element relative displacements, to strains, in order to determine the average stresses at the concrete fibres and, consequently the overall sectional resisting moment. In other words, it corresponds to an equivalent length along which it is expected the concrete strains to develop, assuming a constant distribution of concrete stresses in depth and with no transversal "spreading" of the axial stresses, unlike what occurs in reality. In this case, given that the base of the foundation is much larger than the area of the column section, it is expected that the concrete strains and stresses reduce significantly as they approach the base of the foundation due to such transversal "spreading". The solution to somehow account for this more realistic condition is to increase the value of L_i. The amount of this increase is however subjective and requires some engineer judgement. In Figure 6.36, the SP rotations are evaluated for values that are equal and twice the foundation height. In addition, the values determined with the linear spring at the base are presented for comparison purposes.

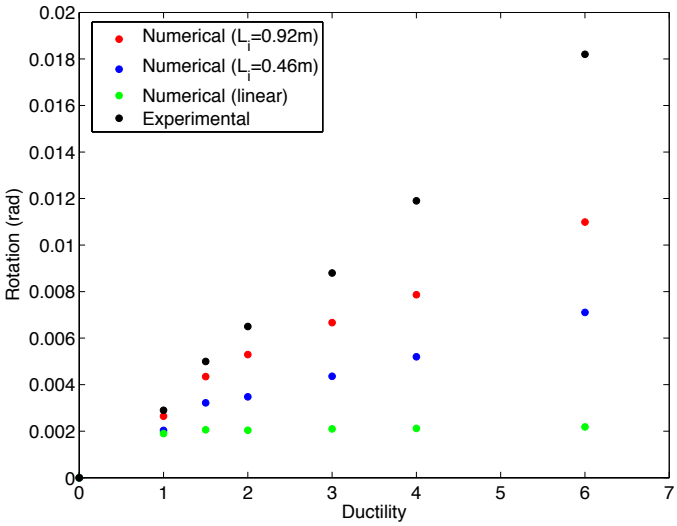

Figure 6.36. Comparison between experimental and numerical SP rotations of Test 9 for different ductility levels

Despite the noteworthy improvements obtained with the new bond-slip model with respect to the simple linear spring, the results presented above reveal a considerable underestimation of the SP rotations determined with the different numerical models with respect to the experimental ones. In order to further investigate the response of the new SP model, Figure 6.37 presents the evolution of slip at the extreme rebars of the cross-section for different levels of displacement demand. It is important to note that the numerical results include a cycle that was impossible to measure experimentally in the left rebar. Hence the comparison of the two top plots should be made only up the previous cycle, whose maximum displacement is around -0.13 m. Moreover, it is noted that for a better interpretation of the results, the axes in the following plots have the same limits.

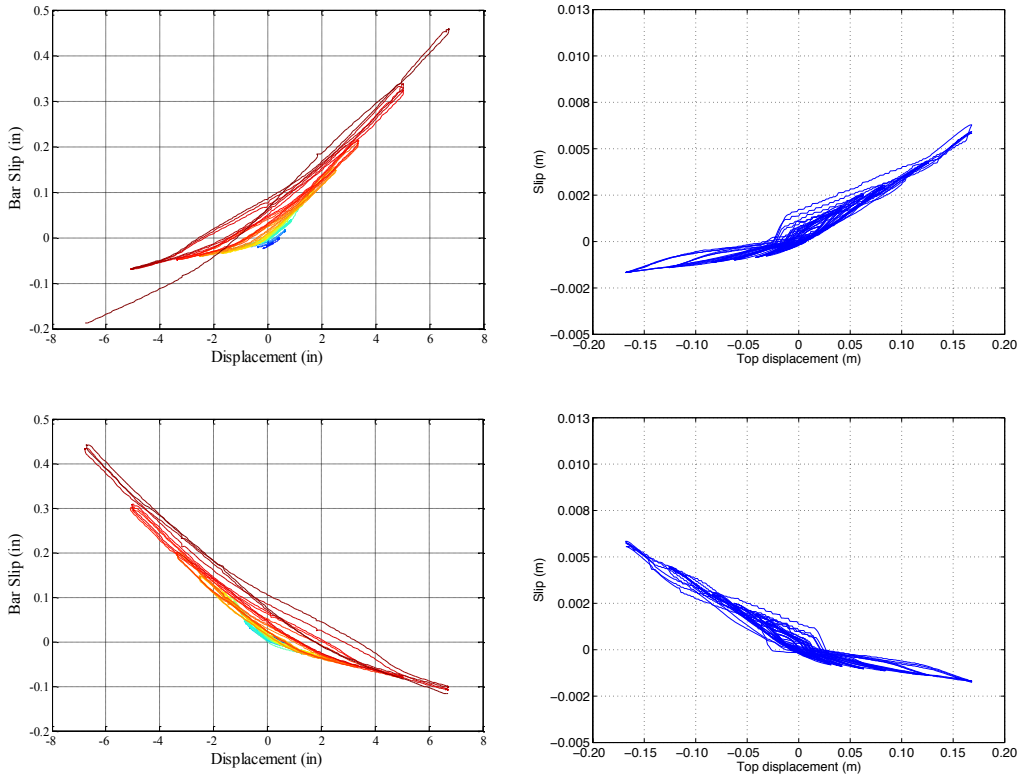

Figure 6.37. Experimental (left) and numerical (right) slip hysteresis at extreme rebars of the base section of Test 9 (1 in = 0.0254 m)

The evolution of the slip at the extreme rebars presented in the previous plots shows that the computed slip under tensile forces is significantly underestimated. On the other hand, the behaviour under compression seems to be captured with a better accuracy. It is important to note that under compression, it is expected the response to be essentially

governed by the contribution of the concrete fibres. Thus, these results indicate that the use of an influence length that approaches two times the foundation height seems appropriate. On the other hand, the slip under tensile force exhibit larger differences, which suggest that the resisting bond stresses adopted in the constitutive model could be overestimated with respect to the experimental conditions. To demonstrate this hypothesis, the set of plots presented in Figure 6.38 shows the evolution of slip at extreme rebars considering L_i = 0.92 m, but with a maximum bond stress that is 80 % the one used in the previous results ($\tau_{max} = 2\sqrt{fc}$ instead of $\tau_{max} = 2.5\sqrt{fc}$).

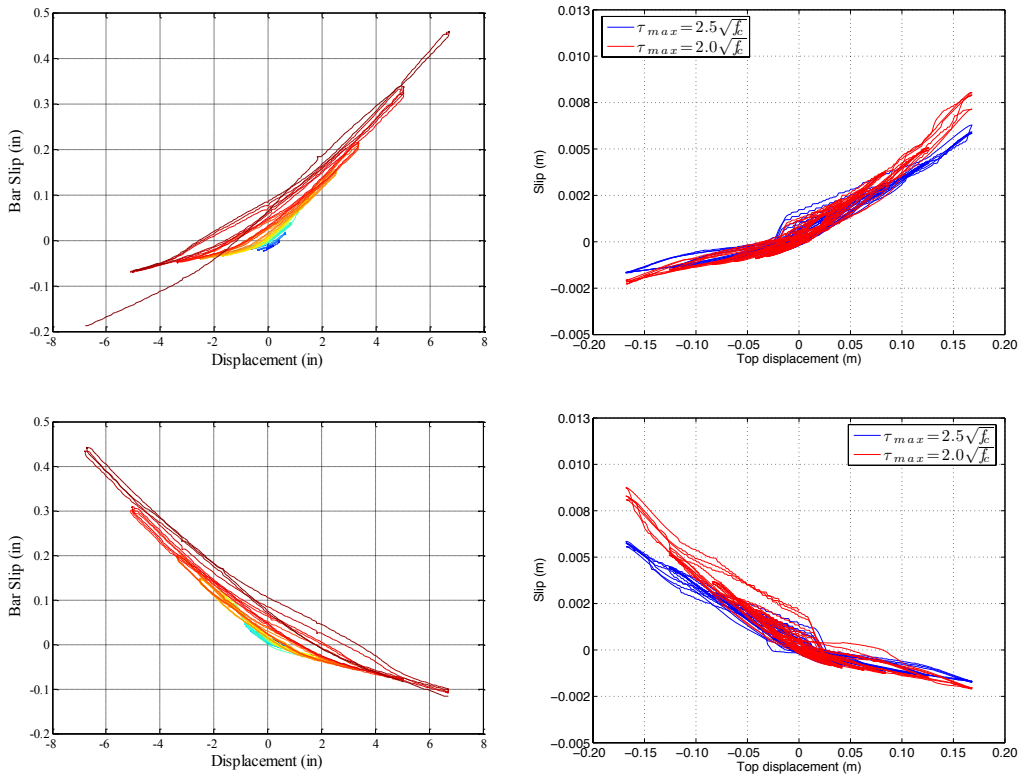

Figure 6.38. Experimental (left) and numerical (right) slip hysteresis at extreme rebars of the base section of Test 9, with different bond stresses (1 in = 0.0254 m)

The numerical results computed with lower bond strength show a better approximation to the experimental observations regarding the slip values at extreme rebars (Figure 6.38), as well as for the SP rotations (Figure 6.39) measured at the base section of the column. The latter presenting the evolution of the SP rotations for increased ductility levels. Moreover, it is evident that the slip values under tensile forces increase significantly more than the slip values in compression. These results seems to indicate that the use of

L_i = 0.92 m is appropriate; at the same time it is apparent that the standard values for the bond parameters are overestimated, as already noted in the previous section. Naturally, one could further adjust the bond stress-slip parameters, introducing modifications at both slip and bond stress limits, in order to improve the numerical fit to the experimental results. Nonetheless, the main purpose of this study is to assess the potential of the new bond-slip model to adequately represent strain penetration effects under different anchorage and loading conditions, and not necessarily to match the experimental observations.

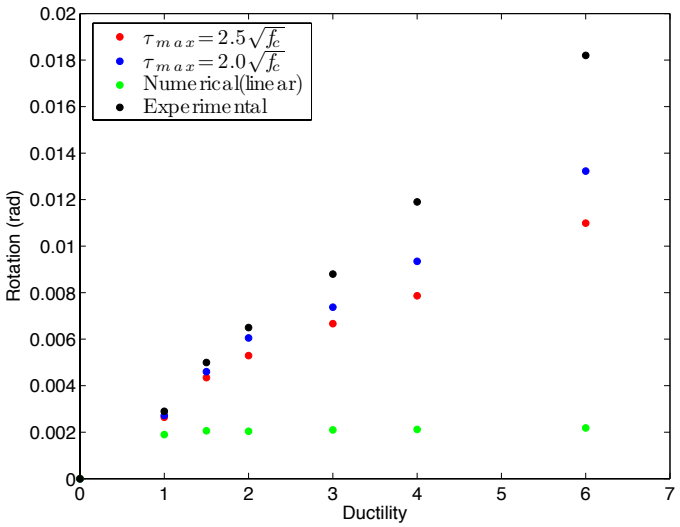

Figure 6.39. Comparison between experimental and numerical SP rotations of Test 9 for different ductility levels

Finally, the evolution of the column's base curvatures for increasing ductility levels is shown in Figure 6.40. Given that the loading protocol is based on a set of imposed displacements, this is an alternative way to assess the importance of SP effects on the specimen. A first important observation is related to the significant reduction in the curvature demand with the new bond-slip model in comparison with all the simpler modelling methods considered in the sensitivity study carried out in Section 3.4.3. This reduction occurs because the base rotations due to SP effects computed with the proposed bond-slip model are always larger than with the others methods. Hence, the curvature demand at the column's base required to produce the same top displacement is necessarily lower. In addition to the previous observation, one can verify that the curvatures computed with the new model only approach the experimental ones at the highest ductility demand (μ = 6) – before that, the curvatures are always underestimated, as opposed to what is verified with the other simplified models. Such underestimation is

probably related to the column adopted discretization scheme, which was defined on the basis of the experimental response at $\mu = 6$. Therefore, and despite the curvatures at this stage approache very closely the experimental ones (as opposed to what is observed with the alternative SP methods) it should be noted that for lower ductility levels, the curvatures are considerably underestimated. This issue can only be avoided with the implementation of suitable strain regularization techniques, capable to adjust the integration weights of the different IPs according to the expected length of plastic hinge region at different ductility levels. Unfortunately, such methods are still at a research stage and are unavailable in most common structural analysis software packages.

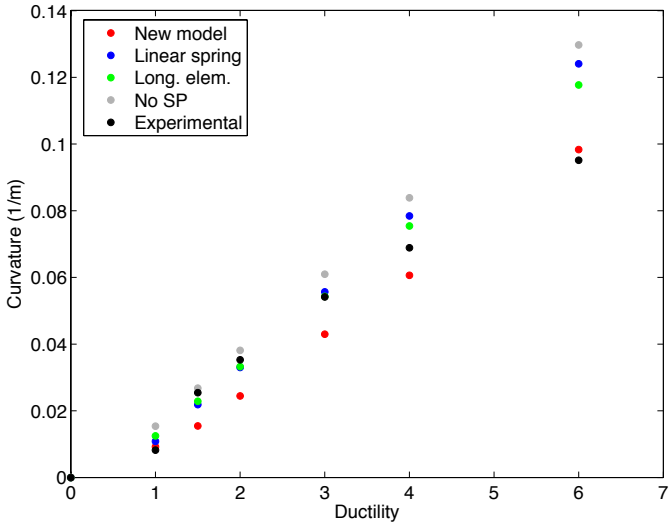

Figure 6.40. Comparison between experimental and numerical curvatures at the base section of Test 9 for different ductility levels

Similar analyses are now performed for Test 19. In this case, the experimental program is similar to the one of Test 9 but differs on the diameter of the cross-section, number of rebars, concrete strength and axial load ratio (approximately twice the value considered before). Moreover, despite following an identical loading protocol, the displacement amplitudes are now larger for the same level of ductility demand.

Similarly to the previous case, the comparison in terms of base shear-top displacement (Figure 6.41 and Figure 6.42) shows numerical results that approximate relatively well the experimental ones, revealing, nonetheless, slightly lower base shear values. This points to a clear underestimation of the bending moment capacity, which may be related with possible deviations in the definition of the geometric properties of the cross-section or in

the material properties. As for Test 9, the effects of different SP modelling options are also visible in this case.

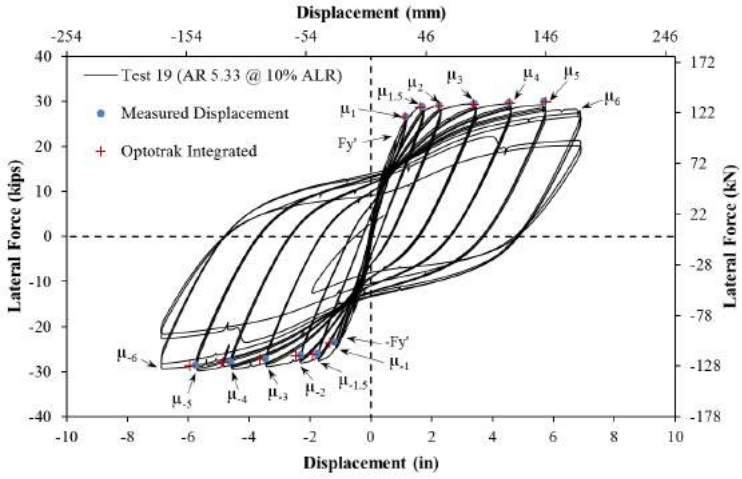

Figure 6.41. Experimental base shear – top displacement relation for Test 19 [Goodnight *et al.*, 2015b]

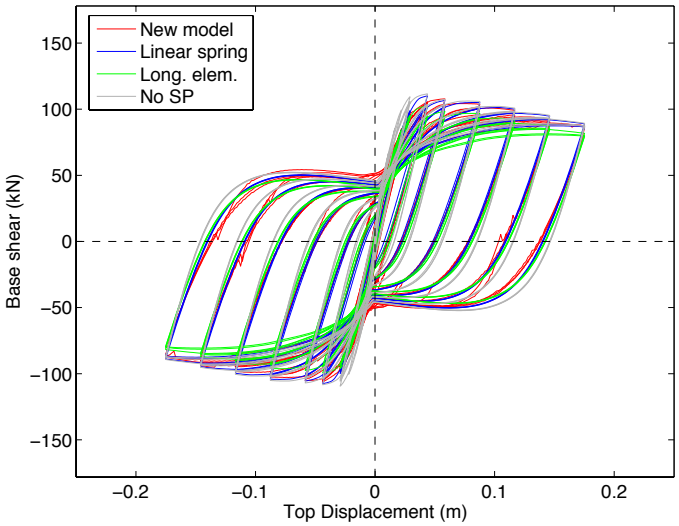

Figure 6.42. Numerical base shear – top displacement relation for Test 19

Regarding the SP rotations measured at the base of the column, which are presented in Figure 6.43, the numerical results for this case approach more closely the experimental ones. Similarly to Test 9, the rotations determined with L_i = 0.92 m are once more closer to the experimental values but, they are now slightly overestimated.

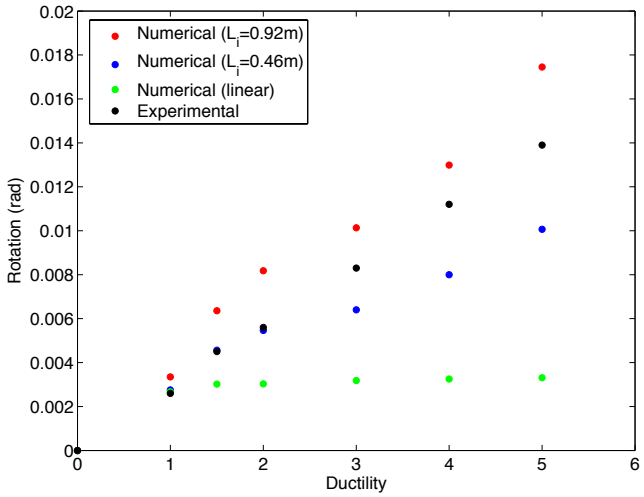

Figure 6.43. Comparison between experimental and numerical SP rotations of Test 19 for different ductility levels

The SP rotations determined with a linear spring, as previously, are largely underestimated for increased ductility levels. Given the linearity of the rotational spring, once the column reaches its yielding capacity, the SP rotations remain essentially unchanged given that the bending moment only increase marginally for larger ductility levels.

Looking in more detail to the source of the SP rotations, the variations in slip measures at the extreme rebars of the cross-section are presented in Figure 6.44. Once more, the slip at the extreme rebars is approached with remarkable accuracy, especially considering the large number of cycles and magnitude of the imposed load.

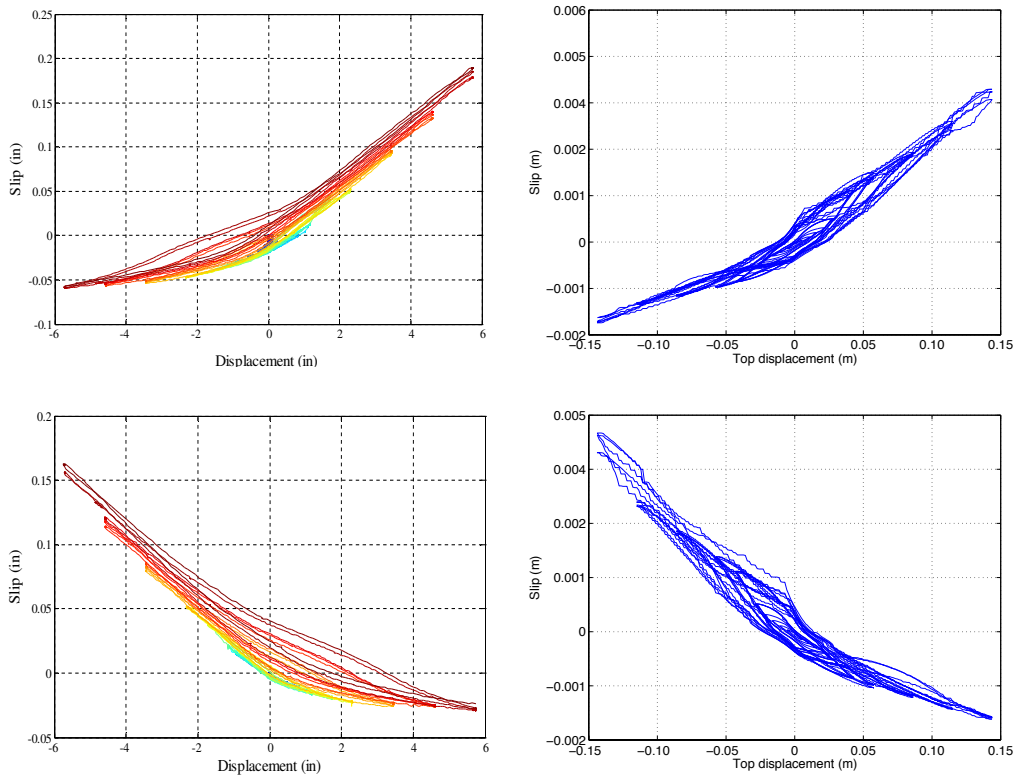

Figure 6.44. Experimental (left) and numerical (right) slip hysteresis at extreme rebars of the base section of Test 19 due to strain penetration (1 in = 0.0254 m)

In what concerns the evolution of curvatures at the base of the column, as illustrated in Figure 6.45, the results reveal, as in the previous case, a significant reduction of the values determined with the proposed model with respect to the more simplified ones. The curvature demand reduced up to about 50% with respect to the case where no SP effects are accounted for in the numerical model. Nonetheless, the plot shows a clear underestimation with respect to the experimental ones. These large deviations between the experimental values and the proposed model can be explained by the fact that the displacements obtained through integration of the Optotrak readings (device used to measure the reinforcement strains) in the pull direction of loading are uniformly overpredicted, as referred in Goodnight *et al.* [2015a]. This observation indicates that one of the two main contributions to the overall lateral displacement (strain penetration rotation and flexural deformation at the plastic hinge region) has been overestimated. Although the source of such discrepancy has not been identified, the numerical results provide a clear indication that it resides in the column curvature values.

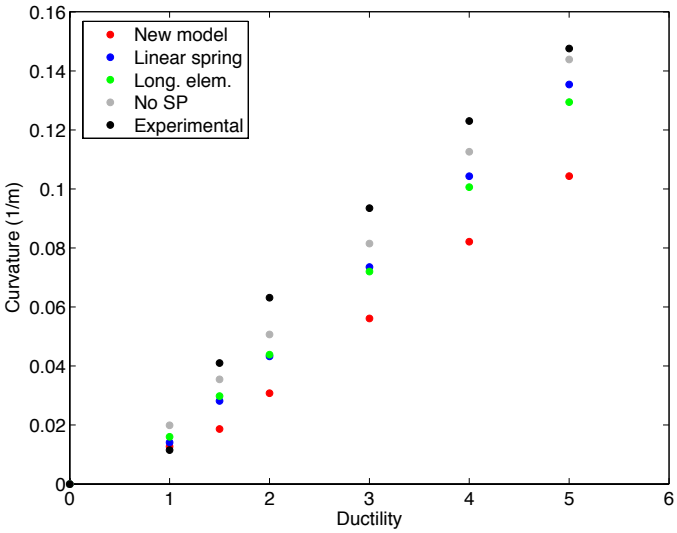

Figure 6.45. Comparison between experimental and numerical curvatures at the base section of Test 19 for different ductility levels

6.2.3 Validation at global level through nonlinear dynamic analysis

The validation tests presented in the previous sections comprised a series of analysis of increasing complexity. In this case, the performance of the proposed bond-slip element is assessed by means of shake table tests on a RC frame subjected to a set of five consecutive ground motion records. This particular case presents some challenging conditions with respect to the previous ones, namely in what respects the comparatively more complex nature of the input load and the number of bond-slip elements considered in the structure, as described hereafter along with other modelling options adopted.

The structure considered was experimentally tested at LNEC-3D shake table, under the scope of the blind prediction contest 'Prémio Ricardo Teixeira Duarte - PRTD' launched at the occasion of the Portuguese Conference on Structural Engineering - JPEE2014. The design geometry and detailing drawings can be downloaded from the conference website: http://jpee2014.lnec.pt/concurs_2.html.

The RC frame is composed of 2 storeys and 2 bays and was designed to exhibit low ductility, representing older structures built without seismic regulation. The general dimensions of the specimen, corresponding to a geometric scaling factor of 1:1.5, are shown in Figure 6.46.

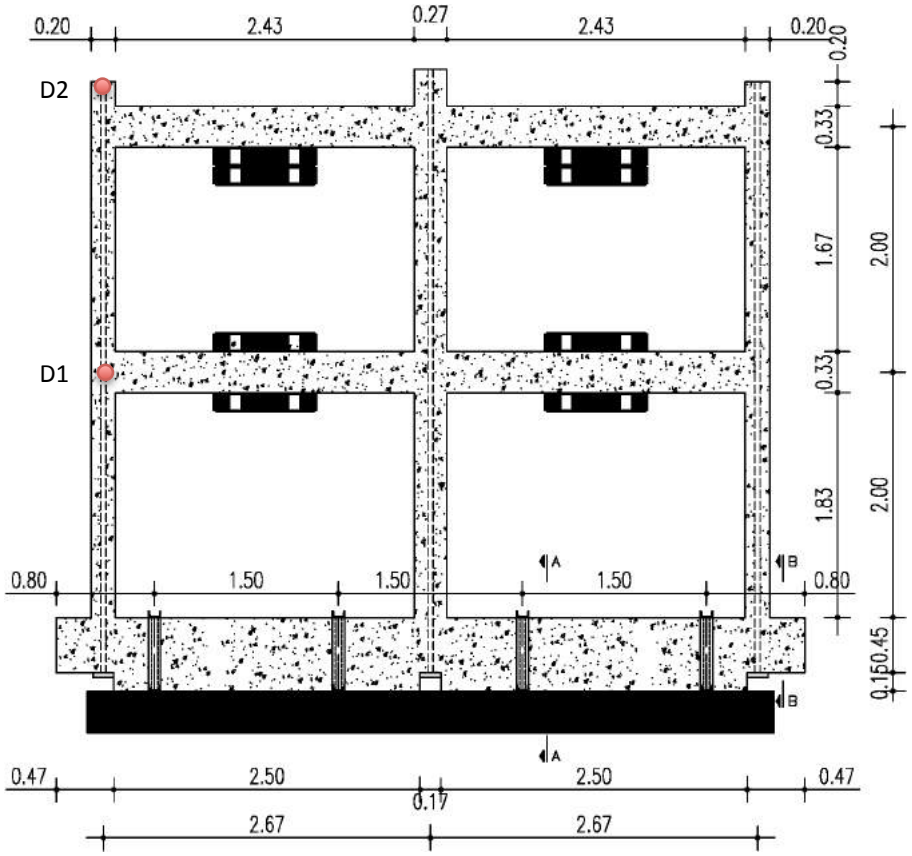

Figure 6.46. General dimensions of the PRTD RC frame

In addition to the self-weight of the frame, lumped masses of about 1.2 tonnes per span were placed on the structure, as illustrated in the previous figure. In order to simulate the compressive load in the columns corresponding to two additional floors in the building not existing in the reduced scaled model, an unbounded post-tensioning centered force of approximately 20 kN and 30 kN was applied to the lateral columns and to the central column, respectively.

An additional auxiliary guidance structure was used to constrain the RC frame at the top beams, in order to prevent the frame to have out-of-plane displacements (image on the right of Figure 6.47). Despite not being considered in the numerical model described subsequently, this additional structure and the shake table itself introduces modifications to the mass and stiffness of the complete system, changing its dynamic properties and making it more difficult to the numerically simulate the experimental test.

Figure 6.47. General view of the PRTD RC frame on the shake table without (left) and with (right) the auxiliary guidance structure (courtesy of LNEC)

The material properties were determined based on tests conducted on samples of the concrete and reinforcement used in the frame. The values adopted in the numerical model were determined based on the average of the individual tests and are summarised in Table 6.6.

Table 6.6. Material properties adopted to model the RC frame

	f'_y (MPa)	f_u (MPa)	E_s (GPa)	$E_{s,p}$ (GPa)	f'_c (MPa)	$f'_{c,t}$ (MPa)	C_{clear} (m)
Ø 6	600	648	214	1.7	14	2.3	0.02
Ø 8	550	657	191	0.92			

It should be noted that the compressive strength value adopted for the concrete is slightly larger than the one corresponding to the average of the compressive tests on concrete cubes. Considering that the tests on the concrete samples were performed about two years before the shake table test, the corresponding average value (12.3 MPa) was increased by 15 % in order to account for the concrete aging effect. Finally, a summary of the different cross-sectional properties is presented in Table 6.7.

Table 6.7. Cross-sectional properties of the different members of the PRTD RC frame

	Dimensions (m)	Long. Rebars (ρ_l)	Transv. Rebars (ρ_v)
Lateral columns	0.2 x 0.2	6Ø8 (0.75 %)	Ø6//0.15m (0.34 %)
Central column	0.27 x 0.2	8Ø8 (0.74 %)	Ø6//0.15m (0.30 %)
Beams	0.33 x 0.2	8Ø8 (0.61 %)	Ø6//0.15m (0.28 %)

ρ_l - Longitudinal reinforcement ratio

ρ_v - Volumetric ratio of transverse reinforcement

Regarding the seismic demand, five successive records of increasing intensity were imposed along the strong direction of the frame, corresponding to PGAs of 0.10, 0.20, 0.32, 0.52 and 0.72 g. The response spectra for the different intensity levels are presented in Figure 6.48 (left). The corresponding accelerograms were artificially generated to match the response spectrum for the different intensity levels. This is clearly identified by the unrealistic large number of cycles with large amplitude illustrated in the reference accelerogram of Figure 6.48 (right).

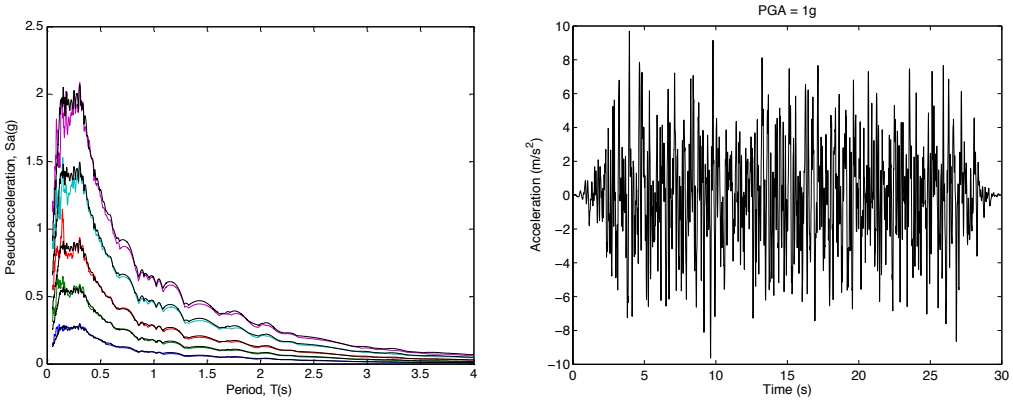

Figure 6.48. Target and actual response spectra for different intensity levels (left) and reference acceleration record for PGA=1g (right)

The results presented hereafter comprise the comparison of the experimental results with the response obtained through numerical simulations considering (i) the model adopted during the blind prediction challenge, which simulates SP effects by using elongated columns, (ii) a model featuring the actual geometry and without any consideration for strain penetration effects and (iii) a model featuring the actual geometry but with the strain penetration effects simulated with the proposed bond-slip model. Apart from the

definition of the strain penetration effects, all the other modelling parameters were kept constant with respect to the model developed during the blind prediction challenge.

Regarding the model adopted for the blind prediction challenge, the axial behaviour for the reinforcement is simulated through the well-known stress-strain relation proposed by Menegotto and Pinto [1973]. On the other hand, the concrete follows the uniaxial nonlinear model proposed by Mander *et al.* [1988], with the cyclic rules proposed by Martinez-Rueda and Elnashai [1997]. The confinement effect provided by the transverse reinforcement is incorporated using the rules proposed by Mander *et al.* [1988], whereby a limited constant confining parameter of 1.06 is adopted for the core region of the cross-section.

The nonlinear response of both RC columns and beams is simulated through force-based elements featuring 4 IPs per member. In the absence of a more appropriate regularization technique, the number of IPs was defined so that the weight of the first IP approaches 0.15 m which corresponds to the expected plastic hinge length determined according with Equation (3.1). This option is in line with the preliminary conclusions drawn at the end of chapter 3.

The dynamic analyses were carried out using the well-known Hilber-Hughes-Taylor time integration algorithm [Hilber *et al.*, 1977], considering the original time-step of the records provided by the organization, i.e., 0.005 s. In addition, a small amount of equivalent viscous damping was assigned through the definition of 1.5 % mass proportional damping. This option was taken according to the discussion and results presented in Section 2.1 and Section 3.4.1.

Taking into account that at the latter records the structure is expected to undergo large ductility demand, it is essential that the numerical analyses account for geometric nonlinearities, in particular P-Δ effects. In order to accurately consider the second-order effects, as well as the elongation of the RC members during nonlinear response, the simulation of the post-tension system cannot be accomplished through a series of constant axial loads applied at the top of the columns. Therefore, the consideration of the unbounded post-tension of the columns, together with the incorporation of the nonlinearities in the response, requires the definition of a creative and unconventional modelling solution, as described in the following.

The post-tensioning was thus simulated through the consideration of two additional truss elements that run along the height of the different columns. These elements feature an elastic behaviour, defined according with the cross-section of the strands and the modulus of elasticity of the steel. The connections of the truss elements with the RC frame feature different constraints depending on their location. In detail, the connection

of the truss elements at the top nodes of the frame is restrained for all the translational DOF, while at the intermediate and bottom levels, i.e., at the beam-column joints of the first storey and at the foundations, the nodes of the trusses are constrained to move with the columns' ones only in the horizontal direction. In order to impose the post-tension load, equivalent forces are assigned at the end nodes of the trusses at the foundation level. In this way, each column presents the desired level of axial force, keeping the load path always aligned with the columns' axes, regardless of their deformation during the dynamic analyses.

A general view of the numerical model is presented in Figure 6.49. It is possible to visualize the different truss elements aligned at both sides of each column together with the axial forces (blue arrows) applied at the bottom ends. In addition it is also possible to identify the dynamic loads by the green arrows and the mid-span masses with the green cubes. Simply for symmetry purposes, two trusses were defined per column. Naturally, the force applied to each one represents half the actual pre-stressing force applied to the corresponding column.

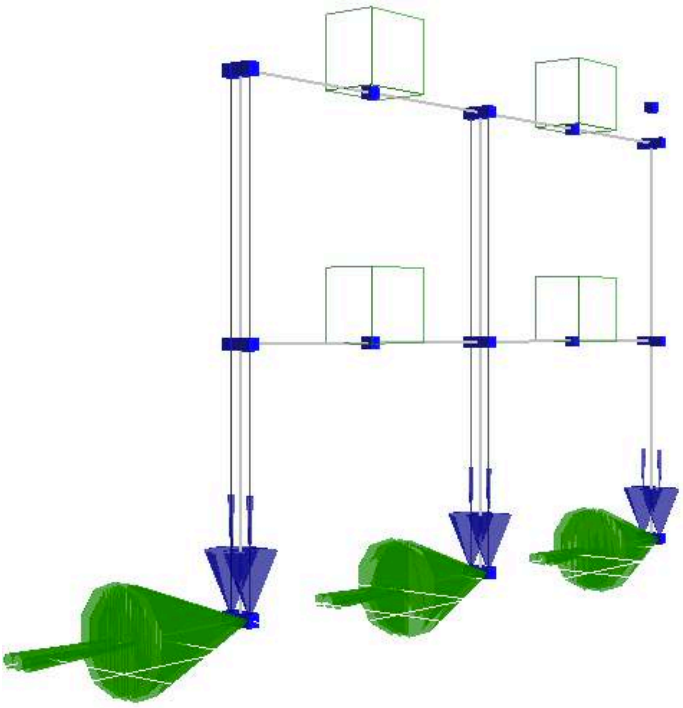

Figure 6.49. General view of the numerical model developed for the PRTD RC frame

As previously mentioned, in addition to a model were no SP effects were considered, two additional models with alternative SP modelling solutions are presented in this section. The first, corresponding to the model submitted for the blind prediction competition, considers a simplified approach previously described in Section 2.3 where the length of the columns of the first storey is increased by the expected strain penetration length determined with Equation (2.10). In this case, each column of the first storey was elongated of 0.1 m.

Finally, an additional model is defined considering the new bond-slip model presented in this thesis. In this case, zero-length bond-slip elements are assigned at the base of the columns as well as at all the beams and columns' ends of the beam-column joints of the first storey. At the upper joints of the frame, no additional elements were defined considering the expected lower seismic demand and reduced contribution of the SP deformations to the overall frame behaviour.

Considering that at the time the numerical simulations with the proposed bond-slip model were performed the experimental results were already available, the parameters associated with the bond stress-slip constitutive model were defined recognizing the significant damage observed both at the columns/foundations and beams/columns joints at the first storey, as illustrated in Figure 6.50. It should be recalled that the proposed element was not yet implemented at the time of the blind prediction challenge.

Naturally, the development of large cracks and, in some cases, concrete spalling induces a drastic reduction in the bond strength of the anchorage regions. Therefore, the bond stress-slip parameters adopted follow the values recommended by Model Code 2010 [fib, 2011] for an expected splitting failure, as presented in Table 5.3. Considering the limited or, in some cases, absence of transverse reinforcement in the spalled regions (see figure below), the parameters adopted correspond to an unconfined condition. Moreover, in order to reflect the severe damage observed, the parameters selected combine the lower bound parameters attributed to both "good" and "other" bond conditions. A residual friction bond stress is assumed ($\tau_f = 0.2\ \tau_{max}$) for numerical stability purposes.

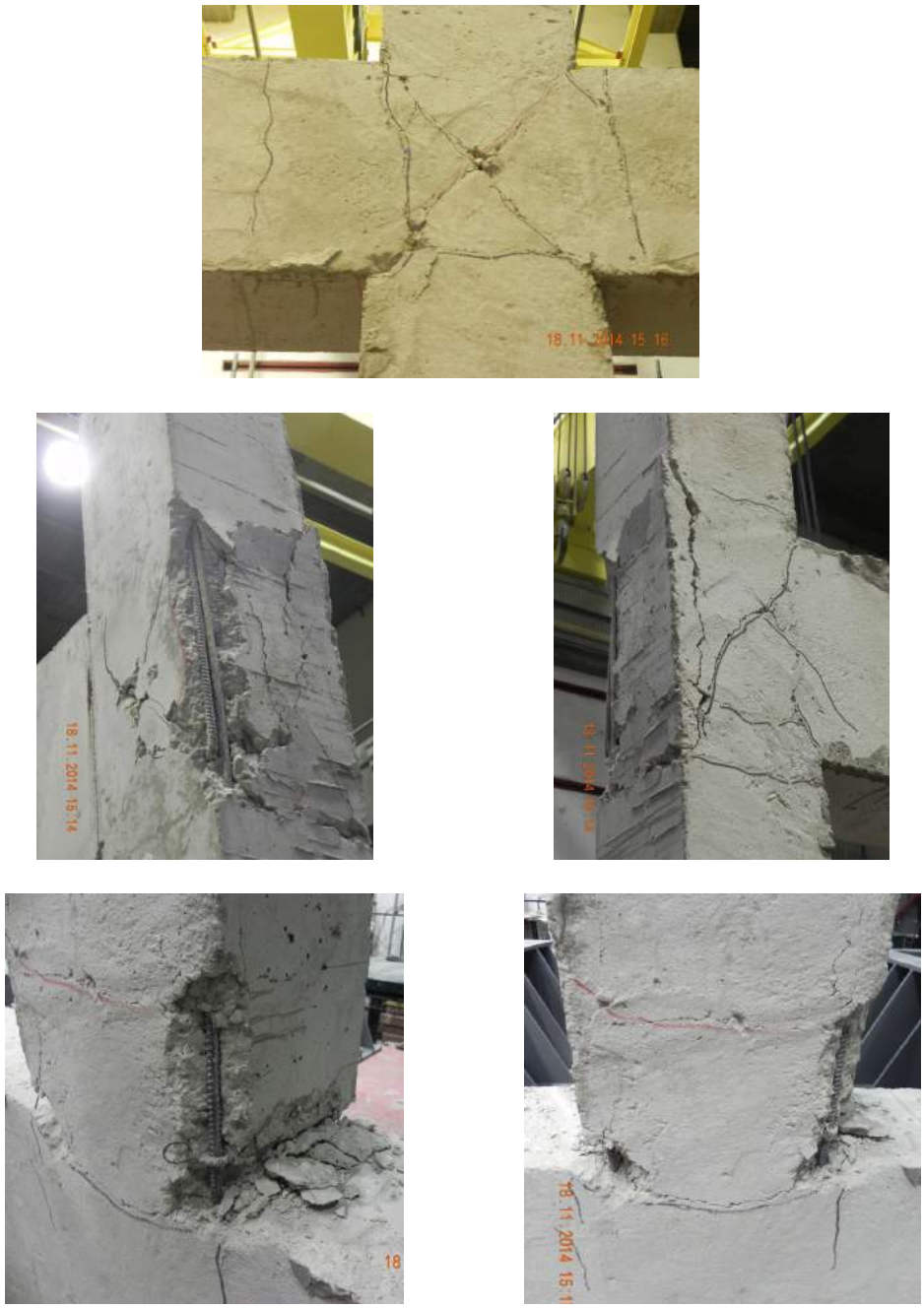

Figure 6.50. From top to bottom: details of the damages exhibited at the beam-column joints and at the base of the columns (courtesy of LNEC)

In addition, it should be recognized that the expressions prescribed to determine the maximum bond strength could be overestimated considering that the expressions proposed in Model Code 2010 are statistically valid for concrete strength higher than 15 MPa. In this case, the mean value considered is 14 MPa and hence, it is possible that the maximum strength values determined with the proposed expressions may be overestimated. In light of the previous considerations, and in order to account for the generalized cracking of cover concrete, the presence of concrete cracks with w_{cr} = 0.5 mm were assumed at different locations, resulting in a reduction of the bond stresses to about half the initial, uncracked, value. Finally, and following the comments made in previous sections of this chapter, in beam-column joints, the influence length (L_i) is assumed to be equal to the width of the joint. On the other hand, in foundation regions, an L_i that approaches twice the value of the foundation height seems to be a more appropriate value.

A summary of the values adopted for the bond-slip parameters is presented in Table 6.8.

Table 6.8. Bond-slip parameters adopted for the PRTD RC frame

Bond-slip parameters	
w_{cr} (m)	0.0005
α	0.4
S_1 (m)	0.0003
S_2 (m)	0.0003
S_3 (m)	0.0004
τ_{max} (MPa)	1.15√fc
τ_f (MPa)	0.2 τ_{max}
$L_{e,column}$ (m)	0.5 *
$L_{i,column/foundation}$ (m)	1.2
$L_{i,column/beam}$ (m)	0.33
$L_{e,beams}$ (m)	0.5 *
$L_{i,beams}$ (m)	0.27

* Approximate value based on available detailing information

A first and simple approach to assess the validity of the numerical model consists in comparing the initial dynamic properties of the structure. Table 6.9 presents the periods of vibration measured in the real structure together with the ones obtained for the different numerical models.

Table 6.9. Comparison between experimental and numerical periods of vibration of the RC frame

Mode	Period of vibration – T (s)			
	Experimental	Numerical		
		No SP	Submitted	Bond-slip model
1	0.263	0.17	0.18	0.19
2	0.244	-	-	-
3	0.128	-	-	-
4	0.083	0.06	0.06	0.06

It should be noted that experimental modes 2 and 3 refer to modal shapes with significant contributions of the auxiliary structure and the shake table system itself. On the other hand, mode 1 and 4 reflect essentially the dynamic properties of the RC frame (1st and 2nd frame modes), being, in this way, appropriate to assess the validity of the dynamic properties of the numerical model.

Based on the table values, it is clear that the numerical model is slightly stiffer than the experimental one. Considering the simplicity of the model, part of this difference may results from the presence of concrete cracks in the frame before the dynamic test. These could result from concrete shrinkage (generalised smeared cracks apparent in Figure 6.47) or due to lifting, transportation and positioning of the frame on the shake table.

Considering the divergences observe in the modal properties, it is not surprising that under low seismic demand, where the structure responds essentially in the elastic domain, the computed displacements are significantly underestimated with respect to the experimental ones, as illustrated in the top plots of Figure 6.51. It is also interesting to note that at the first intensity level (PGA = 0.1 g), all numerical models converge to approximately the same maximum displacements. In fact, at that stage, the structural response is controlled by its dynamic elastic properties wich, as shown in Table 6.9, are very similar regardless of how strain penetration effects are modelled.

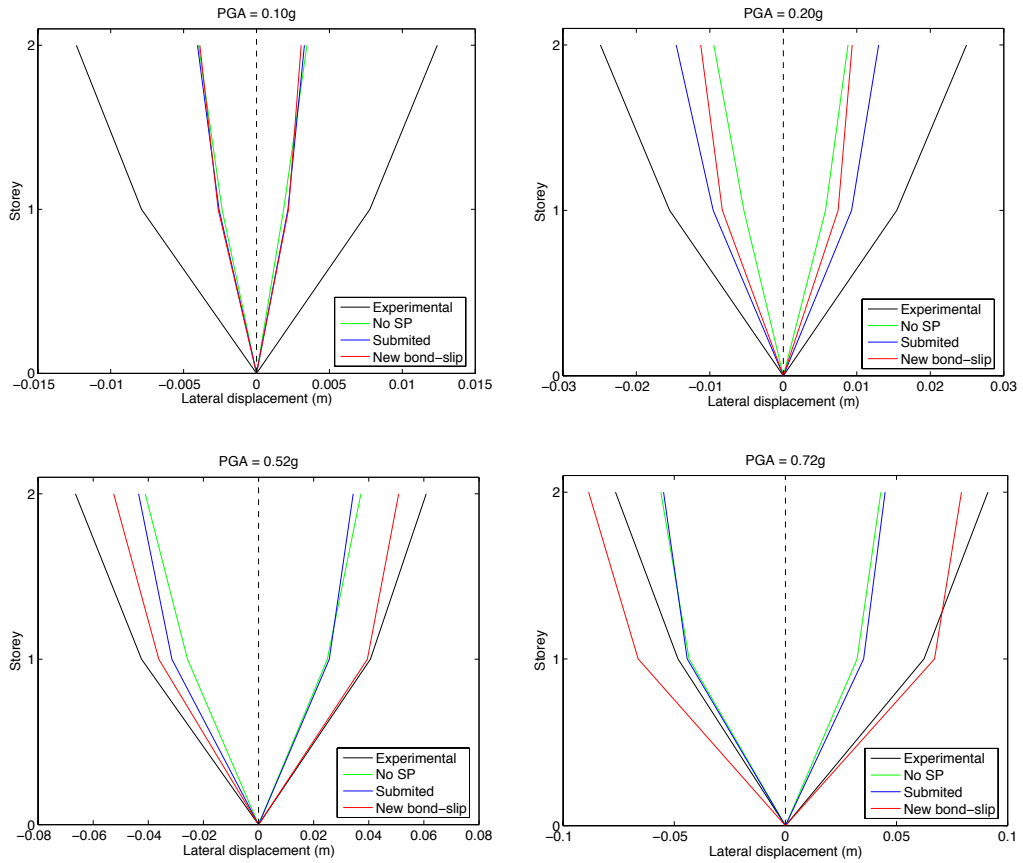

Figure 6.51. Comparison of maximum lateral displacements obtained experimentally with the ones computed with alternative numerical models, for different intensity levels

For increased seismic demand, the maximum displacements computed with the model featuring the new bond-slip model start to diverge from the other numerical models, and approach the maximum displacements measured in the experimental model. The evolution of both numerical and experimental displacements measured during the strongest record is depicted in Figure 6.52 and Figure 6.53.

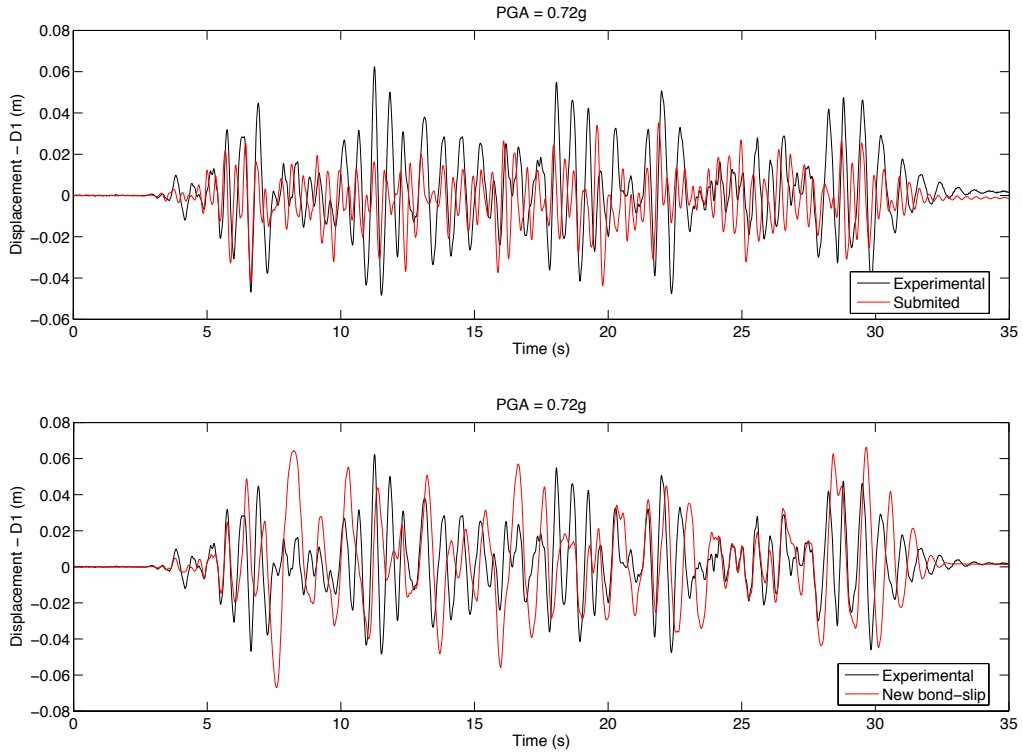

Figure 6.52. Time-history of lateral displacements at point D1 (1st floor) during the record corresponding to a PGA = 0.72g, considering the numerical model submitted (top) and a model featuring the new bond-slip element (bottom)

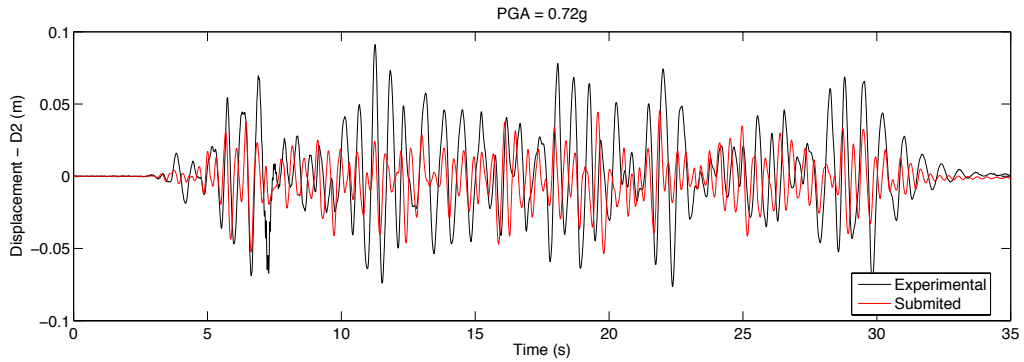

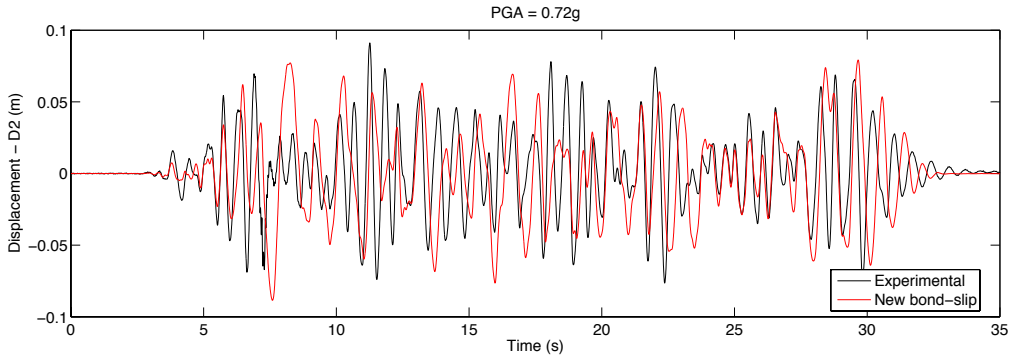

Figure 6.53. Time-history of lateral displacements at point D2 (2nd floor) during the record corresponding to a PGA = 0.72g, considering the numerical model submitted (top) and a model featuring the new bond-slip element (bottom)

Despite the divergences observed, it is clear that the numerical model featuring the new bond-slip model approaches the experimental values in a more satisfactory manner. The good performance of the proposed bond-slip model is emphasized by considering the characteristics of the damage observed in the RC frame during the experimental test. As shown in Figure 6.50, significant and generalized damage was observed at the 1st floor beam-column joints as well as at the interface between the columns and the foundation. The extension of the damage can be appraised by the elongation of the fundamental period of vibration measured before and after the experimental tests, which increased from 0.263 s to 0.5s, respectively. This evolution indicates that the stiffness of the experimental model was reduced to about one fourth of the initial one.

A strong reduction in stiffness is also observed in the numerical model. Figure 6.54, for instance, shoes the hysteretic response of the bond-slip model at the base of the column where the displacements were monitored.

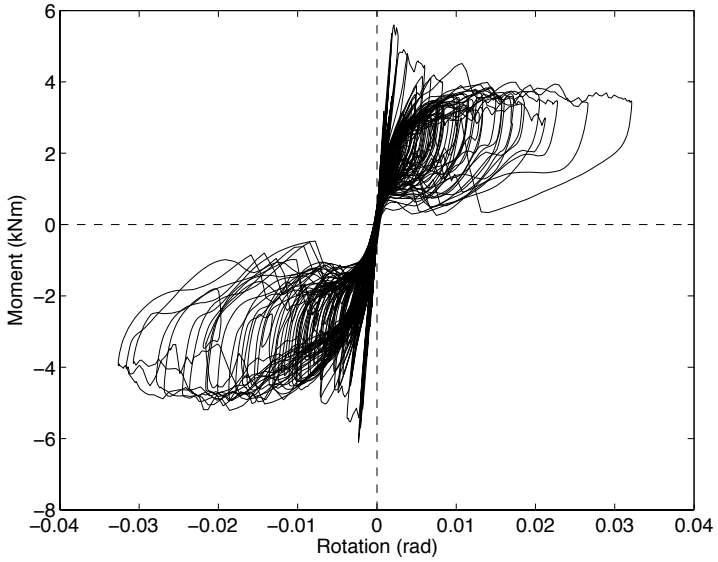

Figure 6.54. Hysteretic behaviour of the bond-slip element at the base of the lateral column below the controlling points, during the five intensity levels

Considering that the bond-slip rotations computed at the base of the other 1st storey columns are of the same order of magnitude of the ones shown above, the previous figure reveals that strain penetration effects have a relevant contribution to the overall lateral deformation of the frame. As the seismic demand increases, the bond-slip stiffness is considerably reduced and the bond-slip rotations are significantly increased. At the same time a pronounced pinching effect (reflected in a classical flag shaped response) is observed, indicating an insufficient anchorage strength of the reinforcement.

The previous comments are in line with the damage observed in the real structure, which is essentially reflected by major cracks developed at the connections between the different RC members (column-foundation and beam-column joints). The absence of plastic hinge regions, where the flexural cracks spread along the elements, indicates that the anchorage strength is not adequate and therefore the slip of the reinforcement results in important member-end rotations.

6.3 SUMMARY

After being implemented in the well-known *SeismoStruct* software package, a detailed parametric study together with an extensive validation procedure was conducted and presented in this chapter.

Making use of the generic properties of a RC bridge column, a sensitivity analysis was carried out considering variations in several parameters used to describe the bond stress-slip constitutive model. This study showed that the proposed model is capable of reflecting important variations in the anchorage strength both at the rebar and sectional level. Among the properties evaluated, it was verified that the consideration of cyclic degradation effects and rebar yielding, together with variations in the embedment and influence lengths or on the surface characteristics of the rebars, may introduce important modifications in the computed response of the bond-slip element.

In order to assess the validity of the numerical predictions, the model was subjected to numerous validations against experimental tests. Considering progressively more complex structures and loading conditions, the model evidenced a very satisfactory behaviour from modelling a simple anchorage rebar subjected to axial load up to a RC frame subjected to dynamic excitation.

Regarding the computational efficiency, the performance of the element is directly dependent on the number of rebars per section and the embedment length of each rebar. Despite the additional computational effort required, as it may double the analysis time depending on the structural properties, its employment in practical applications is very convenient, contributing to significantly improved structural response predictions.

7. CONCLUSIONS AND FUTURE DEVELOPMENTS

7.1 CONCLUSIONS

The main focus of this thesis was centered on the evaluation of current numerical approaches to describe the seismic behaviour of reinforced concrete structures and on the development of innovative models and procedures where needed. In this context, the present work can be divided in two main parts. In the first one, covered in Chapters 2 and 3, a study was undertaken to identify and review some of the modelling challenges faced by engineers and researchers when using fibre-based distributed plasticity beam models to simulate the nonlinear dynamic behaviour of RC framed structures. Based on the conclusions drawn at the end of Chapter 3, the following chapter revises in detail the effects of strain penetration in RC members, while Chapters 5 and 6 develop and validate an innovative bond-slip model applicable to distributed plasticity frame models. The main conclusions arrived at through this endeavour are presented in two groups, in accordance with the abovementioned subdivision.

In the first part, three RC structures tested in past shake table blind prediction challenges were numerically simulated considering alternative modelling options. The goodness-of-fit evaluation of different engineering demand parameters was appraised based on the comparison between lateral displacements and accelerations obtained numerically and the ones measured experimentally. The main conclusions from the sensitivity study carried out are summarised in the following points:

- Based on the detailed analysis of the different error measures it became apparent that amongst the limited sample of concrete models analysed, those proposed by Mander *et al.* [1988] and Kappos and Konstantinidis [1999] provided improved numerical results. Moreover, it was shown that neglecting the tensile strength of the concrete does not impact on the estimates of structural response along nonlinear excursions. However, for response assessment during essentially elastic behaviour, the consideration of the tensile strength is advised, despite potential convergence difficulties. Regarding the steel models, the present study indicates that the well-known Menegotto and Pinto [1973] steel model combines both accuracy and numerical stability.

- Regarding the time-domain integration algorithms, the results obtained in the current parametric study confirm that the Hilber-Hughes-Taylor (HHT) algorithm is generally more accurate and numerically stable than the more conventional Newmark's family of methods. The differences tended to manifest in the computed accelerations (and consequently the members forces), which increased with the time-step size. The computed displacements, on the other hand, were approximately similar for both integration schemes. As a general conclusion, the consideration of a larger time-step (in order to reduce the computation time) should be carefully validated, even when employing the HHT integration algorithm.
- In nonlinear dynamic analysis featuring distributed plasticity elements, most of the energy dissipation mechanisms are already explicitly modelled through hysteresis and, therefore, the amount of equivalent viscous damping (EVD) to be considered should be limited. Based on the analyses undertaken, enhanced performance was obtained for values of critical damping ranging between 0.5 % and 2 %. Numerical analyses with larger levels of EVD tend to underestimate the structural response, whilst the opposite effect takes place when an undamped response is assumed. Considering that both mass-proportional damping and tangent-stiffness proportional damping exhibit specific modelling limitations, it is not really possible to advocate one with respect to the other. Nonetheless, for small percentages of critical damping (as advocated in this study) the impact of these limitations is reduced. Initial stiffness-proportional damping, as expected, provided the worse results and is thus not advised.
- Regarding the consideration of distinct discretization schemes, it was verified that the differences observed at global level (i.e., with respect to nodal displacements and accelerations) were relatively small for the structures considered. On the other hand, the curvatures, and therefore the material strains, are very sensitive to the adopted discretization. With force-based elements, the definition of a number of integration points per element such that the weighted length associated with the extremity IP matches the expected plastic hinge length seems to produce somewhat more accurate results. This observation can be attributed to the presence of tension-shift effects – which 'linearize' the plastic curvature profile along the length of plastification as confirmed by recent experimental findings – and which can only be indirectly accounted for in the framework of Euler-Bernoulli beam theory. The need to develop, calibrate and apply appropriate 'regularization' techniques for fully hardening post-yield moment-curvature relations is therefore confirmed in the present study.
- Despite the obvious limitations in the use of frame elements to simulate the response of RC walls, it is believed that the application of wide-column models can be a reliable and efficient option to simulate the seismic response of such structures. However, this statement seems valid provided that the structural complexity of the model, and hence the potential to present numerical convergence difficulties, does

not prevent the consideration of the most appropriate numerical modelling options. The analyst should bear in mind that in such cases, the employment of more detailed FE approaches is recommended.

- For what concerns the consideration of strain penetration effects, two simple modelling approaches were shown to reduce estimated response errors. In particular, the elongation of the member's length by an estimation of the strain penetration length tends to produce better results than the use of a rotational spring. Nonetheless, it should be acknowledged that both approaches present important limitations, namely in simulating the dynamic properties of the initially undamaged structure, which can be particularly relevant in models with a rotational spring approach. On the other hand, the use of an elongated element yields a slight underestimation of the member's shear forces.

Different studies have pointed to the non-negligible contribution of strain penetration effects (up to about 40 %) to the overall deformation of RC structures. At the same time, as detailed in Section 3.4.3 and briefly noted in the previous bullet point, the difficulty in modelling these effects with distributed plasticity beam elements is apparent. An improved fibre-based bond-slip model was therefore proposed in the second part of this work to address this issue. Its main properties and features are herein briefly described:

- Devised to work as a zero-length element, the model makes use of an advanced bond stress-slip constitutive relation, capable of describing the physical phenomena associated with strain penetration effects for a wide variety of anchorage conditions such as concrete strength, embedment length, rebar surface characteristics, rebar yielding or cyclic degradation, among others. This represents an appreciable advantage with respect to conventional empirical models, as the analyst can make use of state-of-the-art constitutive models that accurately reproduce different anchorage conditions.
- The anchorage region replicates the cross-section of the adjacent RC member and preserves the plane section's hypothesis. Each of the cross-section's rebars is represented through a number of integration points (IPs) distributed along its anchorage length. Using the Forward Euler method, the response at each IP is determined enforcing both equilibrium and compatibility requirements. Despite requiring small (spatial) step sizes, which leads to a large number of integration points, this option presents some advantages with respect to more conventional approaches, as the response along the embedment region of the rebar can be accurately determined, regardless of the boundary conditions and without the need to define an approximated interpolation function representative of the actual distribution of a given parameter (bond stress, rebar strains or slip).

- The bond-slip response at each rebar is iterated following the bisection method. The member-end forces (axial force and bending moments in the two orthogonal directions) are then determined through the integral of the contribution of the cross-sectional fibres (concrete and reinforcement). The element tangent stiffness matrix is derived directly from the bond stress-slip constitutive relation and is used solely to build up the global stiffness matrix required in iterative procedures at the element and structural levels.
- Implemented in the well-known *SeismoStruct* software package, the proposed model proved capable of simulating the strain penetration effects, both at the rebar and sectional levels. Among the assessed properties it was verified that the consideration of cyclic degradation effects and rebar yielding, together with the surface properties of the rebar, embedment length and influence length, led to significant variations in the response of the bond-slip element.
- The accuracy of the bond-slip model was confirmed through numerous comparisons against experimental tests of different structural complexities – starting from a simple anchored rebar subjected to axial load, up to a shake table test of a RC frame.
- In terms of efficiency, the performance of the element is directly dependent on the number of rebars per section and the number of integration points defined for each rebar. Despite the additional computational effort required (it might double the analysis time depending on the structural properties), its employment in practical applications is still very encouraging, contributing to improve significantly the structural response predictions, both at local (curvature and strains) and global levels (displacements and forces).
- Finally, it should be noted that the formulation developed is general in the sense that it can be used to model alternative bond conditions, namely the use of adhesives (e.g., resins) or spliced rebars. In such cases, it is simply required for the analyst to define a more appropriate constitutive relation.

7.2 FUTURE DEVELOPMENTS

It is felt that this work represents a valuable contribution to the understanding and an improvement to the seismic modelling of reinforced concrete structures, particularly regarding strain penetration effects. The following comments on other simulation issues that appear to require further enhancements seem to be pertinent:

- As nonlinear analyses are becoming ever more refined, more sources of energy dissipation are explicitly modelled. However, as demonstrated in this thesis, optimized simulations still require some level of EVD to be considered. In view of the limitations arising from the use of the different EVD models, it seems important to introduce enhanced solutions to reduce (or ideally eliminate) the negative effects

observed in current models. Some recent efforts have been recently carried out on that direction [Chopra and McKenna, 2015].

- Despite the noteworthy benefits observed with the incorporation of bond-slip member-end rotations, the simulation of local-level quantities such as strains and curvatures may diverge significantly from the experimentally measured ones. Therefore, it is critical to continue these developments and implementation efforts, namely with the incorporation of improved regularization techniques in distributed plasticity elements to account for: (i) tension-shift effects and variation in the length of plastification with the level of ductility demand; (ii) localization of the response in the post-peak branch.

With respect to the performance of the proposed bond-slip element, the results presented in Chapter 6 reveal a noteworthy accuracy and stability of the analysis with varying structural properties and loading conditions. Nonetheless, there is certainly some room for improvement regarding the efficiency of the model:

- It appears important to study the introduction of a convergence criteria that could combine both force and displacement related parameters. This option would allow the determination of the equilibrium point along the embedment length of the rebar without the need to go through all the integration points at every iteration, which would render a significantly more efficient algorithm.
- Along the same lines, and despite the difficulties encountered in adopting an implicit integration method, it is believed that a significantly more efficient and equally stable algorithm can be implemented to replace the bisection method used to iterate the axial force at the loaded-end of the rebars.
- Finally, taking into account that the formulation supporting the proposed bond-slip model can be adapted to any general adhesion/friction model, it appears interesting to explore the use of alternative constitutive relations in order to simulate additional physical phenomena (e.g., slippage effects along lap splices).

REFERENCES

Abrams, A. D. [1913] "Tests of Bond between Concrete and Steel," *Bulletin No. 71*, University of Illinois, USA.

ACI [2003] *ACI Committee 408 - Bond and Development of Straight Reinforcing Bars in Tension*, American Concrete Institute.

Addessi, D., and Ciampi, V. [2007] "A regularized force-based beam element with a damage–plastic section constitutive law," *International Journal for Numerical Methods in Engineering*, Vol. 70, No.5, pp. 610–629.

Adhikari, S. [2000] "Damping Models for Structural Vibration," *PhD thesis*, University of Cambridge Engineering Department, England.

Adhikari, S., and Woodhouse, J. [2000] "Towards Identification of a general model of Damping," *Proceedings of 18th International Modal Analysis Conference*, San Antonio, USA.

Adhikari, S., and Woodhouse, J. [2001] "Identification of damping: Part 2, Non-Viscous Damping," *Journal of Sound and Vibration*, Vol. 243, No.1, pp. 63–88.

Almeida, J. P., Das, S., and Pinho, R. [2012] "Adaptive force-based frame element for regularized softening response," *Computers & Structures*, Vol. 102-103, pp. 1–13.

Almeida, J. P., Prodan, O., Rosso, A., and Beyer, K. [2015] "Tests on thin reinforced concrete walls subjected to in-plane and out-of-plane cyclic loading," *Earthquake Spectra* (under review).

Almeida, J. P., Tarquini, D., and Beyer, K. [2014] "Modelling Approaches for Inelastic Behaviour of RC Walls: Multi-level Assessment and Dependability of Results," *Archives of Computational Methods in Engineering*.

Alsiwat, J., and Saatcioglu, M. [1992] "Reinforcement Anchorage Slip under Monotonic Loading," *Journal of Structural Engineering*, Vol. 118, No.9, pp. 2421–2438.

Arakawa, T., and Yamamoto, K. [2004] "Frequencies and Damping Ratios of a High Rise Building Based on Microtremor Measurement," *Proceedings of 13th World Conference on Earthquake Engineering*, Vancouver, Canada.

Ashtiani, M. S., Dhakal, R., and Scott, A. [2013] "Post-yield bond behaviour of deformed bars in high-strength self-compacting concrete," *Construction & Building Materials*, Elsevier Ltd, Vol. 44, No.C, pp. 236–248.

Babazadeh, A., Burgueno, R., and Silva, P. F. [2015] "Use of 3D Finite-Element Models for Predicting Intermediate Damage Limit States in RC Bridge Columns," *Journal of Structural Engineering*, Vol. 141, No.10.

Bae, S., and Bayrak, O. [2008] "Seismic Performance of Full-Scale Reinforced Concrete Columns," *ACI Structural Journal*, Vol. 105, No.2, pp. 123–133.

Bae, S., Mieses, A. M., and Bayrak, O. [2005] "Inelastic Buckling of Reinforcing Bars," *Journal of Structural Engineering*, Vol. 131, No.2, pp. 314–321.

Bentz, A., and Kijewski-Correa, T. [2008] "Predictive Models for Damping in Buildings: The Role of Structural System Characteristics," *Proceedings of 18th Analysis and Computation Specialty Conference*, Vancouver, Canada.

Bernal, D. [1994] "Viscous Damping in Inelastic Structural Response," *Journal of Structural Engineering*, Vol. 120, No.4, pp. 1240–1254.

Berry, M., Lehman, D., and Lowes, L. [2008] "Lumped-Plasticity Models for Performance Simulation of Bridge Columns," *ACI Structural Journal*, Vol. 105, No.3, pp. 270–279.

Beyer, K., Dazio, A., and Priestley, N. [2008] "Inelastic Wide-Column Models for U-Shaped Reinforced Concrete Walls," *Journal of Earthquake Engineering*, Vol. 12, No.sup1, pp. 1–33.

Bianchi, F., Sousa, R., and Pinho, R. [2011] "Blind Prediction of a Full-Scale RC Bridge Column Tested Under Dynamic Conditions," *Proceedings of 3rd International Conference on Computational Methods in Structural Dynamics & Earthquake Engineering*, Corfu, Greece.

Bigaj, A. J. [1995] "Bopd behaviour of deformed bars in NSC and HSC," *Experimental Study*, Delft University of Technology, Netherlands.

Blandon, C. [2012] "Sensibility of Non Linear Time History Analysis of a RC Column Using Large Scale Shaking Table Results as Benchmark," *Proceedings of 15th World Conference on Earthquake Engineering*, Lisbon, Portugal.

Brownjohn, J., and Carden, P. [2007] "Reliability of Frequency and Damping Estimates from Free Vibration Response," *Proceedings of 2nd International Operational Modal Analysis Conference,* Copenhagen, Denmark.

Calabrese, A., Almeida, J. P., and Pinho, R. [2010] "Numerical Issues in Distributed Inelasticity Modeling of RC Frame Elements for Seismic Analysis," *Journal of Earthquake Engineering*, Vol. 14, No.sup1, pp. 38–68.

Campos Costa, A., Morais, P., Wainwright, B., and Martins, A. [1996] *Characterization of the new LNEC Shaking Table*, Laboratório Nacional de Engenharia Civil. Lisbon, Portugal.

Casanova, A., Jason, L., and Davenne, L. [2012] "Bond slip model for the simulation of reinforced concrete structures," *Engineering Structures*, Vol. 39, pp. 66–78.

Casanova, A., Jason, L., Davenne, L., and Pinelli, X. [2013] "Confinement effects on the steel-concrete bond strength and pull-out failure," *Engineering Fracture Mechanics*, Vol. 97, No. 1, pp. 92–104.

Caughey, T. K. [1960] " Classical normal modes in damped linear dynamic systems," *Journal of Applied Mechanics*, No.27, pp. 269–271.

CEN. [2004a] *Eurocode 8: Design of structures for earthquake resistance - Part 1: General rules, seismic actions and rules for buildings*, EN 1998-1, Comité Européen de Normalisation, Brussels, Belgium.

CEN. [2004b] *Eurocode 2: Design of concrete structures - Part 1-1: General rules and rules for buildings*, EN 1992-1-1, Comité Européen de Normalisation, Brussels, Belgium.

CEN. [2005] *Eurocode 8: Design of structures for earthquake resistance - Part 3: Assessment and retrofitting of buildings*, EN 1998-3, Comité Européen de Normalisation, Brussels, Belgium.

Chao, S.-H., Naaman, A. E., and Parra-Montesinos, J. P. [2009] "Bond Behavior of Reinforcing Bars in Tensile Strain-Hardening Fiber-Reinforced Cement Composites," *ACI Structural Journal*, Vol. 106, No.6, pp. 897–906.

Choi, C. O., Hadje-Ghaffari, H., Darwin, D., and McCabe, S. L. [1990] *Bond of Epoxy-Coated Reinforcement to Concrete: Bar Parameters*, Center for Research, University of Kansas, USA.

Chopra, A. K. [1995] *Dynamic of Structures*, Prentice Hall, Englewood Cliffs, New Jersey, USA.

Chopra, A. K. and McKenna, F. [2015] "Modeling viscous damping in nonlinear response history analysis of buildings for earthquake excitation, " *Earthquake Engineering and Structural Dynamics*.

Ciampi, V., Eligehausen, R., Bertero, V., and Popov, E. [1981] "Analytical model for deformed bar bond under generalized excitations," *Proceedings of IABSE Colloquium on Advanced Mechanics in Reinforced Concrete*, Delft, Netherlands.

Clark, A. P. [1946] "Comparative Bond Efficiency of Deformed Concrete Reinforcing Bars," *Journal of Research of the National Bureau of Standards*, Vol. 37, pp. 399–407.

Coleman, J., and Spacone, E. [2001] "Localization Issues in Force-Based Frame Elements," *Journal of Structural Engineering*, Vol. 127, No.11, pp. 1257–1265.

Correia, A. A. [2011] "A Pile-Head Macro-Element Approach to Seismic Design of Monoshaft-Supported Bridges," *PhD Thesis*, Università degli Studi di Pavia, IUSS Pavia, Pavia, Italy.

Correia, A. A., Almeida, J. P., and Pinho, R. [2013] "Seismic Energy Dissipation in Inelastic Frames: Understanding State-of-the-Practice Damping Models," *Structural Engineering International*, Vol. 23, No.2, pp. 148–158.

Correia, A. A., Almeida, J. P., and Pinho, R. [2015] "Force-based higher-order beam element with flexural-shear-torsional interaction in 3D frames. Part I: Theory," *Engineering Structures*, Vol. 89, pp. 204–217.

Cosenza, E., and Prota, A. [2006] "Experimental Behaviour and Numerical Modelling of Smooth Steel Bars Under Compression," *Journal of Earthquake Engineering*, Vol. 10, No.3, pp. 313–329.

Costa, A., Campos Costa, A., Candeias, P., Guerreiro, L., and Mendes, L. [2012] *15WCEE Blind test challenge - Design report*, World Conference on Earthquake Engineering, Lisbon, Portugal.

Cowel, A. D., Bertero, V. V. and Popov, E. P. [1982] *An Investigation of Local Bond Slip Under Variation of Specimen Parameters*, Earthquake Engineering Research Center, Report No. UCB/EERC-82/23, University of California, Berkeley, USA.

CSI [2009] "SAP2000 v.14," Computers and Structures, Inc.

Darwin, D., and Graham, E. [1993] "Effect of deformation height and spacing on bond strength of reinforcing bars," *Report*, Center for Research, University of Kansas, USA.

Darwin, D., Tholen, M., Idun, E., and Zuo, J. [1996] "Splice Strength of High Relative Rib Area Reinforcing Bars," *ACI Structural Journal*, Vol. 93, No.1, pp. 95–107.

Dorr, K. [1978] "Bond Behavior of Ribbed Reinforcement under Transverse Pressure," *Proceedings of IASS Symposium on Nonlinear Behaviour of Reinforced Concrete Spatial Structures*, Preliminary Report, Werner Verner, Dusseldorf.

Eligehausen, R., Popov, E., and Bertero, V. [1983] "Local Bond Stress-Slip Relationships of Deformed Bars Under Generalized Excitations," *Report No. UCB/EERC-83/23*, Earthquake Engineering Research Center, University of California, Berkeley, USA.

Erwin, S., Kijewski-Correa, T., and Yoon, S. W. [2007] "Full Scale Verification of Dynamic Properties from Short Duration Records," *Proceedings of Structures Congress: New Horizons and Better Practices*, Long Beach, California, USA.

Fang, J. Q., Jeary, A., Li, Q. S., and Wong, C. K. [1999] "Random damping in buildings and its AR model," *Journal of Wind Engineering and Industrial Aerodynamics*, No.79, pp. 159–167.

Fardis, M. [2009] *Seismic Design, Assessment and Retrofitting of Concrete Buildings*, Springer.

Feng, Y., Goodnight, J. C., Kowalsky, M. J., and Nau, J. M. [2015] "The Effects of Load History and Design Variables on Performance Limit States of Circular Bridge Columns – Volume 3: Analysis Methods," *Technical Report,* Alaska Department of Transportation and Public Facilities, USA.

Feng, Y., Kowalsky, M. J., and Nau, J. M. [2014] "Fiber-Based Modeling of Circular Reinforced Concrete Bridge Columns," *Journal of Earthquake Engineering*, Vol. 18, No.5, pp. 714–734.

Fernandes Ruiz, M., Muttoni, A., and Gambarova, P. G. [2007] "Analytical Modeling of the Pre- and Postyield Behavior of Bond in Reinforced Concrete," *Journal of Structural Engineering*, Vol. 133, No.10, pp. 1364–1372.

fib [2000] *fib Bulletin10: Bond of reinforcement in concrete*, International Federation for Structural Concrete, Lausanne, Switzerland.

fib [2011] *Model Code 2010*, International Federation for Structural Concrete, Lausanne, Switzerland.

fib [2014] *Bond and Anchorage of Embedded Reinforcement: Background to the fib Model Code for Concrete Structures 2010*, International Federation for Structural Concrete, Lausanne, Switzerland.

Filippou, F., Popov, E., and Bertero, V. [1983] "Effects of Bond Deterioration on Hysteretic Behaviour of Reinforced Concrete Joints," *Report No. UCB/EERC-83/19*, Earthquake Engineering Research Center, University of California, Berkeley, USA..

Fragiadakis, M., Pinho, R., and Antoniou, S. [2008] "Modelling Inelastic Buckling of Reinforcing Bars Under Earthquake Loading," *Computational Structural Dynamics and Earthquake Engineering: Structures and Infrastructures*, Vol. 2, pp. 363–377.

Goodnight, J. C., Feng, Y., Kowalsky, M. J., and Nau, J. M. [2015a] "The Effects of Load History and Design Variables on Performance Limit States of Circular Bridge Columns – Volume 2: Experimental Observations," *Technical Report,* Alaska Department of Transportation and Public Facilities, USA.

Goodnight, J. C., Feng, Y., Kowalsky, M. J., and Nau, J. M. [2015b] "The Effects of Load History and Design Variables on Performance Limit States of Circular Bridge Columns – Volume 1," *Technical Report,* Alaska Department of Transportation and Public Facilities, USA.

Goodnight, J. C., Kowalsky, M. J., and Nau, J. M. [2012] "Experimental Observations on the Effect of Load History on Performance Limit States of Circular Bridge Columns," *Proceedings of 15th World Conference on Earthquake Engineering*, Lisbon, Portugal.

Goodnight, J. C., Kowalsky, M. J., and Nau, J. M. [2014] "A New Look at Strain Limits and Plastic Hinge Lengths for Reinforced Concrete Bridge Columns," *Proceedings of 10th U.S. National Conference on Earthquake Engineering*, Anchorage, USA.

Hall, J. [2006] "Problems encountered from the use (or misuse) of Rayleigh damping," *Earthquake Engineering & Structural Dynamics*, Vol. 35, No.5, pp. 525–545.

Hilber, H., Hughes, T., and Taylor, R. [1977] "Improved Numerical Dissipation for Time Integration Algorithms in Structural Dynamics," *Earthquake Engineering & Structural Dynamics*, Vol. 5, pp. 283–292.

Hines, E., Restrepo, J. I., and Seible, F. [2004] "Force-Displacement Characterization of Well-Confined Bridge Piers," *ACI Structural Journal*, Vol. 101, No.4, pp. 537–548.

Jacobsen, L. S. [1930] "Steady forced vibrations as influenced by damping," *ASME Transactions*, Vol. 52, No.1, pp. 169–181.

Jeary, A. [1986] "Damping in tall buildings - A mechanism and a predictor," *Earthquake Engineering & Structural Dynamics*, Vol. 14, No.5, pp. 733–750.

Jeary, A. [1997] "Damping in Structures," *Journal of Wind Engineering and Industrial Aerodynamics*, No.72, pp. 345–355.

Jehel, P., Léger, P., and Ibrahimbegovic, A. [2013] "Initial versus tangent stiffness-based Rayleigh damping in inelastic time history seismic analyses," *Earthquake Engineering & Structural Dynamics*, Vol. 43, No.3, pp. 467–484.

Jendele, L., and Cervenka, J. [2006] "Finite element modelling of reinforcement with bond," *Computers & Structures*, Vol. 84, No.28, pp. 1780–1791.

Jirásek, M. [1997] "Analytical and Numerical Solutions for Frames with Softening Hinges," *Journal of Engineering Mechanics*, Vol. 123, No.1, pp. 8–14.

Kappos, A. J., and Konstantinidis, D. [1999] "Statistical analysis of confined high strength concrete," *Materials and Structures*, Vol. 32, No.10, pp. 734–748.

Kareem, A., and Gurley, K. [1996] "Damping in structures: its evaluation and treatment of uncertainty," *Journal of Wind Engineering and Industrial Aerodynamics*, No.59, pp. 131–157.

Krawinkler, H. [2006] "Importance of good nonlinear analysis," *The Structural Design of Tall and Special Buildings*, Vol. 15, No.5, pp. 515–531.

Lagomarsino, S. [1993] "Forecast Models for Damping and Vibration Periods of Buildings," *Journal of Wind Engineering and Industrial Aerodynamics*, Vol. 48, No.2-3, pp. 221–239.

Lepage, A., Delgado, S., and Dragovich, J. [2008] "Appropriate Models For Practical Nonlinear Dynamic Analysis of Reinforced Concrete Frames," *Proceedings of 14th World Conference on Earthquake Engineering*, Beijing, China.

Louro, A. [2014] "Caracterização da aderência de varões nervurados sujeitos a ações repetidas e alternadas," *PhD Thesis*, Universidade Nova de Lisboa, Lisbon, Portugal. (in Portuguese)

Lowes, L. [1999] "Finite Element Modeling of Reinforced Concrete Beam-Column Bridge Connections," *PhD Thesis*, University of California, Berkeley, USA.

Luu, H., Ghorbanirenani, I., Léger, P., and Tremblay, R. [2013] "Numerical Modeling of Slender Reinforced Concrete Shear Wall Shaking Table Tests Under High-Frequency Ground Motions," *Journal of Earthquake Engineering*, Vol. 17, No.4, pp. 517–542.

Madas, P., and Elnashai, A. [1992] "A New Passive Confinement Model for the Analysis of Concrete Structures Subjected to Cyclic and Transient Dynamic Loading," *Earthquake Engineering & Structural Dynamics*, Vol. 21, No.5, pp. 409–431.

Malvar, L. J. [1991] "Bond of Reinforcement Under Controlled Confinement," *Technical Note*, Naval Civil Engineering Laboratory, Port Hueneme, USA.

Mander, J., Priestley, N., and Park, R. [1988] "Theoretical Stress-Strain Model for Confined Concrete," *Journal of Structural Engineering*, Vol. 114, No.8, pp. 1804–1826.

Mansuri, M. [2009] "Torsional Efects on the Inelstic Seismic Response of Structures," *PhD Thesis*, University of Southern California, USA.

Martinez-Rueda, J., and Elnashai, A. [1997] "Confined concretemodel under cyclic load," *Materials and Structures*, Vol. 30, No.3, pp. 139–147.

McKenna, F., Fenves, G. L., Scott, H. M., and Jeremic, B. [2000] "Open system for earthquake engineering simulation (OpenSEES:)." *Pacific Earthquake Engineering Research Center, University of California*, CA.

Melo, J., Fernandes, C., Varum, H., Rodrigues, H., Costa, A., and Arêde, A. [2011] "Numerical modelling of the cyclic behaviour of RC elements built with plain reinforcing bars," *Engineering Structures*, Vol. 33, No.2, pp. 273–286.

Mendes, L., and Castro, L. [2013] "A new RC bond model suitable for three-dimensional cyclic analyses," *Computers & Structures*, Vol. 120, pp. 47–64.

Menegotto, M., and Pinto, P. [1973] "Method of Analysis for Cyclically Loaded R.C. Plane Frames Including Changes in Geometry and Non-Elastic Behavior of Elements under Combined Normal Force and Bending," *Proceedings of Symposium Resistance and Ultimate Deformability of Structures Acted on by Well-Defined Repeated Loads*, Lisbon, Portugal.

Menq, C., and Yang, B. [1998] "Non-Linear Spring Resistance and Friction Damping of Frictional Constraint Having Two-Dimensional Motion," *Journal of Sound and Vibration*, Vol. 217, No. 1, pp. 127–143.

Monti, G., and Nuti, C. [1992] "Nonlinear Cyclic Behavior of Reinforcing Bars Including Buckling," *Journal of Structural Engineering*, Vol. 118, No.12, pp. 3268–3284.

Monti, G., and Spacone, E. [2000] "Reinforced Concrete Fiber Beam Element With Bond-Slip," *Journal of Structural Engineering*, Vol. 126, No.6, pp. 654–661.

Monti, G., Filippou, F., and Spacone, E. [1997] "Finite Element for Anchored Bars under Cyclic Load Reversals," *Journal of Structural Engineering*, Vol. 123, No.5, pp. 614–623.

Morita, K., and Kanda, J. [1996] "Experimental Evaluation of the Amplitude Dependent Natural Period and Damping Ratio of a Multi-Story Structure," *Proceedings of 11th World Conference on Earthquake Engineering*, Acapulco, Mexico.

Mortezaei, A., and Ronagh, H. R. [2011] "Plastic hinge length of reinforced concrete columns subjected to both far-fault and near-fault ground motions having forward directivity," *The Structural Design of Tall and Special Buildings*, Vol. 22, No.12, pp. 903–926.

Muto, K. [1956] "Seismic Analysis of Reinforced Concrete Buildings," *Proceedings of 1st World Conference on Earthquake Engineering*, Berkeley, USA.

Nagashima, T., Sugano, S., Kimura, H., and Ichikawa, A. [1992] "Monotonic axial compression test on ultra high strength concrete tied columns," *10th World Conference on Earthquake Engineering*, Madrid, Spain.

Neuenhofer, A., and Filippou, F. [1997] "Evaluation of Nonlinear Frame Finite-Element Models," *Journal of Structural Engineering*, Vol. 123, No.7, pp. 958–966.

Newmark, N. [1959] "A Method of Computation for Structural Dynamics," *Journal of the Engineering Mechanics Division, ASCE*, Vol. 85, pp. 67–94.

Orangun, C., Jirsa, J., and Breen, J. [1977] "A reevaluation of Test Data on Development Length and Splices," *ACI Structural Journal*, Vol. 74, No. 3, pp. 114–122.

Otani, S., and Sozen, M. [1972] "Behavior of Multistory Reinforced Concrete Frames During Earthquakes," *Report*, University of Illinois, Urbana, USA.

Pam, H. J., and Ho, J. C. M. [2009] "Length of critical region for confinement steel in limited ductility high-strength reinforced concrete columns," *Engineering Structures*, Vol. 31, No.12, pp. 2896–2908.

PEER/ATC. [2010] *"PEER/ATC-72-1: Modeling and acceptance criteria for seismic design and analysis of tall buildings*," Pacific Earthquake Engineering Research Center / Applied Technology Council, USA.

Petrini, L., Maggi, C., Priestley, N., and Calvi, G. M. [2008] "Experimental Verification of Viscous Damping Modeling for Inelastic Time History Analyzes," *Journal of Earthquake Engineering*, Vol. 12, No.sup1, pp. 125–145.

Pina, H. [1995] *Métodos Numéricos*, McGraw-Hill, New York, USA. (in Portuguese)

Popov, E. [1984] "Bond and Anchorage of Reinforcing Bars Under Cyclic Loading," *ACI Journal*, Vol. 81, No.4, pp. 340–349.

Priestley, N., and Grant, D. [2005] "Viscous Damping in Seismic Design and Analysis," *Journal of Earthquake Engineering*, Vol. 9, No.2, pp. 229–255.

Priestley, N., Calvi, G. M., and Kowalsky, M. J. [2007] *Displacement-Based Seismic Design of Structures*, IUSS Press, Pavia, Italy.

Priestley, N., Seible, F., and Calvi, G. M. [1996] *Seismic Design and Retrofit of Bridges*, John Wiley & Sons Inc., New Jersey, USA.

Rayleigh, L. [1877] *The Theory of Sound*, Dover Publications, New York, USA.

Richard, B., and Chaudat, T. [2014] "Presentation of the SMART 2013 International Benchmark," *Proceedings of Workshop SMART 2013,* Paris, France.

Ruderman, M., and Torsen, B. [2010] "Friction Model with Elasto-Plasticity for Advanced Control Applications," *Proceedings of IEEE/ASME International Conference on Advanced Intelligent Mechatronics*, Montréal, Canada.

Saatcioglu, M., Alsiwat, J., and Ozcebe, G. [1992] "Hysteretic Behavior of Anchorage Slip in R/C Members," *Journal of Structural Engineering*, Vol. 118, No.9, pp. 2439–2458.

Sakai, J., and Unjoh, S. [2007] "Shake Table Experiment on Circular Reinforced Concrete Bridge Column under Multidirectional Seismic Excitation," *Proceedings of Research Frontiers at Structures Congress*, Long Beach, USA.

Salem, H., and Maekawa, K. [2004] "Pre- and Postyield Finite Element Method Simulation of Bond of Ribbed Reinforcing Bars," *Journal of Structural Engineering*, Vol. 130, No.4, pp. 671–680.

Satake, N., Suda, K.-I., Arakawa, T., Sasaki, A., and Tamura, Y. [2003] "Damping Evaluation Using Full-Scale Data of Buildings in Japan," *Journal of Structural Engineering*, Vol. 129, No.4, pp. 470–477.

Schoettler, M. J., Restrepo, J. I., Guerrini, G., Duck, D. E., and Carrea, F. [2015] "A Full-Scale, Single-Column Bridge Bent Tested by Shake-Table Excitation," *PEER Report No. 2015/02*, Pacific Earthquake Engineering Research Center, University of California, Berkeley, USA.

Scott, M., and Fenves, G. [2006] "Plastic Hinge Integration Methods for Force-Based Beam-Column Elements," *Journal of Structural Engineering*, Vol. 132, No.2, pp. 244–252.

Scott, M., and Hamutçuoglu, O. M. [2008] "Numerically consistent regularization of force-based frame elements," *International Journal for Numerical Methods in Engineering*, Vol. 76, No.10, pp. 1612–1631.

Seismosoft [2013] "SeismoStruct v.6.5. - A computer program for static and dynamic nonlinear analysis of framed structures," available online from http://www.seismosoft.com

Sezen, H., and Moehle, J. [2004] "Strength and Deformation Capacity of Reinforced Concrete Columns with Limited Ductility," *Proceedings of 13th World Conference on Earthquake Engineering*, Vancouver, Canada.

Sezen, H., and Setzler, E. [2008] "Reinforcement Slip in Reinforced Concrete Columns," *ACI Structural Journal*, Vol. 105, No. 3 pp. 280–289.

Sheikh, S. A., and Uzumeri, S. M. [1982] "Analytical model for concrete confined in tied columns," *Journal of the Structural Division*, Vol. 108, No.ST12, pp. 2703–2722.

Shima, H., Chou, L.-L., and Okamura, H. [1987a] "Bond characteristics in post-yield range of deformed bars," *Translation from Proceedings of JSCE*, Vol. 6, No. 378, pp. 113–124.

Shima, H., Chou, L.-L., and Okamura, H. [1987b] "Micro and Macro Models for Bond in Reinforced Concrete," *Journal of the Faculty of Engineering, U. Tokyo*, Vol. 39, No.2, pp. 133–194.

Smyrou, E., Priestley, N., and Carr, A. [2011] "Modelling of elastic damping in nonlinear time-history analyses of cantilever RC walls," *Bulletin of Earthquake Engineering*, Vol. 9, No. 5, pp. 1559–1578.

Sousa, R., Eroğlu, T., Kazantzidou Firtinidou, D., Kohrangi, M., Sousa, L., Nascimbene, R., and Pinho, R. [2012] "Effect of Different Modelling Assumptions on the Seismic Response of RC Structures," *Proceedings of 15th World Conference on Earthquake Engineering*, Lisboa, Portugal.

Sritharan, S., Priestley, N., and Seible, F. [2000] "Nonlinear finite element analyses of concrete bridge joint systems subjected to seismic actions," *Finite Elements in Analysis and Design*, Vol. 36, No.3-4, pp. 215–233.

Tassios, T. P., [1979] *Properties of Bond Between Concrete and Steel under Load Cycles Idealizing Seismic Actions*, Comité Euro-Iternational Du Béton, Bulletin No. 131, Paris.

Terzic, V., Schoettler, M. J., Restrepo, J. I., and Mahin, S. [2015] "Concrete Column Blind Prediction Contest 2010: Outcomes and Observations," *PEER Report No. 2015/01*, Pacific Earthquake Engineering Research Center, University of California, Berkeley, USA.

Theil, H. [1961] *Economic forecasts and policy*, North-Holland Publishing Company, Amsterdam, Netherlands.

Ueda, T., Lin, I., and Hawkins, N. M. [1986] "Beam Bar Anchorage in Exterior Column-Beam Connections," *ACI Journal*, Vol. 83, No.3, pp. 412–422.

Untrauer, R., Henry, R.L. [1965] "Influence of Normal Pressure on Bond Strength," *ACI Journal*, Vol. 62, No. 5.

Verderame, G. M., Fabbrocino, G., and Manfredi, G. [2008] "Seismic response of r.c. columns with smooth reinforcement. Part I: Monotonic tests," *Engineering Structures*, Vol. 30, No.9, pp. 2277–2288.

Verderame, G. M., Ricci, P., De Carlo, G., and Manfredi, G. [2009] "Cyclic bond behaviour of plain bars. Part I: Experimental investigation," *Construction & Building Materials*, Elsevier Ltd, Vol. 23, No.12, pp. 3499–3511.

Viwathanatepa, S., Popov, E., and Bertero, V. [1979] "Effects of generalized loadings on bond of reinforcing bars embedded in confined concrete blocks," *Report No. UCB/EERC-79/22*, Earthquake Engineering Research Center, University of California, Berkeley.

Wakabayashi, M. [1986] "Chapter 2 - *Design of earthquake-resistant buildings*," McGraw-Hill, New York, USA.

Wyatt, T. A. [1977] "Mechanisms of damping," *Proceedings of Symposium on dynamic behavior of bridges,* Transport and Road Research Laboratory, Crowthorne, England.

Yalciner, H., Eren, O., and Sensoy, S. [2012] "An experimental study on the bond strength between reinforcement bars and concrete as a function of concrete cover, strength and corrosion level," *Cement and Concrete Research*, Vol. 42, No.5, pp. 643–655.

Yang, B., and Menq, C. [1998] "Characterization of 3D Contact Kinematics and Prediction of Resonant Response of Structures Having 3D Frictional Constraint," *Journal of Sound and Vibration*, Vol. 217, No. 5, pp. 909–925.

Yazgan, U., and Dazio, A. [2011a] "Simulating Maximum and Residual Displacements of RC Structures: I. Accuracy," *Earthquake Spectra*, Vol. 27, No.4, pp. 1187–1202.

Yazgan, U., and Dazio, A. [2011b] "Simulating Maximum and Residual Displacements of RC Structures: II. Sensitivity," *Earthquake Spectra*, Vol. 27, No.4, pp. 1203–1218.

Zhao, J., and Sritharan, S. [2007] "Modeling of Strain Penetration Effects in Fiber-Based Analysis of Reinforced Concrete Structures," *ACI Structural Journal*, Vol. 104, No.2, pp. 133–141.

Zuo, J., and Darwin, D. [2000] "Splice Strength of Conventional and High Relative Rib Area Bars in Normal and High-Strength Concrete," *ACI Structural Journal*, Vol. 97, No.4, pp. 630–641.